FIELD INVESTIGATION AND NUMERICAL MODELLING OF MICRO SCREW PILES UNDER AXIAL AND LATERAL LOADINGS

by

Mujtaba Khidri

A thesis submitted in partial fulfillment of the requirements for the degree of

Doctor of Philosophy

in

GEOTECHNICAL ENGINEERING

Department of Civil and Environmental Engineering

University of Alberta

ABSTRACT

A micro screw pile is a multi-sectional pile that consists of a smooth segment at the top, a threaded segment in the middle and a tapered segment at the bottom. Due to limited information on the performance, design and behaviour of micro screw piles, further research is required to study the axial, axial cyclic and lateral behaviors and capacities of the micro screw piles in cohesive and cohesionless soils. Therefore, six types of micro screw piles were tested at three sites with various soil compositions.

An axial load field test program was performed on full-scale micro screw piles installed in a cohesionless soil site (Sandpit) using the torque method. Selected piles were instrumented with axial strain gauges (SGs). A geotechnical site investigation was carried out involving cone penetration and standard penetration tests. A total of 41 piles, including eight instrumented piles, were tested. The ultimate capacities and the distributions of unit shaft resistances were determined. The shaft resistance was then compared with the tip resistance from cone penetrometer tests (CPTs). The coefficient of lateral earth pressure and combined shaft resistance factor was determined over the individual pile segment, and then an effective stress method based on the combined shaft resistance factor was used to estimate the capacity of 41 test piles. A theoretical torque model was adopted using the CPT sleeve friction. The model was verified by comparing the estimated torque to the measured torque of the test piles. In the end, empirical torque factors were developed.

An axial cyclic load field test program was carried out at Sandpit to examine the axial cyclic response of the micro screw piles. Six one-way compressive and load-controlled axial cyclic tests were performed. Three piles were instrumented with axial SGs to measure the distribution of the unit shaft resistance during the cyclic test. The pile-head cumulative displacement, stiffness and equivalent damping ratios were determined from the load-displacement curves. The effect of

the initial factor of safety on cyclic behavior was examined. The re-distribution of the unit shaft resistances of the individual pile segments was obtained. The equivalent damping ratio and stiffness of the individual pile segments were obtained from the unit shaft resistance hysteresis.

A lateral load field test program was carried out that included six piles at a cohesive soil site in Sherwood Park, 22 at a cohesive soil site on South Campus and 18 at Sandpit. Initially, the lateral capacity, pile shaft response and failure mode of the pile were investigated. Afterward, the effectiveness of Broms's method in estimating the piles' capacities was assessed once the pile failure mode was determined. The estimated capacities of the piles using only shaft resistance and neglecting the effect of the thread are comparable to the measured capacities of the piles.

Numerical models based on the Beam-on-Nonlinear-Winkler-Foundation (BNWF) method were developed on the OpenSEES platform to predict the lateral responses of the micro screw piles at these three sites. Different components of the soil-pile interaction responses, including the lateral shaft resistance, the vertical shaft resistance, the bearing resistance of the threads and the lateral thread resistance, were represented using materials with uniaxial load-deformation responses, such as *p-y*, *t-z*, *q-z* and *t-z* curves, respectively. The failure mode was investigated by examining the distribution of the pile deformation, the bending moment and the shear stress of the pile as well as the lateral normal forces of the soil on the pile shaft. The contributions of different components of soil-pile reactions were assessed. The effect of the thread on the lateral capacity of the pile was evaluated. A sensitivity analysis was conducted to examine the effect of different soil properties and specific pile geometrical features on the lateral response of the pile.

Preface

A version of Chapter 3 has been published in the Canadian Geotechnical Journal (Khidri and Deng 2022), and Chapter 4 has been published in the journal Soil Dynamics and Earthquake Engineering (Khidri and Deng 2021), which the candidate and Dr. Lijun Deng co-authored. The candidate contribution to the content of this research included planning, coordinating, managing and conducting the site characterization program, field test program, data processing and numerical simulation.

The geotechnical site investigation at Sherwood Park was conducted by Guo (2017). The geotechnical investigation at South Campus was jointly conducted by Guo (2017) and the candidate. Additional raw cone penetration test data were obtained from Zhang (1999). The raw data obtained from the geotechnical site investigation at Sherwood Park and South Campus were then analyzed by the candidate to obtain the soil properties, including unit weight, relative density, undrained shear strength and friction angle. In addition, the lateral load field test of piles at Sherwood Park was conducted by Moira Guo. The raw data obtained from the lateral load field test at Sherwood Park were then gathered, interpreted and analyzed by the candidate.

Versions of Chapters 5 and 6 are being prepared as two journal manuscripts.

Acknowledgements

I would like to extend my gratitude to my parents, siblings and wife for supporting me during this program. To my parents, your vision lightened my path to pursue education. Thank you to my father (Ata) for giving me rides and to my mother (Apa) for making lunch for me every day. To my wife and siblings, I thank you for partnering with me to paddle through life's challenges and enjoy its blessings.

I am grateful to Dr. Lijun Deng for serving as my supervisor. With your guidance, consistent support, and constructive feedback, you have opened a new horizon in my career. It was a joy to explore my passion in geotechnical engineering in the exciting academic environment that you enabled. I would like to thank Dr. Dave Chan and Dr. Yong Li for their constructive comments on the technical and editorial aspects of the thesis. It is a great pleasure to learn from your experience.

I would like to sincerely thank Graduate Program Advisors Lorraine Grahn, Arlene Figley, Trina Cattral and Ellie Kim for your kind and friendly assistance. Thanks to Gilbert Wong for supporting me while conducting the laboratory tests.

This research was funded by the Natural Science and Engineering Research Council of Canada under the collaborative R&D program (CRDPJ 469600-14) and Krinner Canada Inc. I would also like to thank Dr. Weidong Li and Dr. Keshab Sharma for your consultancy during my research. I appreciate Tomas Johansson for representing Krinner and Benoit Trudeau of Workonthat Structure Inc for conducting the pile field tests. I would like to also thank Moira Guo, Chao Liu, Allen Gao and Longqi Liu for assisting in the field tests and site investigation programs.

Table of Contents

List of Tables

List of Figures

List of Symbols

α	adhesion coefficient (in Chapter 6)
α, β	friction coefficient and combined shaft resistance factor (in Chapter 3)
γ_t, γ', γ_w	total unit weight of soil, effective unit weight of soil, unit weight of water
ε, ε_y	strain and yield strain
ε_{50}	strain corresponding to half of s_u
η	viscosity of the soil (in Chapter 4)
η	percentage difference of the ultimate lateral capacity (in Chapter 6)
ξ, ζ	equivalent damping ratio of the pile head and the individual pile segment
ρ_{d1}, ρ_{d2}	dry density at a loose state and a dense state
σ_v, σ'_v, σ_{atm}	vertical stress, vertical effective stress and atmospheric pressure
ϕ'_p, ϕ'_{cv}	peak friction angle and constant-volume friction angle
a, f, e	the distance between the pile head and axial force, the distance between the ground surface and the location where plastic hinge is developed and pile stickup
$a_{eq.pk}$, g	equivalent peak vertical acceleration and Earth's gravitational acceleration
A, A_s	cross-sectional area and surface area of pile
$\bar{A}$	adjustment coefficient for static loading condition
n, c, C_e	n is an exponent, c is a constant that defines the normalized stiffness of elasticity of soil reaction curves and C_e is a constant that the normalized stiffness of elasticity of soil reaction curves
C_c, C_u	curvature coefficient and uniformity coefficient
C_1, C_2, C_3	factors defined in API (1993) to estimate p_{ult}
D, D_s, D_h , D_{th}	diameter of pile, diameter of the pile shaft, diameter of the helix, diameter of the pile thread

D_i, D_o; r_o, r_i	inner and outer shaft diameter; inner and outer shaft radius
D_{s1}, D_{s2}	diameter of the pile shaft along the smooth and top threaded segments; diameter of the pile shaft along the bottom threaded segments
D_{th1}, D_{th1}	diameter of the upper threaded segment and the lower threaded segment
D_{10}, D_{50}, D_{60}	particle size diameter corresponding to 10%, 50% and 60% passing
D_{r1}, D_{r2}	relative density at a loose state and at a dense state
e_{max}, e_{min}	maximum void ratio and minimum void ratio
E_D, E_s	dissipated energy and maximum energy during one cycle (in Chapter 4)
E_h, E_s	horizontal soil modulus of clay and sand (in Chapter 6)
E, v	Young's modulus and Poisson's ratio
f_s, q_c, u_2, FR	sleeve friction, tip resistance, dynamic pore pressure and friction ratio of a CPT
FS	factor of safety
GF, V_R	gauge factor and voltage ratio
G_s, w_c	specific gravity and water content
I, Z_p	moment of inertia and plastic section modulus
k	initial modulus of subgrade modulus of sand
k_f	initial slope of the vertical shaft resistance
k_0	modulus of the subgrade reaction of clay
K_0, K_a, K_p	coefficient of earth pressure at rest, coefficient of active and passive earth pressure
K_r, K_{rs}, K_{rc}	relative stiffness of pile, relative stiffness of pile in sand and in clay
K_s	coefficient of lateral earth pressure

K_T	empirical torque factor
K_l, K_u	loading and unloading stiffness of the pile head
k_l	loading stiffness of the individual pile segment
L, L_1, L_2, L_3, L_4, L_5	total length of a pile, length of the smooth, the top threaded, the bottom threaded, the top tapered and the bottom tapered segments
L_{th_c}, L_{th_e}	length of threads along the centerline and along the edge
m	mass of the superstructure
M , M_{max}, M_p, M_y	bending moment, maximum bending moment, plastic bending moment and elastic bending moment
N_{kt}	Site-specific cone factor
N_p	bearing capacity coefficient for wedge failure under lateral loading
N_c, N_q	bearing capacity coefficients
$N_{1,60}$	corrected standard penetration test index
p, p_{ult}, p_{st}, p_{sd}	lateral soil-shaft stress, ultimate lateral soil stress, ultimate lateral soil capacities based on wedge failure on flow failure
P, P_{ult}, $P_{u\text{-}DB}$, $P_{u\text{-}Y}$	lateral capacity of a pile, ultimate lateral capacity of a pile, ultimate lateral capacity of a pile based on DeBeer's method and corresponding to lateral displacement of 12.5 mm
q, q_{ult}	bearing stress of thread and ultimate bearing stress of thread
q_s, q_{sU}	unit shaft resistance and unit shaft resistance corresponding to ultimate axial pile capacity
Q, Q_u, w	axial force, ultimate axial capacity and axial displacement
Q_{bot}, Q_{top}	axial load at the bottom and top of a pile segment
Q_{cyc}, Q_{ini}	cyclic load and initial load during axial cyclic load field test
Q_{max}, Q_{min}	maximum and minimum axial loads during one cycle

r_{eq}, r, R	the radius of the equivalent cylinder, smaller and larger radius of frustum
R, T	coefficients used in Broms's method
R^2	coefficient of regression
s, w_{th}	pitch of the thread or helix and thread width
s_u	undrained shear strength
SBT	soil behavior type
t, t_{ult}	shaft stress and ultimate shaft stress
t_s	thickness of pile shaft
t^e, t^p, t_o^p	elastic and plastic components of the shaft stress, plastic component of the shaft stress at the start of the current plastic loading
T, T_{end}, T_{max}	installation torque, end-installation and maximum-installation torque
T_s, T_{th}	torque contribution from pile shaft and thread
dy/dx, V	cross-sectional plane rotation of shaft, shear force
w_{max}, w_{min}	displacements corresponding to Q_{max} and Q_{min}
y, y_{50}	lateral displacement of below a pile head and lateral displacement corresponding to half to p_{ult}
Y, $Y_{u\text{-}DB}$, $Y_{u\text{-}Y}$	lateral displacement of a pile head, lateral displacement corresponding to $P_{u\text{-}DB}$ and lateral displacement at 12.5 mm
z	depth
z_c	critical depth
z_{t50}, z_{q50}	vertical displacement corresponding to half of t_{ult} and q_{ult}
z^e, z^p, z_o^p	elastic and plastic component of the vertical displacement, vertical displacement at the start of the current plastic loading

List of Publications

Chapter 3:

Khidri, M. and Deng, L. 2022. Field axial loading tests of screw micropiles in sand. Canadian Geotechnical Journal, 59(3): pp. 458–472.

Chapter 4:

Khidri, M. and Deng, L. 2021. Field axial cyclic loading tests of screw micropiles in cohesionless soil. Soil Dynamics and Earthquake Engineering, 143: pp. 106601.

Chapter 5:

Khidri, M. and Deng, L. 2022. Lateral behaviour of screw micropiles in the field. (status in review)

1. Introduction

1.1. Background

Piles are often used to support axial and lateral loads when soft soil is encountered at shallow depths. Piles transfer superstructure loads to deeper and more competent soils. Aside from increasing the load-carrying capacity and stiffness, piles may reduce the settlement of the foundation. Aside from supporting the axial compressive load, piles are also subjected to earthquakes, wind, waves and tidal loads, which are then categorized into axial cyclic and lateral cyclic loads.

Many types of piles are available in the construction industry. They vary in shape, materials, functions and installation methods. Displacement piles such as precast and prestressed concrete, closed-ended steel pipe, H-piles, timber and Franki piles are either driven or jacked into the ground. Other displacement piles that are drilled in place are Omega and APGD piles. Non-displacement piles are drilled and cast-in-place piles. There are also partial displacement piles, such as open-ended pipe piles, CFA piles and drilled displacement piles. In addition, piles have different cross-sections, such as square, round, hexagon, octagon and H-section, and can be tapered. Helical piles have one or more helices located at the lower portion of the shaft, and they are torqued into the ground.

A new type of pile, called a micro screw pile, as mentioned in Guo and Deng (2018), has been used in the Canadian construction industry recently. It is generally used for lightweight structures, such as timber-framed structures, solar-powered generation systems, fencing, garden and landscape construction and advertisement and traffic signs. Some common examples of its application in Canada include storage racks, solar panels, stairwells and flag pole foundations, as shown in Figure 1.1. The pile is a relatively slender and short pile. It is a multi-segmented hollow steel pipe pile that is smooth at the top and continuously threaded in the middle, with closed-ended-

tapered segments at the bottom. It is installed by applying torque at the pile head. It can be classified as a micropile as the shaft diameter is less than 300 mm. Given that the micro screw pile is relatively new in the Canadian construction industry, there is no guidance on the geotechnical design of this type of pile when it is subjected to axial, axial cyclic and lateral loads.

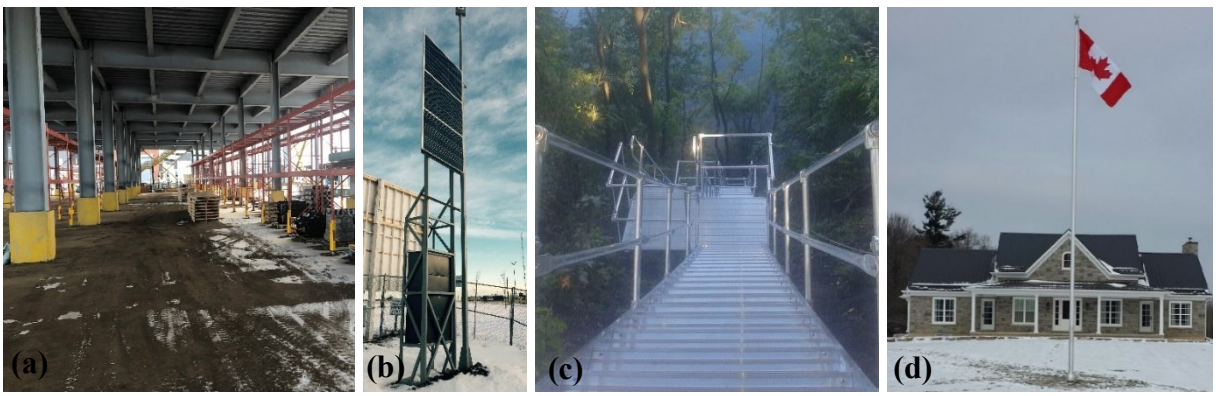

Figure 1.1. Examples of applications of micro screw piles: (a) storage rack in Edmonton, Alberta; (b) solar panel in Whitehorse, Yukon; (c) climbing stairs in Ontario; and (d) flag pole in northern Ontario. (a) and (b): courtesy of Benoit Trudeau; (c) and (d): courtesy of Michael Chaytor.

1.2. Problem Statements

Regarding the axial behaviour of the micro screw pile, additional study is needed in regard to the following:

- Guo and Deng (2018) and Sanzeni and Danesi (2019) have shown that the axial load transfer to the micro screw pile installed in a cohesive soil and design parameter (adhesion coefficient) along the smooth, threaded and tapered segment is a reflection of the development of gaps over the smooth segment, cylindrical shear failure and mobilization of additional lateral pressure over the tapered segment. There is a need to examine the axial load transfer to the micro screw pile installed in cohesionless soil and the possible failure mechanisms.

- The effective stress method, the CPT-based method and the empirical torque factor method with the current design parameters cannot be used to estimate the axial capacity of the micro screw pile.
- Guo and Deng (2018) developed a method to predict the installation torque of the micro screw pile in cohesive soil. These methods need to be evaluated to check their effectiveness in predicting the installation torque of the micro screw pile in cohesionless soil. Guo and Deng (2018) did not examine the effect of the thread on the installation torque.

In regard to the axial cyclic performance of the micro screw pile in cohesionless soil, additional study is needed regarding the following:

- In the literature, key stability parameters have been investigated to assess the axial cyclic response, including the change in pile capacity, pile-head stiffness and displacement accumulation. The cyclic response of the pile depends on many factors, including pile type, soil type and loading pattern. However, the axial cyclic response of the micro screw pile installed in cohesionless soil has never been studied.
- There is limited research into the re-distribution of the shaft resistance of a pile that is based on pile type, pile installation method and soil type. These key stability parameters can be better understood when looking at the axial cyclic response of the individual pile segment with respect to the soil condition in which it is installed.

In regard to the lateral response of the micro screw pile, additional study is needed on the following:

- Broms's (1964a, b) and Meyerhof and Yilcin's criteria may be used to obtain the failure mode of the pile. However, the effectiveness of this method to estimate the failure mode of the micro screw pile needs to be evaluated.
- Several methods are available to estimate the lateral capacity of piles based on full-scale, model-scale and theoretical studies (Broms 1964a, b, Meyerhof et al. 1983, Meyerhof and Yalcin 1984, Meyerhof and Sastry 1985, Sastry et al. 1986). The effectiveness of the Broms method for the micro screw pile needs to be evaluated. The effects of the threads on the lateral capacity of the micro screw pile have not been studied.
- A numerical model for simulating piles' lateral behaviour and capacities is needed. The method should appropriately consider the effects of threads, soil properties and pile material properties.

1.3. Research Objectives

The overall research objectives of the research are to provide a guide to estimate at the axial and lateral capacity of the pile. It is also necessary to understand the overall pile and individual pile segment response to cyclic load. The objectives of the present research are as follows:

- Obtain the capacities and the distribution of the axial load of the micro screw pile. Understand the failure mechanism along the smooth, threaded and tapered segments. Obtain appropriate design parameters by correlating the field test and site characterization results using the CPT-based method, the effective stress method and the empirical torque factor method. Understand the installation torque data and adopt the theoretical torque model.
- Understand the overall pile and the individual pile segment response during cyclic load by assessing key axial cyclic stability parameters, such as pile-head stiffness, equivalent damping

ratio and cumulative displacement. Measure the change in the unit shaft resistance of the individual pile segments in different types of sand during the cyclic test.

- Investigate the lateral capacity, the distribution of the bending moment and the failure mode of the micro screw pile. Evaluate the effect of the tread on the lateral response. Assess the effectiveness of the Broms method in estimating the capacity of piles.
- Develop a numerical model to predict the lateral capacity and soil-pile reactions of the micro screw pile. Investigate the failure mode by examining the pile deformation, the bending moment and the shear stress as well as the lateral forces of the soil on the pile shaft. Quantify the contribution of each component of soil-micro screw pile reaction and the effect of the thread on the lateral capacity of the micro screw pile. Examine the effects of thread and soil properties via numerical sensitivity analysis.

1.4. Methodology and Significance of the Research

The research methodology included geotechnical site characterization, a field test program and numerical modelling. The geotechnical site characterization program included site investigation and laboratory testing. To characterize the site geology, a desktop study, cone penetration tests and standard penetration tests (SPTs) at boreholes (BHs) were conducted at Sandpit. Index tests and direct shear (DS) tests were conducted in the laboratory. In addition, the soil properties were interpreted from CPT readings using empirical equations. The site characterization program for Sherwood Park was performed by Guo (2017). The site characterization program for South Campus was performed by Guo (2017) and the candidate.The data were re-analyzed in the present research.

The field test program and pile resistance prediction method were developed to investigate the axial behaviour of six types of full-scale micro screw piles installed in sand. In total, 41,

including 21 compression and 18 tension tests, were conducted. Eight piles were instrumented with SGs to obtain the axial load transfer. Based on the CPT-based method, the effective stress method and the empirical torque factor method, the appropriate design parameters relevant for the micro screw pile were obtained by correlating the distributions of appropriate soil parameters with unit shaft resistance. The theoretical torque model was adopted for piles in sand.

To examine the axial cyclic behaviour of the piles, six one-way compressive and load-controlled axial cyclic tests were conducted at Sandpit. The axial cyclic load was designed to simulate the vertical loads on the pile during an earthquake load. Three piles were instrumented with SGs. Both overall pile and individual pile segment responses to cyclic load were examined. To assess the stability of the pile, pile-head cumulative displacement, stiffness and equivalent damping ratio were obtained. In addition, the re-distribution of the unit shaft resistances of the individual pile segments in different types of sand during the cyclic load was investigated. The equivalent damping ratio and stiffness of the unit shaft resistance hysteresis of the individual pile segments were determined.

The behaviour of the micro screw piles subjected to lateral loads in cohesive and cohesionless soils was investigated using the field test. Six piles at Sherwood Park, 22 piles at South Campus and 18 piles at Sandpit were tested. Selected piles at Sherwood Park and South Campus were instrumented with SGs to measure the distribution of the bending moment. The location of maximum curvature of piles at Sandpit was documented. Broms's (1964a, b) criterion and Meyerhof and Yilcin's (1984) criterion were used to assess the failure modes of the piles at the three sites. Limited research on the lateral behaviour of helical piles was reviewed to understand the thread's effect. Based on the appropriate pile failure mode, the lateral capacities of the piles were estimated using Broms's (1964a, b) criterion for all the piles at the three sites.

A numerical model based on the BNWF method was developed on the platform of OpenSEES (PEER 2016) to simulate the lateral response of the micro screw pile with various soil-pile reactions. The model incorporated the following innovative techniques: 1) the pile shaft was simulated as fiber sections instead of typical elastic beam-column elements, and 2) the thread-bearing reactions were modelled by a series of soil reaction fiber sections. The model was verified against the field tests conducted at three sites. The contributions of individual soil-pile reactions were assessed. Finally, a sensitivity analysis was performed to evaluate the lateral response of piles to changes in soil properties and specific changes in pile geometry.

The significance of the present research in the geotechnical community may include the following facets. This research provides a guide to estimate the axial and lateral capacity of the micro screw piles to support the field application of this new pile type. The design parameters for the CPT-based method, the effective stress method and the empirical torque factor method specific to the micro screw pile are provided. By examining key stability factors and the axial load transfer during cyclic load, the behaviour of piles with a similar geometry and installation method can be better anticipated. By examining the lateral load field test results, it is understood that both the thread and helix have only minor effects on the overall lateral capacity of the pile. Based on the BNWF method, a numerical model was developed that captures different components of soil-pile reactions by modelling the thread-bearing reactions as a series of zero-length fiber sections with appropriate soil reactions. This method can be extended to predict the lateral-response helical piles with various helical configurations. The field test data can be adopted in further numerical studies for investigating soil-pile interaction.

1.5. Thesis Outline

The thesis contains seven chapters. A literature review on the axial and lateral behaviour of piles is presented individually from Chapter 3 to Chapter 6. A short description of each chapter and appendix is summarized as follows:

Chapter 1: Introduction

The introduction includes the background, problem statement, research objectives, methodology and significance of the research. A review of the literature related to the axial, axial cyclic and lateral behavior and numerical analyses of micro screw piles is reported in the respective chapters.

Chapter 2: Test Sites and Test Piles

In Chapter 2, the site characterization program at the three sites and its results are reported. In addition, the test piles and the pile installation methods are described.

Chapter 3: Axial Load Field Tests of Micro Screw Piles in Sand

This chapter includes a review of the relevant research; the results of the axial load field tests of micro screw piles in sand; and the pile capacity prediction method based on the CPT method, the effective stress method and the empirical torque factor method. The theoretical torque model is compared with measured torque. A version of this chapter constitutes the paper that has been published in the Canadian Geotechnical Journal.

Chapter 4: Axial Cyclic Load Field Tests of Micro Screw Piles in Sand

The result of the axial cyclic load field tests of the micro screw pile is presented. Aside from overall pile stability, the stability of the individual pile segments in different types of sand is examined by analyzing key stability factors, such unit shaft resistance degradation and aggregation, stiffness and equivalent damping ratio. A version of this chapter constitutes the paper that has been published in the journal Soil Dynamics and Earthquake Engineering.

Chapter 5: Lateral Load Field Tests of Micro Screw Piles

This chapter reports the lateral response of the micro screw piles at three sites by examining pile relative stiffness, pile failure mode and pile capacity. A review of the literature is conducted to assess the effect of helices on the lateral capacity of the helical pile, which will aid our understanding of the effect of thread. Finally, the Broms method is used to estimate the capacity of the test piles at the three sites, which is then be validated using the measured lateral capacity.

Chapter 6: Numerical Modelling of the Micro Screw Piles Subjected to Lateral Loading Using the BNWF Method

In this chapter, the numerical model is compared with the field tests results. The failure mode of the piles will be determined by examining the pile deformation, bending moment and shear stress and the lateral forces of the soil on the pile shaft. The individual soil-pile reactions are examined to assess their contribution to the overall lateral response of the micro screw pile. A sensitivity analysis is conducted to check the effects of soil property and key geometrical features on the lateral response of the piles.

Chapter 7: Summary of Conclusions

In the final chapter, a summary of the conclusions of all the parts is reported. In addition, the study's limitations and a list of further research areas are given.

Appendix A: Additional site investigation results at Sandpit and the measured continuous installation torque records of the pile at South Campus are presented in this appendix.

Appendix B: This appendix shows the raw and smooth axial load vs. displacement curves of all piles, the smoothenin process, estimated and measured continuous torque reading of additional piles, the summaries of q_s, α, K_s and β over individual pile segments at different soil types, with their backup calculation, the estimation of the ultimate capacities of piles using coefficient β and

the backup calculation to determine the emprirical torque factor for micro screw piles in compression and tension.

Appendix C: The site layout at Sherwood Park and South Campus, the process to smoothen the raw lateral load vs. displacement of a pile and an example of obtaining the ultimate lateral capacity of a pile based on DeBeer (1968) method are presented in this appendix.

Appendix D: The result of a cyclic lateral load field test of the pile P4 at Sherwood Park which included lateral load vs. displacement, lateral load and displacement time histories, the change in stiffness of the pile and equivalent damping ratio during cyclic load are shown in this appendix.

Appendix E: In this appendix, the OpenSEES code for simulation of micro screw pile subjected to lateral loaded and classical Hermitian polynomials used in the OpenSEES Codes are shown.

2. Test Sites, Test Piles and Pile Installation

2.1. Test Sites

The present research is intended to study the engineering performance of micro screw piles in both cohesive and cohesionless soils. Three sites were selected around Edmonton, Alberta, because of its various surficial soil deposits, as shown in Figure 2.1. The first site is located north of Sherwood Park, southwest of Range Road 232 and Township Road 534, about 3 km north of Yellowhead highway. It consists of surficial backfill overlying glacial clay till. The second site is located at the University of Alberta South Campus farm near 60^{th} avenue and 118^{th} street. It consists of glaciolacustrine clay overlying glacial till (Edwards 1993). The third site is at a sandpit that is located 80 km north of Bruderheim, Alberta. It consists of well-graded fine to medium-grained Pleistocene and Holocene eolian sand deposit overlying lacustrine clay (Bayrock 1958, Fenton et al. 1983). A detailed site investigation including cone penetration tests (CPTs), BHs with SPTs and laboratory tests were conducted at each site.

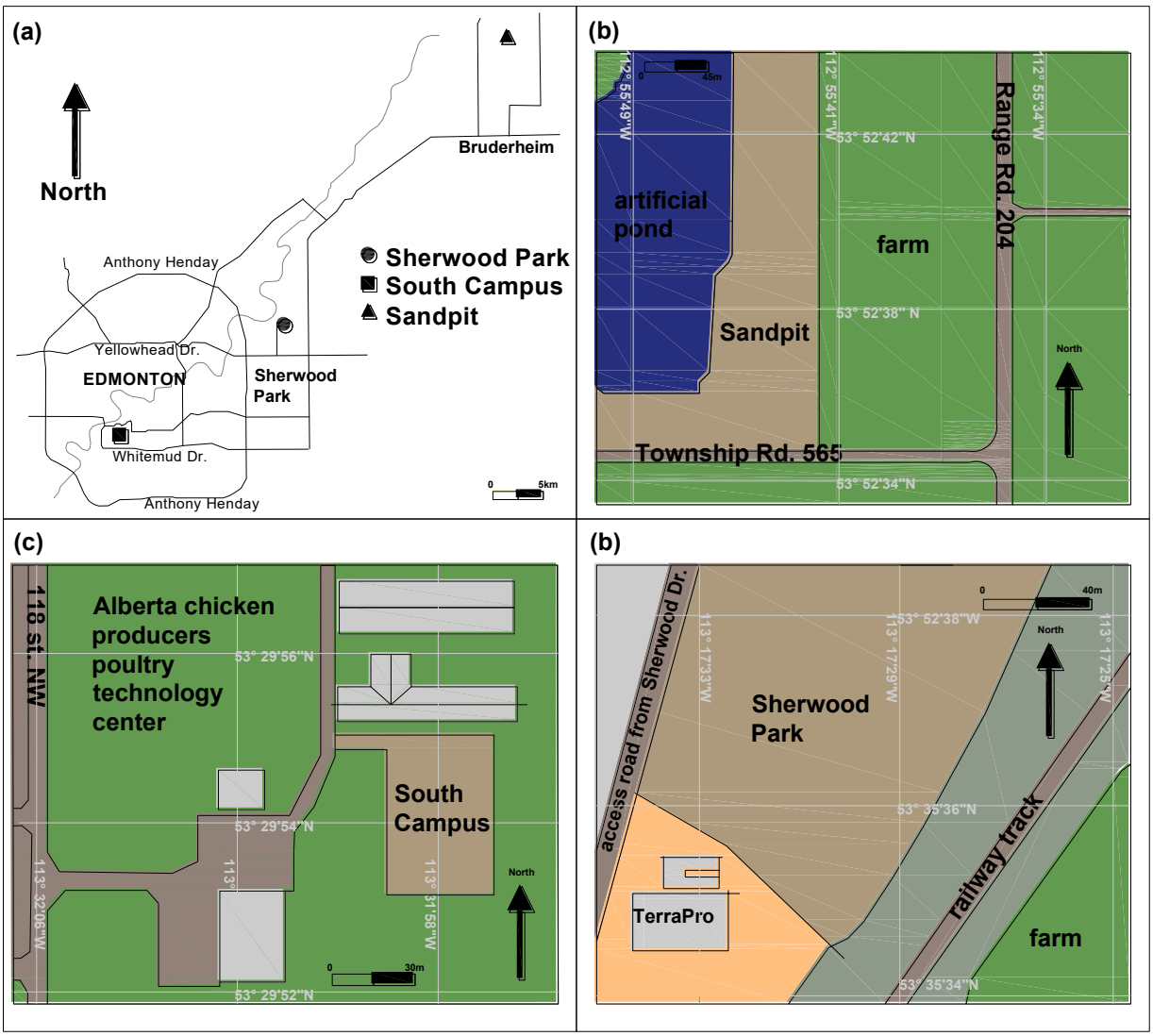

Figure 2.1. (a) Key map of Edmonton showing the locations of the test sites and site layouts at: (b) Sherwood Park (53.5937 N, 113.2919 W), (c) South Campus (53.4983 N, 113.5327 W) and (d) Sandpit (53.8765 N, 112.9290 W).

2.1.1. Sherwood Park

A detailed site investigation was conducted, including two CPTs and two BHs and laboratory tests. The cone penetration results, including tip resistance (q_t), sleeve friction (f_s) and pore pressure (u_2)

measured at Sherwood Park, are shown in Figure 2.2. At Sherwood Park, the undrained shear strength (s_u) of the soils was estimated using Equation 2-1 (Robertson and Cabal 2012):

$$s_u = \frac{q_t - \sigma_v}{N_{kt}} \tag{2-1}$$

where N_{kt} is the site-specific cone factor with a selected value of 14, which was calibrated with triaxial testing of the intact soil. The total unit weight of the soil (γ_t) was assumed at the first iteration. At the second iteration, the value of γ_t was estimated using Equation 2-2 (Mayne et al. 2010):

$$\gamma_t = 1.95\gamma_w \left[\frac{\sigma_v'}{\sigma_{atm}}\right]^{0.06} \left[\frac{f_s}{\sigma_{atm}}\right]^{0.06} \tag{2-2}$$

where γ_w is the unit weight of water and σ_{atm} is the atmospheric pressure.

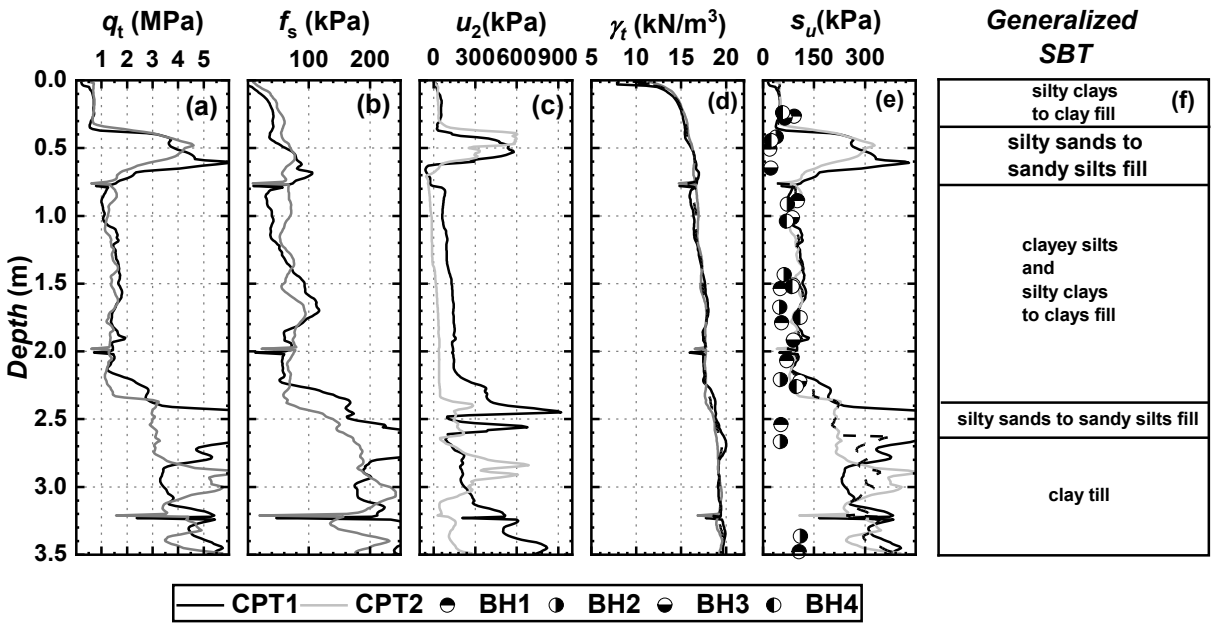

Figure 2.2. Profiles of cone penetration tests at Sherwood Park: (a) tip resistance, (b) sleeve friction, (c) pore pressure, (d) unit weight, (e) estimated undrained shear strength vs. lab-measured undrained shear strength and (f) generalized soil behavior type (SBT).

The soil properties profile including γ_t, s_u and generalized SBT at Sherwood Park, which was empirically interpreted from CPT readings, is shown in Figure 2.2. The s_u of the intact soil samples measured using the unconfined compression test (UCT) is also shown in Figure 2.2. The soil deposit consists of 2.5 m of low plastic and normally consolidated clayey and silty fill, with two thin layers of silty and sandy fills at depths of 0.5 m and 2.5 m and clay till down to BH termination depth. The values of the s_u of the clay fill vary between 50 kPa and 200 kPa, and the values of the s_u of the clay till are between 200 kPa and 400 kPa.

2.1.2. South Campus

As part of the site investigation, seven CPTs, four BHs and laboratory tests were conducted. The CPT results, including q_t, f_s and u_2 measured at South Campus, are shown in Figure 2.3. The value of the s_u of the soil was estimated using Equation 2-1. At South Campus, the value of γ_t was assumed at the first iteration. In the second iteration, the value of γ_t was estimated using Equation 2-2. The soil properties profile, including γ_t, s_u, SBT and generalized SBT at South Campus, which were empirically interpreted from CPT readings, is shown in Figure 2.3. The s_u of the intact soil sample measured using UCT and a vane shear test (VST) is also shown in Figure 2.3. The soil deposit mainly consists of high plastic and normally consolidated silty lacustrine clay. The values of s_u vary between 50 kPa and 110 kPa.

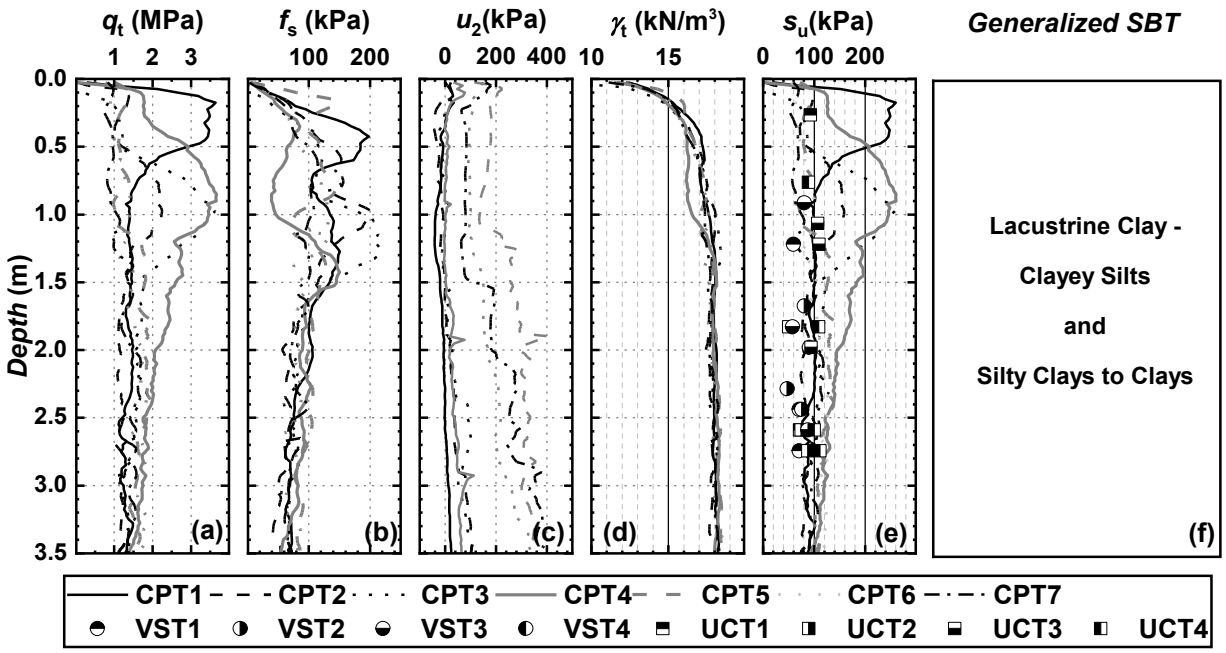

Figure 2.3. Profile of the cone penetration tests at South Campus: (a) tip resistance, (b) sleeve friction, (c) pore pressure, (d) unit weight, (e) estimated undrained shear strength vs. lab-measured undrained shear strength and (f) generalized SBT.

2.1.3. Sandpit

The soil deposit at Sandpit consists of well-graded fine to medium-grained Pleistocene and Holocene eolian sand deposit overlying lacustrine clay (Bayrock 1958, Fenton et al. 1983). A comprehensive site investigation program included four BHs, four CPTs and laboratory tests. The BHs and CPTs were advanced through the sand stratum into the lacustrine clay. The BHs were drilled with a continuous-flight solid stem auger, and the SPTs were conducted at a depth interval of 0.75 m. The measured properties of sand retrieved from grab samples and a split spoon sampler included the water content (w_c), particle size distribution (PSD), specific gravity (G_s), minimum void ratio (e_{min}), maximum void ratio (e_{max}) and friction angle (ϕ'_p). The sand samples were visually examined and classified as per the unified soil classification system (USCS). The locations of the BHs, CPTs and test piles are shown in Figure 2.4.

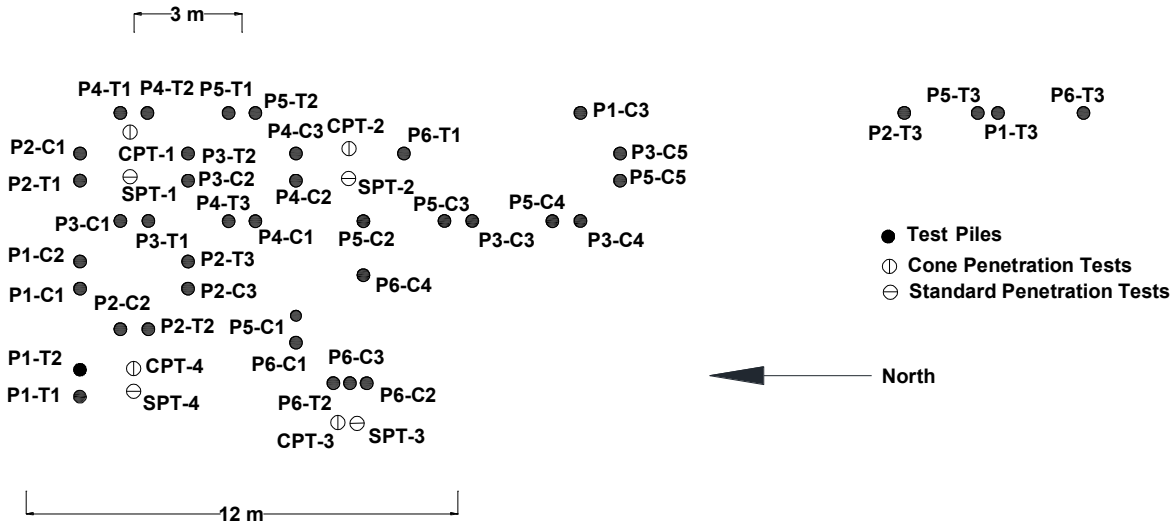

Figure 2.4. Layout of the test piles, cone penetration tests and BHs with SPTs at Sandpit.

The sand properties, which include USCS classification, uniformity coefficient, curvature coefficient, particle size D_{50} and so on are summarized in Table 2.1. The values of SPT-$N_{1,60}$, corrected for overburden stress, are shown in Figure 2.5. The SPT-$N_{1,60}$ values vary between 17 and 23 at the upper sand stratum and 5 and 9 at the lower sand stratum. Based on the values of SPT-$N_{1,60}$ and a visual inspection of soil samples, the 4.3-m-thick sand deposit is composed of two sand strata with distinct compositions and compactness. The upper sand stratum with gravel is compact, well-graded and dry-damp; the lower sand stratum is loose, poorly graded and wet-saturated. The groundwater table (GWT) is 1.7 to 2 m below the ground surface, as measured in the standpipe installed near the test zone.

Table 2.1. Properties of sands from laboratory tests.

Stratum	Upper sand	Lower sand
Depth (m)	0–2	2–4
USCS	SW, SP, SW-G	SW, SP
G_s	2.65	2.6
e_{min}	0.43–0.46	0.48–0.51
e_{max}	0.60–0.71	0.68–0.72
C_u	1.9–4.8	1.8–2.6
C_c	0.5–1.7	0.6–1.1
D_{50} (mm)	0.2–1.3	0.2–0.4
PSD (%)	0–21 G, 77–98 S, 0–5 F	0–6.4 G, 92–99 S, 0–1.6 F
w_c (%)	0–13	13–24

Note: USCS = Unified Soil Classification System; C_u = uniformity coefficient; C_c = curvature coefficient; w_c = water content; G = gravel; S = sand; F = fines.

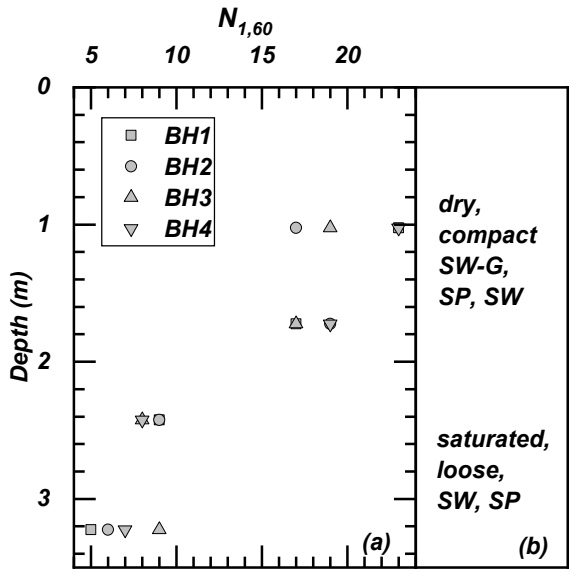

Figure 2.5. (a) SPT index $N_{1,60}$ and (b) description of soil stratum based on SPT and disturbed samples.

The CPT results, including q_t, f_s, friction ratio (FR), u_2 and soil SBT are shown in Figure 2.6. Since the CPTs were conducted in early winter (December), when there was surficial frost, the CPT results of surficial soil might be affected. The effects of frost penetration were shown in the large values of q_t and u_2 to a depth of 0.8–1 m, approximately. The surficial frost at CPT-3 was

removed using heat treatment. Therefore, the surficial soil properties at CPT-3 may represent the normal in-situ properties more accurately. Shear wave velocity (V_s) tests were conducted at CPT-1 and CPT-3, as shown in Figure 4a. The total unit weight of the soil (γ_t) was estimated from V_s results using Equations 2-3 and 2-4 (Mayne 2005):

$$\gamma_t(kN/m^3) = 8.63\log(V_s) - 1.18\log(z) - 0.53 \quad (2\text{-}3)$$

$$\gamma_t(kN/m^3) = 8.64\log(V_s) - 0.74\log(\sigma'_{vo}) - 0.4 \quad (2\text{-}4)$$

where σ'_v is the vertical effective stress, and z is the depth.

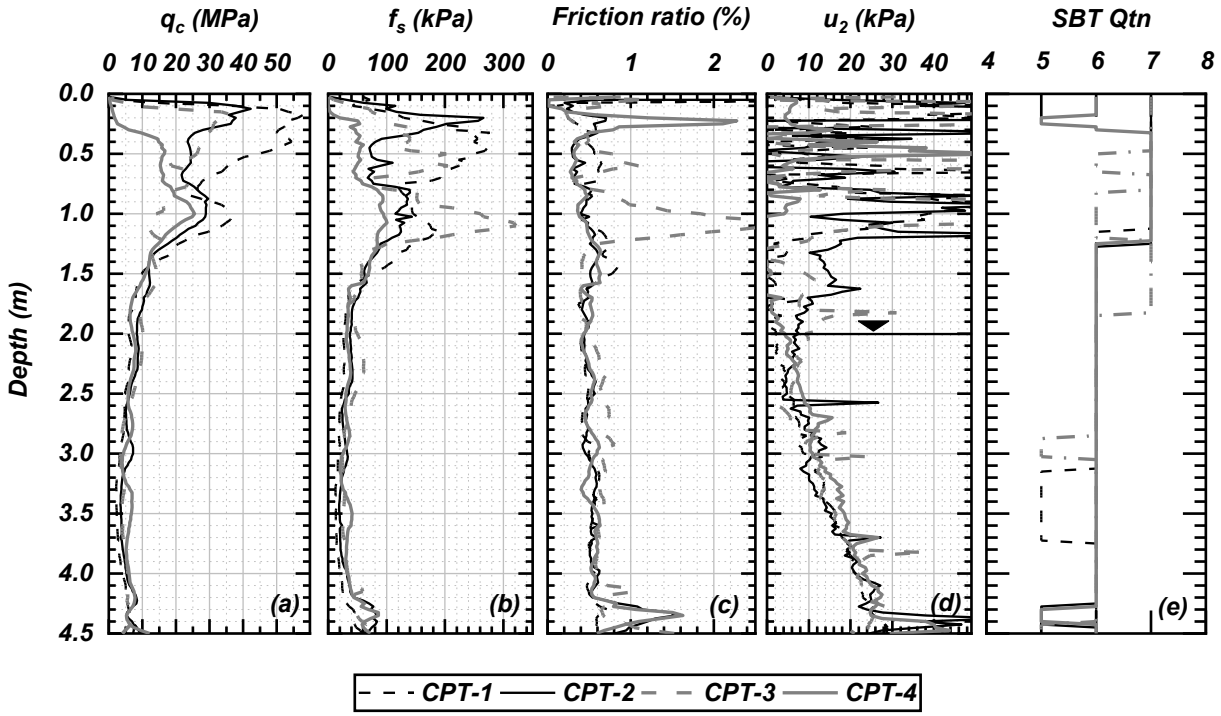

Figure 2.6. Profiles of cone penetration tests at Sandpit: (a) tip resistance, (b) sleeve friction, (c) friction ratio, (D) pore pressure and (e) generalized SBT. Note: SBT Q_{tn} 7: sand with gravel, SBT Q_{tn} 6: clean sand, SBT Q_{tn} 5: silty sand.

The value of peak friction angle (ϕ_p') and relative density (D_r) were estimated using Equations 2-5 to 2-7 (Mayne 2006, Robertson 2004):

$$q_{t1} = \frac{\frac{q_t - \sigma_v}{\sigma_{atm}}}{\sqrt{\frac{\sigma_{atm}}{\sigma_v'}}} \tag{2-5}$$

$$\phi_p' = 17.6^\circ \ldots 0\log(q_{t1}) \tag{2-6}$$

$$D_r = 100(0.268\ln(q_{t1}) - b_x) \tag{2-7}$$

where q_{t1} is the stress-normalized tip resistance, σ_{atm} is 103.1 kPa and b_x is 0.825. The value of D_r varies between 40% and 90% in the upper sand stratum, and D_r is about 40% in the lower sand stratum, as shown in Figure 2.7c.

The SBT suggests that the soil at this site consists of 1.1 to 1.8 m of sand with gravel overlying 2.7 to 3. 5 m of clean sand. The upper sand stratum comprises gravelly sand (SBT = 7) and clean sand (SBT = 6). The lower sand stratum comprises clean sand (SBT = 6), with layers of silty sand and sandy silt (SBT = 5). The SBTs are consistent with the soil descriptions interpreted from the SPT-$N_{1,60}$ values and visual inspection of sand samples.

The friction angles of reconstituted sand samples were measured using a DS device. The reconstituted sand samples were prepared representing in-situ sand at each BH location and depth. Several profiles of in-situ D_r were obtained from the current (Fig. 4c) and historical CPTs. Due to the uncertainties of in-situ densities, the reconstituted sand specimens were prepared at a loose state (i.e., a relatively small D_{r1}) and a dense state (i.e., a relatively large D_{r2}), which were bounded by the D_r ranges shown in Figure 2.7c. The specimens representing the upper sand stratum were prepared with in-situ w_c, and specimens representing the lower sand stratum were saturated. The properties of the reconstituted sand samples including the e_{min}, e_{max}, D_{r1} and D_{r2} used in the DS

program are summarized in Table 2.2. The values of ϕ'_p obtained from DS and CPTs are shown in Figure 2.7d. Generally, the values of ϕ'_p obtained from DS tests are compatible with ϕ'_p obtained from CPTs. The CPT results show that ϕ'_p varies between 40° and 55° in the upper sand stratum and 34° and 42° in the lower sand stratum. Based on the DS results, the average constant-volume friction angle (ϕ'_{cv}) of the upper and the lower sand strata are approximately 42° and 35°, respectively.

Table 2.2. Densities of the reconstituted sand for direct shear (DS) tests.

Depth (m)	D_{r1} (%)	D_{r2} (%)	ρ_{d1} (Mg/m^3)	ρ_{d2} (Mg/m^3)
0	38.5	70.5	1.70	1.77
0.5	59.5	74	1.70–1.77	1.74–1.80
1	63	76	1.71–1.78	1.74–1.80
1.5	71.5	82	1.73–1.79	1.76–1.81
2	49	72.5	1.67–1.75	1.73–1.80
2.5	40	62.0	1.22–1.25	1.26–1.29
3	39	58.0	1.22–1.25	1.25–1.28
3.5	51	69.0	1.24–1.27	1.27–1.30

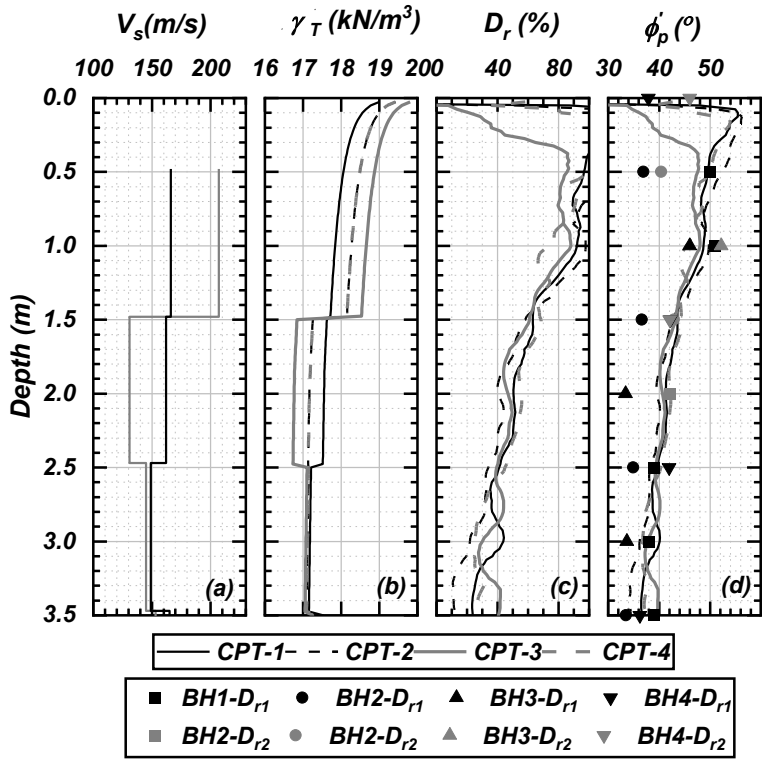

Figure 2.7. Soil properties: (a) shear wave velocity at CPT-1 and CPT-3, (b) unit weight, (c) relative density and (d) estimated peak friction angles vs. lab-measured peak friction angles. Note: D_{r1} denotes the loose state and D_{r2} denotes the dense state of the reconstituted sand in the DS testing.

2.2. Test Piles

In this program, six types of full-scale micro screw piles (P1 to P6, Fig. 2.8) were tested in compression and tension. The pile shaft diameters (D_s) are 114 mm (P1, P2), 89 mm (P3, P4) and 76 mm (P5, P6), and the lengths are 3 m (P1, P3, P5) and 1.5 m (P2, P4, P6). Piles P1 and P2 have five segments: smooth, upper threaded, upper tapered, lower threaded and lower tapered segments. The lower threaded segment has a diameter of 76 mm. Piles P3, P4, P5 and P6 have three segments: smooth, upper threaded and upper tapered segments. The schematic and the dimensions of the six types of micro screw piles are shown in Figure 2.8 and Table 2.3. The shaft wall thickness (t_s) is

3.6 mm along the cylindrical segment. The shaft wall thickness is 3.6 mm at the top of the tapered segment, and it became progressively thicker by a couple of millimetres toward the bottom of the tapered segment. The spiral threads were welded to the pile shaft at 90° from the pile axis. The width (w_{th}), thickness (t_{th}) and pitch (s) of the spiral threads are 12, 2 and 50 mm, respectively. The thread pitch to thread width ratio (S/w_{th}) is 4.2. The thread pitch to thread outer diameter ratio (s/D_s) of piles P1 and P2, P3 and P4 and P5 and P6 are 0.36, 0.44 and 0.50, respectively. The thread outer diameter to shaft outer diameter ratio (D_t/D_s) of piles P1 and P2, P3 and P4 and P5 and P6 are 1.21, 1.27 and 1.32, respectively. The pile shaft and threads were made of structural steel with Young's modulus of 210 GPa and yield strength of 248 MPa and tested by Guo and Deng (2018). The pile material was manufactured in accordance with German standards DIN EN 10219-1 (DIN 2006a) and DIN EN 10219-2 (DIN 2006b).

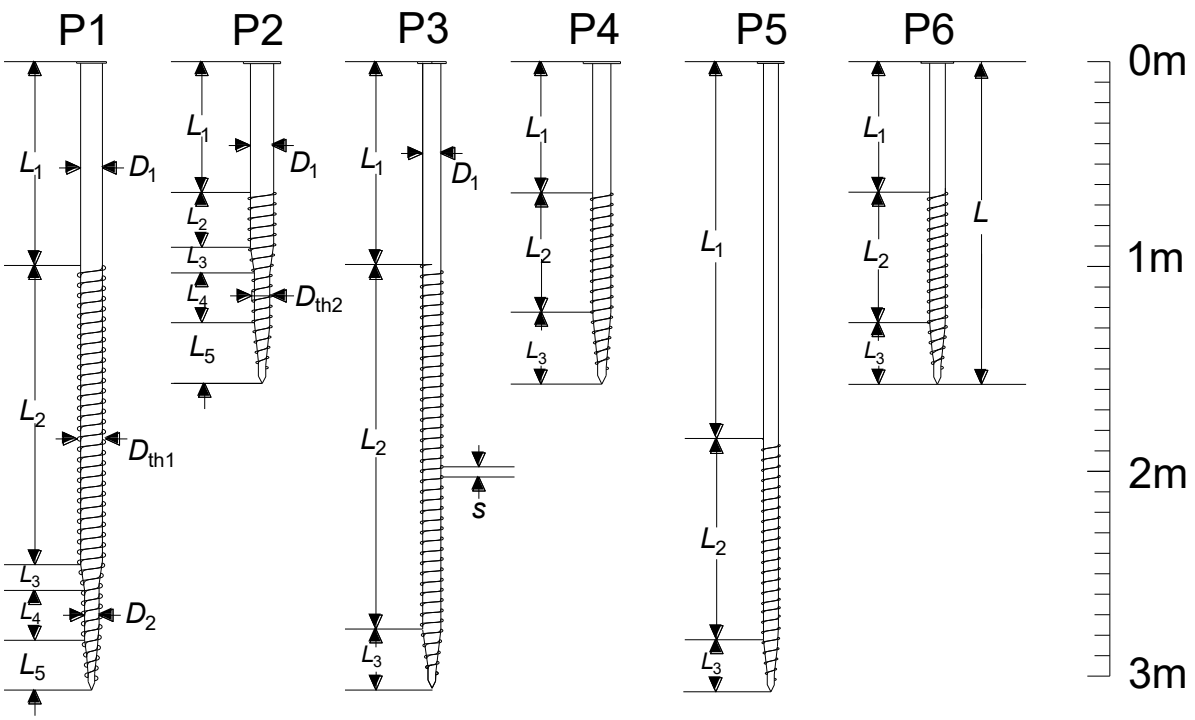

Figure 2.8. Drawing of the pile types.

Table 2.3. Dimensions of the pile types.

	P1	P2	P3	P4	P5	P6
D_1 (mm)	114	114	89	89	76	76
D_2 (mm)	76	76	N.A.	N.A.	N.A.	N.A.
L (mm)	3033	1538	3048	1566	3076	1566
L_1 (mm)	815	626	904	596	1792	594
L_2 (mm)	1501	205	1801	622	922	602
L_3 (mm)	213	200	343	348	362	370
L_4 (mm)	126	112	N.A.	N.A.	N.A.	N.A.
L_5 (mm)	378	395	N.A.	N.A.	N.A.	N.A.
s/D_{th1}	0.36	0.36	0.44	0.44	0.5	0.5
D_{th1}/D_1	1.21	1.21	1.27	1.27	1.32	1.32
D_{th2}/D_2	1.32	1.32	N.A.	N.A.	N.A.	N.A.

Note: Definition of the symbols are shown in Figure 2.8.

2.3. Pile Installation

The piles were installed using a small excavator equipped with a hydraulic torque head (Fig. 2.9). A combination of torque and a small axial load (i.e., the crowd load) at the pile head was applied to advance the piles into the ground. The advancement rate was controlled at nearly one thread pitch per revolution. The inclination of the pile shaft was checked by a level mounted on the torque head. Continuous installation torque was measured with an electronic pin (a pressure differential gauge integrated into the installation equipment) and recorded in a datalogger inside the small excavator. The maximum-installation (T_{max}) and end-installation (T_{end}) torques of each pile were documented. The value of T_{end} was interpreted as the average of the measured torque during the last continuous turn at the pile termination depth. The summary of maximum-installation and end-installation torque at the three sites is shown in Table 2.4.

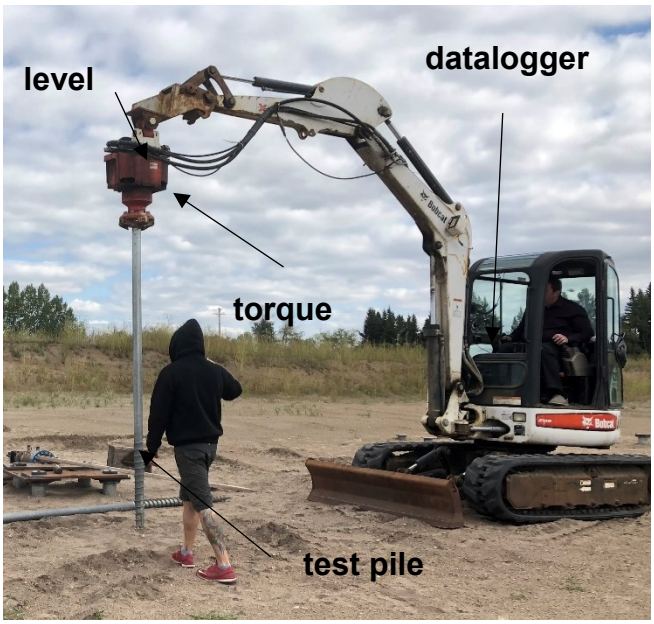

Figure 2.9. Pile installation equipment.

Table 2.4. Summary of the max-installation and end-installation torque at the three sites.

Site	Pile	Test	T_{max} (kN*m)	T_{end} (kN*m)
Sherwood Park	P1	L1	-	3.780
	P2	L1	-	1.467
	P3	L1	-	3.111
	P4	L1	-	0.860
	P5	L1	-	-
	P6	L1	-	0.556
South Campus	P1	L1–L3	3.689,5.084,4.404	3.131,4.805,4.247
	P2	L1–L3	2.728,2.297,2.635	1.891,2.077,2.077
	P3	L1–L3	3.348,2.356,3.792	3.255,1.767,2.821
	P4	L1–L3	2.821,2.108,1.705	0.930,1.922,1.581
	P5	L1–L6	3.534,3.627,1.612,3.379,3.069,2.635	1.488,1.488,1.364,0.496,1.209,1.085
	P6	L1–L4	1.922,3.100,2.046,2.015	0.899, 1.829, 1.891, 1.674
Sandpit	P1	C1–C3	6.200,6.727,4.092	5.613,6.231,4.092
		T1–T3	6.696,6.386,5.115	6.603,5.549,5.115
	P2	C1–C3	2.666,2.852,3.038	2.573,2.604,2.573
		T1–T3	2.387,2.790,2.697	2.139,2.418,2.449
	P3	C1–C2	3.534,4.278	2.480,3.534
		T1–T2	3.255,3.658	2.325,2.914
	P4	C1–C3	1.798,2.356,2.449	1.736,2.046,1.922
		T1–T3	1.984,2.852,1.612	1.891,1.457,1.457
	P5	C1–C3	-	-
		T1–T2	3.348,2.883	2.170,2.542
	P6	C1–C3	-	-
		T1–T3	-	-

3. Axial Load Field Tests of Micro Screw Piles in Sand

3.1. Introduction

The micro screw pile is a unique type of pile because of its shape and installation method. A micro screw pile consists of a smooth shaft at the top, a continuously threaded shaft at the middle and a continuously threaded and tapered shaft at the bottom. The piles are installed using a torque head attached to the arm of a drill rig. The piles are suitable for lightweight structures, including traffic signs, landscape construction, fencing and solar panels. This pile type may be classified as a micropile as the shaft diameters are less than 300 mm.

One of the first studies of the micro screw piles (but only in cohesive soils) was conducted by Guo and Deng (2018). They suggested that the soil-pile shaft adhesion coefficient (i.e., the ratio of unit shaft resistance to undrained shear strength) of the smooth segment in clay was low and that the capacity of the threaded segment was best represented by the cylindrical shear mode (CSM; Mooney et al. 1985, Narasimha Rao et al. 1993, Elsherbiny and El Naggar 2013, Guo and Deng 2018). They reported that the thread pushes the failure surface to the outer edge of the threads and increases the adhesion coefficient to unity and hence increases the pile capacity (Guo and Deng 2018). Sanzeni and Danesi (2019) adopted the prediction model proposed by Guo and Deng (2018) to estimate the axial capacities of the test piles at a stiff silty clay site in Italy. Sanzeni and Danesi (2019) concluded that the adhesion coefficient over the smooth segment was 0.3 and that the average capacity of the tapered segment was 30% greater than that of the equivalent threaded segment, further increasing the adhesion coefficient.

The micro screw piles belong to a family of piles whose shaft is modified in various manners for desired performance advantage. Cutherson-Black (2001) stated that pile helix, concentric rings, lugs and other modifications might increase the soil volume involved in shear failure by moving the failure plane away from the shaft surface. The shaft modification will also

change the displacement behavior of piles. Ladanyi and Guichaoua (1985) tested model corrugated and slightly tapered piles and smooth shaft piles in frozen saturated sand. The results showed that the corrugated shaft capacity was 2 to 3.5 times the smooth shaft capacity. The corrugated shaft exhibited contractive behavior, whereas the smooth shaft exhibited dilative behavior between the pile and soil. The advantageous effects of the tapered shaft piles in cohesionless soil were reported as early as in the 1920s (Robinsky et al. 1964, Rybnikov 1990, Kodikara and Moore 1993). Robinsky et al. (1964) realized these effects when the load test capacities were consistently greater than the estimated capacities. Sakr and El Naggar (2003) and Robinsky and Morrison (1964) reported that the increase in pile capacity was due to the densification of sand during pile installation. Kodikara and Moore (1993), Wei and El Naggar 1998 and Guo and Deng (2018) suggested that the increase in the capacity of the tapered pile was due to the development of additional lateral earth pressure as the pile was penetrated in the ground.

A limited number of studies on micro screw piles (e.g., Guo and Deng 2018, Sanzeni and Danesi 2019) have concentrated on this pile type's behaviour and capacities in cohesive soils. To support the application of this pile type in cohesionless soils, the failure mode, load transfer mechanism and capacities of the micro screw piles in sand are required. Hence, a field test program of six types of full-scale piles was undertaken. Selected piles were instrumented with axial SGs. Axial capacities, load transfer mechanism, methods of estimating shaft resistance and torque mechanism were investigated based on the field test results.

3.2. Field Test Program

3.2.1. Instrumentation

Pile types P1, P3 and P5 were instrumented with five SGs stations, with either a Wheatstone half-bridge or quarter-bridge circuit, to measure the distribution of axial load along the pile. Therefore, the pile was divided into five segments by adjacent strain gauge (SG) stations. The locations of

the SG stations and the indices of the pile segments are shown in Figure 3.1. The SG was installed on the outer shaft of the pile. The electric wires attached to the SG were pulled from a drilled hole adjacent to the SG through the pile head hole. The SG was sealed with a layer of epoxy, a layer of aluminum foil and a layer of blue clay and protected with a metal sheet casing, as shown in Figure 3.2. The layer of blue clay with low permeability was applied between the aluminum foil and the metal sheet casing to provide the SG with waterproofing below the GWT. The metal sheet casing was bolted with a threaded nut rivet into the shaft. The metal sheet casing protected the SG stations from sand abrasion during pile installation. To mitigate the transmission of load to the metal sheet casing, the metal sheet casing was built to be marginally smaller than the pitch of the threads, and the hole in the metal sheet casing was drilled large enough to allow vertical movement of the bolt.

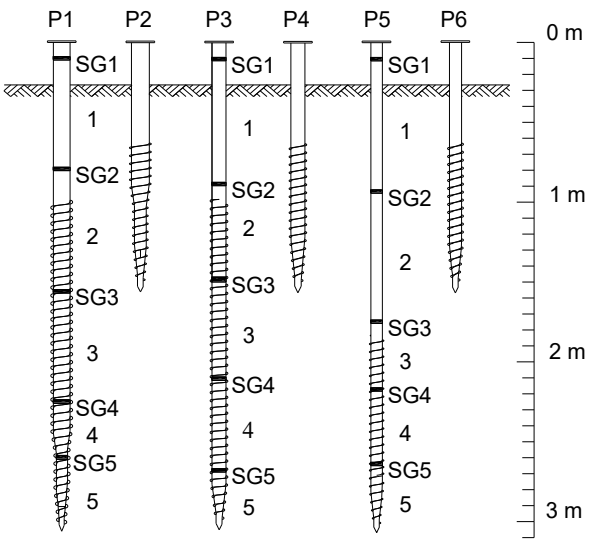

Figure 3.1. Drawing of the pile types. Note: Black strips = SG stations; the indices of segments are labelled beside instrumented piles.

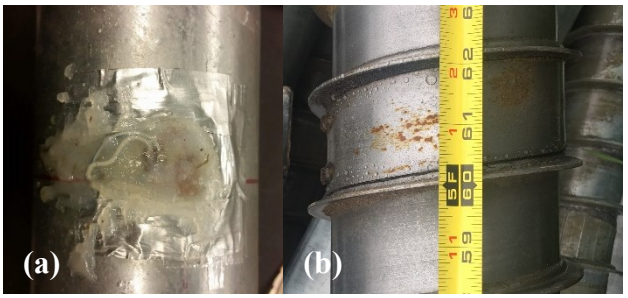

Figure 3.2. (a) A layer of epoxy to be covered by aluminum foil and (b) metal sheet casing.

3.2.2. Test Setup

The general test setup is shown in Figure 3.3. It included a boxed slider, a 4.2-m-long W360X179 I-beam with two 7.9-mm-thick steel plate stiffeners as reaction beams, two groups of four identical 2.1-m-long micro screw piles as reaction piles, lumber blocks, steel rebars as tension rods and steel frames as pile caps. Two groups of reaction piles, each including four identical 2.1-m-long micro screw piles, were installed at a spacing of 2.25 m. The spacing between each pile was at least 0.75 m. Reaction piles were capped using three steel frames bolted to the pile head. The lumber blocks and the tension rods provided support for compression and tension tests, respectively. A two-way hydraulic jack equipped with a load cell of 900 kN capacity was installed below the slider to provide the axial load. The load was supplied by a hydraulic pump, which was equipped with a remote control. Two linear potentiometers were placed between the hydraulic jack and the pile head to measure the axial displacement. The load cell, two linear potentiometers and SG recordings were available in real time (at 1 hz) via a laptop onsite via a datalogger. The recordings were saved after the completion of the tests at end of each test day.

The piles were installed using a small excavator equipped with a hydraulic torque head (Fig. 3.4). A combination of torque and a small axial load (i.e., the crowd load) at the pile head was applied to advance the piles into the ground. The advancement rate was controlled at nearly one thread pitch per revolution. The inclination of the pile shaft was checked by a level mounted

on the torque head. Continuous installation torque was measured with an electronic pin (a pressure differential gauge integrated into the installation equipment) and recorded in a datalogger inside the small excavator. The maximum-installation (T_{max}) and end-installation (T_{end}) torques of each pile were documented. The value of T_{end} was interpreted as the average of the measured torque during the last continuous turn at the pile termination depth.

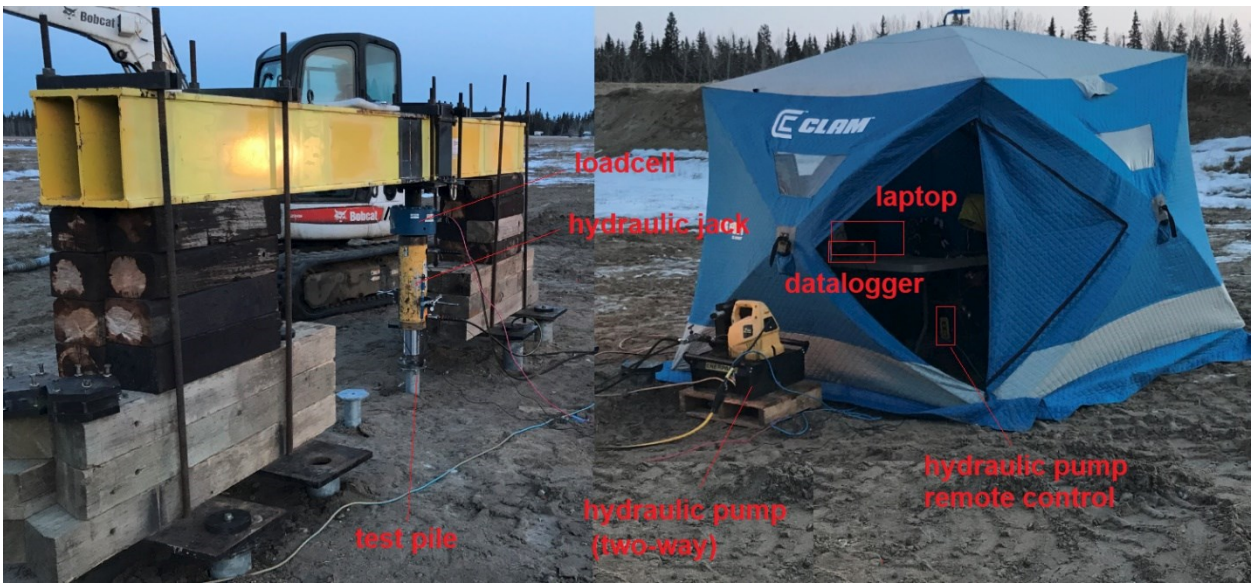

Figure 3.3. Field test setup.

Figure 3.4. Pile installation equipment at Sandpit.

3.2.3. Test Procedure and Summary

The compression tests and the tension tests were conducted in accordance with ASTM standards D1143 (ASTM 2007b) and D3689 (ASTM 2007c), respectively. The quick load test method was adopted. The load was increased manually at an increment of 5% of the anticipated capacity until plunging failure or excessive settlement was observed. Then, the load was decreased at an increment of 25% of the anticipated capacity. The load in the hydraulic jack was supplied by a pump that was equipped with a remote control. The load could be supplied with an accuracy of less than approximately half a kilonewton. The load could be controlled with a reasonable accuracy because of the remote-controlled hydraulic pump and availability of load cell and linear potentiometer readings on site in real time. Each load step was maintained for 5 min until there was a negligible creep. Due to the quick dissipation of the excess pore pressure in the sand that had developed during pile installation, pile setup was not considered. Therefore, there was no specific wait time between pile tests.

A total of 41 tests, which included 23 compression tests and 18 tension tests, were performed on re-used (not laterally loaded) piles as the axial deformations were anticipated to be negligible. To enhance the reliability of the test results, a minimum of three compression tests and a minimum of three tension tests were repeated on each pile type. A minimum of one compression and one tension test was performed on each instrumented pile type of P1, P3 and P5. The summary and the site layout of the test pile are shown in Table 3.1 and Figure 3.5. As an example of test identification, P1-C1 corresponds to the first compression test of pile P1.

Table 3.1. Summary of test piles and Q_u.

Pile type	Comp. Test	Q_u (kN)	Tens. Test	Q_u (kN)
P1	C1–C3	129, 139, 95	T1–T3	103, 75, 84
P2	C1–C3	48, 43, 36	T1–T3	8, 13, 14
P3	C1–C5	82, 118, 86, 64, 64	T1–T3	65, 70, 65
P4	C1–C3	57, 56, 48	T1–T3	15, 14, 15
P5	C1–C5	73, 50, 56, 53, 44	T1–T3	63, 59, 44
P6	C1–C4	27, 21, 17, 39	T1–T3	10, 11, 19

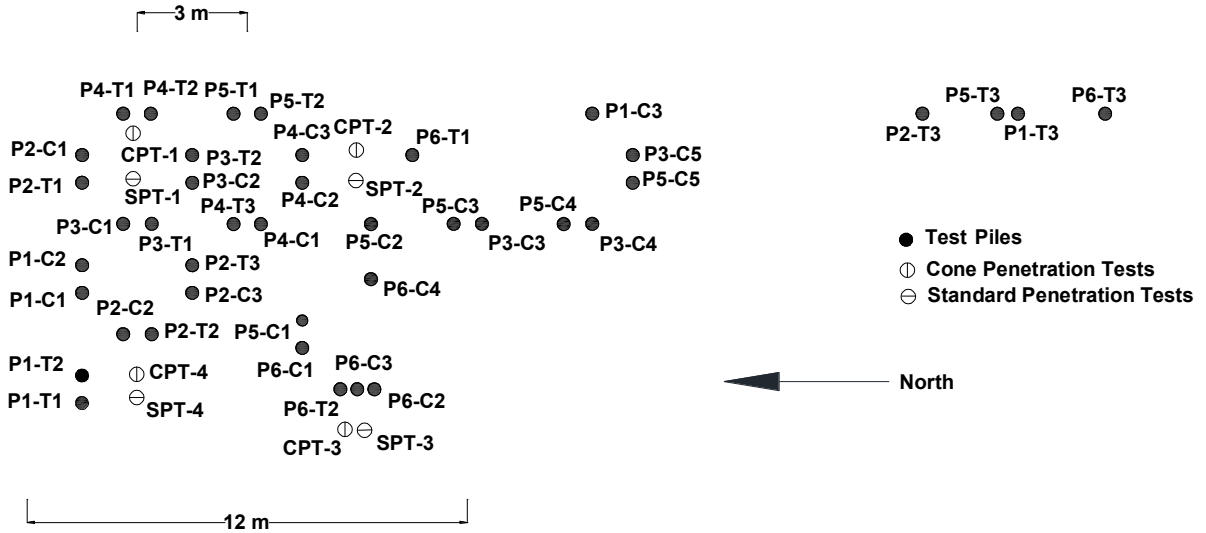

Figure 3.5. Layout of test piles, cone penetration tests and SPTs at Sandpit

3.3. Field Test Results

3.3.1. Axial Load vs. Normalized Displacement

In this research, 41 tests, including 23 compression tests and 18 tension tests, were performed. Each pile was tested a minimum of three times in compression and in tension. The raw data curves of Q vs. w/D of all piles are shown in Figure B1 in Appendix B. The raw curves of Q vs. w/D of pile P1-C1 is shown in Figure 3.6a, as an example. The Q and w time histories are shown in Figure 3.6b. After each small axial load increase, there is a drop in load because the load was applied quickly. There are two mechanisms worth mentioning. First, there is a drop in load because the

hydraulic fluid cooled after the fluid was injected from the hydraulic pump through the hydraulic pump nasal and hydraulic jack nasal. In this case, the load would decrease with no to a very small increase in displacement, as shown in Figure 3.6c. Second, the pile could displace due to the delayed sand response after the increase in load. In ASTM 2007b, it is reported that the displacement measured between readings for a given load increment could be an indication of creep behaviour. The creep in sand consists of a slippage between sand particles and the fracture of sand particles. Therefore, it is assumed that the measured displacement under constant or reduced load could be due to creep, as shown in Figure 3.6d. Therefore, the load was maintained for five minutes to stabilize the load and displacement. A numerical program was developed to smoothen the curve by selecting the stabilized load and displacement, which is shown in Appendix B. The smoothened curves of the axial load (Q) vs. the normalized displacement (w/D) of selected piles are shown in Figure 3.7, and those of all test piles are shown in Appendix B, where w is the axial displacement and D is the outer shaft diameter of the pile along the top smooth segment. The elastic compression of the pile shaft is minimal, and hence it is neglected.

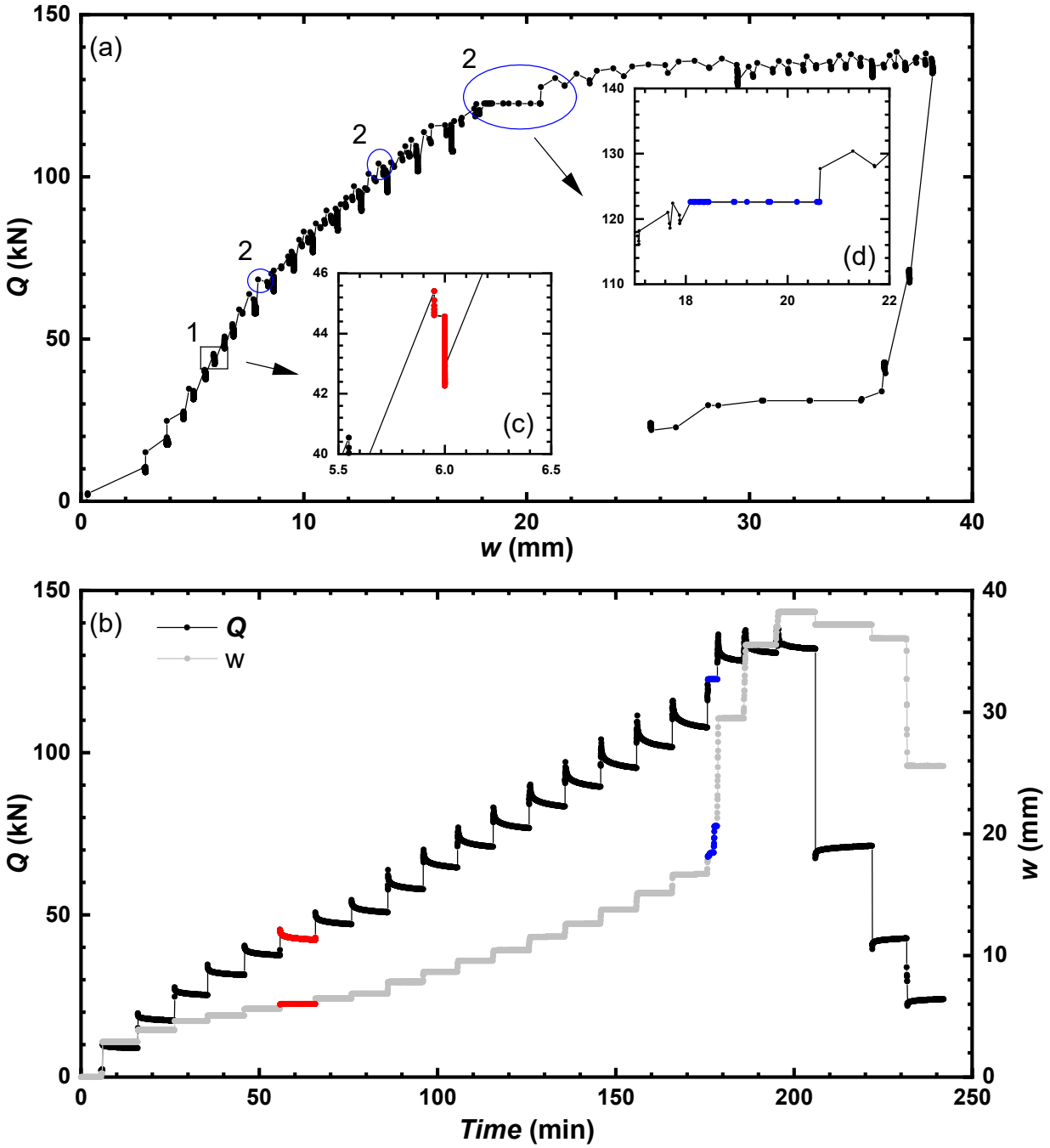

Figure 3.6. (a) Raw axial load vs. displacement and (b) axial load and displacement time histories of pile P1-C1. Note: Figure 3.6c shows the reduction in load with no or a small displacement, and 3.6d shows the measured displacement under constant or reduced axial load.

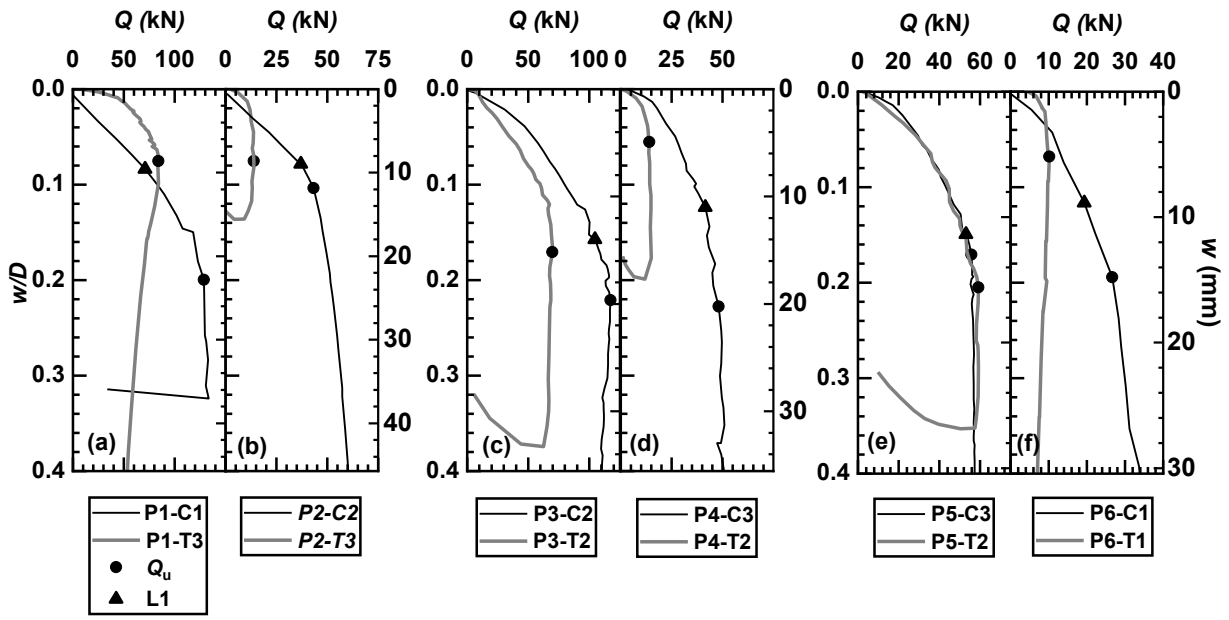

Figure 3.7. Selected curves of smoothened axial load (Q) versus normalized axial displacement (w/D): (a) P1-C1 and P1-T3, (b) P2-C2 and P2-T3, (c) P3-C2 and P3-T2, (d) P4-C3 and P4-T2, (e) P5-C3 and P5-T2 and (f) P6-C1 and P6-T1. Note: L1 is the point where the linear-elastic zone with high stiffness ends.

3.3.2. Ultimate Pile Capacity of the Micro Screw Piles

Piles resist the applied load (Q_t) of the superstructure through shaft resistance (Q_s) and base resistance (Q_b), as shown in Figure 3.8a. As the Q_t at the pile head is increased, the pile w increases until the pile plunges into the ground when the Q_s and Q_b reach their limit values. There is a high localization of shearing within a thin layer of soil around the pile shaft. Typically, a small amount of the w of the pile is required to mobilize the limit shaft resistance (Q_{sL}) because of the thickness of the shear zone. However, a large amount of the w of the pile is required to reach Q_b. In fact, it is very difficult to mobilize the limit base resistance (Q_{bL}) of typical piles with common testing equipment unless the soil is very weak. The typical Q vs. w response of piles is shown in Figure

3.8b. Therefore, the ultimate load (Q_{ult}) based on various load vs. displacement criteria is often used to define the capacity of the pile. Some common criteria include the Davisson Offset Limit, the DeBeer Yield Limit, the Hansen Ultimate Load, the Chin-Kondner Extrapolation and the Decourt Extrapolation.

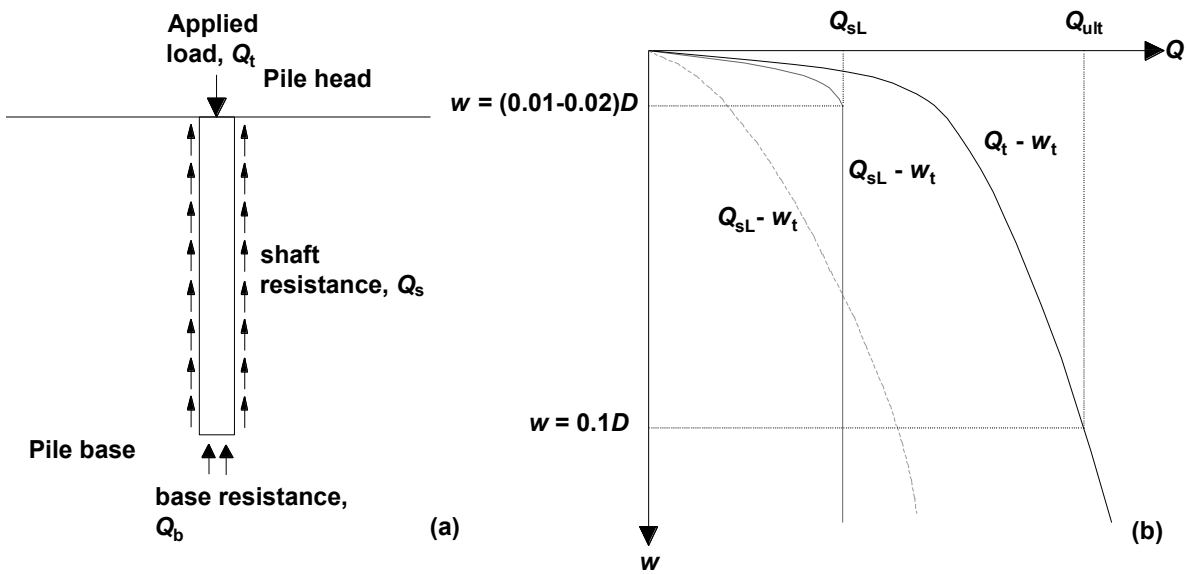

Figure 3.8. (a) Source of pile resistance and (b) typical Q vs w response of the pile (adapted from Salgado 2008)

In the present study, piles do not exhibit apparent plunging failure (i.e., the limit failure as defined in Salgado 2008) in compression tests typically, as would be expected for other pile types in sand, because of the apparent densification of sand and the development of additional lateral earth pressure during installation. However, piles in tension tests do show a peak load. In many test cases, the pile failure is reached at a displacement of more than 10% shaft diameter. Therefore, the ultimate pile capacity (Q_u) was used in the present study to characterize the geotechnical failure of piles. Generally, the following three different zones can be identified for piles in compression tests: the initial linear-elastic zone with high stiffness (the end of which is plotted in Fig. 3.7), the

nonlinear transitional zone with decreased stiffness and the secondary linear zone with low stiffness. Although several failure criteria for Q_u are available (as summarized in Fellenius 1989), the method of Hirany and Kulhawy (1988) seems more suitable for the micro screw piles in this study; applications of the Hirany and Kulhawy criterion in pile tests in sand were reported in Mansour (2019). This criterion selected the value of Q_u corresponding to the start of the secondary linear zone. For piles in tension tests, Q_u was selected corresponding to the peak load achieved. The compressive and tensile Q_u points, with subjective judgment to a reasonable degree, are labelled on the Q vs. w/D curves in Figure 3.7. The values of Q_u and the corresponding w/D of 41 tests are summarized in Figures 3.9 and 3.10. The process to approximate Q_u is shown in Table B1 in Appendix B.

As shown in Figure 3.9, the average compressive Q_u of the piles is greater than the average tensile Q_u because of the greater capacities of the tapered segments in compression than in tension tests. The differences in the compressive and tensile capacities are more pronounced in short piles (i.e., P2, P4 and P6, long piles) and almost insignificant in long piles. Since the ratios of the tapered segment lengths to the total lengths of the short piles are greater than the ratio for long piles, the contribution of the taper to the Q_u is more significant in the short piles. In addition, the tapered segment of the long pile is situated in loose sand, and the tapered segment of the short pile is situated in compact sand.

The value of w/D at the ultimate state of all tests is shown in Figures 3.10a and 3.10b, respectively. The compressive Q_u is mobilized at a w/D of 0.14–0.22, and the tensile Q_u is mobilized at a w/D of 0.06–0.22. It is observed that significant displacement, more than 10% of the pile diameter, is required to reach the ultimate state at this site. The variation of w/D ratios at failure is greater in the tension tests than in the compression tests. There is a visible difference in the values of w/D between the long and the short piles in the tension tests. For the short piles, Q_u

is mobilized at less *w/D* than the long piles in general, perhaps because the tapered segment of the short piles is located within the dense upper stratum.

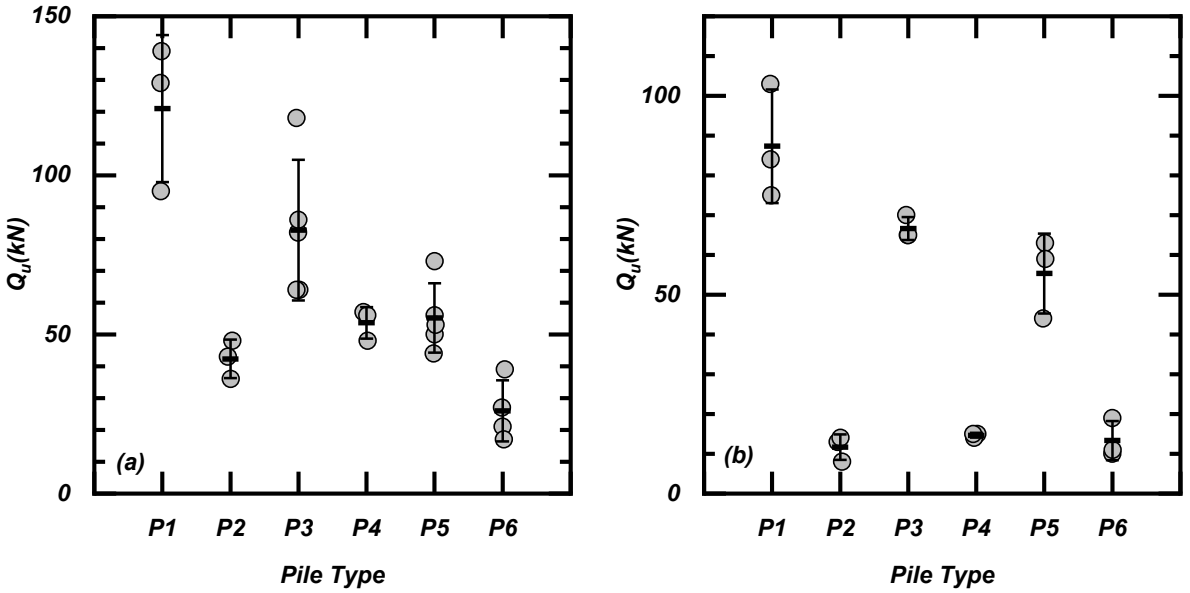

Figure 3.9. Measured Q_u of all the pile types: (a) compression tests and (b) tension tests. Note: The error bars show one standard deviation.

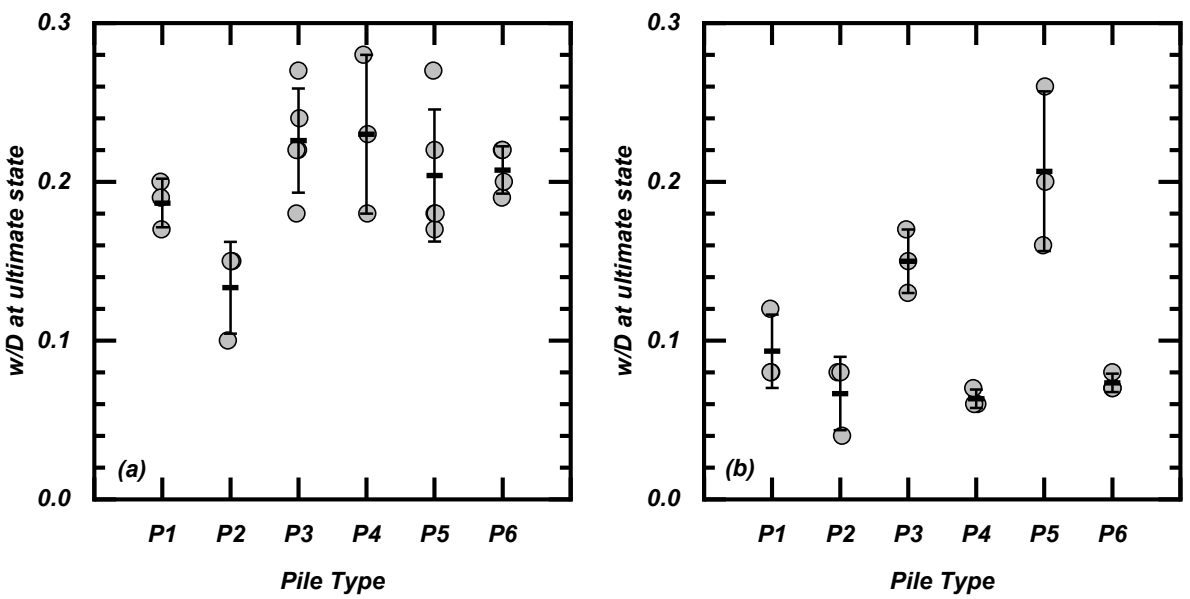

Figure 3.10. Measured *w/D* at the ultimate capacity of all pile types: (a) compression tests and (b) tension tests. Note: The error bars show one standard deviation.

3.3.3. Distribution of Unit Shaft Resistance

In order to determine the axial load transfer mechanism, the axial load Q transferred to each SG station was calculated using Equation 3-1:

$$Q = \varepsilon EA \tag{3-1}$$

where ε is the measured strain, E is Young's modulus of the pile material and A is the cross-sectional area of the pile at the SG location. Figure 3.11 shows selected distributions of Q along the pile shafts at different load steps. The value of Q at the pile tip was assumed to be zero as the cross-sectional area reduced to almost zero.

The ratios of the S/D_h of piles P1 and P2, P3 and P4 and P5 and P6 are 0.36, 0.44 and 0.50, respectively. Several studies have shown that helical pile capacity is best represented by the CSM when the helical plate ratio of S/D_h is less than a range of 2 to 3 (Narasimha Rao et al. 1993, Al-Baghdadi 2018). Al-Baghdadi (2018) reported that the ratio of helix diameter to shaft diameter (D_h/D_s) also affected the helical pile's capacity. The ratios of D_h/D_s for piles P1 and P2, P3 and P4 and P5 and P6 are 1.21, 1.27 and 1.32, respectively. Al-Baghdadi (2018) showed that the effectiveness of this ratio increases with the D_h/D_s value and reaches a constant value at a ratio of 2. Although it was expected that this ratio would affect the capacity of the pile, it is hard to quantify this amongst the variability associated with pile installation and soil heterogeneity. From the pull-out of the micro screw piles in cohesionless soils in this study, it was observed that the soil failed along the outer edge of the threads. In addition, a back analysis of pile capacities suggested that the capacities would be significantly overestimated if the soil had failed on the individual threads. Hence, it may be reasonable to assume that the CSM applies to the tests in the present study.

Hence, the unit shaft resistance (q_s) of the individual pile segment between adjacent SGs was calculated using Equation 3-2:

$$q_s = \frac{Q_{top} - Q_{bot}}{A_s} \tag{3-2}$$

where Q_{top} and Q_{bot} are the measured axial loads at the top and bottom of a specific shaft segment, and A_s is the outer surface area of the segment. Figure 3.12a shows a free-body diagram of a cylindrical shaft segment. For the tapered segment, it is inappropriate to calculate q_s directly from the perspective of force equilibrium. Instead, the method that treats the taper as an equivalent cylinder was adopted, which was used by El Naggar and Sakr (2000) and Guo and Deng (2018). As shown in Figures 3.12b and c, the equivalent cylinder has the same volume as the tapered segment, and then q_s was calculated based on the CSM failure of the equivalent cylinder. The radius of the equivalent cylinder r_{eq} was calculated using Equation 3-3 according to the principle of equal volume:

$$r_{eq} = \sqrt{\frac{R^2 + r^2 + Rr}{3}} \tag{3-3}$$

where r and R are the smaller and larger radii of the frustum. The outer surface area of an equivalent cylinder could then be calculated from r_{eq} and the length of the equivalent cylinder.

The distribution of unit shaft resistance at the ultimate state (q_{sU}) along various piles is shown in Figure 3.11. Although the values of q_{sU} change considerably with the depth, because of the nature of such field tests, several important observations can still be drawn. Figure 3.11 implies that the q_{sU} along the smooth and threaded segments are not significantly affected by the loading direction; this is similar to what was reported in previous research (e.g., Dennis and Olsen 1983, O'Neill 2001, Fellenius 2002, O'Neill 2002). The values of q_{sU} at the smooth segment in sand are relatively large. Guo and Deng (2018) reported that the average adhesion coefficient between the clay and the smooth segment was less than 0.1 because the torsional installation process had

created annular gaps between the clay and the smooth segment. However, the annular gaps are not formed in sand because the sand might have fallen in.

Figures 3.11a and 3.11b imply that the loading direction affects q_{sU} at the tapered segment. For example, the q_{sU} along pile P1-C3 segment 4 and segment 5 are 222.0 kPa and 271.2 kPa, whereas the q_{sU} along pile P1-T3 segment 4 and segment 5 are 118.6 kPa and 136.6 kPa. The compressive taper capacity comprises end-bearing capacity and shaft capacity components (Manandhar and Yasufuku 2013). The tensile taper capacity is composed of only shaft capacity. During pile installation and testing, the soil around the taper pile may be densified both vertically and horizontally. Moreover, additional lateral earth pressure is developed due to cavity expansion (Wei and El Naggar 1998, Guo and Deng 2018, Kodikara and Moore 1993) when the pile is installed and loaded. The shaft capacity may increase due to dilation of the soil which imposes addition lateral stresses on the pile. The q_{sU} value along the tapered segment of piles in tension tests is shown in Figures 3.11b and 3.11e. Notably, the q_{sU} at the tapered segment of the piles in the tension test is still high, which may be due to the dilative behavior of the shaft component.

The average and standard deviation of q_{sU} along the smooth segment of instrumented piles are 84 kPa and 27 kPa. In the upper sand stratum, the average and standard deviation of q_{sU} along the threaded segment are 60 kPa and 29 kPa. The average q_{sU} along the threaded segment is lower than the average q_{sU} along the smooth segment; this is primarily caused by the decrease in relative density, the friction angle of sand (as indicated in the site investigation) and an increase in the shearing area. By normalizing q_{sU} to similar soil conditions and shearing area, q_{sU} along the threaded segment would be significantly greater than the smooth segment.

In the lower sand stratum, the average and standard deviation of the q_{sU} over the cylindrical threaded segments (Fig. 3.11a to 3.11f) are 19 kPa and 8 kPa. This low average q_{sU} is again due to the decrease in relative density and friction angle. The average and standard deviation of the q_{sU}

along the tapered segment are 135.9 kPa and 79.3 kPa. The average and standard deviation of the q_{sU} along the tapered segment in compression are 199 kPa and 86 kPa. The average and standard deviation of the q_{sU} along the tapered segment in tension are 134 kPa and 15 kPa. In general, the average q_{sU} along the tapered segments in compression and tension are 10 times (=199/19) and 7 times (=134/19) the average of the q_{sU} along the threaded segment within the same loose sand, which suggests the effects of the taper on increasing the pile resistance. Generally, the q_s along the tapered segment in compression is higher than in tension. The q_{sU} of 40.3 kPa and 48.3 kPa along the tapered segment 5 of pile P5-C4 and P3-C4 are abnormally low. Therefore, these values are not considered valid.

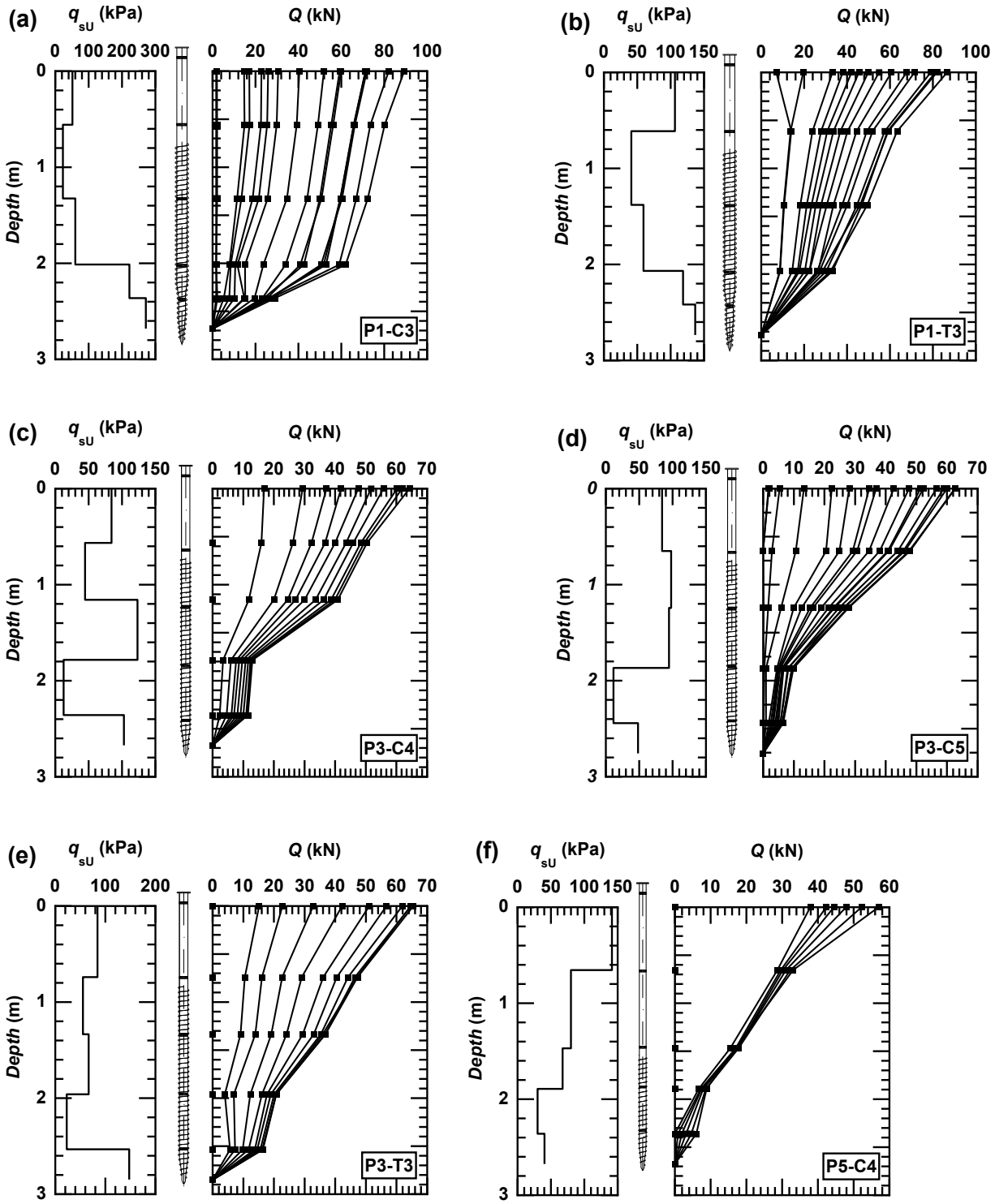

Figure 3.11. Ultimate unit shaft resistance (q_{sU}) and the distribution of axial load at various load increments for tests (a) P1-C3, (b) P1-T3, (c) P3-C3, (d) P3-C5, (e) P3-T3 and (f) P5-C4.

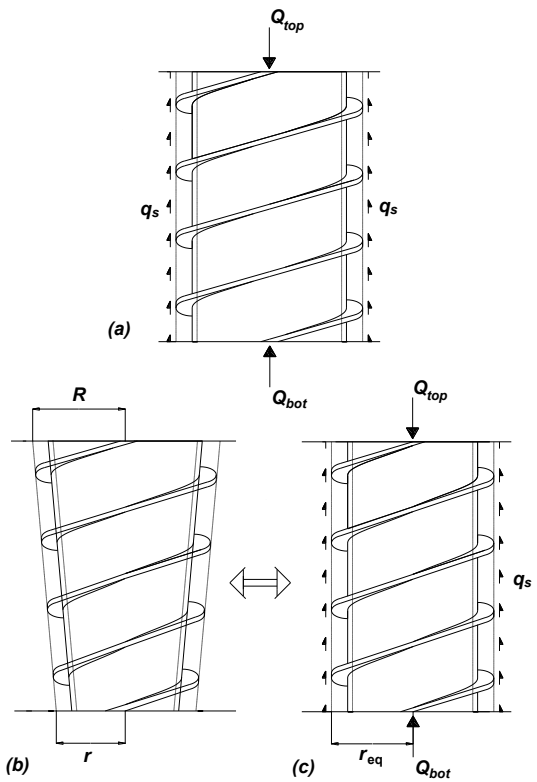

Figure 3.12. (a) Assumption of CSM, (b) schematic of a tapered segment and (c) equivalent cylindrical segment.

3.3.4. Progressive Development of q_s

The curves of the q_s vs. *w/D* of selected instrumented piles were obtained to understand the development of shaft resistance during loading, shown in Figure 3.13. The values of *w/D* corresponding to 10% and the ultimate state (Hirany and Kulhawy's criterion) are also displayed as references. In compression tests (Fig. 3.13a and b), a large, normalized displacement (or *w/D*) greater than 20% is needed to reach the peak q_s along the tapered segment, and this large displacement is compatible with the displacement needed to reach the ultimate state. In tension tests (Fig. 3.13c and d), the displacement (*w/D*) required to mobilize the peak q_s is slightly greater than 10%. The displacement needed to mobilize the peak q_s at the cylindrical segments varies with the piles and loading directions but, in general, is about 10% *w/D*.

As shown by the curve of the smooth segments (segment 1) in Figure 3.13, the value of q_s increases with displacement until it reaches a peak q_s. Then, q_s gradually decreases with increasing displacement. The contributing factors to this behavior are low confining stress, dense sand and small diameter. Boulon and Foray (1986) and Houlsby (1991) suggested that the dilation of the soil-pile interface for small-diameter piles was the main contributing factor in developing large shaft resistance. As shown by the curve of the threaded segments (segments 2 and 3), located within the dense zone, the value of q_s increases with displacement until it reaches a peak q_s. Then, q_s gradually decreases with increasing displacement, perhaps due to the rough surface and presence of dense sand. As shown by the curve of the threaded segments (segment 4 of P3-C4 and P3-T3) located within the loose zone, the value of q_s increases with displacement without reaching a peak q_s. As shown by the curves of the tapered segments (segment 5 of P3-C3, segment 4 and segment 5 of P1-C4) in compression, the value of q_s increases with displacement without reaching a peak q_s. As shown by the curves of the tapered segments (segment 5 of P3-T3 and segments 4 and 5 of P1-T3) in tension, the value of q_s increases with displacement, then, it gradually decreases with increasing displacement. It should be noted that these behaviours are based on stabilized q_s or the lower bound of the q_s vs. w/D curves.

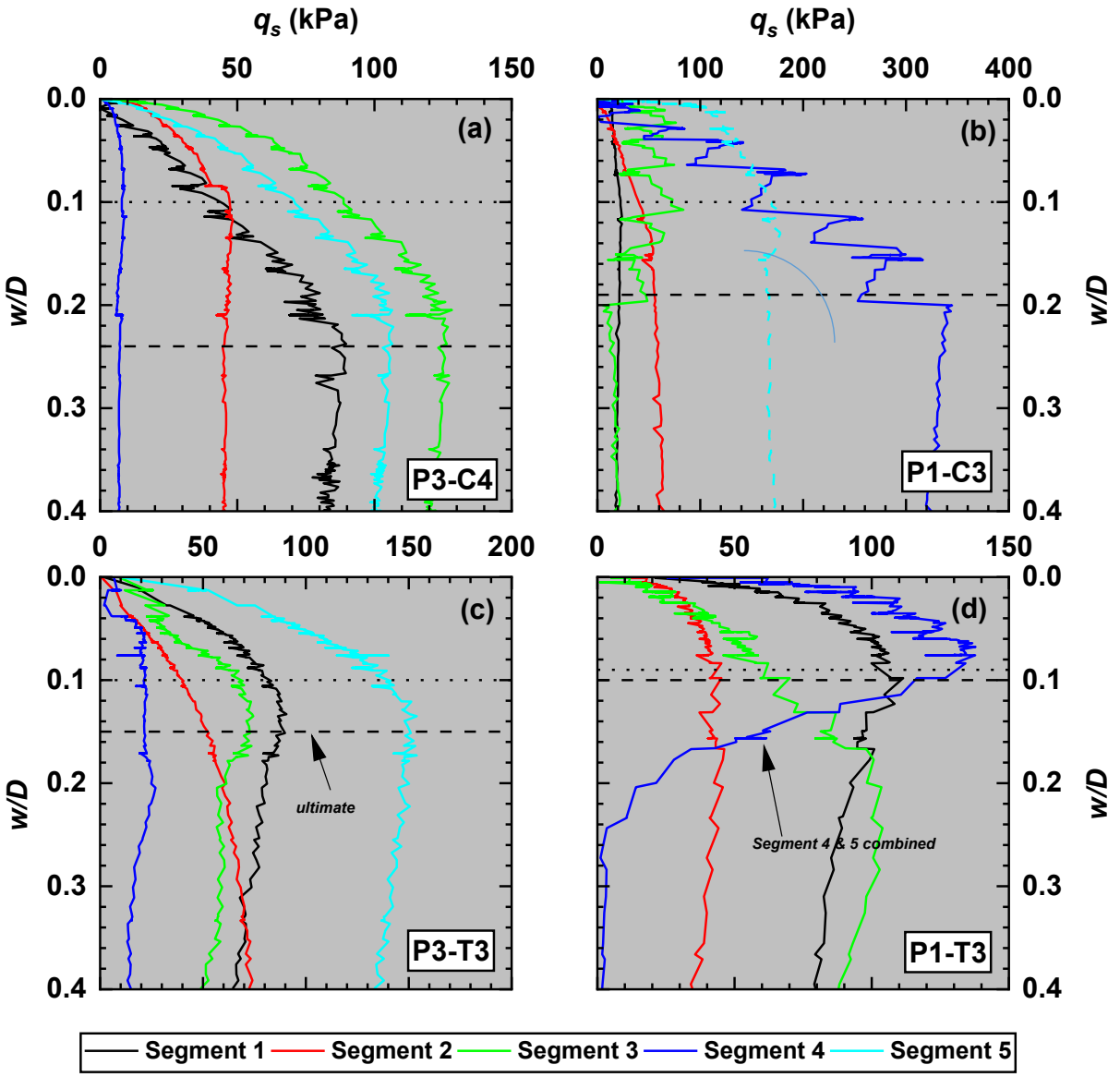

Figure 3.13. Unit shaft resistance (q_s) vs. normalized axial displacement (w/D) for tests: (a) P3-C4, (b) P1-C3, (c) P3-T3 and (d) P1-T3.

3.3.5. Method of Calculating the Unit Shaft Resistance

The CPT-based method and the effective stress methods with the current design parameters cannot be used to estimate the axial capacity of the micro screw pile. These methods can be used by obtaining design parameters appropriate for the micro screw pile by correlating the measured q_{sU} and relevant soil parameters interpreted from the CPT readings. Eight piles were instrumented with

SG to obtain the distribution of q_{sU}. The measured value of q_{sU} over 34 different segment types and two soil types is shown in Tables B1 and B2 in Appendix B. Five instrumented piles were tested under compressive load, and three instrumented piles were tested under tensile load. Thereafter, the effective stress method was used to estimate the axial capacity of 41 piles, where 21 piles were tested under compressive load, and 18 piles were tested under tensile loads.

3.3.5.1. CPT-Based Method

Bustamante and Gianeselli (1982), using data from 197 full-scale compression and tension tests of different piles in various soil types, suggested a CPT-based method for pile capacity prediction. Typically, a friction coefficient (also known as a reduction factor) is used to account for scale effects, loading rate, difference in installation technique, position of the CPT friction sleeve and differences in horizontal soil displacements (Lunne et al. 1997). Following the CPT-based method, the friction coefficients (α) over the different shaft segment types of micro screw piles were determined using the relationship between q_{sU} and average cone penetration resistance ($q_{c,avg}$), as in Equation 3-4:

$$q_{sU} = \frac{1}{\alpha} q_{c,avg} \quad (3\text{-}4)$$

The values of q_c herein are averaged ($q_{c,avg}$) from the CPT logs along the corresponding pile segment. A summary of the values of α, $q_{c,avg}$ and q_{sU} over 35 corresponding shaft segments and backup calculations is shown in Appendix B. The estimated values of α are categorized by segment type and soil type. The median values of coefficient friction (α_{med}) based on shaft segment type and soil type are shown in Figure 3.14a and Table 3.2. The estimated friction coefficient was categorized by shaft shape and soil type. The correlation of the average q_{sU} versus the average q_c

was plotted against the curves recommended by Bustamante and Gianeselli (1983). It seems that the measured q_{sU} and q_c over the smooth segment are comparable to Curve 2 (screw-in pile installed in fine sand with q_c > 3,495 kPa). A description of the pile used is given in Table 3.3. The small median value of α_{med} of the tapered segments is due to the tapered shape.

Table 3.2. Summary of coefficient α_{med} at the individual pile segments at different soil conditions.

Soil type	q_c (MPa)	Coefficient α_{med}			
		Smooth segment	Threaded segment	Tapered segment in compression	Tapered segment in tension
Moderate compact sand with gravel	5-12	102	183	36	42
Compact to very compact sand with gravel	>12	223	397	No data	No data

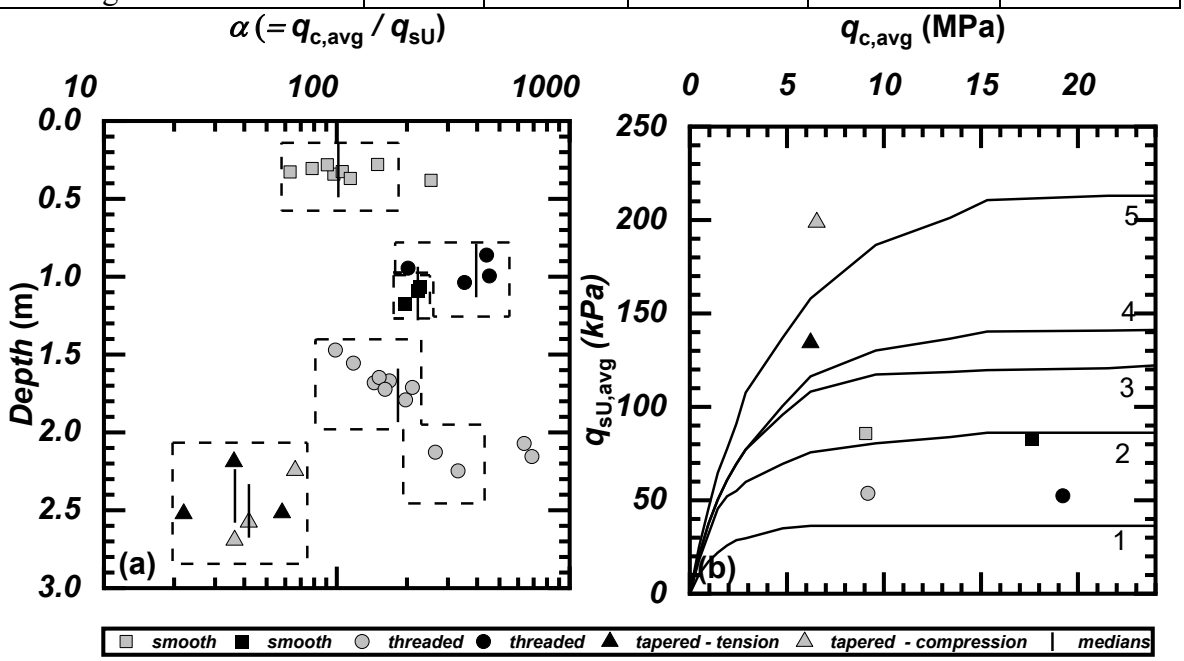

Figure 3.14. (a) Values of friction coefficients (α) at the middle of each pile segment and (b) average q_{sU} vs. average q_c values compared with the recommendation of Bustamante and Gianeselli (1983). Numbers 1–5 in (b) refer to curves for soil types and q_c magnitude in Bustamante and Gianeselli (1983).

Table 3.3. Description of piles used in combination of Figure 3.14b (after Bustamante and Gianeselli 1983).

Pile	Description	Remarks	CPT q_c (ksf)	CPT q_c (MPa)	Soil	Curve
Screwed -in	Screw-type tool placed in front of corrugated pipe that is pushed or screwed in place; reverse rotation to pull casing while placing concrete		any	any	Clay-Silt	1
		q_c < 53ksf	> 25	> 1.2	Clay-Silt	2
		Slow penetration	> 94	> 4.5	Clay-Silt	3
		Slow penetration	any	any	Sand-Gravel	1
		Fine sand with load test	> 73	> 3.5	Sand-Gravel	2
		Coarse gravelly sand/gravel	> 153	> 7.3	Sand-Gravel	3
		Coarse gravelly sand/gravel	any	any	Chalk	1
		q_c < 146 ksf without load test	> 63	> 3.0	Chalk	2
		q_c < 146 ksf with load test	> 63	> 3.0	Chalk	3
		Above water table; immediate concrete placement; slow penetration	> 94	> 4.5	Chalk	3
		Above water table with load test	> 250	> 12.0	Chalk	4

3.3.5.2. Effective Stress Methods

At the preliminary design stage, another common practice is to estimate q_{sU} at the ultimate state using the effective stress method for piles in cohesionless soils, as in Equation 3-5:

$$q_{sU} = \sigma'_{v1,avg} K_s \tan(\delta_{avg}) = \beta \sigma'_{v2,avg} \quad (3\text{-}5)$$

where K_s is the coefficient of lateral earth pressure, δ is the angle of friction between the pile and the soil, β is the combined shaft resistance factor and $\sigma'_{v,avg}$ is the average vertical effective stress over a shaft segment. The values of σ'_v were determined from γ_t and the GWT. The values of $\sigma'_{v1,avg}$ were obtained from CPT-3 only as the ϕ'_p interpreted from CPT-3 was not affected by frost.

The values of $\sigma'_{v1,avg}$ were obtained from all of the CPTs because γ_t was not affected by frost. The value of δ over the smooth segment was assumed to be $0.8\phi'_p$, and δ over the threaded segment was taken as the ϕ'_p of sand. A summary of the values of K_s and β obtained by using appropriate q_{sU}, σ'_{v1} and σ'_{v2} over 34 corresponding segment types and backup calculations is shown in Appendix B. The estimated values of K_s and β were categorized by shaft segment type and soil type. The median value of lateral earth pressure ($K_{s,med}$) and the median value of combined shaft resistance factor (β_{med}) are shown in Table 3.4.

The values of K_s, categorized by shaft segment types, are shown in Figure 3.15. The distributions of K_s in Mitsch and Clemence (1985) and Meyerhof and Adams (1968) are also shown for comparison. The values of $2K_0$, where K_0 is the coefficient of earth pressure at rest and the coefficient of passive earth pressure (K_p), were plotted because $2K_0$ and K_p are sometimes used to estimate the preliminary shaft resistance of driven piles. The median value of K_s over the upper smooth segment and the lower smooth segment in dense sand are 20.6 and 5.4 in dense sand. The median value of K_s over the upper smooth segment in compact sand is very high. The median value of K_s over the threaded segments is 2.6 in dense sand and 0.6 in loose sand. The median K_s over the lower smooth and threaded segments in compact sand is near the K_s recommended by Mitsch and Adams (1985) and K_p; this fact implies that pile installation should have loaded the compact sand to nearly passive failure. The median K_s over the uniform segments in the loose sand is close to $2K_0$; these small K_s values may be attributed to the contractive behavior of soil. The distributions of K_s in Mitsch and Clemence (1985) and Meyerhof and Adams (1968) were compared with the distribution of K_s for CHD piles by Jeffrey et al. (2016). Jeffrey et al. (2016) reported relatively high K_s for CHD piles, which provides additional confidence in the present results. The tapered segment exhibits a significantly high K_s value, 7.7 in compression and 4.5 in tension.

Table 3.4. Summary of coefficients $K_{s,med}$ and β_{med} over the individual pile segments.

Pile shaft segment type	Soil type	D_r (%)	β_{med}	$K_{s,med}$
upper smooth segment	compact sand with gravel	57	13.8	20.6
lower smooth segment	compact sand with gravel	78	4.1	5.4
threaded segment	compact sand with gravel	66	2.3	2.6
threaded segment	loose sand	48	0.5	0.6
tapered segment in comp.	loose sand	45	6.3	7.7
tapered segment in tens.	loose sand	46	3.3	4.5

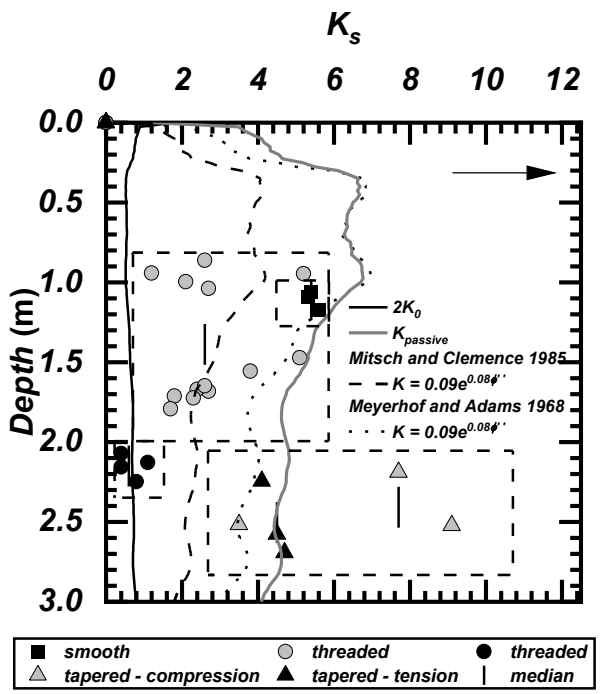

Figure 3.15. Coefficient of lateral earth pressure (K_s) at the middle of each pile segment.

The median of the coefficient β_{med} over the individual pile segment at different soil types are summarized in Table 3.4 and shown in Figure 3.16. The values of β_{med} are very large at shallow depths. They decrease with depth and then increase at the bottom of the tapered segment. The q_{sU} along the cylindrical segments in compression and tension are combined because loading direction does not affect q_{sU} along the cylindrical segment. CGS (2006) recommended values of β between

0.8 and 1.5 for driven piles in gravel, but the value of β_{med} along the top two segments appears relatively high. However, it should be noted that most studies behind this recommendation were carried out on long piles, as stated in CGS (2006). In the present study, σ'_v is low, and D_r is relatively high at shallow depths, which led to relatively high β values. Theoretically, the value of β should be very high at shallow depths. An observation of high β near shallow surface was also noted in Stuedlein and Gurtowski (2012).

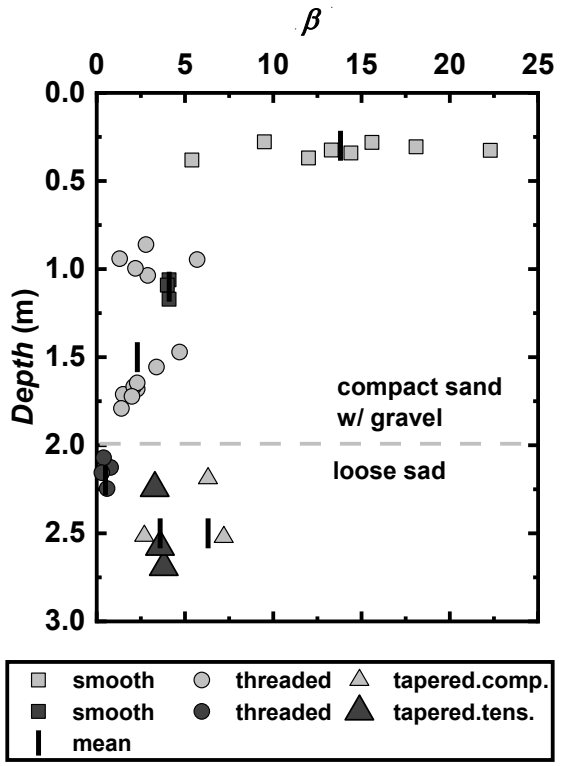

Figure 3.16. Values of β at the middle of each pile segment: (a) P1, (b) P3 and (c) P5.

3.3.5.3. Estimation of the ultimate capacity of the micro screw pile

The ultimate compressive capacities ($Q_{u,C}$) and ultimate tensile capacities ($Q_{u,T}$) of the 41 micro screw piles were estimated using the effective stress method, as in Equations 3-6 and 3-7:

$$Q_{u.C} = \sum \beta_{sm} \sigma_{v2,avg} A_s + \sum \beta_{th} \sigma_{v2,avg} A_s + \sum \beta_{t.c} \sigma_{v2,avg} A_s \quad (3\text{-}6)$$

$$Q_{u.T} = \sum \beta_{sm} \sigma_{v2,avg} A_s + \sum \beta_{th} \sigma_{v2,avg} A_s + \sum \beta_{t.t} \sigma_{v2,avg} A_s \quad (3\text{-}7)$$

where β_{sm} is the combined shaft resistance factor of the smooth segment, β_{th} is the combined shaft resistance factor over the threaded segment and $\beta_{t.c}$ and $\beta_{t.t}$ are the combined shaft resistance factor over the tapered segment in compression and tension. The relevant values of β that are needed to calculate the ultimate capacities of each pile are shown in Figure 3.17. As shown in Table 3.4, the values of β over all the segments are known except over the tapered segment in compact sand. The values of $\beta_{t,c}$ and $\beta_{t,t}$ over the tapered segment in compact sand were back-calculated from Equation 3-7 using all the other combined unit shaft resistance factors and the measured Q_u of Piles P2, P4 and P6. The values of $\beta_{t.c}$ and $\beta_{t.t}$ over the tapered segment in compact sand are estimated as 6.2 and 1.2. The value of $\beta_{t.c}$ over the tapered segment in compact sand is similar to $\beta_{t,c}$ over the tapered segment in loose sand. However, the value of $\beta_{t,t}$ over the tapered segment in compact sand is about one-third of the value of $\beta_{t,t}$ over the tapered segment in loose sand, as inferred from the low Q_u values of the short piles (see Fig. 3.9b).

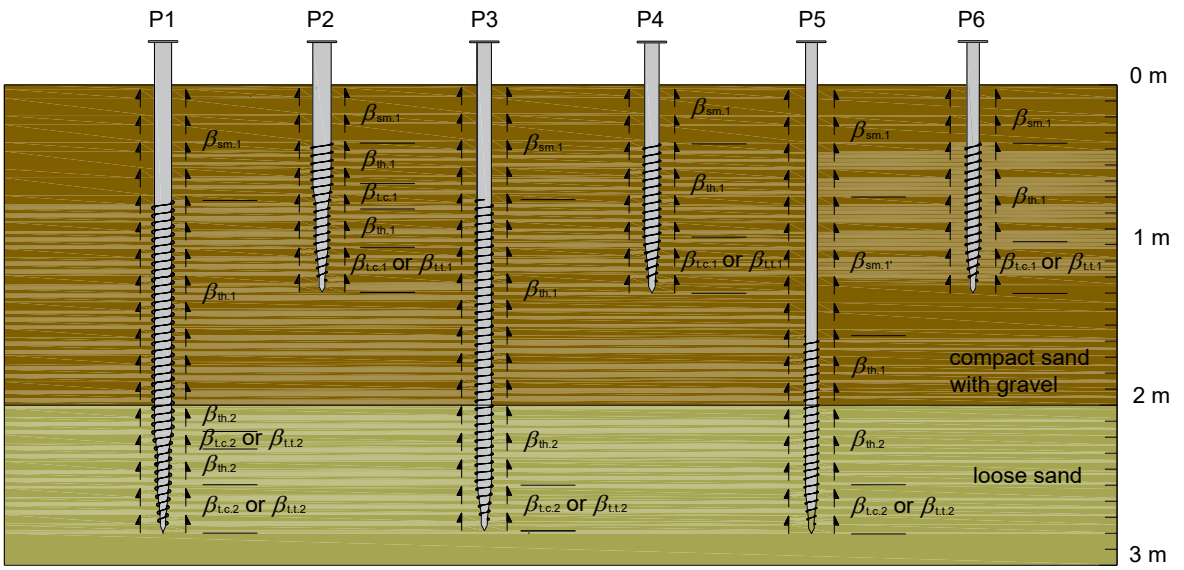

Figure 3.17. Relevant combined unit shaft resistance factor over different shaft segments.

To examine the accuracy of the values of β, the aforementioned values of β_{min} along appropriate segments were used to estimate Q_u. The estimated and measured Q_u values of 41 piles are plotted in Figure 3.18. The coefficient of the determination (R^2) of the estimated and measured ultimate capacity is 0.76, which indicates a relatively strong prediction. Alternatively, the estimated Q_u is only 4% greater than the measured Q_u on average. The method seemed to have a better estimation of the capacity of the piles in tension tests than in compression tests. In addition, the β method underestimates the capacities of pile types P1 and P4 in compression tests. The reason for underestimating P1 capacities is that the value of the β_{med} of the tapered segment is less than the measured value of the β_{med} of P1 in compression tests.

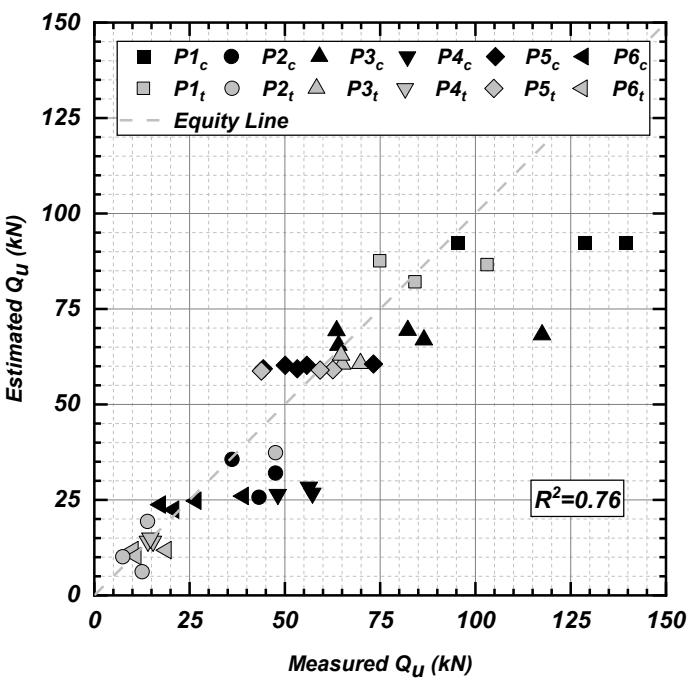

Figure 3.18. Estimated Q_u using β_{med} vs. the measured Q_u of 41 test piles.

3.3.6. Installation Torque Model

The torque recorded during pile installation provides a method for verifying pile capacity and soil properties. In the present study, the installation torques were recorded manually and electronically. Figure 3.19 summarizes the T_{end} and T_{max} of five pile types; the records of pile P6 were unavailable because the torque data were not collected correctly. The average T_{end} and one standard deviation, shown as error bars in Figure 3.19, imply that the T_{end} of each pile type is reasonably consistent among each pile type except for P1. The long piles exhibit greater T_{end} than the short piles, as would be expected. Figure 3.20 shows the profiles of the measured installation torque (T) of selected pile types. In general, the installation torque (T) increases with depth because of increasing soil-shaft interface area and reaches the peak near the end. As shown in Figure 3.20, the pile type P3-T1 exhibits exceptionally high torques when breaking ground to a depth of 0.6 m. The frozen ground likely caused this high torsional resistance because those piles were installed in early winter (December). As the piles break through, T drops and then increases until reaching the peak.

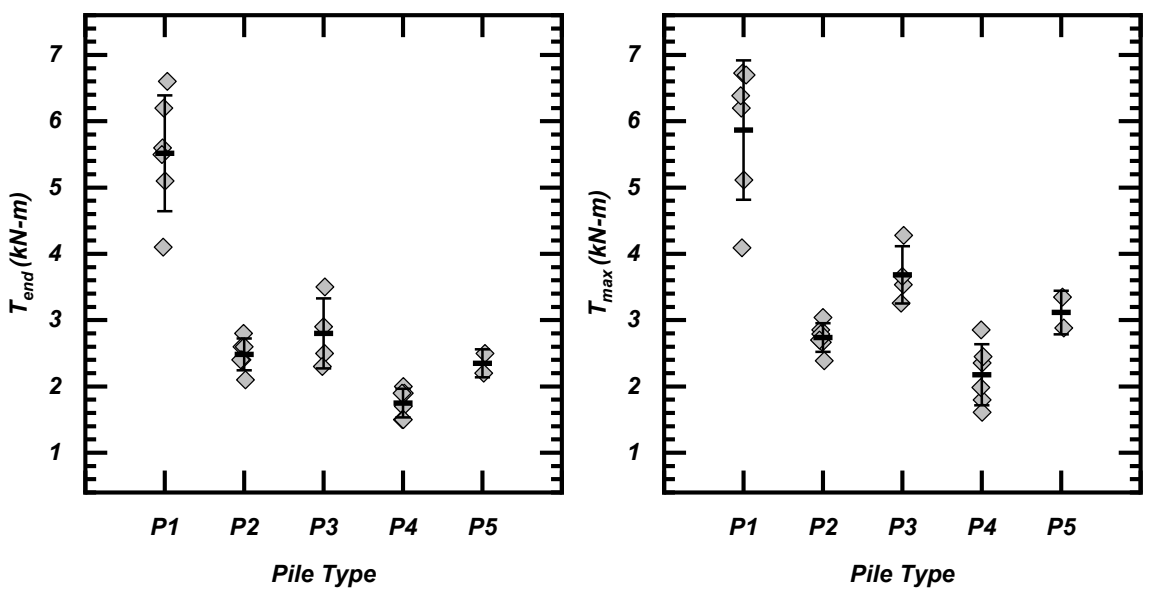

Figure 3.19. Summary of the measured T_{end} and T_{max} of five pile types. Error bars are the average and one standard deviation of T_{end} and T_{max}.

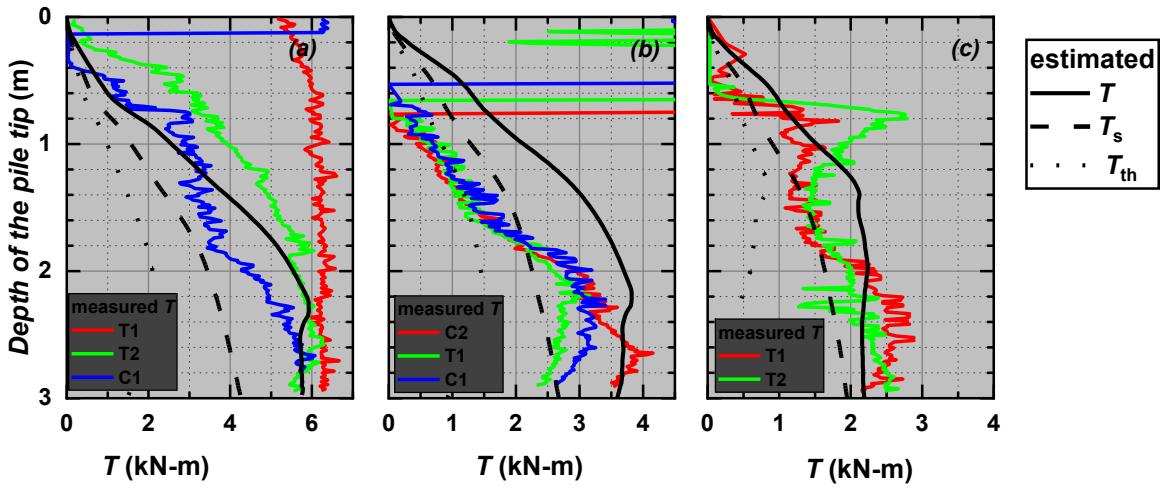

Figure 3.20. Estimated and measured continuous installation torques with the depth of the pile tip for selected pile types: (a) P1, (b) P3 and (c) P5.

Estimating the installation torque is essential for selecting an appropriate torque head, but it can also be used in the empirical torque factor method to obtain the pile capacity. Several researchers have attempted to develop correlations between the CPT tip resistance and installation torque of helical piles (Gavin et al. 2013, Spagnoli 2016, Al-Baghdadi et al. 2017, Davidson et al. 2018). Guo and Deng (2018) developed a theoretical torque model based on the soil-pile interface shearing resistance of the pile shaft and threads, as shown in Figure 3.21, where the interface shearing resistance was taken as the CPT f_s readings. When estimating T, it might be reasonable to adopt the CPT f_s in sand because f_s reflects the shearing mechanism at the soil-pile interface. The torque of a test pile was estimated based on moment equilibrium in horizontal plane using Equation 3-8:

$$T = T_s + T_{th} \tag{3-8}$$

where T_s and T_{th} are the torque contributions from shaft and threads, respectively, which were estimated from Equations 3-9 and 3-10:

$$T_s = \sum \left(0.5 \Delta z \pi D_s^2 f_s \right) \tag{3-9}$$

$$T_{th} = \sum \left((D_h + D_s) f_s \pi (D_{th}^2 - D_s^2) (\frac{\Delta z}{s}) \right) + \sum \left(0.5 D_h f_s \sqrt{(0.5\pi D_h)^2 + s^2} t_{th} (\frac{\Delta z}{s}) \right) \tag{3-10}$$

where D_s = pile shaft diameter, D_{th} = thread diameter, s = the spacing of the thread, t_{th} = thread thickness and Δz = the length of an arbitrary segment. A free body diagram (in terms of torque) of an arbitrary segment is shown in Figure 3.21. Equations 3-8 to 3-10 were based on two assumptions. First, the installation torque was counter-balanced by the resisting torque determined from the soil-pile interface area and friction. The surface area of the pile includes the surface area of the shaft, the horizontal projection of the upper and lower surface area of the thread and the surface area of the edge of the thread. The horizontal projection of the surface area of the thread is the surface area of a disc, which is represented by the first term in Equation 3-10. Secondly, the interface friction was represented by the CPT f_s at the same depth because the soil was expanded and sheared in a similar manner during CPT advancement and pile torsion.

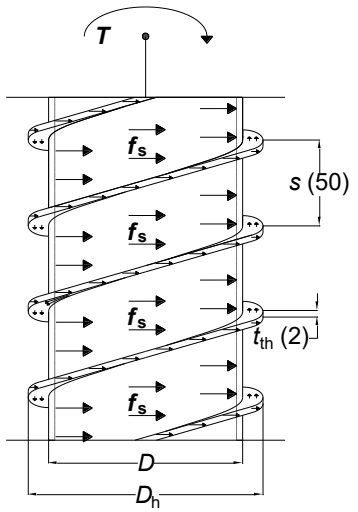

Figure 3.21. Schematic of a torque model. Dimension unit: mm.

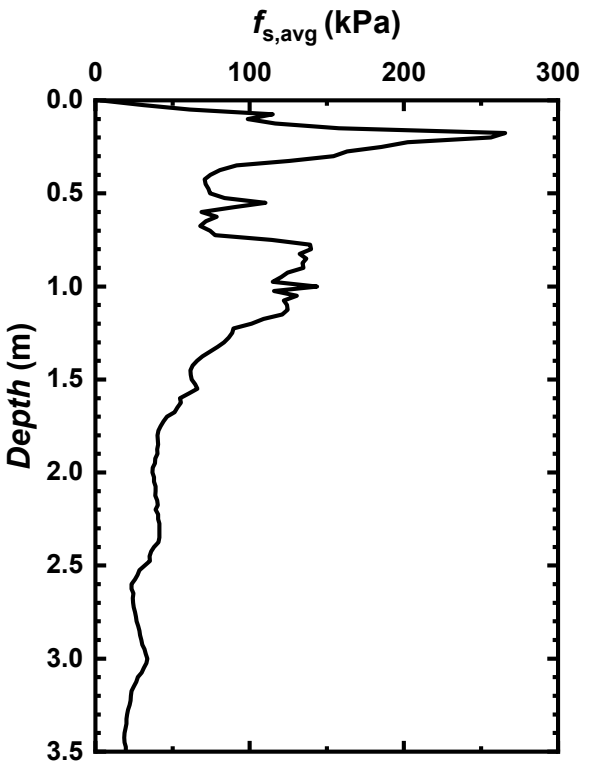

Figure 3.22. Average of the four CPT f_s values used to estimate *T*.

Profiles of installation torques were estimated following this simple torque model. The average of the four CPT f_s values was used to estimate *T,* as shown in Figure 3.22. The curves of

estimated total torque (T), torque due to threads (T_{th}) and torque due to shaft (T_s) are compared with the curves of measured T in Figure 3.20. It can be seen that the estimated T increased rapidly as the pile passed through the dense sand, reached a maximum T, and then decreased very slowly as the pile traversed through the loose sand. The trend of estimated T is approximately similar to the trend of measured T, particularly at the deeper level. However, the measured T is abnormally higher than the estimated T below 0.6 m ground depth, likely because of the effects of surface frost. By comparing the estimated and measured torque profiles, it can be seen that the excessively high T is due to the frozen ground since such a high torque cannot be developed based on the unfrozen f_s profiles. The reasonable similarity at greater depth may suggest the validity of the present torque model based on the CPT f_s profiles. On the other hand, the torsional resistance is predominantly due to the T_s because of the large surface shaft area.

The correlation of the measured T_{max} vs. estimated T_{max} and the measured T_{end} vs. the estimated T_{end} of 24 piles is shown in Figure 3.23. The R^2 of the measured and estimated T_{max} is 0.75, and the R^2 of the measured and the estimated T_{end} is 0.78. There is some variation between the measured and estimated T_{max} and T_{end}, which can be due to soil heterogeneity and the operator's error in installing a pile (e.g., pile oscillating near the end, as noted in the field). Although not perfect, the R^2 values suggest consistency in the measured and estimated values to some extent. It is, therefore, legitimate to conclude that the present torque model can estimate the installation torque with reasonable accuracy.

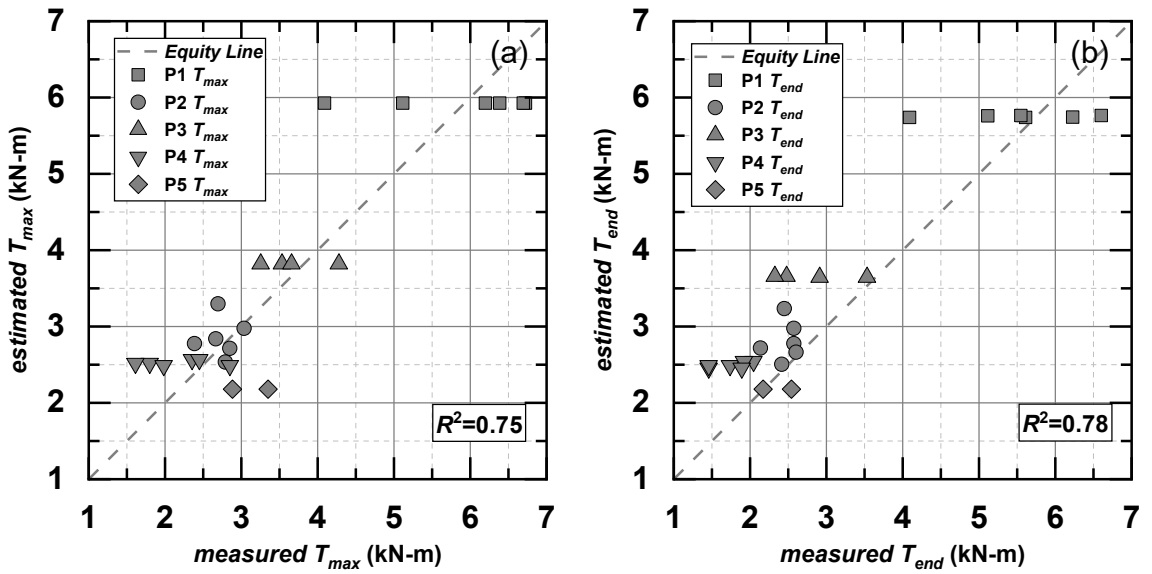

Figure 3.23. (a) Measured T_{max} vs. estimated T_{max} and (b) measured T_{end} vs. estimated T_{end}.

3.3.7. Torque versus Capacity

The method based on the empirical torque factor is often used to estimate the capacities of piles (such as helical piles; Hoyt and Clemence 1989) that are screwed into the ground. Given that the geometrical properties of the micro screw pile thread are different those of other helical piles' helices, there is a need to obtain an empirical torque factor (K_T) that is unique to these piles. Following this torque vs. capacity concept, an empirical torque factor K_T of the micro screw piles was determined using the relationship between the measured Q_u and measured T_{end}, as in Equation 3-11:

$$Q_u = K_T T_{end} \tag{3-11}$$

Since the diameters of the test piles are similar, the piles were grouped only by loading directions. The measured Q_u versus T_{end}, with line of best fit, of each pile in compression and tension tests are plotted in Figures 3.24a and 3.24b. The empirical torque factor of each micro screw pile, with corresponding regression coefficients, is shown in Table 3.5. The regression

coefficients of piles P1 and P3 in compression and piles P1 and P2 in tension that are satisfactory are shown. However, the regression coefficients of other piles in compression and tension are quite low, which can be due to the limitation on the number of tests and the scatter in the data. Nevertheless, it can be seen that the empirical torque factor of the screw micropiles increases with decreasing pile diameter and increasing pile length. Perko (2009) related the value of K_T with the effective diameter of the pile shaft, as in Equation 3-12:

$$K_T = \frac{\lambda^k}{d_{eff}^{0.92}} \tag{3-12}$$

where λ^k is a fitting factor equal to 1433 $mm^{0.92}$/m. In addition, Sakr (2015) mentioned that for a specific helical pile, the ratio of K_T for tension to compression is equal to the ratio of tensile to compressive capacities as the installation torque is the same in both cases. The average ratio of K_T for tension to compression is 0.53, which is nearly equal to the average ratio of the tensile to compressive capacities of 0.48. However, the influence of the location of the threads and the number and angle of the tapered segment of micro screw piles on both lateral capacity and torque should be noted.

As a comparison, the empirical torque factor ($K_{T\text{-}P}$) of the micro screw piles in compression tests were estimated based on Perko (2009). The $K_{T\text{-}P}$ of the micro screw piles in tension tests were estimated by taking the $K_{T\text{-}P}$ of a pile in compression and multiplying it by the average ratio of tensile to compressive capacity. It was found that the method provided by Perko (2009) generally underestimated the empirical torque factor of the micro screw piles. The limitation of the torque factor approach should be noted. The factor K_T is only used for estimating pile capacities at the preliminary stage. The values of K_T in Figure 3.24 are based on a limited number of tests at a single test site. More data on the capacity and torque of the micro screw piles from various sites may be

warranted to provide a more credible K_T. The backup calculation to get the K_T of each micro screw pile in compression and tension is shown in Appendix B.

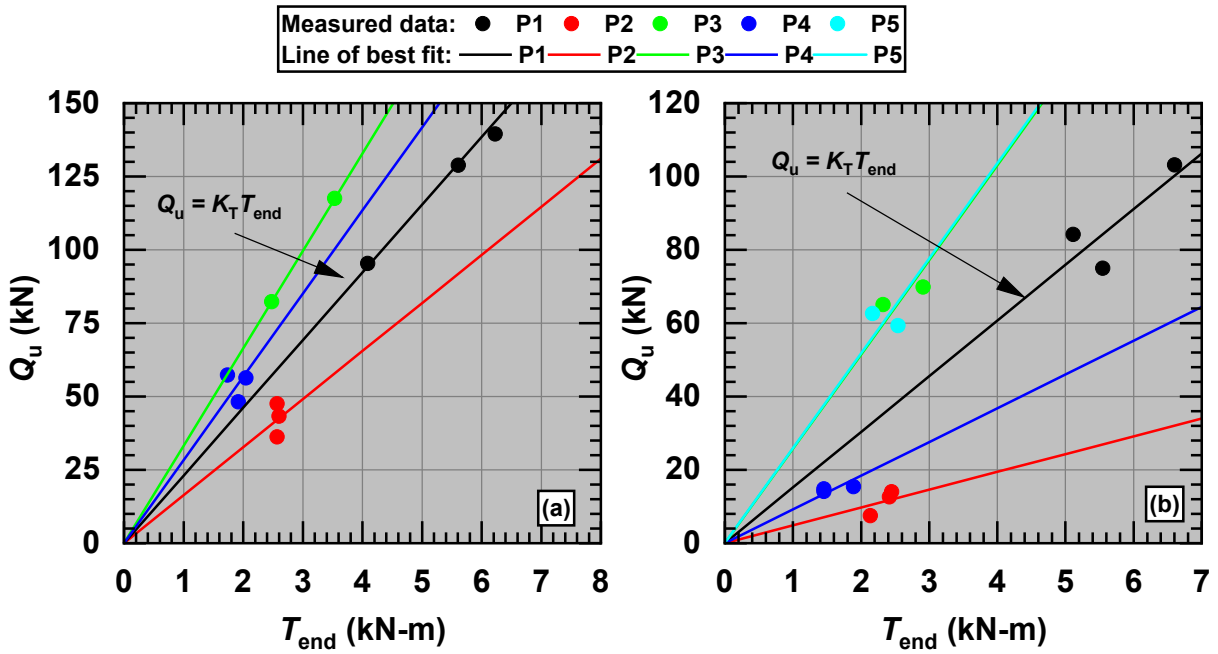

Figure 3.24. The measured Q_u vs. T_{end} of piles for (a) compression tests and (b) tension tests.

Table 3.5. The empirical torque factor of each pile in compression and tension as obtained in this research and estimated using Perko (2009).

Pile	Compression				Tension				
	K_T	R^2	$K_{T\text{-}P}$	$K_{T\text{-}P}/K_T$	K_T	R^2	Average comp. / tens. Q_u	$K_{T\text{-}P}$	$K_{T\text{-}P}/K_T$
	(m^{-1})	(%)	(m^{-1})	(%)	(m^{-1})	(%)	(%)	(m^{-1})	(%)
P1	20.8	98.9	18.3	88	15.2	66.8	72	13.2	87
P2	16.4	N.A.	18.3	112	4.9	42.7	27	4.9	101
P3	33.2	100	23.1	69	25.8	N.A.	68	15.6	61
P4	28.4	N.A.	23.1	81	9.2	N.A.	27	6.3	69
P5	N.A.	N.A.	26.6	N.A.	25.9	N.A.	100	26.6	103
P6	N.A.	N.A.	26.6	N.A.	N.A.	N.A.	N.A.	N.A.	N.A.

3.4. Conclusions

A field test program of 41 full-scale micro screw piles was carried out in a sandpit site. The following conclusions may be drawn:

1. The tapered segment contributes significantly to the compressive Q_u; the tensile Q_u at the tapered segment is also considerable, particularly for tapers in the loose sand stratum.
2. The compressive and tensile Q_u are mobilized at the w/D ranges of 0.14–22 and 0.06–0.22, respectively. Significant displacement is required to achieve the ultimate state. The curves of the q_s vs. w/D over the smooth and threaded segments in dense sand increase with increasing displacement until reaching a peak q_s; then, q_s gradually decreases with displacement. The curves of the q_s vs. w/D over the threaded segment in loose sand increase with increasing displacement without reaching a peak q_s. The curves of the q_s vs. w/D over the tapered segment in loose sand and in compression increase with increasing displacement without showing a peak q_s. The curves of the q_s vs. w/D over the tapered segment in loose sand and in tension increase with increasing displacement until reaching a peak q_s. Then, q_s gradually decreases with displacement.
3. The cylindrical shearing mode governs the failure of the threaded segment. The value of q_s, which increases with increasing displacement, exhibits dilative behavior. The interface of the threaded segment in loose sand exhibits contractive behavior.
4. The cylindrical shearing mode governs the failure of the threaded segment. The values of q_{sU} along the smooth and the threaded segments are not visibly affected by the load direction. The value of q_{sU} along the tapered segment of the pile is estimated using CSM on the equivalent cylinder area. The average q_{sU} along the tapered segment is 7.1 times that of the value at the threaded segment.

5. A correlation between shaft resistance q_s and cone tip resistance q_c was developed for the CPT-based prediction method for pile capacities. The measured q_s and q_c along the smooth segment trend are comparable to Curve 2 provided by Bustamante and Gianeselli (1983). The median value of α along the threaded segment is less than that of the smooth segment, while the median value of α along the tapered segment is significantly less than that of the uniform segment.
6. The median value of K_s along the uniform segments in compact sand is near the passive-state pressure coefficient. The median value of K_s along the uniform segments in loose sand is near $2K_0$. The value of β_{med} along the tapered segment is greater than the uniform segment because of the soil-pile failure mechanism along the tapered segment.
7. A theoretical torque model was adopted to estimate the profiles of torque, max-installation torque and end-installation torque based on the soil-pile interface shearing resistance (or CPT f_s) developed along the pile shaft and thread during the pile installation. The estimated T profile is comparable with the measured torque profile.
8. The empirical torque factor of each micro screw pile in compression tests and tension tests were obtained. The empirical torque factor increases with decreasing pile diameter and increasing pile length. The average ratio of the empirical torque factor of the micro screw piles in tension to compression is 0.53, which is nearly equal to the average ratio of tensile to the compressive capacities of 0.48. The empirical torque factor of micro screw piles is generally underestimated by the method provided by Perko (2009).

4. Axial Cyclic Load Field Tests of Micro Screw Piles in Sand

4.1. Introduction

A new type of pile has been introduced in the Canadian construction industry. It consists of a smooth segment at the top, a threaded segment at the middle and a tapered segment at the bottom. It has a relatively small diameter and short length, which is aimed for various lightweight structures. It is screwed into the ground using the torque method. Therefore, it is referred to as a "screw micropile" (Guo and Deng 2018). When piles are used in areas where cyclic (dynamic) loads are persistent, the cyclic performance of piles becomes as important as their static performance. Many structures, including offshore structures, transmission poles, residential buildings, commercial buildings and machine foundations, are founded on piles. These structures are subjected to various cyclic loads from earthquakes, wind, waves, tides and machine vibrations. These cyclic loads on the superstructure are transferred to the underpinning pile foundation as axial cyclic loads, in addition to the lateral cyclic loads. As noted in Kunnath et al. (2008), axial cyclic loads have an adverse effect on the soil-structure interaction (SSI) particularly when the superstructure is significantly wide. Therefore, it is essential to study the performance of piles subjected to axial cyclic loads.

Several studies have been dedicated to the axial cyclic performance of piles. In the research where physical testing is adopted, axial cyclic loads are often decoupled from lateral loads due to the limited capability of hydraulic loading equipment. In the literature, changes in pile capacity, pile-head stiffness and cumulative displacement are often examined to indicate axial cyclic performance. El Naggar and Abdelghany (2007) and El Naggar and Sakr (2002) observed a reduction of pile capacity. However, the reduction of pile capacity may not be observed in the case of load-controlled cyclic tests. During a load-controlled cyclic test, pile shaft resistance may be redistributed, and base capacity may increase. Poulos (1989) suggested that the shaft resistance

degradation depends on cyclic displacement, number of cycles, soil type and pile type. Drbe and El Naggar (2015) reported the results of cyclic compression tests on hollow-bar micropiles. The shaft resistance had re-distributed, and the base capacity had increased slightly. El Sharnouby and El Naggar (2012) reported that the shaft resistance had degraded but that the load transferred to the lead section had increased. El Sharnouby and El Naggar (2012) observed that both the static and cyclic responses of piles could be enhanced by changing pile diameter or stiffness. El Sharnouby and El Naggar (2012) observed that the shaft resistance had degraded and that the base capacity of a tapered pile in loose sand had increased; the increase in base capacity was related to the densification of the sand around the tapered pile.

Pile-head stiffness, defined as the ratio of change in axial load to change in axial displacement, has been widely examined in the literature because stiffness may be an indicator of pile stability. Li et al. (2010) investigated the cyclic performance of a pile in dense sand with different installation procedures using centrifuge modelling tests and found that pile-head stiffness had decreased with several cycles. Abd Elaziz and El Naggar (2011), El Sharnouby and El Naggar (2012) and El Naggar and Abdelghany (2007) reported that pile stiffness had remained unchanged during a cyclic loading test. El Naggar and Sakr (2000) and El Naggar and Wei (2000) suggested that an increase in stiffness was associated with the densification of sand around the tapered pile. Hanna et al. (1978) reported that the displacement of an anchor increased with an increase in loading amplitude during a one-way uplift cyclic test. However, it should be noted that the cumulative displacement mainly occurred during a one-way cyclic loading test, especially at a strain-softening soil-pile interface (Poulos 1989, Abd Elaziz and El Naggar 2011). In all cases, the cumulative displacement increased with the number of cycles in models or field tests (Li et al. 2010, Abd Elaziz and El Naggar 2011, Hanna et al. 1978).

The axial capacities and failure mechanism of the micro screw pile in a cohesive soil site were first examined by Guo and Deng (2018) via a static loading test program. Similar testing programs were carried out by Sanzeni and Danesi (2019) at a cohesive soil site and Khidri and Deng (2022) at a cohesionless soil site. Guo et al. (2019) performed axial cyclic tests on the micro screw piles at a cohesive soil site; small cumulative displacement was observed to decrease with increasing pile diameter and shaft length. However, the axial load cyclic performance of the micro screw pile installed in cohesionless soil has never been studied. Hence, research on the axial cyclic performance of the micro screw pile subjected to axial cyclic loads is required. In addition, most previous research into the axial cyclic behavior of piles often lacks a detailed study of the re-distribution of shaft resistance. Furthermore, micro screw piles consist of several segments with unique shapes and outer surfaces. It will be insightful to inspect the soil-segment interaction of these piles during cyclic loads.

In the present research, the axial cyclic performance of the micro screw pile in cohesionless soil was investigated. Six types of micro screw piles installed at Sandpit were tested in the field with one-way load-controlled cyclic load to simulate the loading pattern of an "earthquake." Three types of micro screw piles were instrumented with axial SG stations to measure the distribution of the unit shaft resistance and time histories of the unit shaft resistance. A geotechnical site characterization program was undertaken to obtain the soil profile and properties. The first objective of the research was to obtain the overall axial cyclic response of the pile, including an examination of load vs. displacement curve, cumulative displacement, pile-head stiffness and pile-head damping ratio. The second objective was to obtain the axial cyclic response of the individual segments, including examining the unit shaft resistance, segment stiffness and segment damping ratio.

4.2. Field Test Program

4.2.1. Test Setup

The test setup was designed for axial static load field test as per ASTM (2007b) standard D1143 and ASTM (2007c) standard D3689 by Guo and Deng (2018). The layout and setup of the test are shown in Figure 4.1 and Figure 3.3, respectively. The test setup was designed to conduct both compression and tension testing. Four reaction piles, 2.1-m-long micro screw piles, were installed at each side of the test pile. The reaction piles were 3 m apart. Each setup allowed for at least two tests while maintaining a minimum spacing equal to five times the diameter of the pile. A slider was designed that allowed the movement of the hydraulic jack under the reaction beam. Before loading the pile, the slider was moved on top of the pile, and the hydraulic jack's piston was extended just enough to be touching the pile head. Then, one set of the bolt was used to fix the slider on the reaction beam, and another set of the bolt was used to fix the hydraulic jack piston to the test pile head. Then, two linear potentiometers were attached between the hydraulic jack and the pile head. The two-way hydraulic jack was equipped with a load cell of 900 kN capacity to measure load. The load cell, two linear potentiometers and SGs were recorded in a datalogger at a time interval of 1 sec. Piles P1, P3 and P5 were instrumented with axial SGs to measure the distribution of the axial load along the pile, which is shown in Figure 3.1.

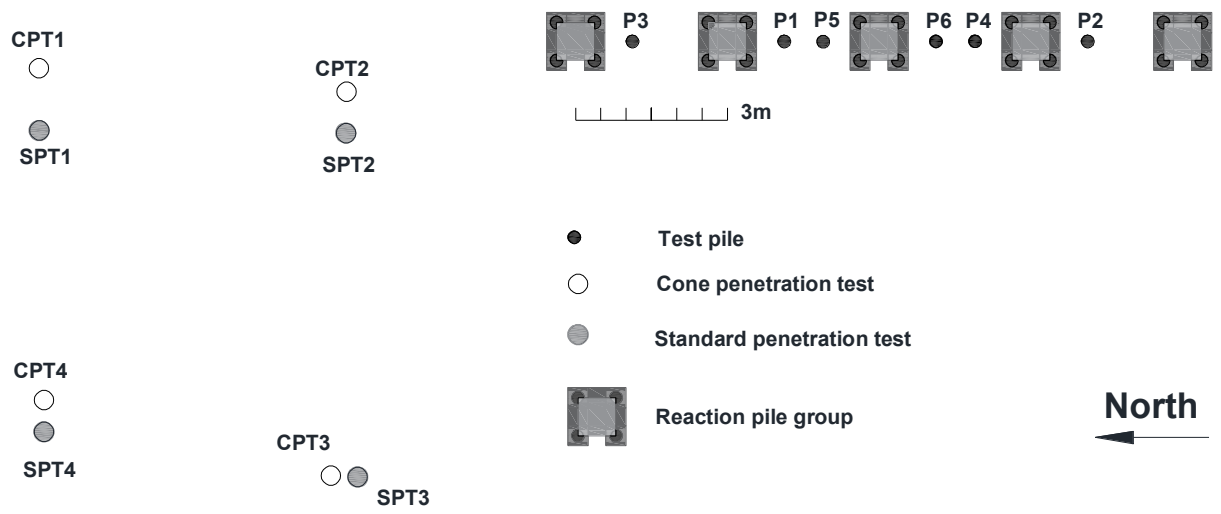

Figure 4.1. Layout of cone penetration tests, BHs with SPTs and test piles.

4.2.2. Test Procedure

During an earthquake, seismic waves emanate from the source and propagate through the Earth's crust, as shown in Figure 4.2. Seismic waves can generally be categorized as body waves, which travel through the Earth, and surface waves, which travel at the surface of the Earth. Body waves include primary or compressive waves and secondary or shear waves. Surface waves include Rayleigh or ground roll waves and Love or horizontally polarized shear waves. During an earthquake, the superstructure may experience rocking motion which includes vertical and lateral vibrations. The rocking motion of the superstructure causes vertical and lateral cyclic load on the underpinning pile foundation.

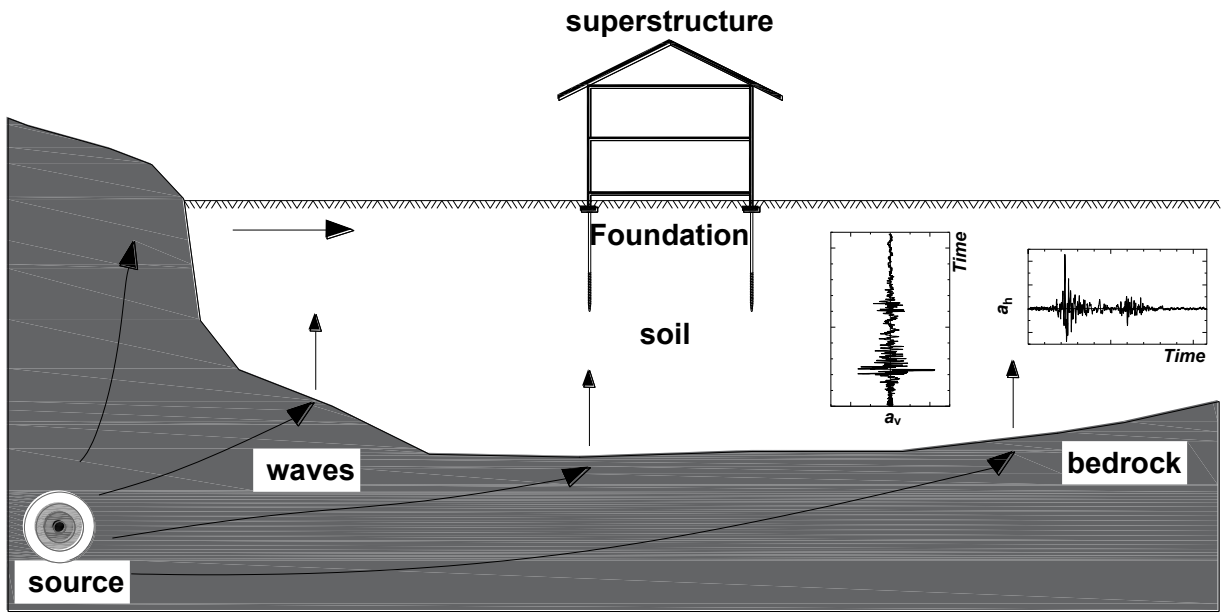

Figure 4.2. The effect of an earthquake on a superstructure (drawing not to scale).

Dynamic soil-foundation-structure interaction (SFSI) during earthquake shaking has been extensively studied in the literature. A common experimental method to investigate the SFSI is the dynamic shaking table test (e.g., Elsawy et al. 2019), for which the soil-foundation-structure system is shaken at the base of the shaking table, as shown in Figure 4.3a and Figure 4.3b. Shaking table tests at 1 g or on a geotechnical centrifuge can be expensive, and the equipment may be unavailable in an institution. Hence, other test methods, including mass (or force) vibration test (e.g. Algie 2011, Elkasabgy and El Naggar 2013) and pseudo-static cyclic load tests (e.g., El Naggar and Abdelghany 2007, Drbe and El Naggar 2015, El Sharnouby and El Naggar 2012, Abd Elaziz and El Naggar 2011), as shown in Figure 4.3, are also carried out instead of the shaking tests. As shown in Figure 4.3c and Figure 4.3d, a dynamic test shakes the soil-foundation system in the lateral direction, a mass vibration test exerts a high-frequency vibratory force on the pile or building top, and a pseudo-static cyclic test applies slow cyclic loading on the pile top in the vertical or lateral direction.

When a pseudo-static cyclic test is carried out, as in Figure 4.3e and Figure 4.3f, the cyclic loading is applied at a sufficiently slow speed such that the inertia force of the mass (if the mass exists) is negligible. The cyclic behavior of the soil-foundation system provides the equivalent-linear properties or backbone curves of the soil-foundation system that can be later used to assess the dynamic behaviour of the system.

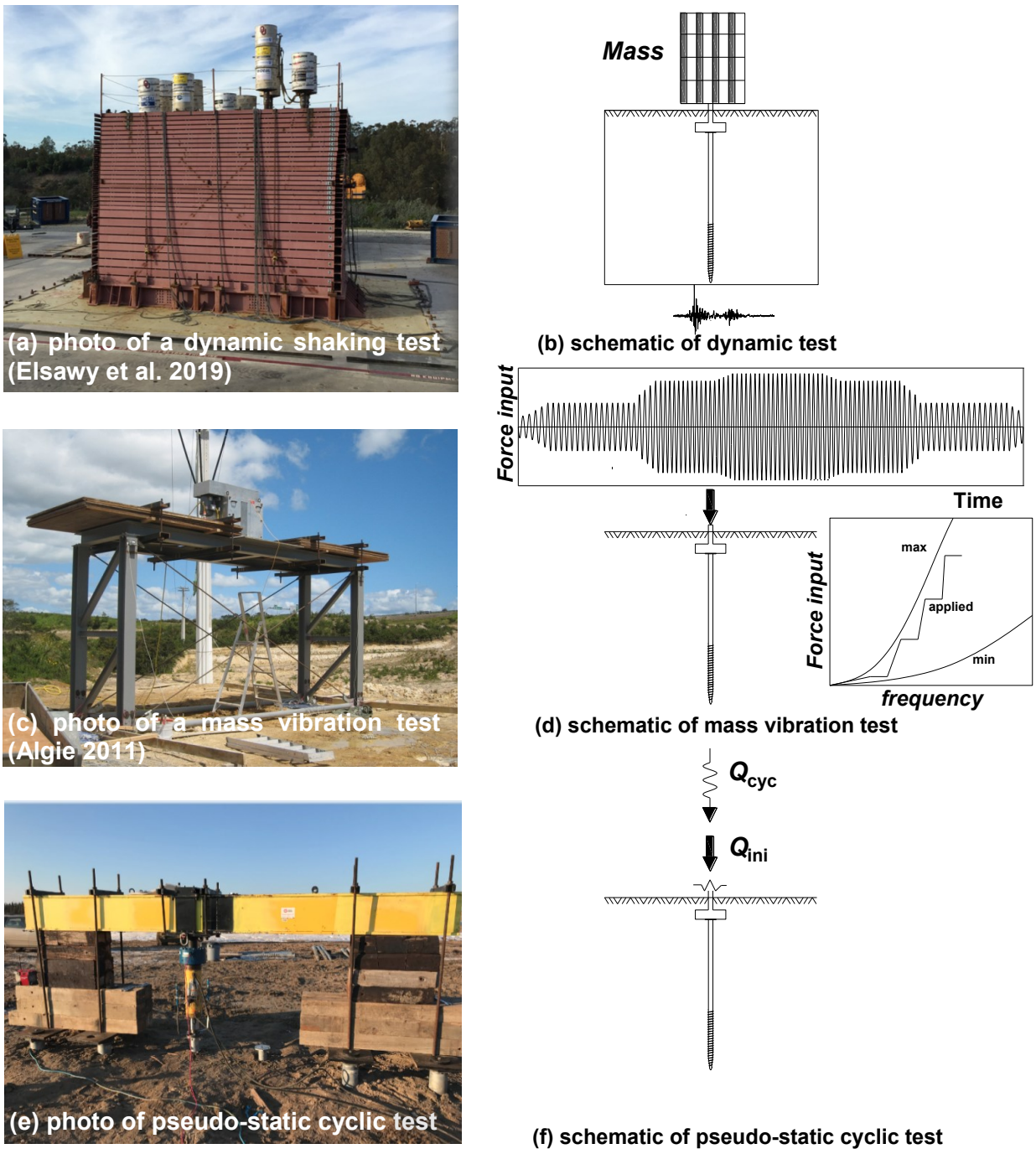

Figure 4.3. Experimental testing methods for a general SFSI study: (a) and (b) dynamic shaking test, (c) and (d) mass (or force) vibration test and (e) and (f) pseudo-static cyclic test. Note: the mass vibration and pseudo-static cyclic loading tests can also be applied in the lateral direction; (b), (d) and (f) are illustrative only and do not necessarily match the actual experimental setup.

In the present research, axial cyclic loading tests, which were pseudo-static and one-way compressive, were designed to simulate the vertical loading pattern of an earthquake. One-way cycles are more analogous than two-way cycles to the scenario where a pile is subjected to axial cyclic loads from the superstructure. Seed et al. (1975) provided a chart of the number of representative cycles vs. the earthquake magnitude and suggested 15 cycles for an earthquake magnitude of 7.5. Although the chart was initially developed for a liquefaction potential assessment (Liu et al. 2001), 15 cycles were adopted for the soil-pile interaction research when earthquake loads were concerned (e.g., Rollins et al. 2003, Guo et al. 2019, El Naggar and Abdelghany 2012).

As shown in Figure 4.4, the pile was initially loaded to an initial load (Q_{ini}), corresponding to a factor of safety (FS) as in Equation 4-1:

$$FS = \frac{Q_u}{Q_{ini}} \tag{4-1}$$

where Q_u is the ultimate compressive capacity that was approximated by Kulhawy's approach (Khidri and Deng 2022). The value of Q_u was taken as the arithmetic mean of three or four monotonic load field tests of the respective pile type (as reported in Khidri and Deng 2022). The target FS was 1.5, which is common for the ultimate state design of a pile. However, the actual FS varied between 0.6 and 1.9. This deviance was because the Q_u measured from monotonic load field tests differed among piles mainly due to installation disturbance or soil heterogeneity. An FS < 1 does not actually imply a pile failure in the initial stage of this specific pile, as shown in subsequent curves of cyclic load vs. displacement.

Afterward, the load was increased and decreased by an amplitude of Q_{cyc} 15 times in 15.6 min on average as this frequency is sufficiently low to eliminate any dynamic effects. The time

over which the cyclic loads were applied varied between 9.1 min and 24.0 min. The value of Q_{cyc} may be evaluated by Equation 4-2a:

$$Q_{cyc} = m \cdot a_{eq.pk} = (m \cdot g) \cdot \frac{a_{eq.pk}}{g} = Q_{ini} \cdot \frac{a_{eq.pk}}{g} \tag{4-2a}$$

where m is the mass of the superstructure, $a_{eq.pk}$ is defined as the equivalent peak vertical acceleration and g is the Earth's gravitational acceleration (= 9.81 m/s^2). Hence, $a_{eq.pk}$ can be calculated using Equation 4-2b:

$$a_{eq.pk} = \frac{Q_{cyc}}{Q_{ini}} \cdot g \tag{4-2b}$$

Currently, there is a lack of guidance on sel ecting peak vertical acceleration for applications in which this pile type would be potentially used. For ordinary highway bridges, as an example, the Seismic Design Criteria of California recommends an equivalent vertical load at a magnitude of 25% of the dead load in the upward and downward directions if a horizontal peak rock acceleration of 0.6 g or more is expected at a site (Kunnath et al. 2008, Caltrans 2019). This is approximately equivalent to an $a_{eq.pk}$ of 0.25 g. In the present study, an $\alpha_{eq.pk}$ of 0.5 g was selected, representing a very high equivalent peak vertical acceleration. Nonetheless, the actual $a_{eq.pk}$ varied coincidently from 0.4 to 0.6 g because it was difficult to apply the exact Q_{cyc} manually. Upon completing the cyclic load, the load was decreased in four equal increments. Table 4.1 summarizes the Q_{ini} with the corresponding FS and Q_{cyc} with the corresponding $a_{eq.pk}$.

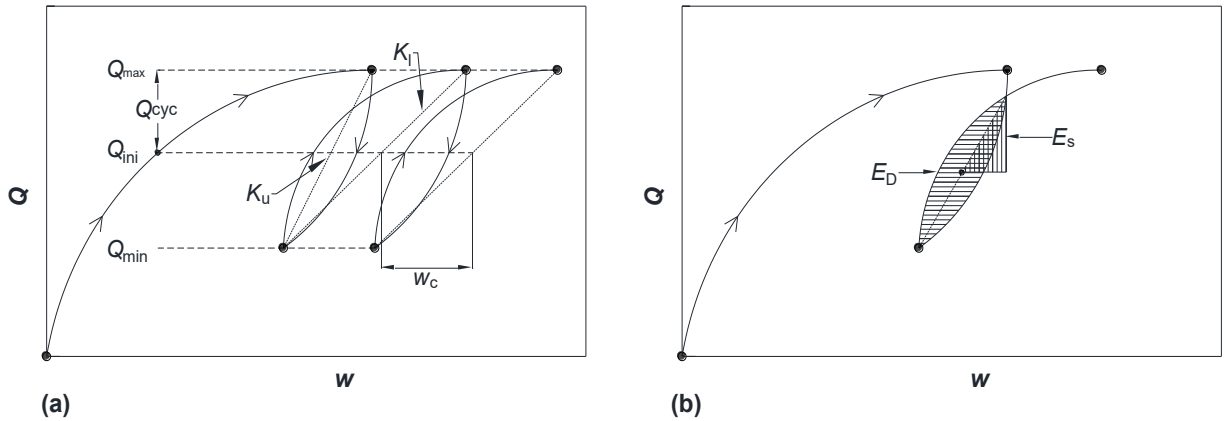

Figure 4.4. A schematic of the (a) axial cyclic load test procedure and (b) dissipated energy and maximum strain energy.

Table 4.1. Cyclic test matrix.

Test pile	Q_u (kN) [2]	Q_{ini} (kN)	FS	Q_{cyc} (kN)	$a_{eq.pk}$ (g)	Cycles (#)	Test duration (min)
P1[1]	92.3	55.5	1.7	34.0	0.61	15	14.2
P2	36.9	39.5	0.9	14.1	0.36	15	9.1
P3[1]	57.2	34.4	1.7	21.8	0.63	15	19.5
P4	37.7	31.9	1.2	17.1	0.54	15	24.0
P5[1]	37.4	28.1	1.3	16.5	0.59	15	16.3
P6	18.8	29.3	0.6	12.3	0.42	15	10.4

Note: 1. These piles are instrumented with axial SGs; 2. Arithmetic mean of Q_u of 3 to 4 axial compressive tests.

4.3. Field Test Results

The first objective of the research is to understand the cyclic response of the micro screw piles at a particular cyclic loading magnitude and soil condition. The axial load vs. displacement curves of the tests is presented. The curve of cumulative displacement vs. the number of cycles was obtained. The equivalent linear method, which is based on a secant stiffness and a damping ratio, is often a

design method for piles when earthquake loads are concerned. Hence, the pile-head stiffness and damping ratio was obtained with the number of cycles.

4.3.1. Axial Load vs. Displacement Curves

The axial load vs. displacement curves of the test piles is shown in Figure 4.5. Generally, the loading curves are nonlinear. During the cyclic loading stage, piles P2, P4, P5 and P6 exhibit two distinctive nonlinear loading curves (elastic and plastic deformation) because they were loaded to a lower initial FS. Piles P1 and P3 exhibit only one distinctive nonlinear hysteresis curve because they are loaded to a greater initial FS. These features are shown using dashed boxes in Figures 4.5a and 4.5e. The piles do not exhibit a plunging failure or a significant reduction in pile capacity during the cyclic test. However, the piles reach the serviceability limit state, which can be defined as a pile-head displacement of 10% shaft diameter because a large amount of displacement is accumulated.

Cumulative displacement (w_c, Fig. 4.4) is defined as the increment in the average displacement with respect to the first cycle. The value of w_c was calculated starting from the first Q_{min} and the second Q_{max}, as shown in Figure 4.4. The curves of w_c vs. the number of cycles of the six test piles are shown in Figure 4.6, which is grouped into long (P1, P3, P5) and short piles (P2, P4, P6). The value of w_c increases, but at a decreasing rate, with an increased number of cycles in a nearly linear pattern because the sand might have densified and flown around the tapered segment. The patterns of curves in Figure 4.6 suggest the key effect of the initial FS on the pile settlement. Based on the limited number of tests, it appears that a lower initial FS leads to a greater w_c.

Several studies adopted the concept of the stability interaction diagram in classifying piles subjected to axial cyclic wind load (e.g., Rimoy et al. 2013, Jardine and Standing 2012). Rimoy et al. (2013) presented a stability interaction diagram for assessing the cyclic response of driven piles

in sand. The diagram indicates the stable, metastable and unstable regions based on the results of several pile tests. As per Rimoy et al. (2013), piles that accumulate 1 mm of axial displacement in 1,000 and greater cycles are classified as stable, those accumulating 1 mm between 100 and 1,000 cycles as metastable and those accumulating 1 mm in less than 100 cycles as unstable. The cyclic response of the micro screw pile in terms of the number of cycles required to accumulate 1 mm of displacement is shown in the stability interaction diagram (Fig. 4.7) and compared with the classification of Rimoy et al. (2013). It can be seen that all the piles may be classified as "unstable" as these points are located within or beyond the unstable zone. The reasons may be twofold: 1) the initial values of FS are low, and 2) the selected values of $a_{eq.pk}$ are high due to the high demand of the earthquake load. Although comparing the cyclic response of different piles may not be ideal, the stability interaction diagram offers a mean of examining the axial cyclic stability of piles; the diagram for the present piles would be more valuable if more test results at various FS or $a_{eq.pk}$ were available.

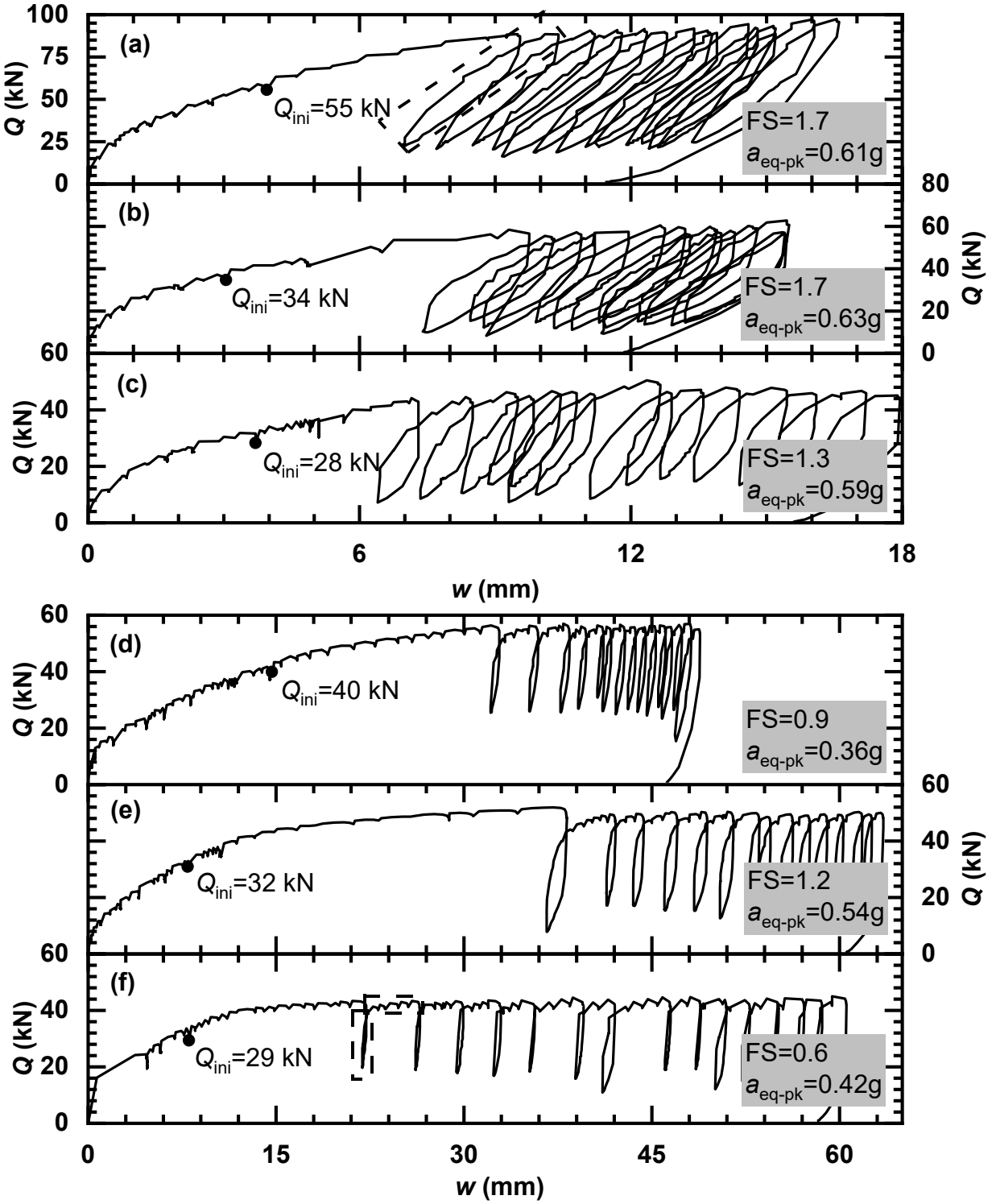

Figure 4.5. The axial load vs. displacement curves of the test piles: (a) P1, (b) P3, (c) P5, (d) P2, (e) P4 and (f) P6. Note: The dashed box in (a) shows one nonlinear stiffness, and the dashed box in (f) shows two distinct loading stiffnesses.

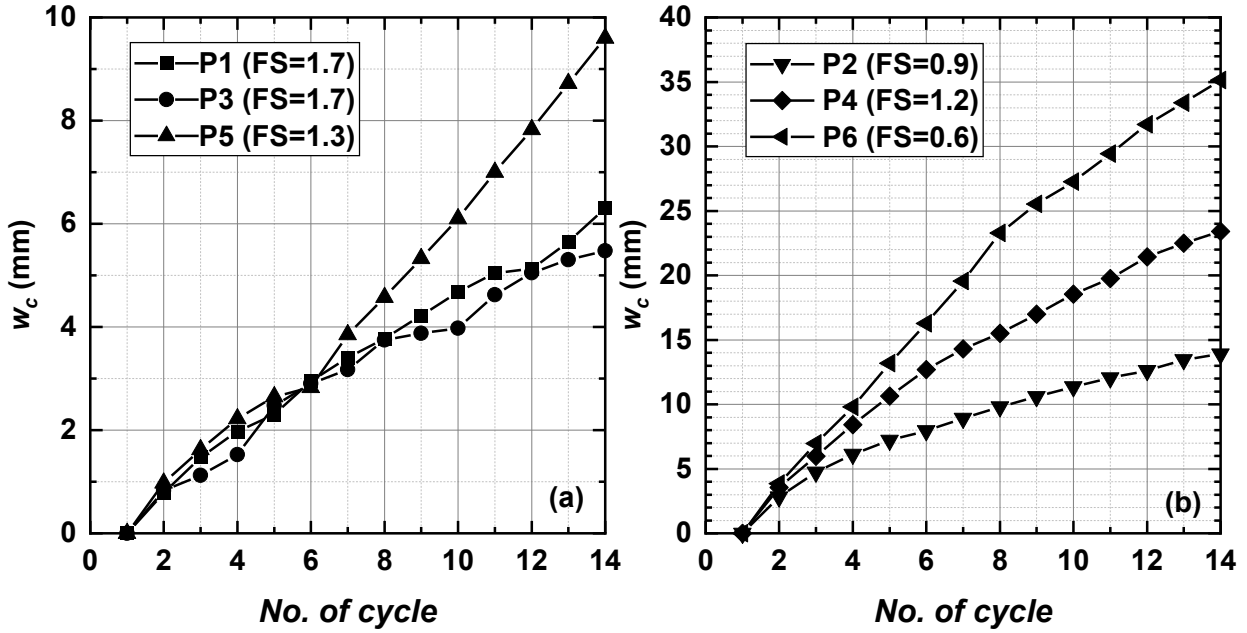

Figure 4.6. Cumulative displacement vs. the number of cycles of the test piles: (a) P1, P3 and P5 and (b) P2, P4 and P6.

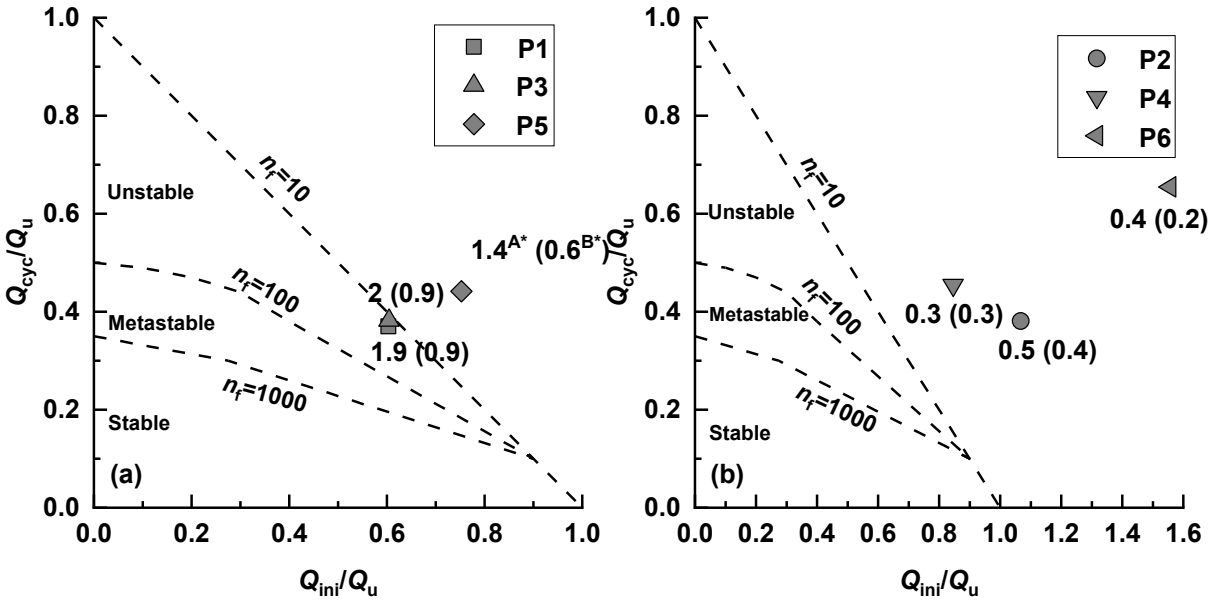

Figure 4.7. Normalized cyclic stability diagram of the test piles: (a) P1, P3 and P5 and (b) P2, P4 and P6. The dashed curves were adapted from Rimoy et al. (2013) for driven piles in sand. Note: A* denotes the number of cycles per 1 mm of w_c, and B* denotes the average ratio of K_l/K_u over 14 cycles.

4.3.2. Pile-head Stiffness

As shown in Figure 4.4, the pile-head loading stiffness (K_l) and unloading stiffness (K_u) were calculated using Equations 4-3 and 4-4:

$$K_{l_i} = \frac{Q_{\max_{i+1}} - Q_{\min_i}}{w_{\max_{i+1}} - w_{\min_i}} \tag{4-3}$$

$$K_{u_i} = \frac{Q_{\max_i} - Q_{\min_i}}{w_{\max_i} - w_{\min_i}} \tag{4-4}$$

where Q_{max} and Q_{min} are the maximum and minimum loads, respectively, w_{max} and w_{min} are the displacements corresponding to Q_{max} and Q_{min} and i is the index of the cycle. The values of K_l and K_u vs. the number of cycles are shown in Figures 4.8a and 4.8b, respectively. The initial values of the K_l of the short piles are smaller than the long piles. Although the K_l of all the piles increases with increasing cycles, the K_l of the short piles increases much more than the long piles. Note that these piles have a relatively greater taper length to total length proportion. The increase in K_l is caused by densified sand around the tapered segment. This observation and interpretation were also made by Abd Elaziz and El Naggar (2011), El Sharnouby and El Naggar (2012) and El Naggar and Abdelghany (2012), where tapered piles were cyclically loaded in sand.

The value of K_u is steady with an increasing number of cycles; this response may be due to the elasticity of the soil. Given that the short piles were entirely situated in compact sand and that the long piles were situated in both compact and loose sand, it is reasonable to observe that the K_u of the short piles (P2, P4, P6) is greater than the long piles (P1, P3, P5). Hence, the unloading response of the pile in denser sand is stiffer. Furthermore, K_l is smaller than K_u due to nonlinear soil deformation response in the calculation of the loading stiffness.

The ratio of average K_l over average K_u (termed the K_l/K_u ratio for convenience) over all cycles was obtained and labelled beside the data points in the stability interaction diagram (Fig.

4.7). As K_u is relatively steady, the K_l/K_u ratio may be considered another indicator of pile stability. As observed in Figure 4.7, a more stable pile, which had been loaded to a greater FS, has a greater K_l/K_u ratio where the cyclic response is predominantly elastic. On the contrary, a more unstable pile, loaded to a lower FS, has a lower K_l/K_u ratio, where the cyclic response includes more plastic deformation.

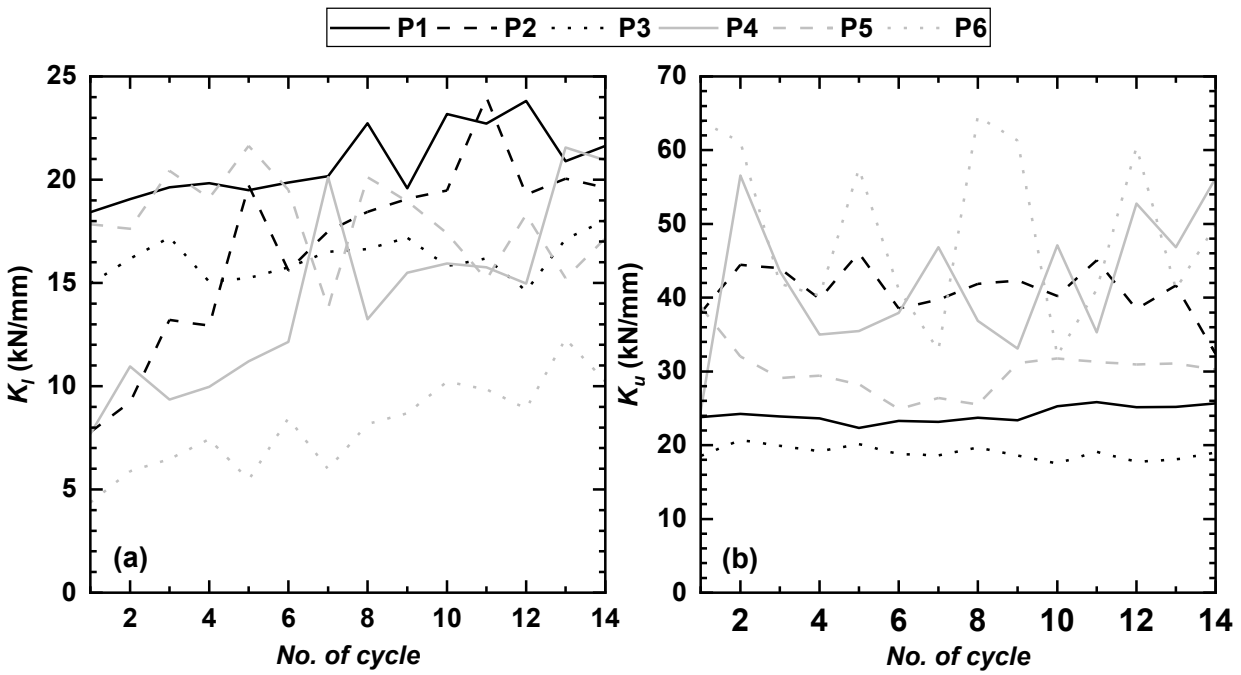

Figure 4.8. (a) Pile-head loading stiffness and (b) unloading stiffness vs. the number of cycles.

4.3.3. Pile-head Equivalent Damping Ratio

Energy can be dissipated in soils, foundations and structures by many mechanisms, including the friction, grain slippage, heat generation and plastic yielding. These mechanisms are not adequately understood for them to be modelled separately. Therefore, the contribution of each energy dissipation mechanism is typically lumped as a damping coefficient. Kelvin-Voigt solid is a common model for representing the stress-strain relationship of a soil element subjected to shearing where the shear stress is represented as the sum of the elastic spring component and a viscous dashpot component, as shown in Figure 4.9a.

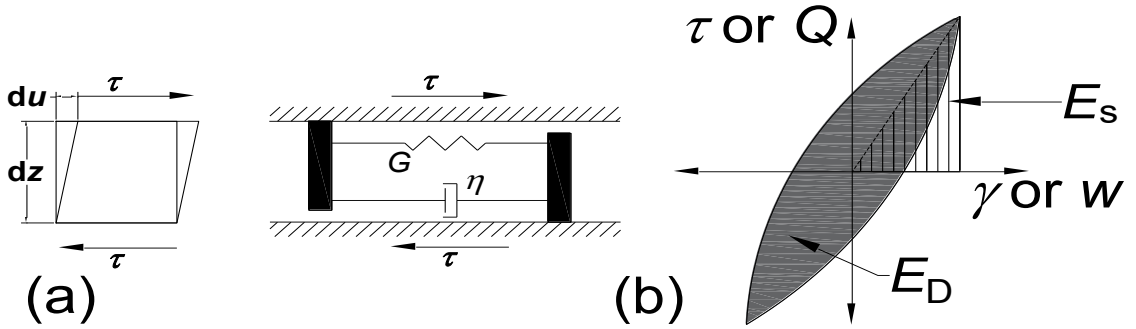

Figure 4.9. (a) A schematic of Kelvin-Voigt solid and (b) stress-strain (or load vs. displacement) relationship during one cycle (after Kramer 1996).

As shown in Figure 4.9b, the stress-strain relationship of a Kelvin-Voigt solid in shear is defined as in Equation 4-5 (Kramer 1996):

$$\tau = G\gamma + \eta \frac{\partial \gamma}{\partial t} \tag{4-5}$$

where G is the shear modulus of the soil, η is the viscosity of the soil, γ (=du/dz) is the shear strain and t is the time. By considering a harmonic shear strain response, as in Equation 4-6:

$$\gamma = \gamma_0 \sin(\omega t) \tag{4-6}$$

where ω is the angular frequency of the harmonic shearing and γ_0 is the amplitude of the shear strain; the shear stress can be expressed as in Equation 4-7:

$$\tau = G\gamma_0 \sin(\omega t) + \omega\eta\gamma_0 \cos(\omega t) \tag{4-7}$$

The dissipated energy (E_D) is equal to the enclosed area of the ellipse and maximum strain energy (E_s) is the maximum energy stored in one cycle, as expressed in Equation 4-8a and 4-8b, respectively (Kramer 1996):

$$E_D = \int_0^{T=2\pi/\omega} \tau \frac{\partial \gamma}{\partial t} dt = \pi\eta\omega\gamma_0^2 \tag{4-8a}$$

$$E_s = \frac{1}{2} G \gamma_0^2 \quad \text{(4-8b)}$$

Then, the equivalent damping ratio (ξ) during one cycle is defined as the ratio of the viscosity η to the critical viscosity of soil η_c:

$$\xi = \frac{\eta}{\eta_c} = \frac{\eta \omega_n}{2G} \quad \text{(4-9)}$$

where η_c is equal to $2G/\omega_n$ and ω_n is the natural angular frequeny of the system (herein the Kelvin-Voigt solid). The critical viscosity η_c is similar to the critical damping coefficient (=$2k/\omega_n$, where k is the lateral stiffness, refer to Chopra 2007) of a single-degree-of-freedom "lollipop" structure. The critical viscosity of soil is the magnitude of viscosity that brings a freely excited system to an equilibrium in the shortest duration. By combining Equations 4-8 and 4-9, ξ can be expressed in terms of E_D and E_s (Chopra 2007):

$$\xi = \frac{1}{4\pi} \frac{1}{\omega / \omega_n} \frac{E_D}{E_s} \quad \text{(4-10)}$$

When ω is equal to ω_n, where the system is most responsive to damping, ξ is expressed as (Kramer 1996, Chopra 2007):

$$\xi = \frac{1}{4\pi} \frac{E_D}{E_s} \quad \text{(4-11)}$$

Equation 4-11 would be a satisfactory approximation to ξ at the harmonic excitation frequency ω other than the natural frequency ω_n. The concept of the equivalent damping coefficient is a convenient method for accounting for seismic energy dissipation and is applicable to soil elements and soil-pile interaction subjected to dynamic loading. Moreover, the concept is adopted to approximate the energy dissipation capability of elements even subjected to slow cyclic loading.

Following the method of calculating ξ, the energy dissipation characteristics of piles can then be quantified. The value of E_D of the entire pile is equal to the enclosed area within a Q vs. w curve for one cycle, and the E_s of the entire pile is equal to the elastic energy stored within a Q vs. w curve over one cycle, as shown in Figure 4.4b. The values of the ξ of the long and short piles are shown in Figure 4.10a and Figure 4.10b. It seems that ξ remains more or less unchanged with the increasing number of cycles. The values of the ξ of piles P4 and P3 fluctuate to a certain level caused by the uneven plastic displacement of piles. The values of the ξ of piles P1, P3 are lower than the other piles. These piles are loaded to a greater corresponding FS. A cyclic load that is closer to the elastic region has a smaller ξ. However, it dissipates less energy in the soil, which can potentially cause damage to the superstructure.

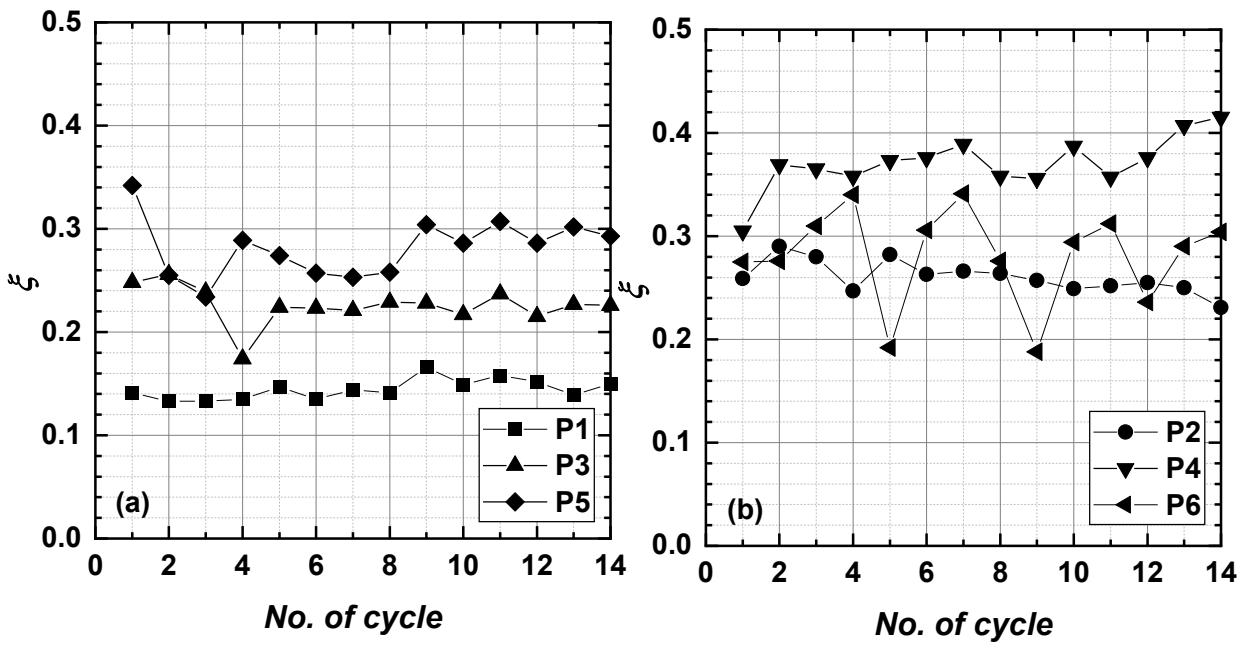

Figure 4.10. Pile-head equivalent damping ratio vs. the number of cycles of the test piles: (a) P1, P3, P5 and (b) P2, P4, P6.

4.3.4. Performance of Individual Segments: Shaft Resistance

The second objective of the research is to understand the cyclic response of the individual pile segments. The re-distribution of unit shaft resistance with the increasing number of cycles was then assessed from the time histories. The axial load (Q) at each SG station was calculated using Equation 4-12:

$$Q = \varepsilon EA \tag{4-12}$$

where ε is the measured strain, E is the elasticity modulus of the pile shaft and A is the cross-sectional area of the pile at each SG location. One SG was installed above the ground surface to calibrate the SG data against the load cell reading. The tapered segment was considered as one segment with no base. The unit shaft resistance (q_s) of the individual segment was calculated using Equation 4-13:

$$q_s = \frac{Q_{top} - Q_{bot.}}{A_s} \tag{4-13}$$

where Q_{top} and $Q_{bot.}$ are the axial load at the top SG station and the bottom SG station, and A_s is the outer surface shaft area of the individual segment. Khidri and Deng (2022) suggested that the failure of the threaded segment in cohesionless soil was best represented by the cylindrical shearing mode, which means the failure surface likely occurs along the outer shaft surface (i.e., edges of threads). As such, the outer shaft area of the threaded segment was taken as the shear surfaces. As shown in Figure 4.11, the shaft area of the tapered segment was calculated based on the principle of the equivalent cylindrical method (refer to El Naggar and Sakr 2000, Guo and Deng 2018, Khidri and Deng 2022). The SG3 of pile P3 was damaged. A combined q_s over segment 2 and segment 3 was obtained using SG2 and SG4.

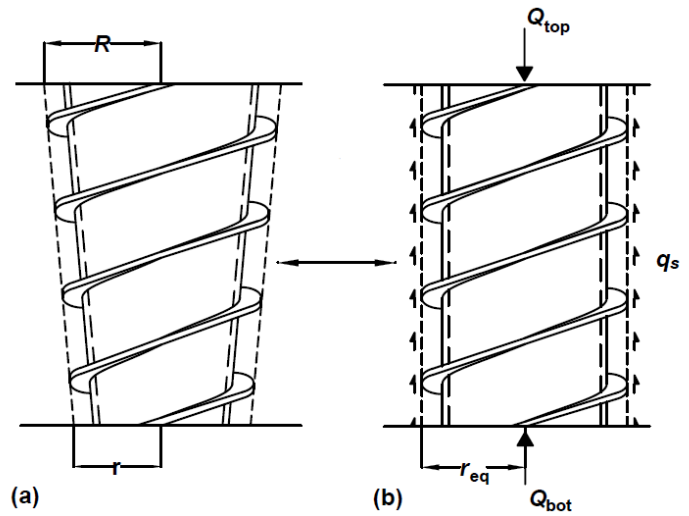

Figure 4.11. Schematics of equivalency: (a) tapered segment and (b) equivalent cylindrical segment.

The initial q_s distribution of test pile P3 during the initial loading stage is shown in Figure 4.12. The value of the q_s of the smooth and the threaded segments is great in compact sand and small in loose sand, and the q_s of the tapered segment is the greatest even though the segment was located in a zone with loose sand. The initial distribution of q_s reflects the effect of soil layering and the tapered shape. The initial distribution of q_s is consistent with the pattern of measured q_s during the monotonic test (Khidri and Deng 2022).

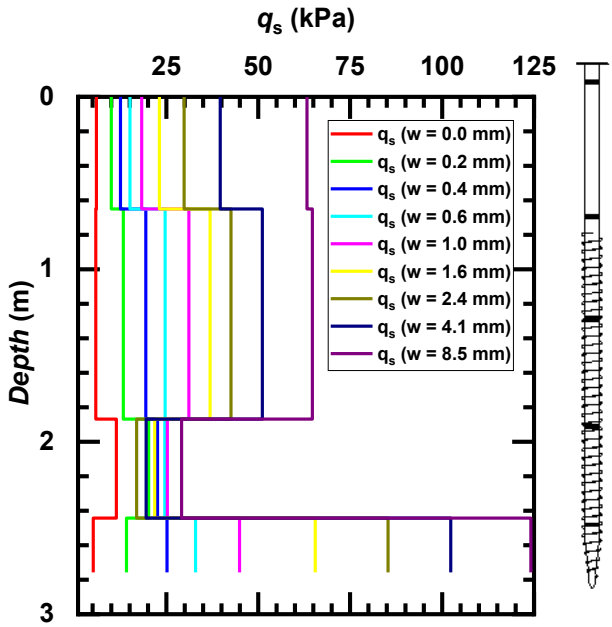

Figure 4.12. Initial distribution of unit shaft resistance along test pile P3 at selected deformation. Note: SG3 was not functional. Therefore, the combined q_s of segment 2 and segment 3 was taken based on SG2 and SG4.

Time histories of q_s of the individual segments of piles P1 and P3 are shown in Figures 4.11 and 4.12. Refer to Figure 3.1 for the positions of the piles' segments. The values of the q_s of the smooth and threaded segments of all piles in compact sand remain steady with an increasing number of cycles as the compact sand tends to dilate during shearing at the interface. However, the q_s of the threaded segment (segment 4 in Fig. 4.14c) of test pile P3 in loose sand degrades with the increasing number of cycles. This may be due to the contractive behavior of loose sand, which causes sand volume to shrink. The value of the q_s of the lower threaded segment (segment 3 in Fig. 4.13c) of pile P1 even in the compact sand degrades with the increasing number of cycles; the degradation can be due to the re-distribution of the total pile load. As for the tapered segments (segment 4 in Fig. 4.13d, segment 5 in 4.14d), q_s increases significantly with the increasing number of cycles although these segments were placed in loose sand; the loose sand might have been

significantly densified from shearing and sloughing, thereby significantly increasing shaft resistance.

The lower taper (segment 5 in Fig. 4.13e) of test pile P1 does not increase with the increasing number of cycles. The values of the q_s of the lower taper is smaller than the q_s of the upper taper. It is suspected that a cavity in the soil could have developed beneath the lower tapered segment; the presence of an unexpected cavity may be supported by the development of negative q_s at the smooth segment (segment 1 in Fig. 4.13a) of test pile P1 before the cyclic load. However, the negative q_s is eliminated during the cyclic loading stage (Fig. 4.13a).

A similar program of axial cyclic testing of micro screw piles was conducted at a cohesive soil site by Guo et al. (2019). Their results show that piles with greater length and diameter experienced less w_c. In addition, the piles loaded to Q_{ini}, corresponding to a greater FS, exhibited less w_c. Generally, the piles were considered stable as they experienced a small amount w_c in Guo et al. (2019). The piles at the cohesive soil site exhibited less w_c than the piles in current research because the piles were loaded to Q_{ini}, corresponding to a greater FS. The amplitude of q_s reduced with an increasing number of cycles in Guo et al. (2019), which actually indicated that the soil was remoulded by cyclic shearing and approached the residual state.

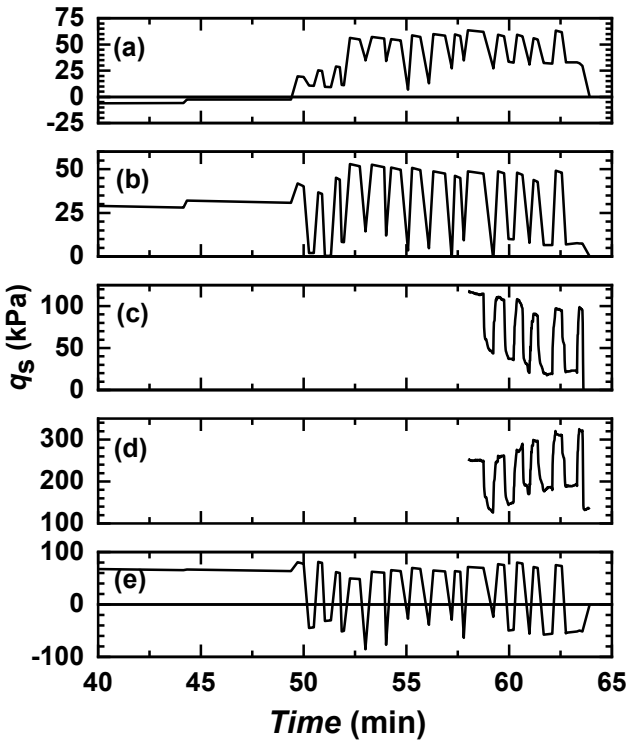

Figure 4.13. Time history of the unit shaft resistance of test pile P1: (a) segment 1, (b) segment 2, (c) segment 3, (d) segment 4 and (e) segment 5.

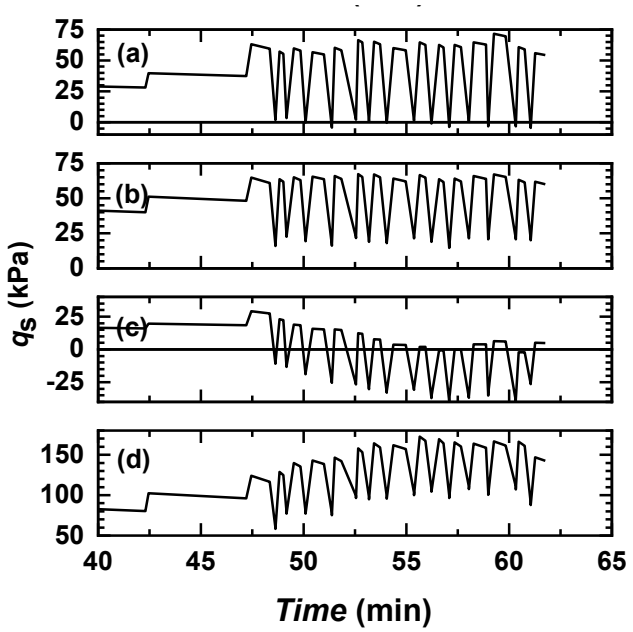

Figure 4.14. Time history of the unit shaft resistance of test pile P3: (a) segment 1, (b) combined segment 2 and segment 3, (c) segment 4 and (d) segment 5. Note: The SG3 was not functional. Therefore, the combined q_s of segment 2 and segment 3 was taken based on SG2 and SG4.

4.3.5. Performance of Individual Segments: Stiffness and Damping

The hysteresis curves of q_s vs. the normalized displacement (w/D) of the individual segment of test pile P1 are shown in Figure 4.15, where D is the diameter of the shaft. Note that only the last five hysteresis loops are shown in Figure 4.15c and 4.15d because the SG readings are not reasonable for the first nine cycles. The loading stiffness k_l (unit: kPa /mm) of the individual pile segment was determined in a similar way as in Equation 4-3 but based on the q_s vs. w hysteresis. The curves of k_l vs. the number of cycles of the individual segments are shown in Figure 4.16a. The values of k_l of the tapered segments (segments 4 and 5 in Fig. 4.16a) are the greatest, while the k_l of the smooth segment (segment 1 in Fig. 4.16a) is the least. The values of the k_l of the lower threaded segment (segment 3) are generally greater than the upper threaded segment (segment 2), possibly because of the greater confining stress. The values of the k_l of the lower tapered segment (segment 5) are smaller than the upper tapered segment (segment 4), perhaps because of the

presence of a cavity near the lower taper. Notably, the magnitude of k_1 presumably depends on shaft shape, soil characteristics, vertical confining stress and so on. Hence, it may not be a good practice to compare the magnitude of k_1 of all segments explicitly.

The value of k_1 increases significantly in the tapered segment, as shown in Figure 4.16a, and this explains the increase in the K_1 of test pile P1 with the increasing number of cycles (Fig. 4.8). The tapered segment has the greatest increase in k_1, whereas the smooth and threaded segments exhibit a small increase in k_1. The increase in k_1 at the smooth segment is likely attributed to the dilative behavior of compact sand during cyclic loading.

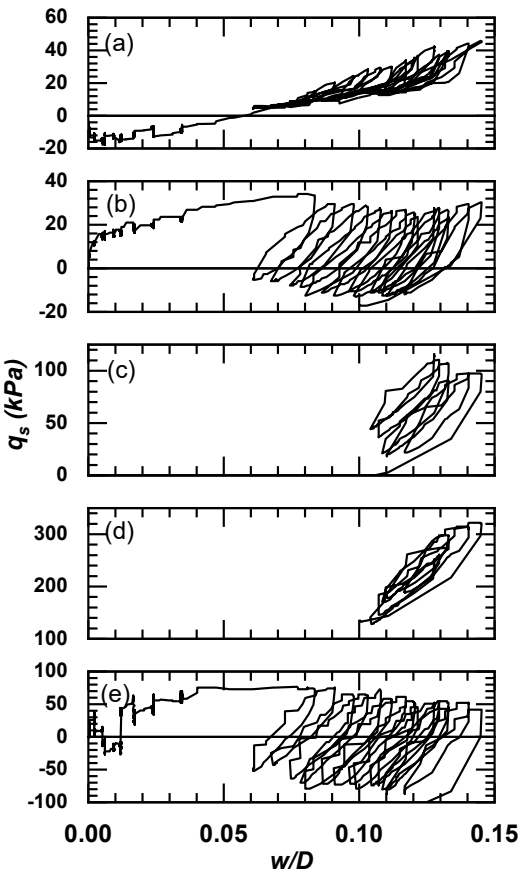

Figure 4.15. The unit shaft resistance vs. the normalized pile displacement of the individual segments in test pile P1: (a) segment 1, (b) segment 2, (c) segment 3, (d) segment 4 and (e) segment 5. Note: Only a portion of the hysteresis response is shown in (c) and (d).

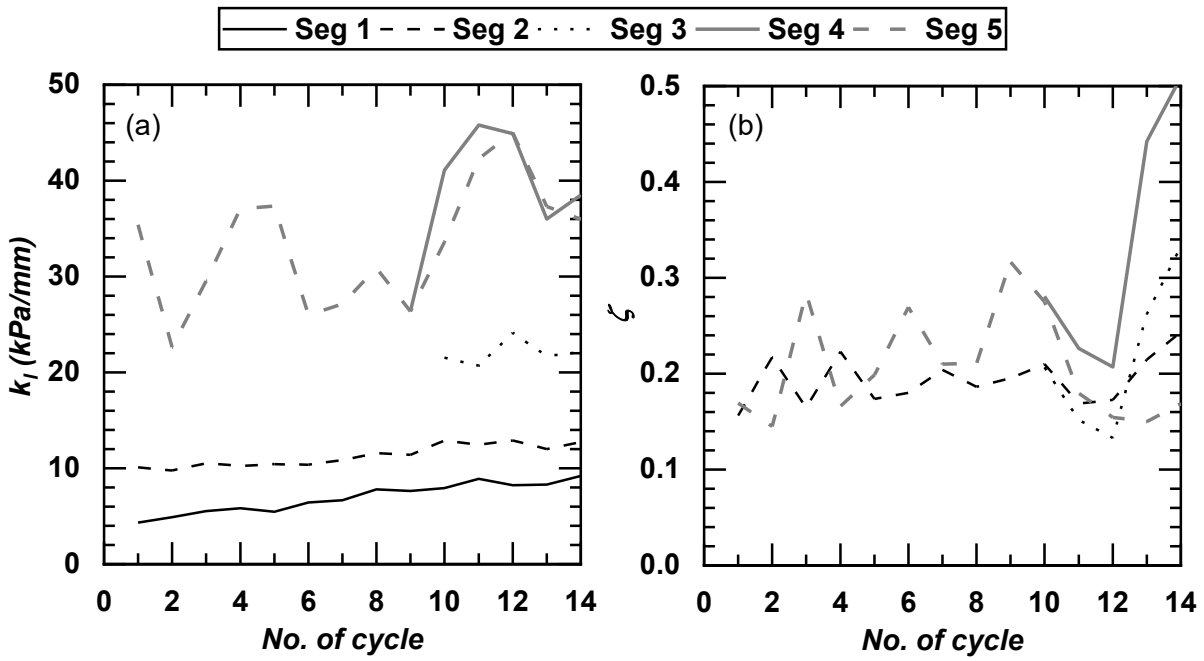

Figure 4.16. (a) Segment loading stiffness and (b) segment equivalent damping ratios of test pile P1.

The curves of equivalent damping ratio (ζ) for the individual segments were obtained in a similar way as in Equation 4-11 but based on the q_s vs. w/D hysteresis of test pile P1. Figure 4.16b shows the progress of ζ vs. the number of cycles. The values of the ζ of the tapered segments are the greatest, whereas the ζ of the smooth segment are the least. The values indicate that more energy is dissipated through the soil-pile interaction around the tapered and threaded segments. The amount of dissipated energy may be due to the densification of sand around the tapered segment, as mentioned previously. The value of the ζ of the lower tapered segment is smaller than the upper tapered segment. Overall, the ζ of the individual segments remains unchanged with the increasing number of cycles, which is also shown in the pile-head ξ history. This fact suggests that the piles provide a great energy dissipation capability but that the piles undergo a large w_c.

4.4. Conclusions

Six axial cyclic load field tests on micro screw piles were conducted at Sandpit. The following conclusions may be drawn.

1. The piles do not develop plunging failure or exhibit a reduction in axial capacity. The piles reach the serviceability limit state by accumulating a displacement during the cyclic load. The value of w_c increases with an increasing number of cycles in a nearly linear pattern. The final w_c ranges from 5 mm to 35 mm. All piles may be considered unstable based on the normalized cyclic stability interaction diagram.
2. The initial FS has a significant effect on cyclic behavior. A pile loaded to lower FS exhibits a greater w_c and a lower K_l/K_u ratio, where the cyclic response included more plastic deformation and is more unstable.
3. The loading stiffness K_l of all piles increases with an increasing number of cycles, and the K_l of the short piles increases much more than the long piles because of the effects of a greater taper length to total length proportion. The unloading stiffness K_u remains steady with an increasing number of cycles. The damping ratio ξ remains more or less unchanged with an increasing number of cycles. The values of the ξ of test piles P1 and P3 are smaller than other piles because these piles are loaded to a greater FS.
4. The value of the q_s of the individual segment re-distributes during the cyclic loading: the q_s of the smooth and threaded segments in compact sand remains unchanged with an increasing number of cycles, the q_s of the threaded segment in loose sand degrades because of the contractive behavior of loose sand and the q_s of the tapered segment in loose sand increases significantly.
5. The values of the k_l of the tapered segment are the greatest, while the k_l of the smooth segment are the least. The tapered segment k_l exhibits the greatest increase, which means the taper

contributes the most to the overall increase in the stiffness of the entire pile. The values of the ζ of the individual segments remain unchanged with an increasing number of cycles. The values of the ζ of the tapered segments are the greatest, while the ζ of the smooth and threaded segments are the least.

The following limitations should be noted if the results are to be used in practice. First, more tests at a variety of $a_{eq.pk}$ and FS are needed to establish the comprehensive cyclic behavior of piles subjected to a large spectrum of cyclic loads (e.g., earthquakes, wind and waves). Secondly, the loading scheme is pseudo-static instead of dynamic, and hence the effects of the loading rates were neglected.

5. Lateral Load Field Tests of Micro Screw Piles

5.1. Introduction

Piles are often subjected to lateral load from the superstructure due to earthquakes, wind, lateral soil spreading and so on. The design of piles subjected to lateral load considers the requirements for both the ultimate limit state and the serviceability limit state. The ultimate limit state corresponds to the situation where the applied lateral load exceeds either the pile's structural capacity or the adjacent soil's capacity. The structural capacity of the pile can be exceeded either in bending or shear. The serviceability limit state corresponds to exceeding an allowable lateral displacement that causes non-structural damage to the superstructure. Therefore, it is necessary to obtain both the lateral load versus displacement response of the pile and the capacity of the pile. The lateral capacity of the pile is governed by either the short pile failure or long pile failure modes. Meyerhof and Yalcin (1984) suggested that the lateral capacity of a long pile could be estimated by treating the effective length of the pile as a short pile. Several studies have provided methods to estimate the lateral capacity of conventional piles based on full-scale, model-scale and theoretical studies (Broms 1964a, b, Meyerhof and Ranjan 1972, Poulos 1980, Meyerhof et al. 1981, Meyerhof et al. 1983, Meyerhof and Yalcin 1984, Meyerhof and Sastry 1985, Sastry et al. 1986). A more comprehensive solution to the lateral soil-pile interaction can be obtained by utilizing numerical simulations based on the Beam-on-Nonlinear-Winkler-Foundation (BNWF) method.

Although adequate research has been performed on the lateral response of conventional piles, such as cast-in-place and driven steel piles, research on the lateral performance of micro screw piles has been absent. In the present study, a lateral test program of micro screw piles was carried out in the field at three test sites. The objectives of the lateral load field test program were to 1) investigate the lateral capacity, pile shaft response and failure mode; 2) assess the

effectiveness of Broms's method in predicting the lateral capacities of piles; 3) evaluate the effect of thread and taper on the lateral response of micro screw piles; and 4) gather field test data that could be used for the further numerical modelling of lateral soil-micro screw pile interaction.

For this research, six piles at Sherwood Park, 22 piles at South Campus and 18 piles at Sandpit were tested. These piles, with two shaft lengths and three shaft diameters, were selected to examine the effects of the pile geometry on the lateral behaviour of piles. Selected piles were instrumented with full-bridge SGs for measuring bending moments. Site characterization, including cone penetration tests, SPTs and laboratory tests, was carried out at each site to obtain the soil profile and properties. The lateral load vs. displacement curves at the three sites was obtained. The distributions of the bending moment along the instrumented piles at Sherwood Park and South Campus were obtained and compared with the bending moment capacities of the pile shaft in order to derive the failure mode of the test piles. The effectiveness of the Broms method was examined by compiling the measured and estimated capacities of all piles.

5.2. Literature Review and Background

This section reviews two criteria for lateral pile failure, including the Broms criterion to define short pile failure and Meyerhof and Yilcin's (1984) criterion for flexible piles based on pile relative stiffness (Poulos and Davis 1980). A summary of the typical values of allowable lateral displacement is reported. Thereafter, the method provided by Broms (1964a, b) to estimate the ultimate capacity of a long pile installed in cohesionless and cohesive soils loaded under free-head conditions is reviewed. Finally, the effects of helical plates and tapering on the lateral capacity of the piles are reviewed.

5.2.1. Relative Stiffness of Piles

The response of a laterally loaded pile depends on the relative stiffness (k_r) of the pile, which is a function of the bending stiffness of the pile, soil stiffness, pile length, pile fixity and base fixity (Banerjee and Davis 1978, Poulos and Davis 1980). Pile response can exhibit either a rigid response, as in a short pile failure mode, or a flexible response, as in a long pile failure mode. A long pile has sufficient length embedded in the ground, where deformation and movement are minimal ear the pile base. On the contrary, a short pile with insufficient embedment length moves as a rigid body and experiences a small deformation. Therefore, the soil adjacent to the short pile fails. Broms (1964a, b) defined short piles that met the following criterion, shown here in Equations 5-1 and 5-2:

$$\frac{L}{T} \leq 2 \text{ for sandy soils} \tag{5-1}$$

$$\frac{L}{R} \leq 2 \text{ for clayey soils} \tag{5-2}$$

where L is the length of the pile, and the values of T and R are as defined in Equations 5-3 and 5-4:

$$T = \left[\frac{EI}{k}\right]^{1/5} \quad \text{for sandy soils} \tag{5-3}$$

$$R = \left[\frac{EI}{k_0}\right]^{1/4} \quad \text{for clayey soils} \tag{5-4}$$

where E is the pile Young's modulus, I is the pile cross-sectional moment of inertia, k is the initial modulus of the subgrade reaction of sand and k_0 is the modulus of the subgrade reaction of clay. The value of k_g as a function of relative density (D_r) was adapted from API (1993), as shown in Figure 5.1. The value k_0 was defined as in Equation 5-5:

$$k_0 = \frac{p_{ult}}{5\varepsilon_{50}D} \tag{5-5}$$

where D is the pile diameter, p_{ult} is the ultimate soil lateral stress and ε_{50} is the strain corresponding to half of the undrained shear strength. The value of p_{ult} is equal to $3Ds_u$. The value of ε_{50} was provided by Matlock (1970).

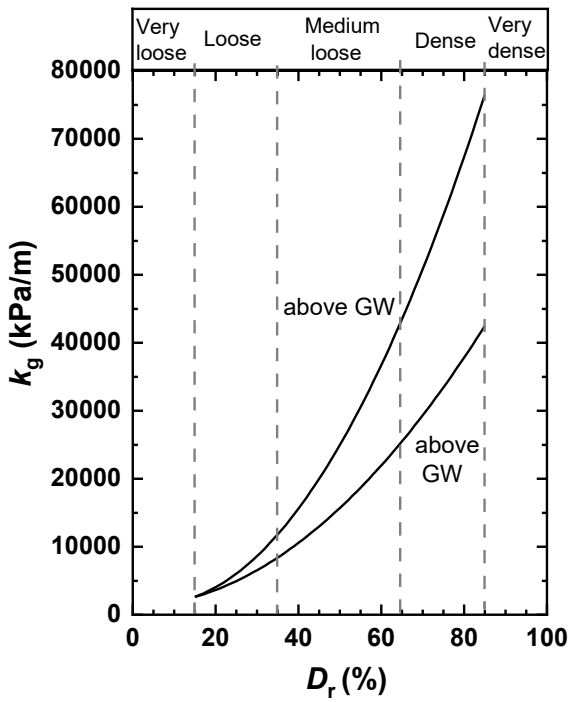

Figure 5.1. Initial modulus of subgrade reaction versus relative density (adapted from API 1993).

The relative stiffness (K_{rs}) of the pile in sandy soil is defined as in Equation 5-6 (Banerjee and Davis 1978; Poulos and Davis 1980):

$$K_{rs} = \frac{EI}{E_h D^4} \tag{5-6}$$

where E_h is the horizontal soil modulus of sand. The relative stiffness (K_{rc}) of the pile in clayey soils is defined as in Equation 5-7 (Poulos and Davis 1980):

$$K_{rc} = \frac{EI}{E_s D^4} \tag{5-7}$$

where E_s is the average horizontal soil modulus of clay.

5.2.2. Criteria for the Lateral Capacities of Piles

The lateral capacity of the pile is based on either the ultimate or serviceability limit state. The ultimate limit state corresponds to the structural failure of the pile or the failure of the soil. The serviceability limit state corresponds to a lateral displacement that causes nonstructural damage to the superstructure. However, there is no widely accepted allowable lateral displacement. The allowable lateral displacement for buildings and other structures is often defined by a structural engineer or the owner for each project. Bozozok (1978) provided a graph of the horizontal and vertical movement of bridge foundations that could cause visible structural damage. A summary of the ultimate lateral capacity criteria based on allowable lateral displacement is shown in Table 5.1. Typical allowable lateral displacement varies from 5 to 50 mm. In the research, the ultimate lateral capacity corresponding to a lateral displacement of 12.5 mm ($Y_{u\text{-}Y}$), which is also adopted by USACE (1991), Elkasaby and El Naggar (2015) and ICC (2013).

Table 5.1. Summary of ultimate lateral capacity criteria based on the lateral displacement or tilting of piles.

Reference	**Criteria**
O'Neill and Reese (1999)	5% of the shaft diameter
Li (2016)	10% of the pile diameter
Prakash and Sharma (1999) and Sakr (2009)	6.25 mm
US-ACE (1991) and Elkasaby and El Naggar (2015)	6.25 to 12.5 mm
Al-Baghdadi (2018)	0.25° tilt of the pile at the ground
ICC (2013) for helical piles	Half of the load required to mobilize 25.4 mm (1 inch)
ICC (2012) for micro screw piles	Half of the load required to mobilize 19.1 mm (3/4 inch)

When it is difficult to find a trend in the lateral load-displacement curve, the DeBeer (1968) method of logarithmic linearity can be used by plotting the load and displacement in a logarithmic scale. Two straight tangent lines can be drawn on the curve and the ultimate capacity corresponds to the intersection of these two lines. This method is linked to the initial yielding of the soil-pile system when subjected to lateral loads. Therefore, this method is also adopted in the present study to obtain the ultimate lateral capacity of test screw piles.

Pile lateral capacities can also be defined depending on either the short or long pile failure mode. Broms (1964a) provided a method to estimate the ultimate lateral capacity of a long pile in cohesionless soil under the free-head condition. The distributions of deflections, soil reactions and bending moments of a long pile in cohesionless soil under the free-head condition are shown in Figure 5.2. A long pile subjected to lateral load under the free-head condition fails by developing a plastic hinge (at the location of the maximum bending moment) at a distance below the ground surface. The maximum bending moment (M_{max}) and the distance (f) to the location where the

plastic hinge forms are determined by assuming the lateral earth pressure as three times the passive Rankine earth pressure. On the basis that the total shear force on the pile shaft to the depth of f is equal to zero, f is determined by:

$$f = 0.82\sqrt{\frac{P}{\gamma D K_P}} \tag{5-8}$$

where P is the lateral capacity of the pile, and K_p is the coefficient of passive earth pressure. The corresponding maximum positive bending moment, M_{max}, was determined, as in Equation 5-9:

$$M_{max} = P(e + 0.67f) + M_{applied} \tag{5-9}$$

where e is the pile stickup length, $M_{applied}$ is the moment applied at the pile head. The values of P and f can be determined from Equations 5.8 and 5.9 by setting M_{max} equal to the fully plastic bending moment capacity of pile (M_p), where M_p can be determined from the cross-sectional properties of the pile.

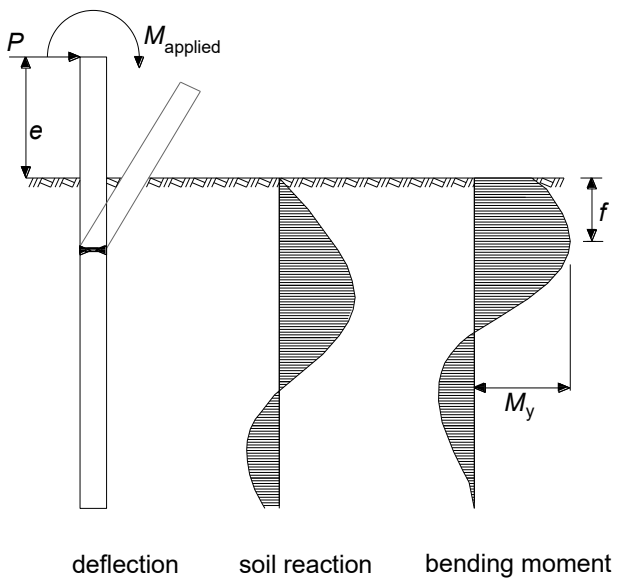

Figure 5.2. Distributions of deflection, soil reaction and bending moment of a long free-headed pile in cohesionless soil (adapted from Broms 1964a).

Broms (1964b) also provided a method to estimate the ultimate lateral capacity of a long pile installed in cohesive soil under the free-head condition. The distributions of deflections, soil reactions and bending moments of a long pile in cohesive soil under the free-head condition are shown in Figure 5.3. A long pile with the free-head condition fails when a plastic hinge is formed at some distance *f* below the ground surface. It was assumed that a full passive resistance of soil was mobilized to the depth corresponding to the location of the maximum bending moment. Based on the rule of equilibrium, *f* and M_{max} were determined as in Equation 5-10 and 5-11, respectively:

$$f = \frac{P}{9 s_u D} \tag{5-10}$$

$$M_{max} = P(e + 1.5D + 0.5f) \tag{5-11}$$

where s_u is the undrained shear strength. The values of *P* and *f* can be determined using Equations 5.10 and 5.11 by setting M_{max} equal to M_p.

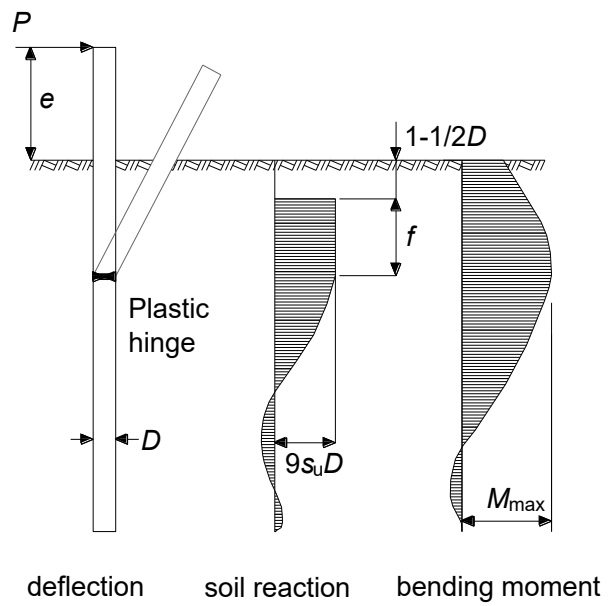

Figure 5.3. Distributions of deflection, soil reaction and bending moment of a long free-headed pile in cohesive soil (adapted from Broms 1964b).

5.2.3. Review of the Effects of Helical Plates and Tapering on Lateral Capacity

The equations for lateral capacities in Broms (1964a, b) were developed for conventional straight-shaft piles, such as driven piles or bored shafts. The micro screw piles are different from conventional piles in that the shaft is modified to enhance the axial resistance, and the piles are installed by torque. Although the lateral soil-micro screw pile interaction has not been investigated in the literature, research conducted in other screw pile types, such as helical piles whose shaft is modified with helical plates, may give us insight into the anticipated lateral behaviour of micro screw piles.

A limited number of studies has investigated the lateral response of helical piles. Zhang (1999) performed lateral load field tests of four instrumented helical piles with three-helices in clay and sand. The lateral resistance of the pile was observed to increase with the thickness of the pile, and the contribution of a helix that was located at a large depth was minimal. El Aziz (2012) calibrated the results of a numerical model using the L-Pile software with lateral load field tests on hollow bar micropiles and reported that piles' lateral response was mainly influenced by soil to a depth of 10*D*. Sakr (2009) noted that the ultimate lateral capacities of single- and double-helix piles were similar. The lateral response of helical piles, evaluated in L-Pile software without taking the contribution of the helix, is comparable with the measured curve of single- and double-helix piles. The evaluation reports ICC (2012) for micro screw piles and ICC (2013) for helical piles recommended that the lateral capacity consider shaft resistance only and that the lateral capacity of the threads and helix should not permitted.

Elkasabgy and El Naggar (2015) conducted lateral load field tests on two large-diameter helical piles with double helices and with the same lead sections but different extension lengths and observed that long piles had a higher lateral load capacity than short piles. Prasad and Narasimha Rao (1996) experimentally investigated the lateral behaviour of rigid helical model

piles having two and four helices relative to a straight pile in soft to medium stiff clayey soils. It was observed that lateral capacity was increased with embedment depth and soil shear strength. The capacity of helical piles was 1.2 to 1.5 times the capacity of straight piles where pile capacity increased with the number of helices. El Shernouby (2012) suggested that the differing results of previous research could be related to the helix location relative to the active zone. It was observed that helix resistance was mobilized for short piles and that helix resistance was not mobilized for piles where the helix was situated in a zone where there was no rotation.

Tapered piles have a better lateral performance than straight piles because the pile material is distributed more efficiently. Wei and El Naggar (1999) conducted numerous lateral load tests on instrumented large-scale model piles installed in cohesionless soil in the laboratory. They observed that tapered piles had a lateral capacity that was 77% more than straight piles with the same average diameter. Since the cross-sectional area of tapered piles at the location of the maximum moment was more than the straight pile, lower stress was developed. Sakr et al. (2004) investigated the lateral response of composite tapered piles driven in dense sand. Tapered piles, having the same volume as straight piles, had a lateral capacity that was 66% more. Fahmy and El Naggar (2015) conducted lateral load tests on spun-cast ductile iron helical and helical tapered piles. It was observed that helical plates increased the lateral capacity of the short pile. In addition, tapered piles had a higher ultimate capacity and stiffer response than straight shaft piles due to greater pile diameter and stiffness at the upper portion.

In summary, several researchers have conducted small-scale laboratory and full-scale field tests of various helical piles in conjunction with theoretical and numerical analyses. Based on this limited research, it can be concluded that mainly the pile shaft affects the lateral response of helical piles. The contribution of helices to pile lateral behaviour depends on the location of the helices. In fact, ICC (2012) for micro screw piles and ICC (2013) for helical piles recommended that lateral

capacity consider shaft resistance only and that the lateral capacity of thread and helix not be permitted although there was no prior evidence on the contribution of the threads of the micro screw piles. In the present study, the lateral capacity of the micro screw pile was estimated using the Brom method and neglecting consideration of the threads. A numerical model further investigates the lateral soil-pile interaction of this pile in the next chapter.

5.3. Field Test Program

5.3.1. Test setup

There are many types of micro screw piles that are suitable for various applications. The micro screw pile varies in diameter, length, the length and location of the thread, angle and tapering. Regardless of their differences, they are similar in that they have a relatively small diameter (< 114 mm) and short length (< 3 m) compared to conventional piles, and they have thread and tapered segments. Therefore, six out of the available 13 M-series micro screw piles (P1–P6) were laterally loaded at three sites. There is a need to study the lateral response of the micro screw pile and the effects of such pile variation on the lateral response of the micro screw pile installed in various soils.

The details of the test piles and the results of the site investigation program conducted at each site were elaborated in Chapter 3. The lateral load field test setup is shown in Figure 5.4. Initially, four micro screw piles, each with a diameter of 140 mm and a length of 2.1 m, were installed in a square grid. The spacing between the micro screw piles was 0.75 m, which was five times the shaft diameter (D_s) of the largest pile. The reaction system was specifically designed and fabricated for the present field test program. Four steel frames were laid out and bolted on the pile cap to form a rigid reaction pile group cap. The hydraulic jack, equipped with two special adapters, was lowered on top of a lumber block between the rigid reaction pile group and the test pile. One

adapter was designed and built to connect the piston of the hydraulic jack with the pile cap of the test pile, and another adapter was designed and built to connect the load cell and the rigid reaction pile group cap. Each adapter was equipped with a hinge that eliminated the possibility of moment and vertical load development at the pile cap. Initially, the adapter was bolted to the rigid reaction pile group cap. Then, the piston was slowly extended until the other adapter was bolted on top of the pile cap. This setup was generally stable during the field tests. The lateral displacement of the reaction pile group was observed to be negligible, as shown in the lateral load field test result example in Appendix C.

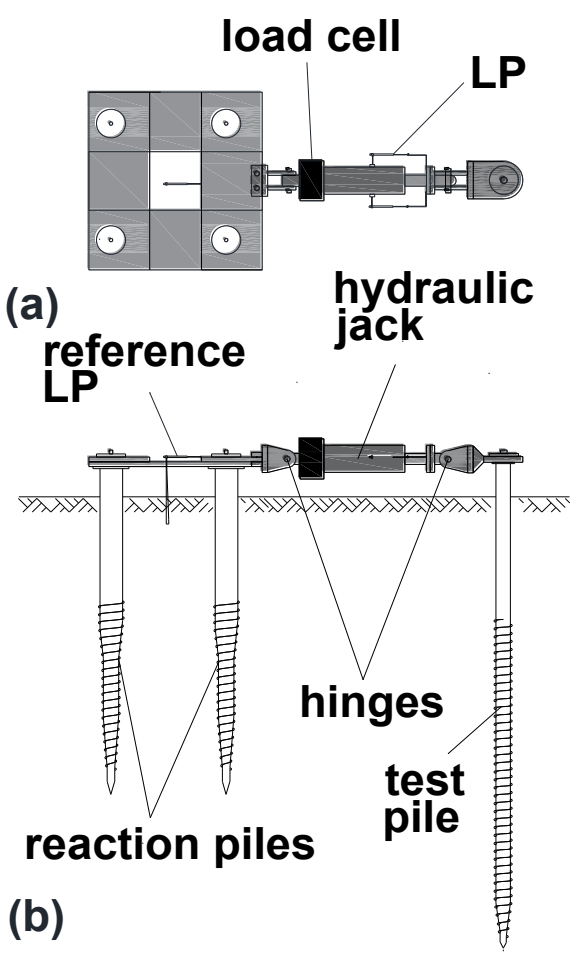

Figure 5.4. Schematic of the lateral test setup: (a) top view; (b) side view and (c) a photo.

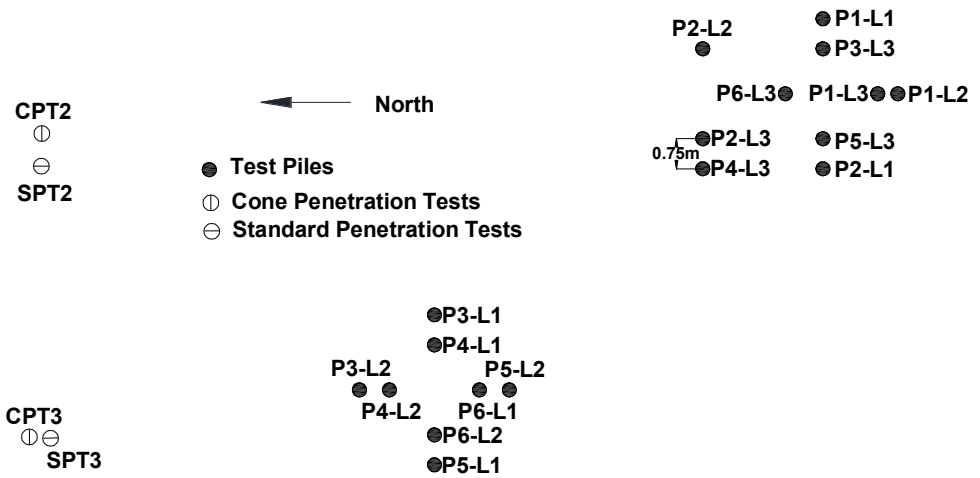

Figure 5.5. The layout of the test piles and the CPT logs at Sandpit. The layouts at the other two sites are similar.

5.3.2. Instrumentation

The hydraulic jack was equipped with a load cell of 900 kN capacity to measure the applied lateral load. Two linear potentiometers were positioned horizontally adjacent to the hydraulic jack and along the applied load. The linear potentiometers were attached to the hydraulic jack using a magnet and a clamp, and the tip of linear potentiometer was bolted into the leading edge of the hydraulic piston. Another linear potentiometer was connected to a reference steel frame to measure the movement of the reaction pile group. The pile P6 at Sherwood Park, pile P1, P3 and P5 were instrumented with several SG stations along the pile depth. The schematic of the instrumented piles is shown in Figure 5.6. A Poisson SG was applied to the outer shaft of the pile. A small hole was drilled adjacent to the SG station. The electric wires, attached to the SG, were pulled from the pile hollow shaft and through the pile cap hole. The SG station was covered by epoxy and aluminum foil, which provided waterproofing below the GWT. A metal sheet casing was welded on top of these layers to protect the SG stations during pile installation. The load cell and two linear potentiometers and SG readings were recorded at a time interval of 1 to 2 sec.

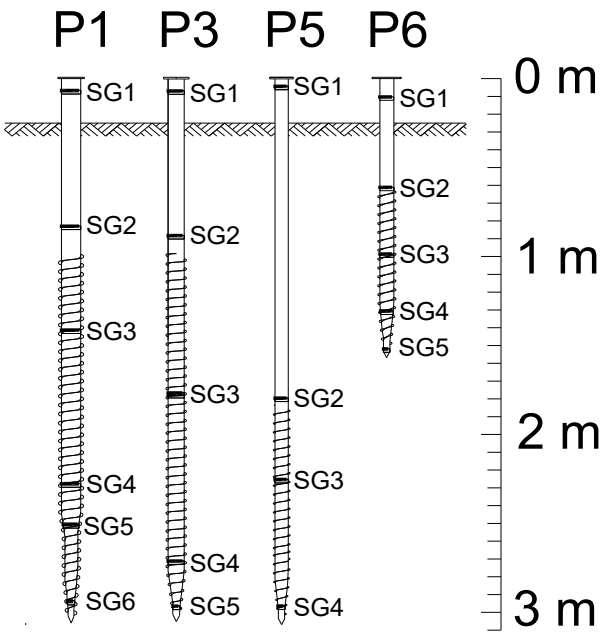

Figure 5.6. Schematic of instrumented piles. Note: Black strips = bending SG stations; the indices of SG stations are labelled beside the instrumented pile.

5.3.3. Test Procedure

The lateral load field test procedure was generally conducted in accordance with ASTM standards D 3966 (ASTM 2007a). Procedure A and Procedure B of the ASTM standards were modified and adopted. Initially, the load was increased at 12.5% up to 75% anticipated capacity. After an increase of 10%, the load was increased at an increment of 5% of the anticipated capacity until ultimate lateral pile capacity was reached. The first two load steps were maintained for 15 minutes, and the remaining load step was maintained for 10 minutes. In the unloading stage, the load was decreased by 25% of the anticipated capacity and each load step was maintained for five minutes. The piles in Sherwood Park and South Campus were tested at least three days after the piles were installed. The piles in Sandpit were tested without considering pile setup.

The layout of the test piles, SPT tests and CPTs at Sandpit are shown in Figure 5.5. The layout of the test piles, SPT tests and CPTs at Sherwood Park and South Campus are shown in

Appendix C. A summary of the piles tested at Sherwood Park, South Campus and Sandpit is shown in Table 5.2. Each of the six piles was tested a minimum of three times at South Campus and Sandpit to improve the reliability of the test data. Each of the six piles was tested once at Sherwood Park. In total, 46 piles were tested. The tests were performed on the piles that were not laterally loaded. As an example of a test identification, P1-L1 corresponds to the first lateral test of pile P1.

5.4. Field Test Results

5.4.1. Lateral Load vs. Displacement Behaviour

The lateral load vs. displacement curves (*P* vs. *Y* curve) of the piles at the three sites are shown in Figure 5.7. The raw P vs. Y curves of the piles had fluctuations due to the hydraulic jack fluid heating and cooling and delayed soil response. The curve was smoothened by selecting the stabilized lateral load vs. displacement. An example of the smoothening of the curve for pile P1-L1 is shown in Appendix C. The load-displacement curve is highly nonlinear. In this research, two ultimate lateral loads were defined for the convenience of use and comparison. The first ultimate lateral load (termed $P_{u\text{-}Y}$ herein) is defined as the load corresponding to a lateral displacement of 12.5 mm. It adopts the allowable lateral load defined by ICC (2012) for the micro screw piles. It has also been used by USACE (1991), Elkasaby and El Naggar (2015) and ICC (2013) for helical piles. The second ultimate lateral load ($P_{u\text{-}DB}$) is defined based on the DeBeer (1968) criterion. When plotting the *P* vs. *Y* curve in a double-logarithmic diagram, two approximate lines will appear, one before and one after the ultimate lateral load. The intersection of these two lines is defined as the second ultimate lateral load ($P_{u\text{-}DB}$). An example of this method is shown in Appendix C. The ultimate lateral loads $P_{u\text{-}Y}$ and $P_{u\text{-}DB}$ are labelled on the load-displacement curve in Figure 5.7. A summary of $P_{u\text{-}Y}$, $P_{u\text{-}DB}$ and the lateral displacement corresponding to the $P_{u\text{-}DB}$

($Y_{u\text{-}DB}$) of the piles tested at Sherwood Park, South, Campus and Sandpit is shown in Table 5.2 and Figure 5.8.

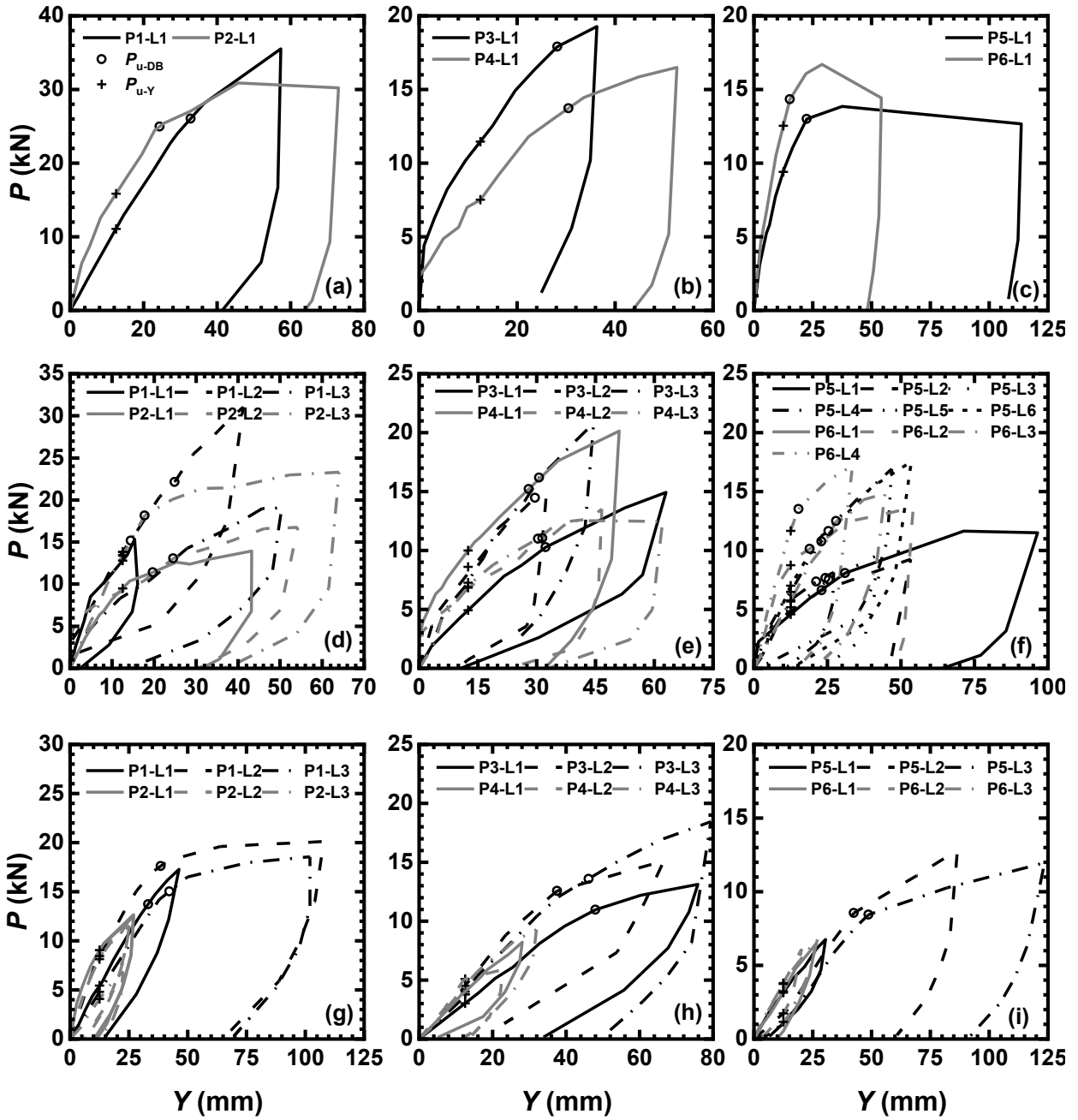

Figure 5.7. Lateral load-lateral displacement of the test piles at the three sites: (a) to (c) Sherwood Park, (d) to (f) South Campus and (g) to (i) Sandpit. Lateral capacities at Y=12.5 mm and the capacities by DeBeer's method are marked in the figure.

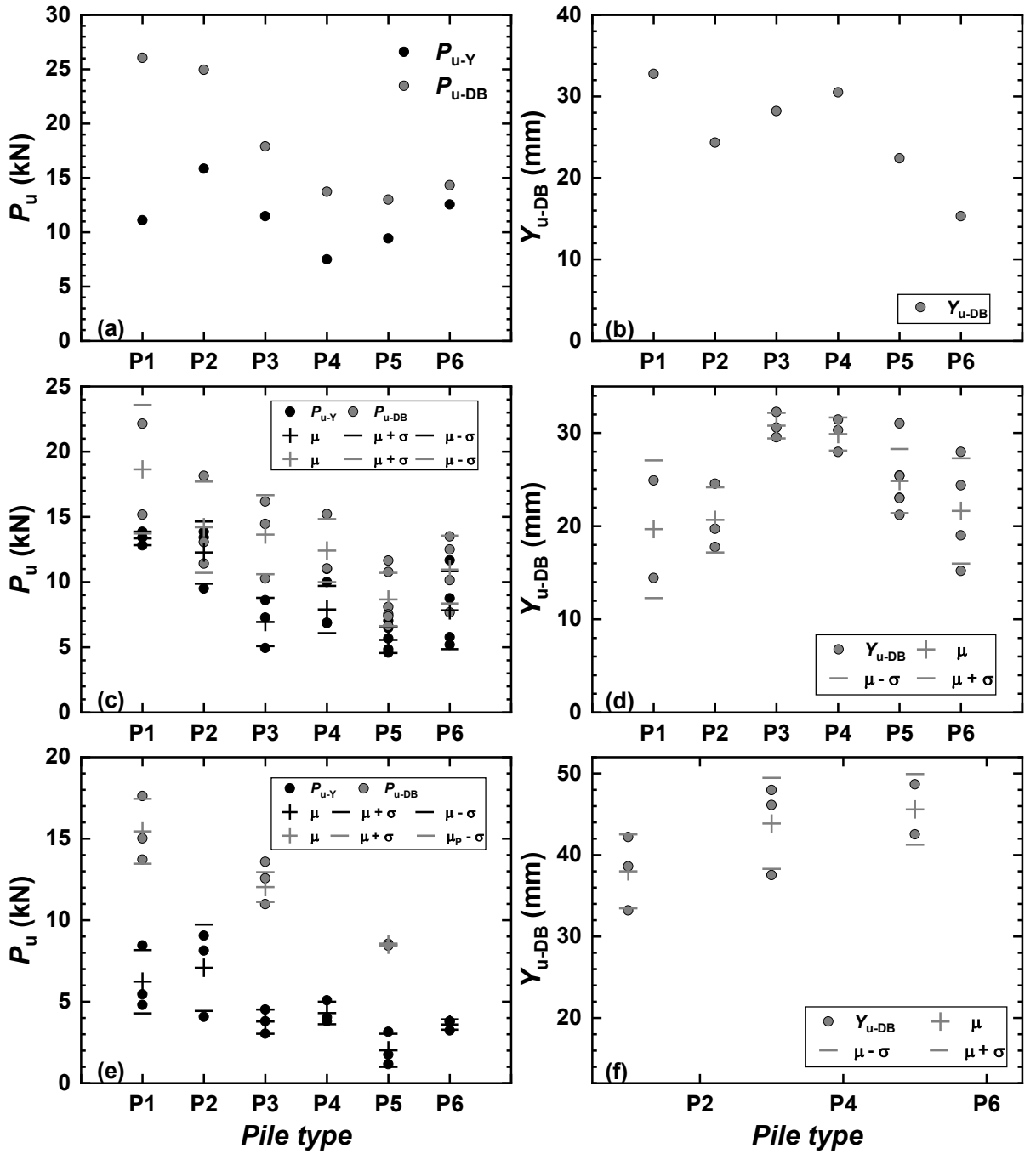

Figure 5.8. Summary of ultimate lateral loads and ultimate lateral displacement (a) the $P_{u\text{-}Y}$ and $P_{u\text{-}DB}$ of the piles at Sherwood Park, (b) the $Y_{u\text{-}DB}$ of the piles at Sherwood Park, (c) the $P_{u\text{-}Y}$ and $P_{u\text{-}DB}$ of the piles at South Campus, (d) the $Y_{u\text{-}DB}$ of the piles at South Campus, (e) the $P_{u\text{-}Y}$ and $P_{u\text{-}DB}$ of the piles at Sandpit and (f) the $Y_{u\text{-}DB}$ of the piles at Sandpit.

Table 5.2. Summary of the test matrix and lateral capacities of the test piles according to two criteria.

Site	Pile	Test	$P_{u\text{-}Y}$ (kN)	$P_{u\text{-}DB}$ (kN)	Instrumented	Soil type
Sherwood Park	P1	L1	11.1	26.0	No	clay fill
	P2	L1	15.9	25.0	No	
	P3	L1	11.5	17.9	No	
	P4	L1	7.5	13.7	No	
	P5	L1	9.4	13.0	No	
	P6	L1	12.5	14.3	L1 only	
South Campus	P1	L1–L3	12.8,13.9,13.4	N.A., 22.1, 15.2	L1 only	Glacio lacustrine clay
	P2	L1–L3	9.5, 13.9, 13.4	11.4, 13.1, 18.1	No	
	P3	L1–L3	4.9, 8.6, 7.3	10.3, 14.5, 16.2	L2 only	
	P4	L1–L3	10.0,6.9,6.8	15.2, 11.0, 11.0	No	
	P5	L1–L6	4.6,4.8,4.8,5.7,6.5,7.0	8.1, 6.6, 7.5, 7.3, 11.7, 10.7	L4 only	
	P6	L1–L4	5.2,8.8,5.8,11.7	24.4, 19.0, 28.0, 15.2	No	
Sandpit	P1	L1–L3	5.4, 8.4,4.8	13.7, 17.6, 15.0	No	Eolian sand
	P2	L1–L3	9.1,8.1,4.1	N.A.	No	
	P3	L1–L3	3.0,4.5,3.8	11.0, 12.6, 13.6	No	
	P4	L1–L3	4.0,5.1,3.8	N.A.	No	
	P5	L1–L3	3.1,17.7,1.2	-, 8.5, 8.4	No	
	P6	L1–L3	3.2,3.8,3.7	N.A.	No	

Note: P6–L1 at Sherwood Park, P1–L1, P3–L2 and P5–L4 were instrumented with SG. The location of maximum curvature of piles P1, P3 and P5 was measured.

Generally, these piles were loaded corresponding to a large displacement in excess of the lateral displacement of 25 mm and 19 mm needed to mobilize the ultimate lateral capacities of the helical and the micro screw piles, respectively. The *P*-*Y* curves of piles P1, P3 and P4 at Sherwood Park have a ductile feature, where the load keeps increasing without achieving a peak load. This can perhaps be due to a long pile failure and the mobilization of deep soil resistance. On the contrary, a short pile would likely have failed abruptly as the soil fails due to pile rotation. The *P*-*Y* curves of piles P2, P5 and P6 (refer to Fig. 5.7a and Fig. 5.7c) have a brittle feature with a plunging failure where the load decreases after reaching a peak load. Piles P2 and P6 are shorter

than the other pile. The *P-Y* of all the piles at South Campus and Sandpit has a ductile feature, which indicate that the piles at these sites also failed as long piles.

The measured capacities $P_{u\text{-}Y}$ and $P_{u\text{-}DB}$ and with their means and coefficients of variations of the piles at Sherwood Park, South Campus and Sandpit are shown in Table 5.2 and Figure 5.8. It is seen that $P_{u\text{-}Y}$ and $P_{u\text{-}DB}$ generally increase with pile diameter and not so much with pile length. Therefore, the *P-Y* curves of these piles are shown in the same figure. It is possible that the effective lengths of piles P1 and P2, P3 and P4 and P5 and P6 at Sherwood Park and South Campus are identical. It is observed that pile P6 has a higher $P_{u\text{-}Y}$ and $P_{u\text{-}DB}$ than pile P5 even though pile P6 is shorter than pile P5. This can be caused either by soil heterogeneity, by variation in pile stickup and the presence of a cavity system or by the fact that pile P6 had thread at shallow depths. The variation of the pile capacities of the piles at Sandpit is relatively smaller than the piles at South Campus because the soil susceptibility to develop a cavity and the effect of pile setup with a sandy soil are less. The value of the $Y_{u\text{-}DB}$ of the pile tested at Sherwood Park increases with pile diameter. However, the value of the $Y_{u\text{-}DB}$ of the piles tested at Sandpit decreases with pile diameter.

5.4.2. Distribution of the Bending Moment

The pile P6 at Sherwood Park and piles P1, P3 and P5 were instrumented with several SG stations along the pile depth that measured the distribution of the bending moment. The longitudinal strain (ε) was calculated from the measured voltage ratio (V_r) using Equation 5-12a, and the bending moment (M) was calculated using Equation 5-12b:

$$\varepsilon = \frac{-2V_r}{GF(\nu+1)} \tag{5-12a}$$

$$M = \frac{\varepsilon EI}{r_o} \tag{5-12b}$$

where *GF* is the gauge factor of the SG, and r_o and *v* are the outer shaft radius and Poisson's ratio of the pile shaft material. Examples of the time histories of ε are shown in Figure 5.9. The main form of deformation along the pile length is bending of the pile shaft due to lateral loading. Along the direction of the applied load, a maximum positive and negative longitudinal strain with a corresponding Poisson's negative and positive latitudinal strain is developed on the pile's outer circumference at each SG station, which is shown in Figure 5.9b.

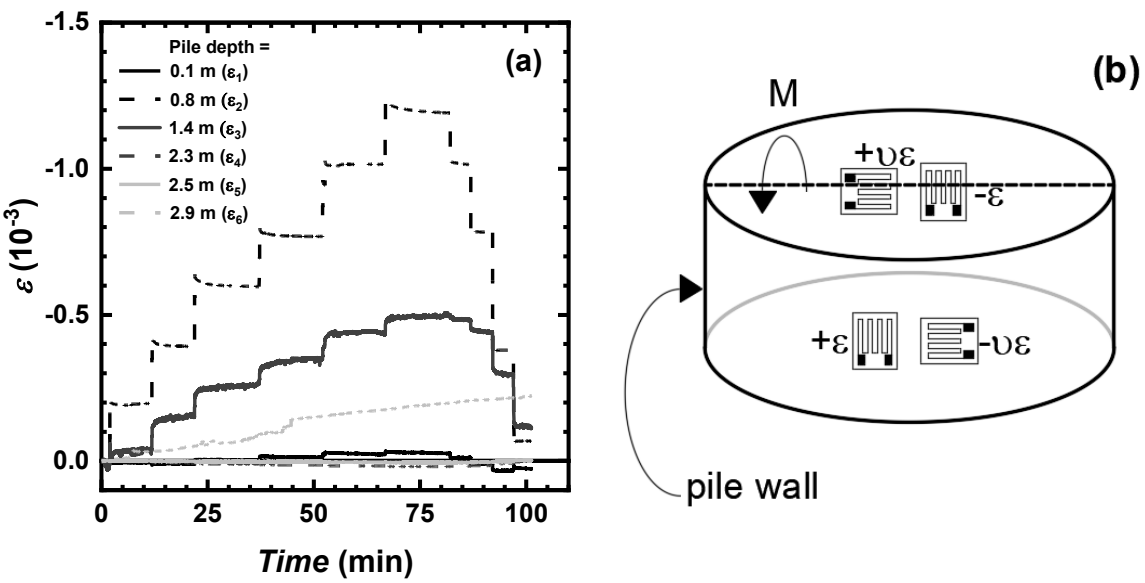

Figure 5.9. (a) Example results of longitudinal strain at six locations along pile P1 during lateral loading at South Campus; (b) the location of the SGs for a full Wheatstone bridge for measuring the bending moment at one cross-sectional plane of pile shaft wall; gauges are placed at opposite sides of the wall. SGs ε_1 to ε_6 were placed at different pile depths from the pile top to the pile toe.

In order to determine whether the pile shaft experienced any plastic bending, elastic (M_y) and fully plastic (M_p) bending moments are calculated using Equations 5-13 and 5-14 (Beer et al. 2006):

$$M_y = \frac{\sigma_y}{r_o}\frac{\pi(r_o^4 - r_i^4)}{4} \tag{5-13}$$

$$M_p = \sigma_y \frac{8\left(r_o^3 - r_i^3\right)}{6} \tag{5-14}$$

where σ_y is the yield strength of the pile steel material (=248 MPa), and r_i is the inner shaft radius of the pile. The parameter M_y is the bending moment when the pile shaft cross-section begins to yield at the exterior edges, and M_p is the bending moment when the pile shaft yields fully.

The measured distributions of the bending moment (DBMs) of the instrumented pile P6 at Sherwood Park and P1, P3 and P5 at South Campus are shown in Figures 5.10 and 5.11, respectively. The bending moment at the SG locations are also shown in these figures as to compare with the measured DBMs. The measured DBMs of these piles have the qualitative representative shape of a long pile under the free-head condition. The distributions are minimal near the pile head. The measured M_{max} of pile P6 at Sherwood Park and P1 and P3 at South Campus are measured at a depth of 0.55 m ($7D_s$), 0.84 m ($7D_s$) and 0.89 m ($10D_s$), respectively. The SG at the location of the maximum moment of pile P5 at South Campus could have been damaged due to excessive deformation given that piles P1 and P3, with a larger diameter, had yielded. The measured M of pile P6 at Sherwood Park and P1, P3 and P5 at South Campus are minimal below the depths of 0.91 ($12D_s$), 2.5 m ($22D_s$), 1.8 m ($20D_s$) and 1.8 m ($24D_s$), respectively. The measured M_{max} of pile P6 (Fig. 5.10) is less than M_y, indicating that the pile has apparently not yielded. However, it should be noted that M was measured at discrete locations, and so the location of M_{max} may be uncertain. The pile may have yielded at some location where the SG was not installed. The measured M_{max} of pile P1, P3 and P5 at South Campus exceed M_y indicating that the piles have yielded.

Another method of inferring the pile failure mode from limited M readings is to check the ratio of the change in M (ΔM) to the change in the lateral displacement (ΔY). As shown in Figure 5.10, this ratio $\Delta M/\Delta Y$ is large when the pile shaft deforms elastically. Once the pile lateral

displacement reaches into the vicinity of $Y_{u\text{-}Y}$ and $Y_{u\text{-}DB}$, $\Delta M/\Delta Y$ decreases because the pile has yielded. On the other hand, since the values of M are negligible near the tapered segments, the effect of the taper on the lateral response is negligible. The values of M are the greatest along the uniform (smooth and threaded) segments, where the pile diameter are the greatest. Therefore, a higher pile shaft capacity and soil resistance are mobilized along the uniform segments. The observation indicates that the distribution of pile material is efficient for pile to provide the lateral resistance.

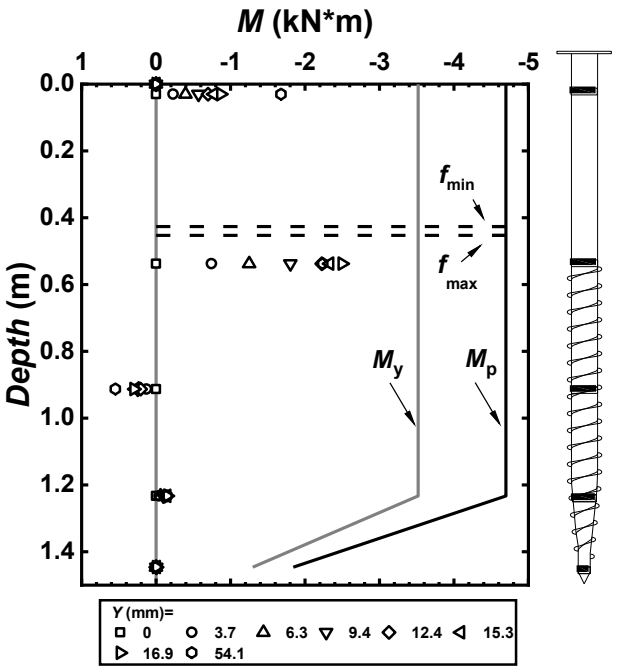

Figure 5.10. Distribution of the bending moment along the instrumented pile P6 at Sherwood Park. Note: f_{min} and f_{max} is the range of the location of the maximum moment as estimated from Broms (1964b) from several CPT readings.

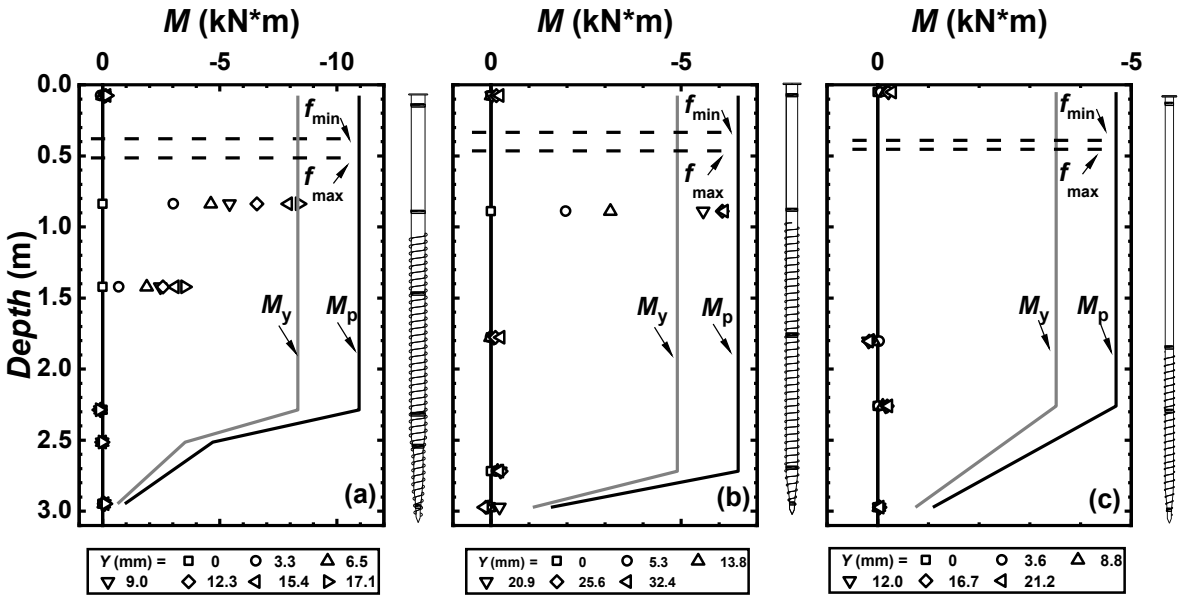

Figure 5.11. Distribution of the bending moment along the instrumented piles at selected lateral displacements at South Campus: (a) P1, (b) P3 and (c) P5. Note: f_{min} and f_{max} is the range of the location of maximum moment as estimated from Broms (1964b) from several CPT readings.

Upon completing the lateral tests at Sandpit, the test piles were removed from the soil, and the permanent deformed shapes of the piles were carefully examined. Photos of the permanently deformed piles, with the locations of maximum curvature and permanent displacements of the pile heads, are shown in Figure 5.12. The distance between the pile head and bent plane can be denoted as f. The measured ratios f/D_s of piles P1, P3 and P5 laterally loaded under the free-head condition are $8D_s$, $10D_s$ and 9-$10D_s$, respectively. The measured distance f decreases with decreasing pile diameter. In addition, the pile deformation clearly indicates that the pile fails as a long pile. Notably, since these piles are not laterally loaded to an excessively large displacement, the locations of the maximum curvature may be changed as the load continues.

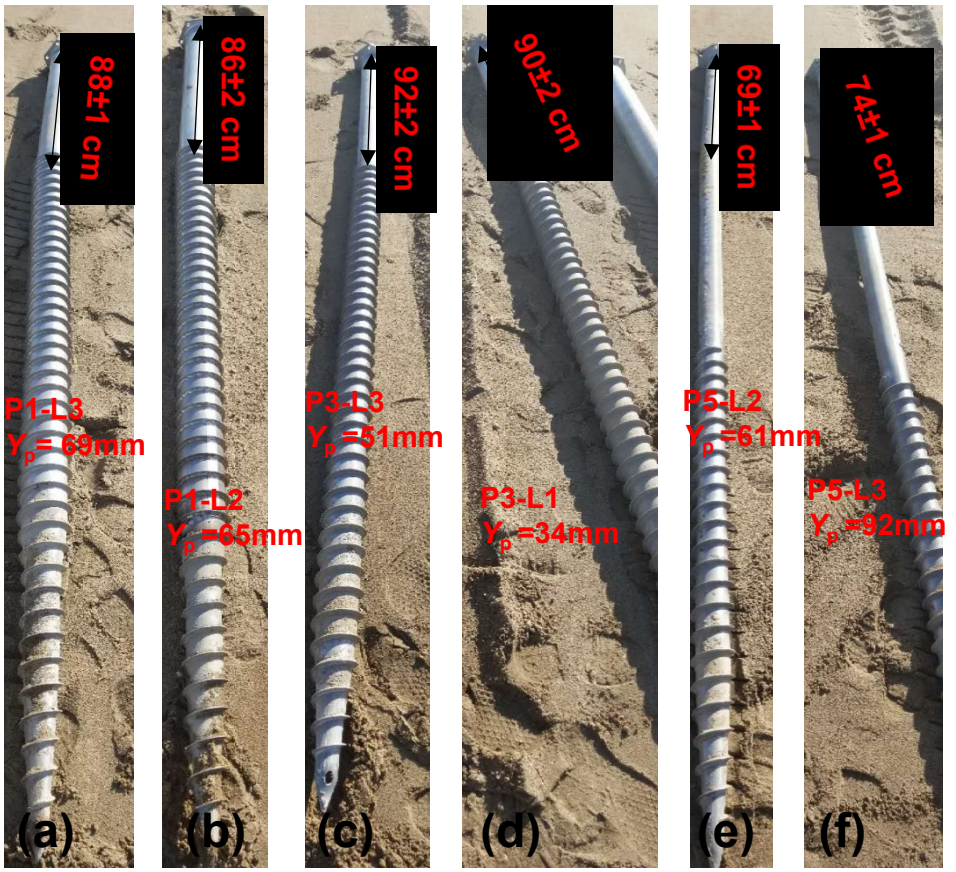

Figure 5.12. The permanent deformed shape of selected piles at Sandpit: (a) and (b) P1; (c) and (d) P3; and (e) and (f) P5. Note: The arrows show the locations of maximum curvature. The symbol Y_p denotes the permanent displacement of the pile head.

5.4.3. Pile Failure Mode

In the present section, the pile failure mode was approximated using Broms's (1964a, b) and Meyerhof and Yilcin's (1984) criteria. It was compared with the observed failure mode based on the distribution of the bending moment of the piles at Sherwood Park and South Campus and photos of the deformed pile with the location of maximum curvature. Thereafter, the lateral capacity of the pile was obtained using an appropriate failure mode. The soil parameters were interpreted from CPT readings. Given that the lateral capacity was mainly influenced by the pile shaft resistance and the soil to a shallow depth such as $10D_s$ (El Aziz 2012), the pile was assumed

to have a uniform shaft, and the effect of the thread was neglected. Finally, the estimated lateral capacity of the pile was compared with the measured $P_{u\text{-}DB}$ to assess its effectiveness.

Based on Broms (1964a, b), the ratio of the L/R of the piles tested at Sherwood Park and South Campus and the ratio of the L/T of the piles tested at Sandpit are shown in Table 5.3 and Figure 5.13a. The required soil parameters, such as D_r and s_u, were interpreted from CPT readings. It can be seen that the ratio of the L/R of the piles tested at Sherwood Park and South Campus and Sandpit are greater than the value of 2, which suggests that all these piles met the criteria of long piles. The suggested failure mode is consistent with the observed failure mode based on the distribution of the bending moment of pile P1 at Sherwood Park; P1, P3 and P5 at South Campus; and photos of the deformed piles with the location of maximum curvature. These piles generally have small shaft thickness and diameter compared to their length. It can be seen that there are two linear trends, where piles P1, P3 and P5 form one trend and piles P2, P4 and P6 form another trend. The ratios L/R and L/T of piles P1, P3 and P5 are greater than piles P2, P4 and P6. The ratios of L/R and L/T increase with decreasing pile diameter for piles with similar lengths. The relative stiffnesses of the piles tested at Sherwood Park, South Campus and Sandpit were obtained using the equations provided by Benerjee and Davis (1978) and Poulos and Davis (1980). The required soil parameters, such as horizontal soil modulus (E_h) and soil modulus (E_s), were interpreted from CPT readings. The relative pile stiffnesses (K_r) of the piles tested at Sherwood Park, South Campus and Sandpit are shown in Table 5.3 and Figure 5.13b. The K_r of all the piles tested at the three sites is smaller than the 10^{-1} to 10^{-2} that meets Meyerhof and Yalcin's (1984) criterion suggested for a long pile. The K_r of pile P2 tested at Sherwood Park and South Campus is at the margin of these criteria. Pile P2 has the largest diameter and a shorter length than other piles. As noted previously, two linear trends are observed, where piles P1, P3 and P5 form one trend and P2, P4 and P6 form another trend. The value of K_r decreases with decreasing diameter, which means the pile behaves

more like a long pile. The values of the K_r of P1, P3 and P5 are less than piles P2, P4 and P6 because K_r decreases with decreasing pile diameter for piles with similar lengths.

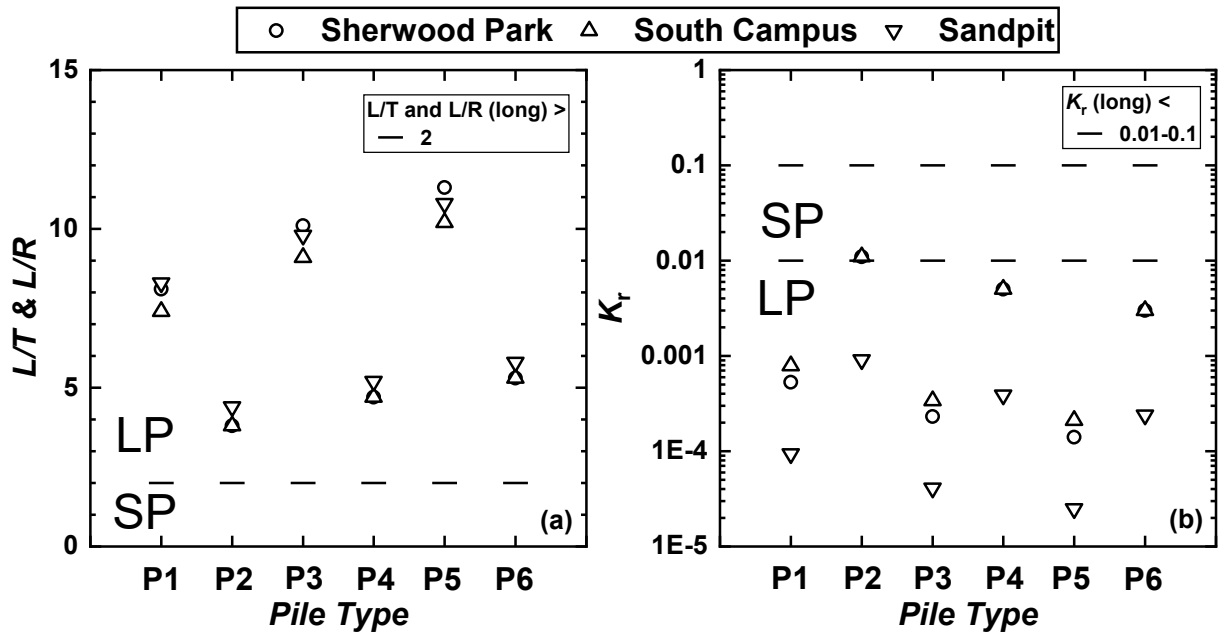

Figure 5.13. (a) Ratios of L/R and L/T and (b) the relative stiffnesses of the piles tested at the three sites. Note: LP denotes long pile and SP denotes short pile.

Table 5.3 Summary of pile relative stiffness and the ratio of L/R and L/T and the failure modes of all test piles.

Pile	D_s	L	Sherwood Park			South Campus			Sandpit		
	(mm)	(m)	K_{rc}	L/R	FM	K_{rc}	L/R	FM	K_{rs}	L/T	FM
P1	114.3	3.04	5.3e-4	8.1	LP	7.9e-4	7.4	LP	9.4e-5	8.3	LP
P2	114.3	1.55	0.011	3.8	TP	0.011	3.8	TP	9.1e-4	4.4	LP
P3	88.9	3.09	2.3e-4	10.1	LP	3.4e-4	9.1	LP	4.1e-5	9.8	LP
P4	88.9	1.58	0.005	4.7	LP	0.005	4.7	LP	3.9e-4	5.2	LP
P5	76.1	3.08	1.4e-4	11.3	LP	2.1e-4	10.2	LP	2.5e-5	10.8	LP
P6	76.1	1.57	0.003	5.3	LP	0.003	5.3	LP	2.4e-4	5.8	LP

Note: Failure mode, FM;, long pile failure mode, LP;, short pile failure mode, SP; and transitional pile failure mode, TP.

5.4.4. Estimation of the Ultimate Lateral Capacity Using the Broms Method

The ultimate lateral capacities of the six piles at Sherwood Park, the 22 piles at South Campus and the 18 piles at Sandpit were estimated using the Broms method with the following assumptions: 1) The pile fails as a long pile because the measured DBM of pile P6 at Sherwood Park; piles P1, P3 and P5 at South Campus; and the permanent deformed shape of piles P1, P3 and P5 at Sandpit resembled long piles. In addition, all the piles met Broms's (1964a, b) and Meyerhof and Yilcin's (1984) criteria for long piles. 2) The pile was assumed to have a uniform shaft, and the effect of the thread was neglected because the top thread of this pile is located at depths of 7 (P1), 5 (P2), 10 (P3), 7 (P4), 24 (P5) and 8 (P6) times the pile diameter. El Aziz (2012) observed that pile response was mainly influenced by soil to a depth of $10D_s$. Puri et al. (1984) and Sakr (2009) reported that the lateral capacity of a helical pile was mainly influenced by shaft resistance and that the influence of thread was minimal. In addition, the evaluation report ICC (2013) for micro screw piles and ICC (2013) for helical piles recommended that lateral capacity should only consider shaft resistance and that the lateral capacity of threads and helices should not be permitted. 3) The pile is subjected to lateral loaded under the free-head condition with negligible moment because there was a hinge between the pile head and the hydraulic jack and another hinge between the hydraulic jack and the reaction piles. 4) The required soil parameter, the s_u of cohesive soils and the γ, ϕ_p of cohesionless soils were interpreted from the CPT readings, as shown in Chapter 2. 5) The value of M_{max} was set as M_p.

The use of Broms's (1964b) method to estimate the ultimate lateral capacity (P_u) of a long pile in cohesive soils under the free-head condition may be an appropriate method. This method assumes that a plastic hinge (M_{max}) would develop in the pile as some distance (f) and full passive earth pressure would develop above this distance. The P_u of the six piles tested at Sherwood Park and the 22 piles tested at South Campus were estimated as a function of s_u, pile stickup, pile

diameter and M_{max} (or M_p). The required soil parameter s_u was interpreted from two CPT readings at Sherwood Park and seven CPT readings at South Campus.

The estimated and measured P_u of the piles tested at Sherwood Park and South Campus are shown in Figures 5.14a and 5.14b, respectively. The estimated P_u of the piles tested at Sherwood Park is 19% less than the measured P_u on average. It can be seen that the measured $P_{u.DB}$ of the six piles is marginally underestimated, which can be due to neglecting the thread's effect on the pile's lateral capacity. For the piles at South Campus, it can be seen that the measured P_u of the 22 piles is generally within the margin of the estimated P_u. The estimated P_u is 34% greater than the measured P_u on average. This overestimation can perhaps be due to the development of the cavity (Guo and Deng 2018) and soil disturbance after pile installation (Puri et al. 1984, Bagheri and El Naggar 2013).

The use of Broms's (1964a) method to estimate the P_u of a long pile in cohesionless soils under the free-head condition was used. The method is based on the assumption that a plastic hinge would develop at some distance below the ground surface and that the lateral earth pressure was three times the passive Rankine earth pressure. The required soil parameters γ and ϕ' were interpreted from four CPT readings. The values of the P_u of the piles tested at Sandpit were estimated as a function of γ, ϕ', pile stickup, pile diameter and M_{max} (or M_p). The estimated and measured P_u of the piles tested at Sandpit are shown in Figure 5.14c. The estimated P_u of the pile is 16% less than the measured P_u. It can be seen that the measured P_u of the nine piles is marginally underestimated. Overall, the Broms method provides a reasonable estimate of the measured P_u of micro screw piles without considering the effect of the thread. Therefore, the contribution of the thread to the lateral capacity of pile may be insignificant.

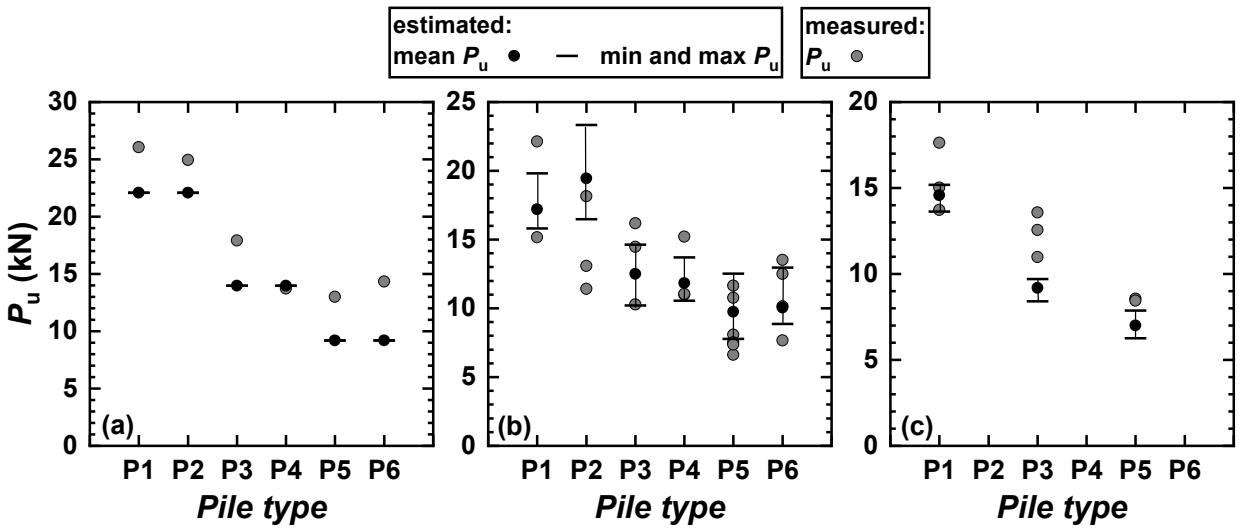

Figure 5.14. Comparison of the estimated and measured P_u of the piles at the three sites: (a) Sherwood Park, (b) South Campus and (c) Sandpit. Note. The minimum and maximum P_u were obtained from CPT readings available on each site.

5.5. Conclusions and Limitations

1. Generally, the pile P_u increases with diameter and not with length because the effective lengths of the piles with the same diameter are the same. The value of the P_u of pile P6 is slightly greater than pile P5 because pile P6 has the thread situated at a shallower depth.
2. The DBM of the instrumented pile P6 at Sherwood Park and P1, P3 and P5 at South Campus exhibits the representative shape of a long pile under the free-head condition, where the pile deformation is minimal near the pile base. Furthermore, the ratio of $\Delta M/\Delta Y$ decreases in the vicinity of $Y_{u\text{-}DB}$ and $Y_{u\text{-}Y}$, which suggests that the pile has failed structurally. The deformed shapes of the piles at Sandpit clearly demonstrates long pile failure.
3. Consistent with the observed failure mode, Broms (1964a, b) and Meyerhof and Yalcin (1984) criteria suggest that all these piles behave as long piles at these sites.

4. Broms's method underestimates the measured P_u of the piles at Sherwood Park and Sandpit. Perhaps, the underestimation could be due to neglecting the thread when estimating the P_u of the piles. The values of P_u of the piles at South Campus are significantly overestimated by this method which can be due to the development of cavity and soil disturbance after the pile installation.
5. The effect of the threads on the values of P_u are minimal as the estimated P_u without considering the effect of thread are comparable with the measured P_u of the piles.
6. The placement of the tapered segment at the bottom of the pile is efficient. The values of M are the greatest along the uniform (smooth and threaded) segments, where the pile diameter are the greatest. Therefore, a higher pile shaft capacity and soil resistance are mobilized along the uniform segments. The distribution of pile material is efficient for pile to provide the lateral resistance.

The following limitations of this research should be noted:

- The pile was loaded laterally under the free-head condition. The hydraulic jack was equipped with two hinges, one adjacent to the load cell and one adjacent to the hydraulic jack piston. However, some moment could have developed at the pile head.
- The smoothened lateral load-displacement curve was accurate to within a couple of kilonewtons because the load fluctuated due to the hydraulic fluid heating and cooling.
- The ultimate lateral capacity was obtained using DeBeer's (1968) method. There is some subjective error introduced by using this approximate method.
- The distributions of the bending moments of selected piles were obtained. The bending moment was obtained at discrete locations along the pile. The actual distribution of the bending moment could be obtained by installing additional SGs.

- The ultimate lateral load was obtained by using the soil properties interpreted from CPT readings. The effect of pile installation on soil disturbance was not considered.

6. Numerical Modelling of Micro Screw Piles Subjected to Lateral Loading using the BNWF Method

6.1. Introduction

The current chapter presents the numerical modelling of micro screw piles subjected to lateral loading in cohesive and cohesionless soils. There are many methods to obtain the lateral response of pile. Theory of elasticity, where a single value is assigned to soil parameter is not accurate. Method such as theory of subgrade reaction have simple assumptions, such as assigning subgrade modulus that increase with depth and assuming linear elastic soil. However, the solution to this method have significant errors. Moreover, the lateral soil-pile interaction of micro screw piles with varying pile diameters and shaft modifications is complex. Therefore, as complementary to field tests of full-scale piles, numerical modelling provides a powerful tool for understanding such a complex problem. In the numerical modelling of laterally loaded piles reported in the literature, soils were modelled as either continuum media (e.g., Papadopoulos et al. 2014, Kurian and Shah 2009, Fahmy and El Naggar 2017, Al-Baghdadi 2018) or discrete soil reaction springs using the BNWF method (e.g., El Naggar et al. 2015, Li 2016).

Micro screw piles are different from other conventional piles in terms of their overall shape and installation method. However, they are similar to helical piles because they both have helix or thread and are torqued into the ground. There have been several numerical studies on the lateral soil-pile interactions of helical piles showing that deeply embedded helical plates had a minimum contribution to helical piles' lateral stiffnesses and load capacities (Kurian and Shah 2009, Al Baghdadi 2018, Fahmy and El Naggar 2017, Li 2016). Nevertheless, the lateral behaviour of micro screw piles has not been studied numerically. Micro screw piles differ from helical piles regarding their overall geometry and shape. Specifically, micro screw piles have continuous threads welded along the pile's lower portion with unique width, thickness, length, pitch, embedment depths and

spacing. Hence, it is necessary to examine the soil-pile interactions of the micro screw pile in detail.

In the present research, numerical models based on the Beam-on-Nonlinear-Winkler-Foundation (BNWF) method were developed using an open-source finite element software framework, OpenSEES (PEER 2016), to simulate the lateral behaviour of the micro screw piles installed at three sites. In these numerical models, the lateral shaft resistance, the vertical shaft resistance, the thread bearing resistance and the lateral thread resistance were represented by *p-y*, *t-z*, *q-z* and t_h-*y* (similar *to t-z*) springs, respectively, each of which was characterized by uniaxial load-displacement curves. The *p-y* spring materials for cohesive and cohesionless soils were approximated by Matlock (1970) and API (1993), respectively. The *t-z* spring materials for cohesive and cohesionless soils were approximated by the equation provided by Boulanger et al. (2003) with soil parameters from Reese and O'Neill (1987) and Mosher (1984), respectively. Furthermore, the *q-z* spring materials for cohesive and cohesionless soils were defined by the equation provided by Boulanger et al. (2003) with soil parameters from Reese and O'Neill (1987) and Vijayvergiya (1990). The required soil parameters for defining the spring material were taken from the continuous CPT readings. The numerical models developed were validated against the field tests of the micro screw piles conducted at the three test sites.

Compared to other models based on the BNWF method in the literature (e.g., Guo et al. 2014, Li 2016, El Naggar et al. 2005), the present numerical models incorporated two techniques as follows: 1) the hollow pipe shaft was simulated by beam-column elements with fiber sections, and the Giuffre-Menegotto-Pinto steel material model (Carreno et al. 2020) was assigned to each fiber with an appropriate post-yield strain hardening ratio; and 2) the thread bearing resistance was modelled by a series of zero-length section elements with fiber sections, and the *q-z* uniaxial spring material was assigned to each fiber. The objectives of the numerical modelling of the micro screw

piles are to 1) propose a tool to predict the lateral behaviour and load capacity of the micro screw piles, 2) investigate the pile shaft deformation and displacement characteristics and failure mode, 3) quantify the contribution of various soil-pile interactions to the lateral load capacity of the micro screw piles and 4) examine the effects of the threads and soil properties via sensitivity analyses.

Different pile shaft and soil responses are obtained from numerical analyses, including the distributions of lateral displacement, cross-sectional plane rotation, bending moment, shear force and the lateral soil stress along the pile depth direction. To examine the pile and the adjacent soil failure, the distributions of the bending moment and lateral soil stress are compared with the distribution of the bending moment capacity and the ultimate lateral soil stress along the pile depth direction, respectively. Furthermore, the mobilization of the lateral shaft resistance, the vertical shaft resistance, the thread bearing resistance and the lateral thread resistance at the middle of the individual pile segments are examined to assess their contributions. Finally, a sensitivity analysis was conducted to evaluate how the lateral behaviour of piles changes as the pile geometry and soil properties vary.

6.2. Literature Review and Background

6.2.1. Numerical Analyses of Similar Piles

There have been a limited number of numerical studies on the lateral behaviour of piles with similarity to micro screw piles. The smooth segment of a micro screw pile may be similar to driven piles and the central shaft of helical piles. The threads in a micro screw pile can be understood by observing the effect of helical plates on helical piles. On the other hand, the tapered pile has been reported to have efficient material distribution when subjected to lateral load. Therefore, a review of the research on these relevant piles can aid our understanding of the lateral behavior of micro screw piles.

Papadopoulos et al. (2014) evaluated the lateral response of helical micropiles by conducting a continuum finite element analysis in the Plaxis program and full-scale in-situ tests. The soil was modelled as a linear elasto-perfectly plastic material according to the Mohr-Coulomb criterion. The numerical model underestimated the failure load but accurately predicted the load at a lateral displacement of 25 mm. The lateral load capacity of micropiles, which behaved as long piles, did not increase after a certain pile length. Kurian and Shah (2009) conducted a finite element analysis and compared the simulation results with experimental results from Narasimha Rao et al. (1991). The soil was modelled as a continuum with a Drucker-Prager constitutive model in that study. The lateral response of the pile with two different blade diameters (D_h) was compared with the counterpart of the pile with no blade. It was found that the ultimate lateral load capacity was increased by 325% with the inclusion of blades when the blades were embedded at a depth between 1.1 and 1.6 times the pile shaft diameter (D_s), which represents a relatively shallow blade embedment. The ratio of pile helix to shaft diameter (D_h/D_s) varied between 2 and 3, representing a relatively large blade compared to the shaft diameter.

Using the ABAQUS program to perform finite element analysis, Fahmy and El Naggar (2017) investigated the lateral behaviour of spun-cast ductile iron tapered piles with a single helix installed in clay. The lateral load capacity of the pile was increased by 5% with the addition of a helix (the ratio of D_h/D_s was 2), which was embedded to a depth of between $7D_s$ and $15D_s$. The helix acted as a restraint at the bottom of a short pile. The lateral load capacity of a long pile was increased by 40% due to tapering, whereas the lateral load capacity of a short pile was increased by 28% due to tapering. Al Baghdadi (2018) investigated the lateral performance of helical piles with a single helix that varied in core diameter and embedment depth installed in sand using centrifuge model tests and finite element analysis. The lateral load capacity of piles was improved by 5–7.5% with a D_h/D_s of 2.5–3.3 and a helix embedment of 90% of the critical depth (where

plastic bending occurs). The lateral load capacity was improved by 15–22% at a helix embedment of 10% of the critical depth. Moreover, the lateral load capacity was improved marginally by increasing the D_h/D_s from 2.5 to 3.3.

El Naggar et al. (2005) modelled the response of offshore piles subjected to earthquake load using the BNWF method in the OpenSEES program. The procedure proposed by Matlock (1970), Reese and Welch (1975) and O'Neill and Murchison (1983) was used to generate the *p-y* springs for piles in soft clay, stiff clay and sand layers. The result from the numerical model compared reasonably well with centrifuge model tests. Guo et al. (2014) simulated the lateral soil-pile interaction of an H-pile in sandy soil in the OpenSEES program using the BNWF method. The soil resistance along the pile was modelled by *p-y* and *t-z* springs, and the soil resistance at the base was modelled by a *q-z* spring. The *p-y* spring from API (1993) and Reese et al. (1974) provided a reasonable load-displacement curve. However, the lateral stiffness and the ultimate load capacity were slightly underestimated. Li (2016) investigated the lateral soil-pile interaction of helical piles using field testing and the BNWF method. The soil resistances, including lateral, shaft and overturning, were represented by *p-y* springs, *t-z* springs and *q-z* springs. The numerical model was calibrated against the experimental tests in Sakr (2009) and Prasad and Narasimha Rao (1996). A chart of the lateral load capacity improvement as a function of helix embedment was provided. The lateral load capacity improvement for piles in cohesionless soil increased with helix embedment. It peaked at a helix embedment up to 36% of the pile length, and it was negligible below a depth equivalent to 90% of the pile length. The lateral load capacity improvement of piles in cohesive soil was the highest at a helix embedment of about 6% of the pile length, and it decreased with embedment depth. The role of overburden stress was noted in the case of helices embedded in cohesionless soil. Also, the lateral load capacity improved by embedding the helix at a depth where the bending moment was high. It was noted that the lateral load capacity could be

improved by increasing the helix diameter up to the point where the torsional strength of the pile shaft is not exceeded (Tsuha et al. 2007).

Overall, the previous research using numerical models of helical piles suggests that the lateral load capacity can be improved by embedding the helix at a shallow depth, where the bending moment along the pile shaft is typically the greatest. The lateral load capacity can also be improved by increasing the helix diameter relative to the shaft diameter. However, the improvement may only be observed at a large displacement. Although the previous research can aid our understanding of the lateral behavior of micro screw piles, there is still a need to investigate the lateral behavior of micro screw piles because the overall geometry and shape of the pile is different. Moreover, a numerical study that considers the various soil-pile interactions, including the lateral shaft, the vertical shaft, the thread bearing and the lateral shaft interactions, of micro screw piles has not been conducted.

6.2.2. Soil-pile Interactions and Soil Springs

In the present research, numerical models that considered the various soil-pile interactions of screw micropiles subjected to lateral load were developed in the OpenSEES program using the BNWF method. Specifically, the lateral shaft resistance, the vertical shaft resistance and the lateral thread resistance were represented by a series of zero-length elements with lateral *p*-*y*, vertical *t*-*z* and vertical *t*-*z* uniaxial spring material models, respectively. The thread bearing resistance was represented by a series of zero-length section elements with nonlinear fiber-sections to generate the thread bearing or overturning reaction with the *q*-*z* uniaxial spring material model assigned to each fiber. The vertical shaft resistance and the lateral thread resistance were modelled by *t*-*z* uniaxial spring materials. It should be noted that the lateral thread resistance is denoted by the t_h-*y* spring material in the next section for the convenience of showing the direction of the resistance;

however, it was in principle represented using *t-z* spring materials in the OpenSEES program. Details about these soil springs are provided as follows.

6.2.2.1. The Lateral Shaft Resistance – *p-y* spring

The lateral shaft resistance of piles in cohesive soils was represented by a series of *p-y* springs as described by Equation 6-1 as per Matlock (1970):

$$\frac{p}{p_{ult}} = 0.5\left(\frac{y}{y_{50}}\right)^{1/3} \tag{6-1}$$

where

$$y_{50} = 2.5\varepsilon_{50}d \tag{6-2}$$

where p and y are the lateral shaft stress and displacement, p_{ult} is the ultimate lateral shaft resistance, y_{50} is the lateral displacement corresponding to half of the ultimate lateral resistance, ε_{50} is the strain of the clay corresponding to half of s_u and d is the diameter of the pile shaft. The recommended values of ε_{50}, as a function of s_u, are shown in Table 6.1. The ultimate lateral shaft resistance was defined in Equation 6-3:

$$p_{ult} = N_p s_u d \tag{6-3}$$

where the coefficient N_p for wedge failure close to the ground surface was defined as in Equation 6-4:

$$N_p = 3 + \frac{\gamma'}{s_u}z + \frac{J}{d}z < 9 \tag{6-4}$$

where z is the depth below the ground surface, γ' is the effective unit weight of soil and J is a constant equal to 0.5 for soft clays (Matlock 1970) and 1.5 for stiff clays (Bhushan et al. 1979) and was interpolated for clays of different consistency. The coefficient N_p is equal to 9 for flow failure at great depth (Matlock 1970).

Table 6.1. Strain ε_{50} corresponding to half of s_u (Matlock 1970).

s_u	ε_{50}
0–24	0.02
24–48	0.01
48–96	0.007
96–192	0.005
192–384	0.004
> 384	0.001996

For piles in cohesionless soils, the lateral shaft resistance was represented by *p-y* springs as described in Equations 6-5 and 6-6 (API 1993):

$$p = \bar{A}\, p_{ult} \tanh\left(\frac{kz}{\bar{A}\, p_{ult}} y\right) \tag{6-5}$$

$$\bar{A} = (3 - 0.8z/d) \geq 0.9 \tag{6-6}$$

where $\bar{A}$ is the adjustment coefficient for static loading condition, and k is the initial subgrade modulus (refer to API 1993). The ultimate lateral shaft resistances based on wedge failure (p_{st}) and flow failure (p_{sd}) were defined as follows:

$$p_{st} = (C_1 \cdot z + C_2 \cdot d)\gamma' \cdot z \tag{6-7}$$

$$p_{sd} = C_3 \cdot d \cdot \gamma' \cdot z \tag{6-8}$$

$$C_1 = \frac{K_0 \tan(\phi)\sin(\beta)}{\tan(\beta-\phi)\cos(\phi/2)} + \frac{\tan^2(\beta)\tan(\phi/2)}{t\,an(\beta-\phi)} + K_0 \tan(\beta)(\tan(\phi)\sin(\beta) - \tan(\phi/2)) \tag{6-9}$$

$$C_2 = \frac{\tan(\beta)}{\tan(\beta-\phi)} - K_a \tag{6-10}$$

$$C_3 = K_0 \tan(\phi)\tan^4(\beta) + K_a(\tan(\beta) - 1) \tag{6-11}$$

where β=45+ϕ_p'/2, K_0 is the horizontal coefficient of earth pressure at rest, and K_a is the horizontal coefficient of earth pressure at active condition. The value of y_{50} was calculated from Equation 6.5. The value of p_{ult} is the smaller of p_{st} and p_{sd}. The backbone curves of the *p-y* springs for the lateral shaft resistances in sand and clay are shown in Figure 6.1a.

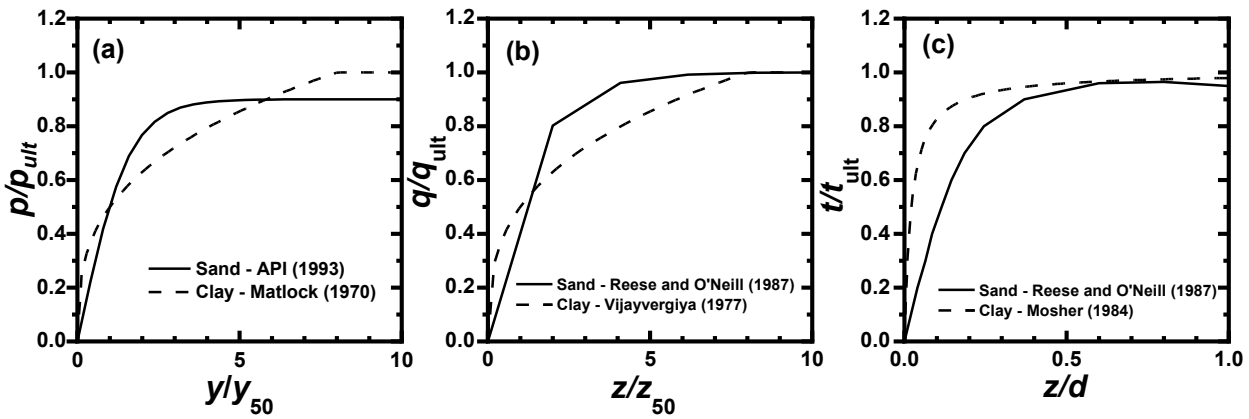

Figure 6.1. Backbone curve of the springs: (a) *p-y* spring, (b) *t-z* spring and (c) *q-z* spring.

6.2.2.2. The Vertical Shaft Resistance and the Lateral Thread Resistance – *t-z* springs

For piles in cohesive soils, the vertical shaft and the lateral thread resistances of soils were represented by *t-z* springs as per Equations 6-12 and 6-13 (Boulanger et al. 2003):

$$t^e = C_e \frac{t_{ult}}{z_{50}} z^e \tag{6-12}$$

$$t^p = t_{ult} - (t_{ult} - t_0^p)\left[\frac{c \cdot z_{50}}{c \cdot z_{50} + (z^p - z_0^p)}\right]^n \tag{6-13}$$

where t_{ult} is the ultimate vertical shaft resistance, z_{50} (or z_{50t}) is the vertical displacement corresponding to half of the ultimate vertical shaft resistance, t^e and t^p are the elastic and plastic components of the shaft stress, t_o^p and z_o^p are the plastic components of the shaft stress and vertical

displacement at the start of the current plastic loading and z^e and z^p are the elastic and plastic components of the vertical displacement, respectively. For piles in clay, Boulanger et al. (2003) used a value of 0.5 for c, 1.5 for n and 0.708 for C_e based on Reese and O'Neill (1987).

The ultimate vertical shaft resistance was defined as in Equation 6-14:

$$t_{ult} = \alpha s_u \tag{6-14}$$

where α is the adhesion coefficient provided by Tomlinson (1957). Coyle and Reese (1966) provided the normalized shaft stress to t_{ult} with vertical displacement, as shown in Figure 6.2. The value of z_{50t} was selected from curve I, which represented soil-pile interaction from the ground surface to 3 m below. Curve II represents soil-pile interaction from 3 m to 6 m, and curve III represents soil pile interaction below 6 m of the ground surface.

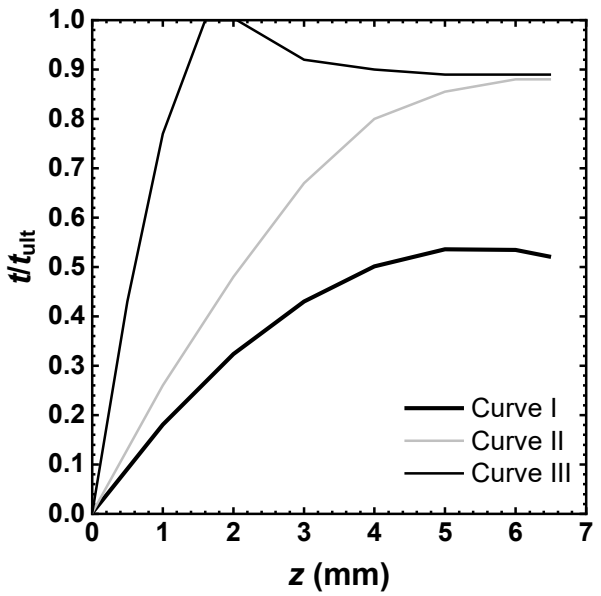

Figure 6.2. Normalized shaft stress vs. axial displacement in clay (after Coyle and Reese 1996).

For piles in cohesionless soils, the vertical shaft and lateral thread resistances of soils were represented as *t-z* springs based on Mosher (1984). The *t-z* spring was defined as in Equation 6-15:

$$t = \frac{z}{1/k_f + z/t_{ult}} \tag{6-15}$$

where t and z are the vertical shaft stress and displacement, and k_f is related to sand's friction angle (Mosher and Dawkins 2000). The value of k_f as a function of the friction angle of sand based on Mosher and Dawkins (2000) is shown in Table 6.2. The ultimate vertical shaft resistance was obtained as in Equation 6-16:

$$t_{ult} = \sigma_v^{'} K_s \tan(\delta) \tag{6-16}$$

where δ is the soil-pile interface friction angle taken as 0.8 times ϕ_p, and K_s is obtained from Castello (1980). The value of z_{50t} was back-calculated from Equation 6-15. The backbone curves of the *t-z* springs for the vertical shaft and the lateral thread resistances in sand and clay are shown in Figure 6.1b.

Table 6.2. Values of k_f versus the friction angle of sand (Mosher and Dawkins 2000).

Friction Angle (°)	k_f (kPa/mm)
28–31	11–19
32–34	19–26
35–38	26–34

6.2.2.3. The Thread Bearing Resistance – *q-z* spring

For piles in cohesive soils, Boulanger et al. (2003) used 0.35 for c, 1.2 for n and 0.2 for C_e based on Reese and O'Neill (1987). The ultimate thread bearing resistance (q_{ult}) was defined as in Equation 6-17:

$$q_{ult} = N_c s_u \tag{6-17}$$

where N_c is the end-bearing capacity factor that is equal to 9. The vertical displacement (z_{50q}), corresponding to half of the ultimate thread bearing resistance, is recommended to be 0.8% of the pile thread diameter by Reese and O'Neill (1987).

The thread bearing resistance in cohesionless soils was represented by the *q*-*z* spring, as in Equation 6-18 (Vijayvergiya 1990):

$$\frac{q}{q_{ult}} = \left(\frac{z}{z_c} \right)^{1/3} \tag{6-18}$$

where z_{cq} is the vertical displacement corresponding to when the stress starts to maintain a constant value, and it is equal to 3 to 9% of the pile diameter (Vijayvergiya 1977). The ultimate thread bearing resistance was defined in Equation 6-19:

$$q_{ult} = N_q \sigma_v^{'} \tag{6-19}$$

where N_q is the bearing capacity factor (Meyerhoff 1976). The backbone curves of the *q*-*z* springs for piles in sand and clay are shown in Figure 6.1c.

6.3. Development of the Numerical Models

The numerical models were developed to simulate the lateral behavior of micro screw piles in the OpenSEES program using the BNWF method. This approach used existing structural elements (e.g., displacement-based fiber beam-column elements to model shafts) to model the pile and some special elements (e.g., zero-length element or zero-length section elements to model well-established soil springs) to model the soil springs. Additionally, the required uniaxial material models for the pile shaft and well-established soil springs were available in the OpenSEES program. Further modelling details are provided in the sections below.

The lateral responses of the six piles tested in Sherwood Park, the 22 piles in South Campus and the 18 piles in Sandpit were obtained from numerical simulations. The lateral loading of the

micro screw pile was simulated by performing displacement-controlled static analyses. The lateral displacement was applied at an increment of 0.1 mm to the maximum displacement that was measured in the field.

6.3.1. Pile Shaft

The pile shaft was modelled using displacement-based fiber beam-column elements, which were defined with two nodes, each having three degrees of freedom (DOF) in the two-dimensional FE model: one horizontal, one vertical and one rotational DOF. This element follows standard finite element procedures where the displacement field was interpolated using classical Hermitian polynomials. An example of the second order classical Hermitian polynomial with 3 corresponding nodes is shown in Appendix E. As shown in Figure 6.3, the pile shaft was discretized into a number of beam elements with a length of 50 mm. Three Gauss-Legendre integration points were used for each element, and each integration point was assigned a nonlinear fiber section. Each fiber section was discretized into nine subdivisions (fibers) in the radial direction and 36 subdivisions (fibers) in the circumferential direction. All the fibers were assigned a uniaxial Giuffre-Menegotto-Pinto steel material model (Carreno et al. 2020) with Young's modulus of 210 GPa, a yield strength of 248 MPa and a post-yield isotropic strain hardening ratio of 0.1. The tapered shaft was modelled as a series of discrete uniform shafts with progressively decreasing diameters. Compared to other models for piles based on the BNWF method in the literature (Li 2016, Guo et al. 2004, Kurian and Shah 2009, El Naggar et al. 2005), the present models used fiber beam-column elements, which allow consideration of the nonlinearity of material fibers over the cross-section. By doing so, the models were able to capture the pile shaft's yielding more accurately than the common method used in the literature.

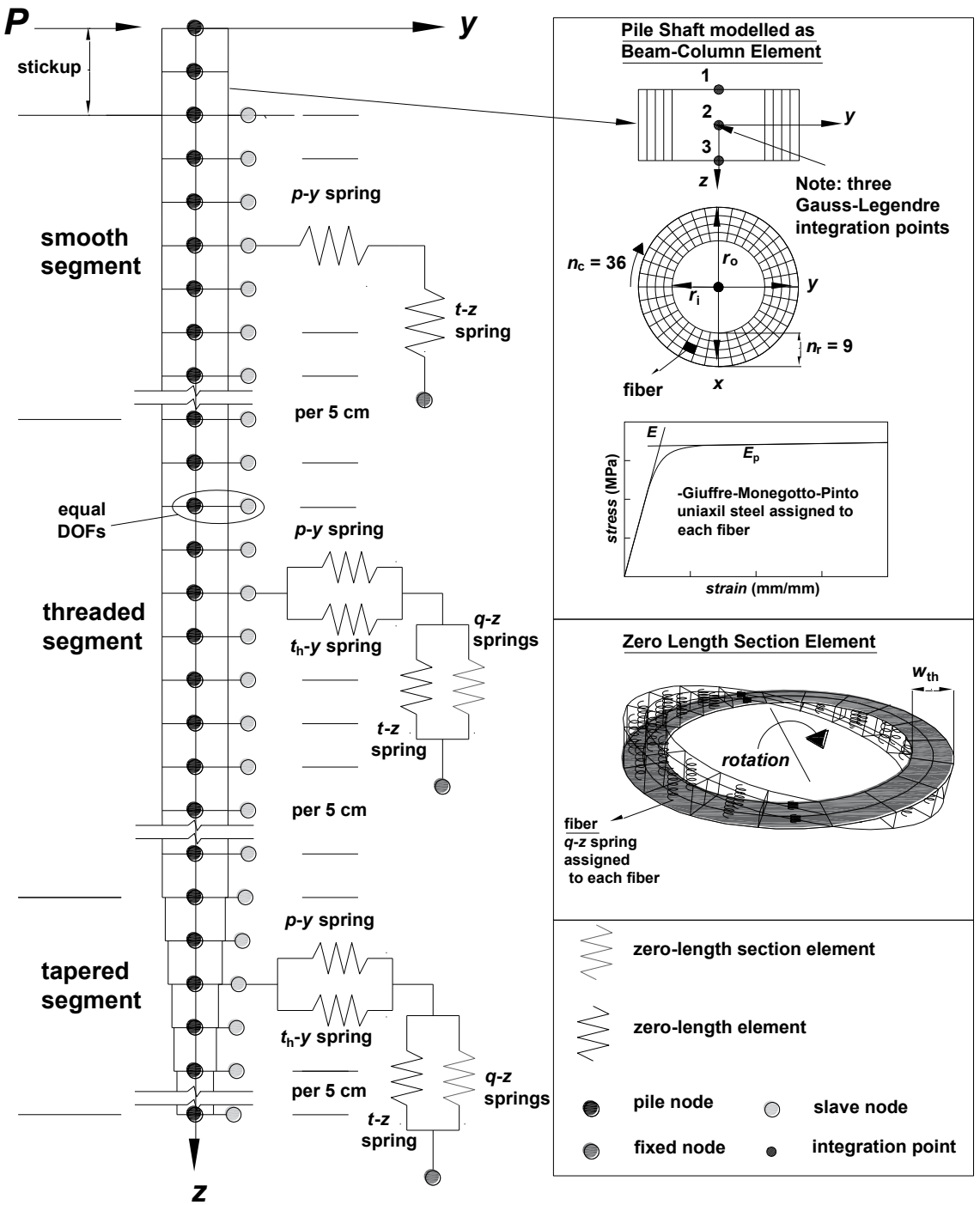

Figure 6.3. Configuration of the soil-pile interactions in the numerical models developed in OpenSEES program. Note: w_{th} = width of threads, n_r = the number of fiber in radial direction and n_c = the number of fibers in circumferential direction. The drawing is not to scale.

6.3.2. Soil-pile Interactions

The different soil-pile interaction mechanisms for micro screw piles are shown in Figure 6.4. The lateral shaft reaction, the vertical shaft reaction, the thread bearing reaction and the lateral thread reactions were represented by a series of zero-length elements with *p-y*, *t-z*, *q-z* and *t-z* (or t_h-*y,* where *h* and *y* stand for the lateral direction) uniaxial springs materials. The thread bearing reaction was represented by a series of zero-length section elements with fibers, and the *q-z* uniaxial spring material was assigned to each fiber. Each zero-length element was connected to a corresponding pile shaft node via a slave node on one side, and it was connected to a corresponding soil side on the other side via a node that was fixed against all DOF (see Fig. 6.3). These elements had a virtual-zero length as the slave, pile and fixed nodes were defined to have the same location (or coordinates).

The lateral shaft reaction was defined based on a series of zero-length elements placed horizontally along the pile shaft. The *p-y* spring materials assigned to the zero-length elements were defined based on Matlock (1970) for piles in cohesive soils. The recommended ε_{50}, as a function of s_u, are shown in Table 6.1. The parameter *J* was set at 0.5 for soft clays (Matlock 1970) and at 1.5 for stiff clays (Bhushan et al. 1979). The *p-y* spring materials were defined based on API (1993) for piles in cohesionless soils. The initial subgrade modulus was provided by API (1993). The values of y_{50} were calculated from the equation provided in API (1993) for the p-y springs. The mechanism of the lateral shaft reaction is shown in Figure 6.4a.

The vertical shaft reaction was defined based on a series of zero-length elements placed vertically along the pile shaft. The *t-z* spring materials assigned to zero-length elements were defined based Boulanger et al. (2003) for piles in cohesive soils. The ultimate vertical shaft resistances were defined based on the adhesion coefficient provided by Tomlinson (1957). Boulanger et al. (2003) used a value of 0.5 for *c*, 1.5 for *n* and 0.708 for C_e to construct the *t-z*

springs based on Reese and O'Neill (1987). The parameter z_{50t} was selected from the normalized shaft stress vs. axial displacement provided by Coyle and Reese 1996. The *t-z* spring materials were defined using the relationship provided by Mosher (1984). The recommended values of k_f, as a function of the friction angle of sand were given by Mosher and Dawkins (2000). The ultimate vertical shaft resistances were defined based on K_s provided by Castello (1980), and the values of z_{50t} were back-calculated from the relationship provided by Mosher (1984). The mechanism of vertical shaft reaction is shown in Figure 6.4b.

The thread bearing reaction was defined based on a series of zero-length sectional elements placed vertically along the pile shaft. The continuous thread was modelled by a series of flat discs, which is a common convenience for piles with helices (e.g., Knappet et al. 2014 and Al-Baghdadi 2018). Al-Baghdadi (2018) showed that the inclination of the helix has a minor effect on the lateral behaviour of the screw pile. The zero-length section elements had inner radii equal to the pile outer radii and outer radii equal to the pile outer radii plus the width of the thread, which is 12 mm. The elements were assigned fiber sections, which were discretized into nine subdivisions (fibers) in the radial direction and 36 subdivisions (fibers) in the circumferential direction. The *q-z* spring materials were assigned to each subdivision. The *q-z* spring materials were defined based on Boulanger (2003) for piles in cohesive soils. The parameters c, n and C_e were set to 0.35, 1.2 and 0.2 based on Reese and O'Neill (1987). The *q-z* spring materials were defined based on Vijayvergiya (1990) for piles in cohesionless soils. The parameter z_{cq} was equal to 3 to 9% of the pile diameter (Vijayvergiya 1977). The parameter N_q was defined by Meyerhoff (1976). The mechanism of the thread bearing reaction where soil stress could develop at individual fibers upon pile rotation or axial movement is shown in Figure 6.4c. This method to model the thread bearing reaction is innovative.

The lateral thread reaction was defined by a series of zero-length elements placed horizontally along the pile shaft. The *t-z* spring materials assigned to zero-length elements were defined using the same method used for the vertical shaft reaction. The t_{ult} was obtained by multiplying the lateral thread stress with the actual thread's top and bottom surface area for each pile depth interval. The mechanism of the lateral thread reaction is shown in Figure 6.4b. Furthermore, this mechanism has not been modelled previously based on the limited literature review.

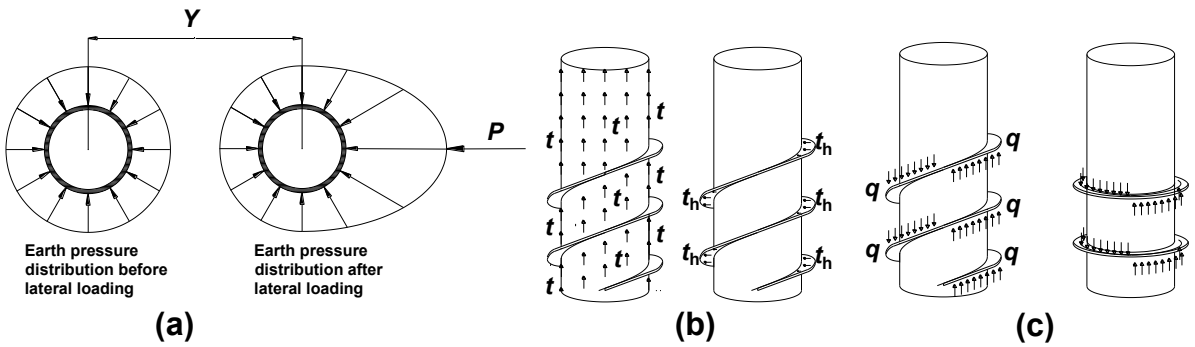

Figure 6.4. Schematics of soil-pile interaction mechanisms during lateral loading: (a) the lateral shaft resistance, (b) the vertical shaft resistance and the lateral thread resistance and (c) the thread bearing resistance.

The spring materials were defined in the OpenSEES program by assigning appropriate soil type (clay or sand) and input parameter, such as the ultimate soil loads (p_{ult}, t_{ult} and q_{ult} in terms of force) and displacement corresponding to half of the ultimate loads. The ultimate soil resistances (or stress), such as p_{ult}, t_{ult} and q_{ult}, were multiplied by the surface area of the shaft and thread, respectively. The required soil parameters, such γ, s_u for clayey and γ, D_r and ϕ'_p for sandy soil, were interpreted from the CPT readings. Several CPTs were conducted at each site, including two CPTs at Sherwood Park, seven CPTs at South Campus and four CPTs at Sandpit. At South Campus, the CPT-7 reading was selected as it was least affected by tree roots. The average of

CPT-1 and CPT-2 was used for soils at Sherwood Park as the two CPT readings were identical. At Sandpit, the CPT-3 reading was used because it was least affected by ground frost.

6.3.3. Verification of the Pile Shaft Model using Elastic Solution

A simple numerical model was developed in the OpenSEES program to simulate the response of a uniform and smooth pile shaft, as shown in Figure 6.5. Pile P1 was modelled as described in Section 6.3.1 without any soil reaction springs. The pile shaft was modelled by a series of discrete displacement-based fiber beam-column elements. The pile shaft was discretized into a number of beam elements with a length of 50 mm. For each element, three Gauss-Legendre integration points were assigned a nonlinear fiber section. Each fiber section was discretized into nine subdivisions (fibers) in the radial direction and 36 subdivisions (fibers) in the circumferential direction. Each fiber was assigned a uniaxial Giuffre-Menegotto-Pinto steel material with isotropic hardening. The pile shaft was fixed at one end, and a transverse load (P) was applied at the free end.

To verify the pile shaft model, the numerical model results were compared with analytical calculation. Based on the elastic solution, the deflection at the free end (Y) and deflection $y(x)$ along the pile shaft were calculated using Equations 6-20 and 6-21 (Beer et al. 2006):

$$Y = -\frac{PL^3}{3EI} \tag{6-20}$$

$$y(x) = \frac{P}{6EI}(-(L-x)^3 + 3L^2(L-x) - 2L^3) \tag{6-21}$$

The graphs of P vs. Y and y vs. L obtained from the numerical model and analytical calculation are shown in Figure 6.6. It seems that the result of the numerical model is comparable with the analytical calculation. Therefore, the numerical model accurately predicts the pile response at least within the elastic range.

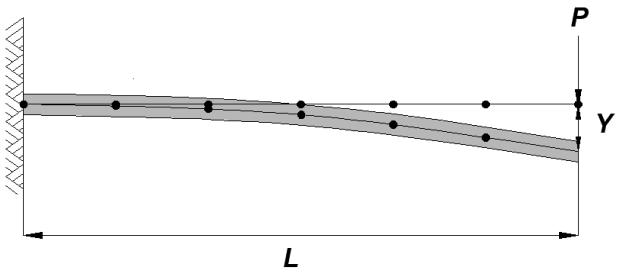

Figure 6.5. A uniform, smooth pile shaft in the OpenSEES program with the same diameter and thickness as pile P1.

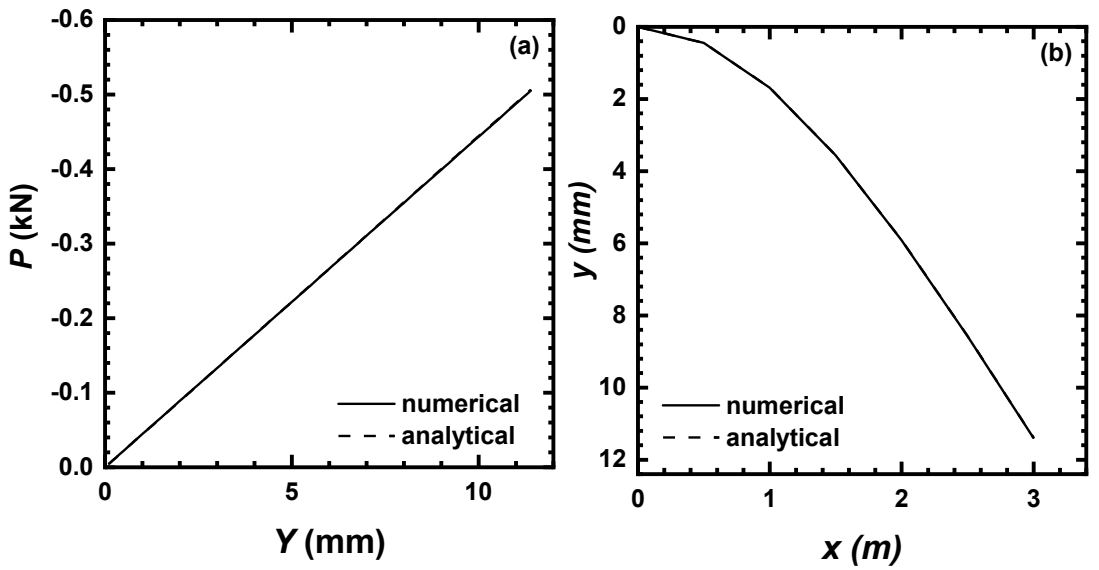

Figure 6.6. Comparing the uniform smooth pile displacement results obtained using the numerical model and analytical method: (a) *P* vs. *Y* at the free end and (b) deflection *y* distribution along the pile shaft.

6.4. Results of the Numerical Models

The numerical models were built to simulate the lateral response of the six piles tested at the three sites. In total, the six piles tested at Sherwood Park, the 22 piles tested at South Campus and the 18 piles tested at Sandpit were simulated. In the following sections, the results and findings of

selected piles are shown. The lateral vs. displacement curve of each pile type at the three sites is presented. The pile shaft and soil response of the instrumented pile P6 at Sherwood Park; piles P1, P3 and P5 at South Campus; and P1 and P4 at Sandpit are presented. Piles P1 and P4 were selected as they have different diameters and lengths.

6.4.1. Load versus Displacement Curves

The predicted and measured lateral load vs. displacement curves (P vs. Y curve) of the six piles tested at Sherwood Park are shown in Figure 6.7. The predicted and measured P vs. Y curves of the piles at this site are relatively comparable. The measured initial stiffnesses of piles P2, P5 and P6 are predicted relatively accurately. The measured initial stiffnesses of piles P1 and P4 are smaller than the predicted initial stiffnesses. The measured initial stiffness of pile P3 is under-predicted. The small measured initial stiffnesses of piles P1 and P4 can be due to the presence of a soil cavity near the pile-head, which was observed for some piles after pile installation. However, the post-yield stiffnesses of all piles, except P5 and P6, are predicted relatively accurately because the soil cavity was closed upon lateral loading. The measured P vs. Y curves of piles P5 and P6 exhibit a slightly softening load with increasing displacement, which can be due to either soil or pile failure resulting in the yielding of the soil-pile interaction mechanisms. Perhaps this is expected as piles P5 and P6 are slenderer than the other piles. Alternatively, it can be due to the strain-softening behaviour of the stiff clay fill layer. However, the predicted P vs. Y curves of piles P5 and P6 do not exhibit a slightly softening load with increasing displacement because the soil was modelled based on Matlock (1970), which does not consider this.

To verify the accuracy of the numerical models, the predicted and measured $P_{u\text{-}Y}$ and $P_{u\text{-}DB}$ of the six test piles at Sherwood Park, where $P_{u\text{-}Y}$ and $P_{u\text{-}DB}$ has been defined in Chapter 5, are summarized and compared in Figure 6.10a. The predicted $P_{u\text{-}Y}$ is 18% greater than the measured

$P_{u\text{-}Y}$ on average. However, the predicted $P_{u\text{-}DB}$ is 20% less than the measured $P_{u\text{-}DB}$ on average. This means that the numerical models generally overpredict the measured $P_{u\text{-}Y}$ and underpredict the measured $P_{u\text{-}DB}$. On the other hand, the numerical models reasonably predict the unloading response of the pile at this site.

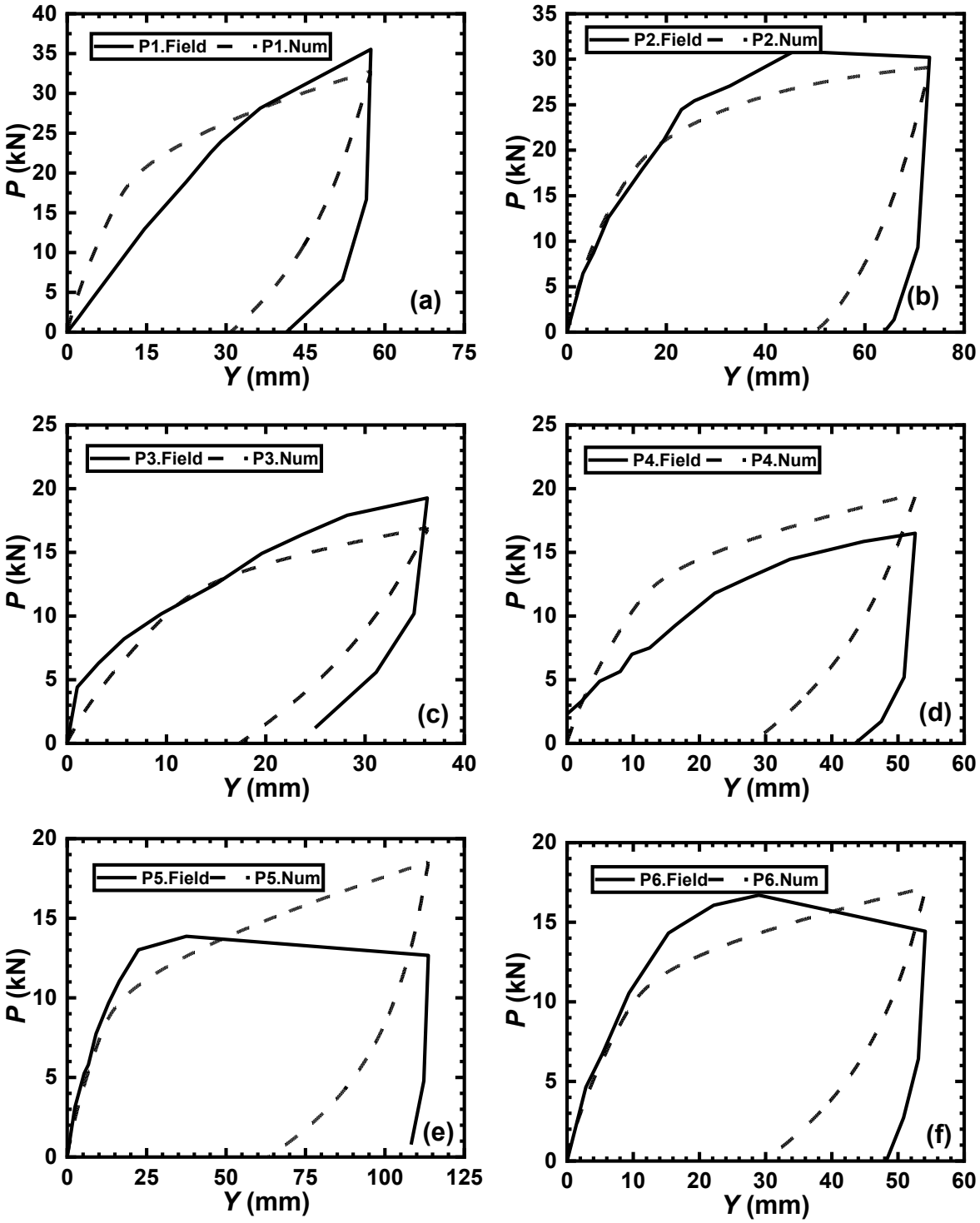

Figure 6.7. Lateral load vs. displacement curves of piles: (a) to (f) for P1 to P6 at Sherwood Park obtained from the numerical models and field tests.

The predicted and measured P vs. Y curves of the piles at South Campus are in substantial agreement aside from minor deviations, as shown by the P-Y curves of selected piles in Figure 6.8. The predicted and measured initial and post-yield stiffnesses of the P vs. Y curves of the piles are similar. The predicted and measured $P_{u\text{-}Y}$ and $P_{u\text{-}DB}$ of the 22 test piles are shown in Figure 6.10a. The predicted $P_{u\text{-}Y}$ is 17% greater than the measured $P_{u\text{-}Y}$ on average, and the predicted $P_{u\text{-}DB}$ is only 4% greater than the measured $P_{u\text{-}DB}$ on average. The numerical models overpredict the pile response at a small displacement and predict quite accurately at a larger displacement. It should be noted that Guo and Deng (2018) reported an adhesion coefficient significantly smaller than the adhesion coefficient suggested by Randolph and Murphy (1985) and Tomlinson (1957). This was associated with the expansion and disturbance of the soil surrounding the smooth segment because of the torsional installation, and the smooth segment had a smaller external diameter than the threaded segment. The annular cavity was also observed in the field following the pile installation. This loss of contact between the soil and pile along the smooth segment can be the reason that the measured $P_{u\text{-}Y}$ is smaller than the predicted $P_{u\text{-}Y}$. Puri et al. (1984) and Bagheri and El Naggar (2013, 2015) reported on the soil's slicing by the helix of the helical pile during pile installation. This reduced the soil's shear strength and the pile's lateral load capacity. However, Jeffrey et al. (2016) reported an increase in radial stress around the pile as it was installed to compensate for this reduction. Notably, the numerical models predict the $P_{u\text{-}DB}$ accurately as the soil cavity was closing upon lateral displacement at a later stage. The other reason that the numerical models predict the measured $P_{u\text{-}DB}$ of the test piles at South Campus better than Sherwood Park is because the soil at South Campus is made of Glacier Lake Edmonton lacustrine clay, which can be represented by Matlock (1970).

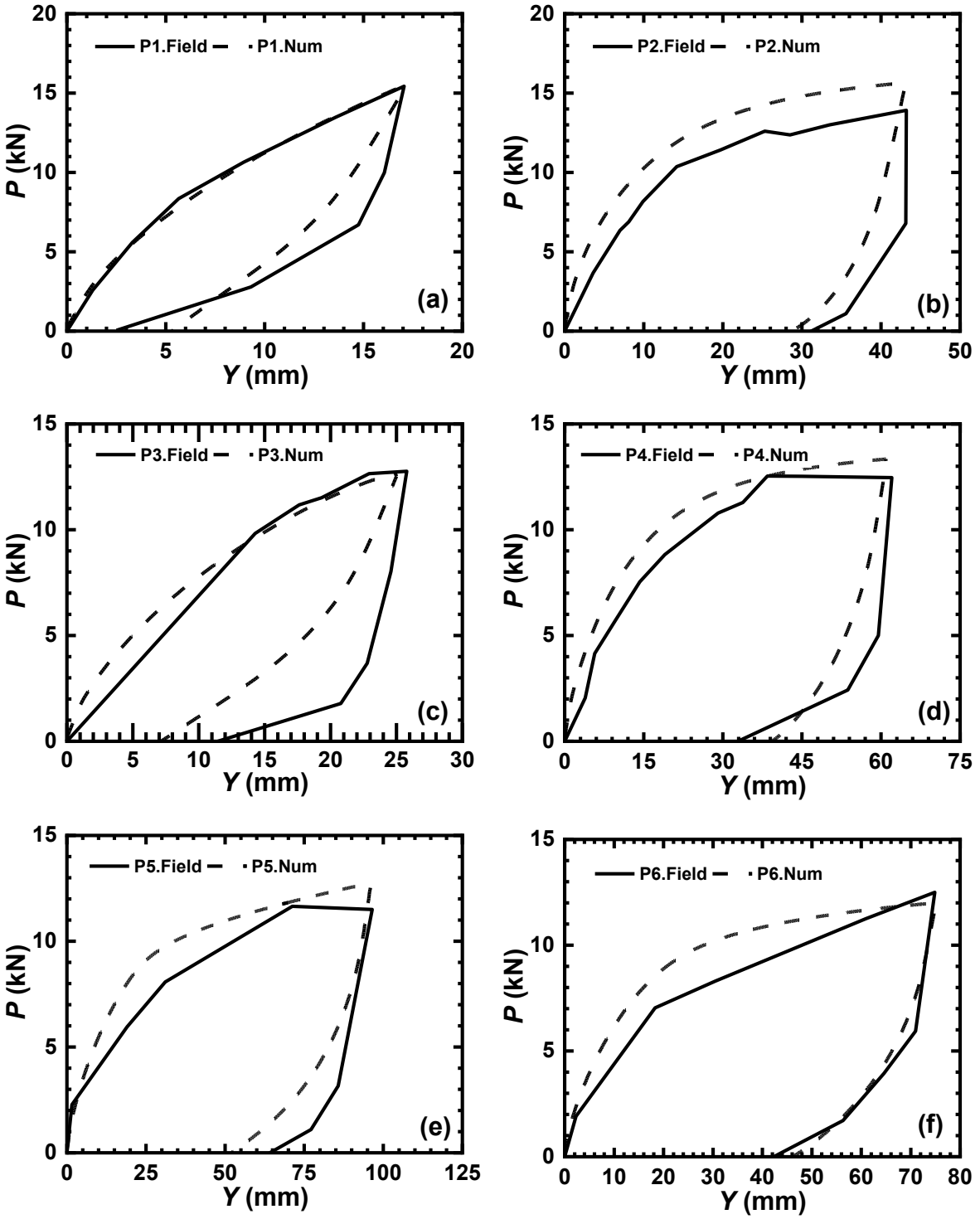

Figure 6.8. Lateral load vs. displacement curves of piles: (a) to (f) for P1 to P6 at South Campus obtained from the numerical models and field tests.

Generally, there is some agreement between the predicted and the measured P vs. Y curves of piles at Sandpit, as shown by the P vs. Y curves of selected piles in Figure 6.9. The numerical models overpredict the initial stiffnesses of all the piles except for P2. The small measured initial stiffnesses can be due to the presence of a sand cavity around the pile. Although a cavity in sand is not usually considered because sand may slip and slough in the cavity, it is possible in compact sand due to sand arch. The numerical models predict the measured post-yield stiffnesses of piles P1, P3 and P5 (3 m long) relatively accurately and under-predict the measured post-yield stiffnesses of piles P2, P4 and P6 (1.5 m long). The predicted P vs. Y curves of these piles has plateaued, but the measured P vs. Y curve has not. The reason could be that the piles in the numerical models had failed as short piles earlier than they should. The flattening of the P vs. Y curve is due to the yielding of soil reactions springs as the pile rotates. The predicted and measured $P_{u\text{-}Y}$ and $P_{u\text{-}DB}$ of the 18 test piles are summarized in Figure 6.10b. The predicted $P_{u\text{-}Y}$ of the 18 piles is 32% greater than the measured $P_{u\text{-}Y}$ on average. The predicted $P_{u\text{-}DB}$ of the nine long piles is 25% less than the measured $P_{u\text{-}DB}$ on average. The numerical models also predict the unloading response of the pile at this site quite accurately.

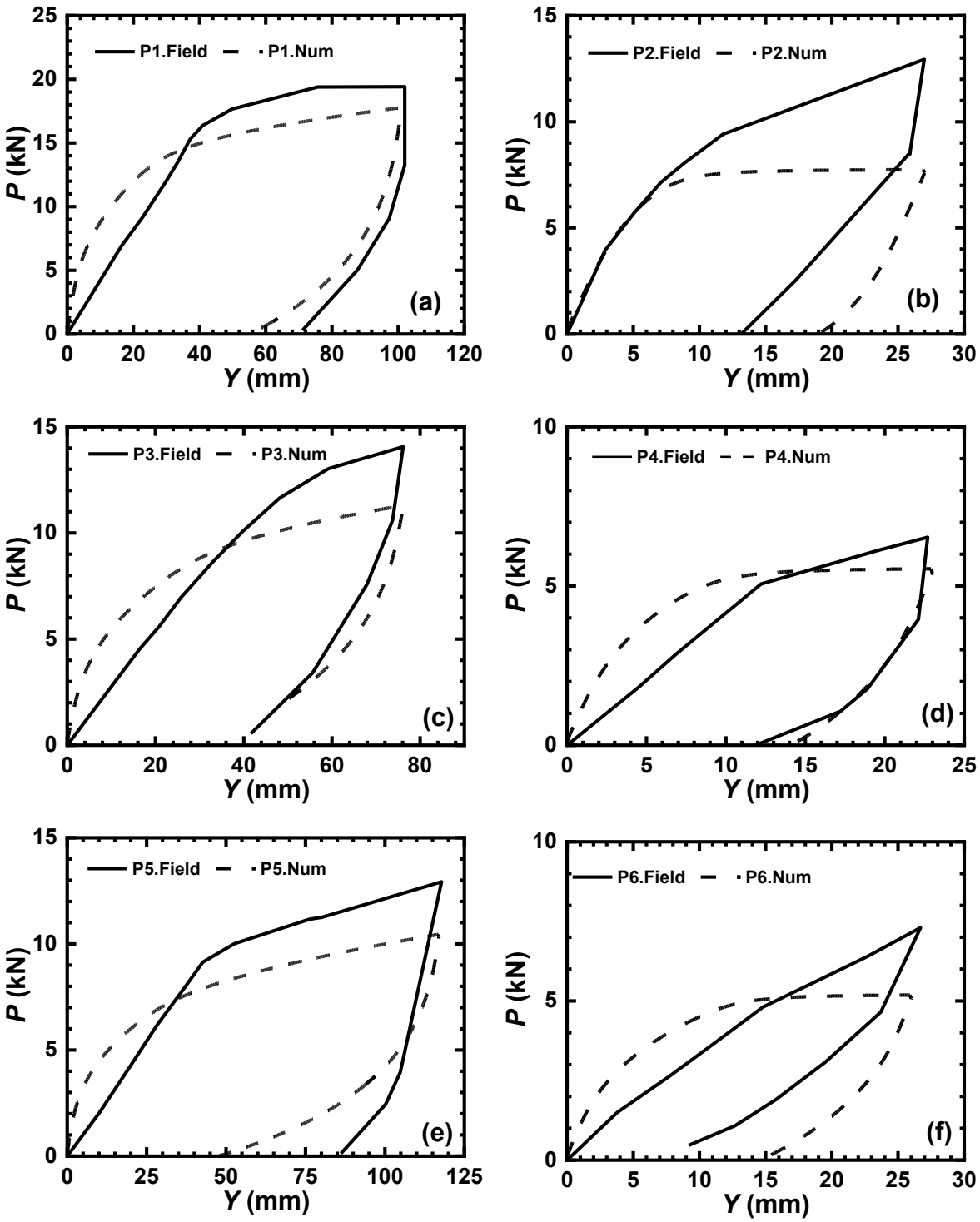

Figure 6.9. Lateral load vs. displacement curves of piles: (a) to (f) for P1 to P6 at Sandpit obtained from the numerical models and field tests.

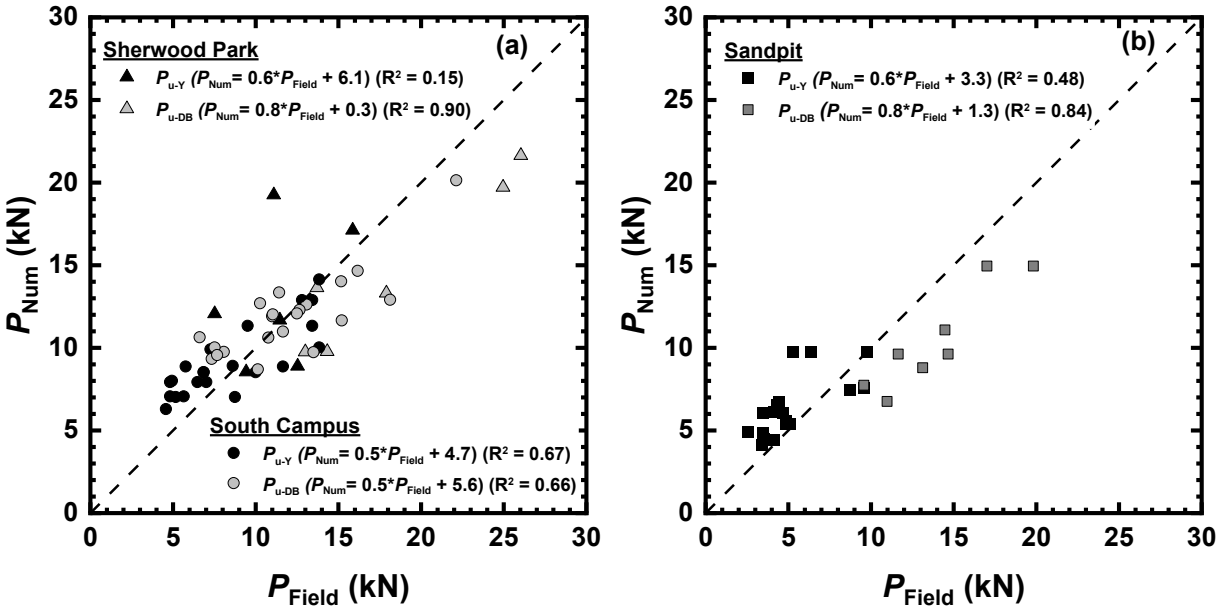

Figure 6.10. Summary of the ultimate lateral load capacities of piles obtained using the numerical modelling and field tests at the three sites: (a) Sherwood Park and South Campus and (b) Sandpit.

Based on the comparison of the predicted and the measured *P* vs. *Y* curves and the ultimate lateral load capacity of the piles at the three sites, the following conclusions are made:

- The numerical models predict the measured *P* vs. *Y* curves of the piles relatively accurately. The measured initial stiffnesses of some piles are smaller than the predicted initial stiffnessess due to the presence of soil cavities . However, the post-yield stiffnessess and $P_{u\text{-}DB}$ of all piles are reasonably predicted once the soil cavities have closed.
- Therefore, the numerical models predict the measured $P_{u\text{-}DB}$ much better than $P_{u\text{-}Y}$. The numerical models predict the $P_{u\text{-}DB}$ of the piles at South Campus better than the piles at Sherwood Park because the soil at South Campus is made of Glacier Lake Edmonton lacustrine clay, which can be better represented by Matlock (1970).

- The numerical models predict the unloading P vs. Y curves of the piles at Sherwood Park and South Campus accurately, and the prediction of the unloading P vs. Y curves of the piles at Sherwood park is also similar.
- In general, the numerical models suitably simulated the lateral response of the micro screw piles, especially at larger lateral displacement.

6.4.2. Pile Shaft and Soil Responses

This section shows the pile shaft and soil responses of selected piles of different lengths (1.5 and 3 m long) tested at the three sites. The pile shaft and soil responses include the lateral displacement (y), cross-sectional plane rotation of the shaft (dy/dx), bending moment (M), shear force long pile shaft (V) and lateral soil-shaft stress (p). The bending moment M is compared with the M_y and M_p of the pile shaft, and lateral soil-shaft stress is compared with ultimate lateral soil-shaft stress (p_{ult}) to assess failure mode. The values of p_{ult} are calculated using Matlock (1970) for cohesive soils and API (1993) for cohesionless soils. The soil parameters are interpreted from the CPT readings. The distributions of the pile shaft and soil responses along pile P6 at Sherwood Park; P1, P3 and P5 at South Campus; and P1 and P4 at Sandpit are shown in Figures 6.11 to 6.16.

The predicted deformation of the pile has the qualitative representative shape of a long pile under the free-head condition. The predicted and measured distribution of the M of pile P6 at Sherwood Park and P1, P3 and P5 at South Campus are shown in Figure 6.11 and Figure 6.12c–6.14c. The bending moment is zero at the pile head. The predicted maximum moment (M_{max}) along pile P6 at Sherwood Park and piles P1, P3 and P5 at South Campus exceeds M_y and M_p at pile depths of 0.6 m (=$7D_s$) and 0.8 m ($7D_s$), corresponding to $Y_{u\text{-}DB}$, which is the displacement corresponding to the lateral load capacity of the pile according to DeBeer's method. This is another way that shows that the pile has yielded, especially for pile P6 at Sherwood Park, where M_{max} is

lower than M_y. The measured M_{max} of pile P6 at Sherwood Park and P1 and P3 at South Campus is reached at pile depths of 0.55 m ($7D_s$), 0.84 m ($7D_s$) and 0.89 m ($10D_s$), respectively. The predicted M_{max} of piles P1 and P3 at South Campus is 7% and 1% greater than the measured M_{max}. The measured and predicted M at a certain pile depth increases rapidly up to the corresponding $Y_{Y\text{-}DB}$ as the pile was deforming elastically. Later, the predicted M increases slowly because the pile was yielding. The predicted M reaches a minimal value at a pile depth of 1.2 m ($16D_s$). The predicted M of piles P1, P3 and P5 reaches a minimal value at pile depths of 1.95 m ($17D_s$), 1.85 m ($21D_s$) and 1.8 m ($24D_s$), respectively. The measured M reached a minimum value at pile depths of 0.91 ($12D$s), 2.5m ($22D_s$), 1.8 ($20D_s$) and 1.8 m ($24D_s$), respectively. Generally, the numerical models accurately predict the M_{max} and location of the M_{max} of the piles at South Campus quite accurately, as can be seen by similarities between the measured and predicted distribution of M. There is some divergence between the predicted and the measured distribution of M of pile P6 at Sherwood Park.

The predicted displacement of pile and soil response can be used to assess the pile failure mode. The mechanism of long pile failure for a free-headed pile in cohesive soils is shown in Figure 5.3. A long pile with the free-head condition fails when a plastic hinge is formed at some distance f below the ground surface. A short pile under the free-head condition generally rotates as a rigid body with minimal deformation. As shown in Figures 6.11–6.14, the distributions of y and dy/dx are the highest near the pile head and are minimal near the pile base. In addition, it can be seen that either the soil does not fail at all or that the soil located within a small pile depth interval has failed by examining the y and p with y_{ult} and p_{ult}. Therefore, it can be seen that the piles fail as long piles (or flexibly pile) as the pile deformation and displacement resemble the qualitative representative shape of long piles and that the soil failed within a small depth interval.

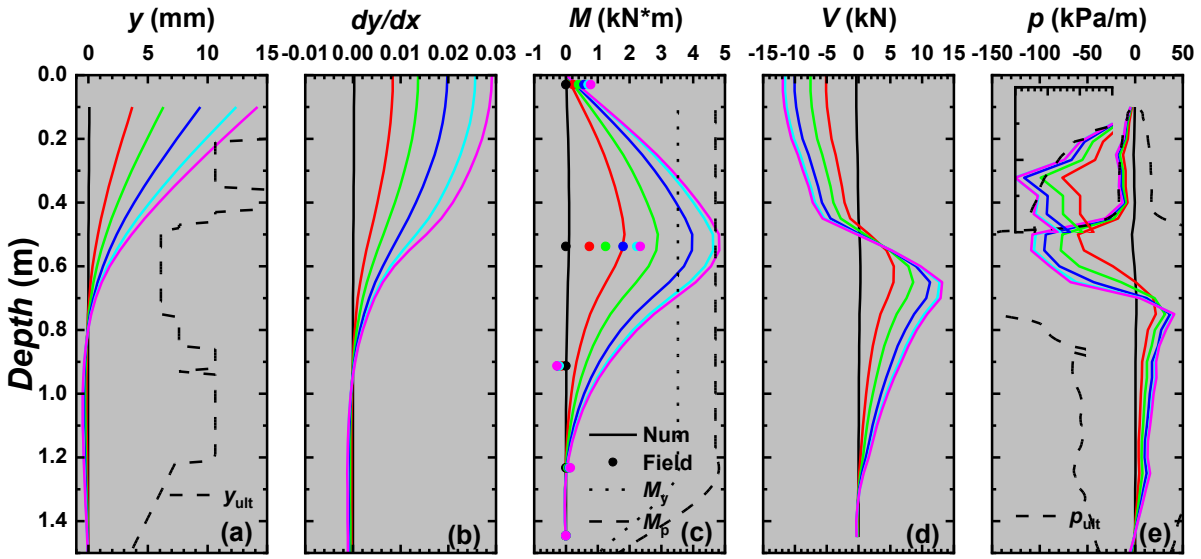

Figure 6.11. The distributions of the (a) lateral displacement, (b) pile shaft cross-sectional plane rotation, (c) bending moment, (d) shear force, and (e) lateral soil-shaft stress of pile P6 at Sherwood Park. Note: The pile exhibited a long pile failure mode.

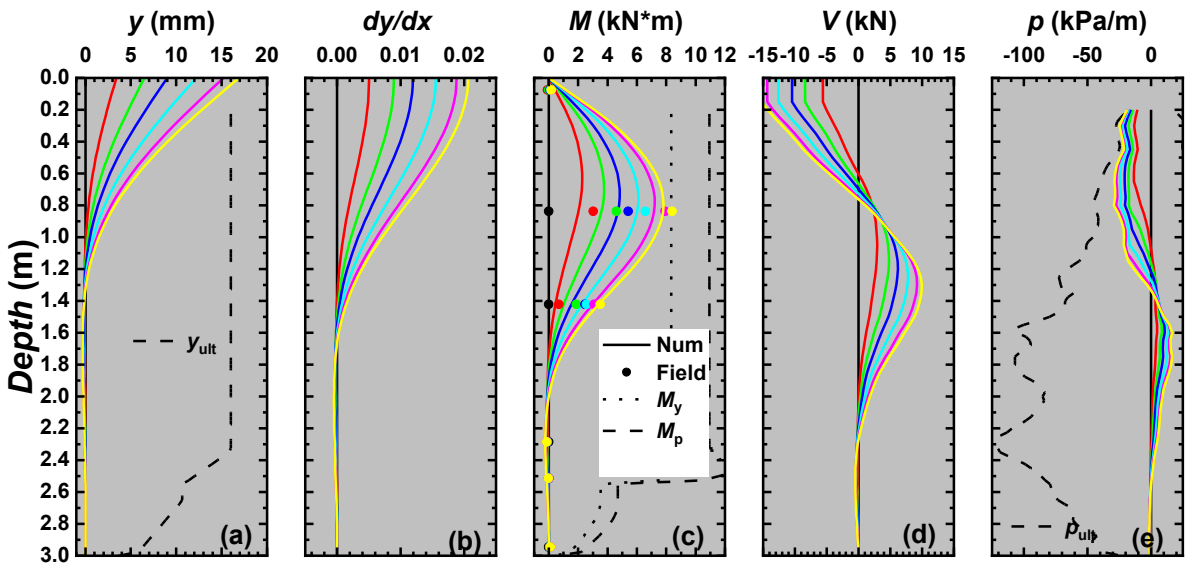

Figure 6.12. The distributions of the (a) lateral displacement, (b) pile shaft cross-sectional plane rotation, (c) bending moment, (d) shear force and (e) lateral soil-shaft stress of pile P1 at South Campus. Note: The pile exhibited a long pile failure mode.

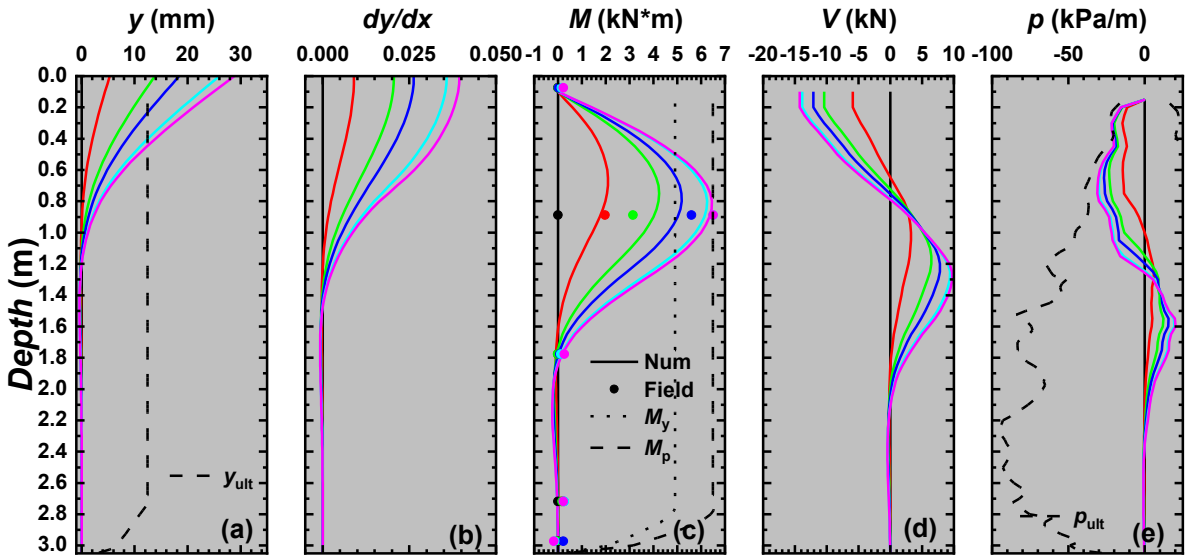

Figure 6.13. The distributions of the (a) lateral displacement, (b) pile shaft cross-sectional plane rotation, (c) bending moment, (d) shear force and (e) lateral soil-shaft stress of pile P3 at South Campus. Note: The pile exhibited a long pile failure mode.

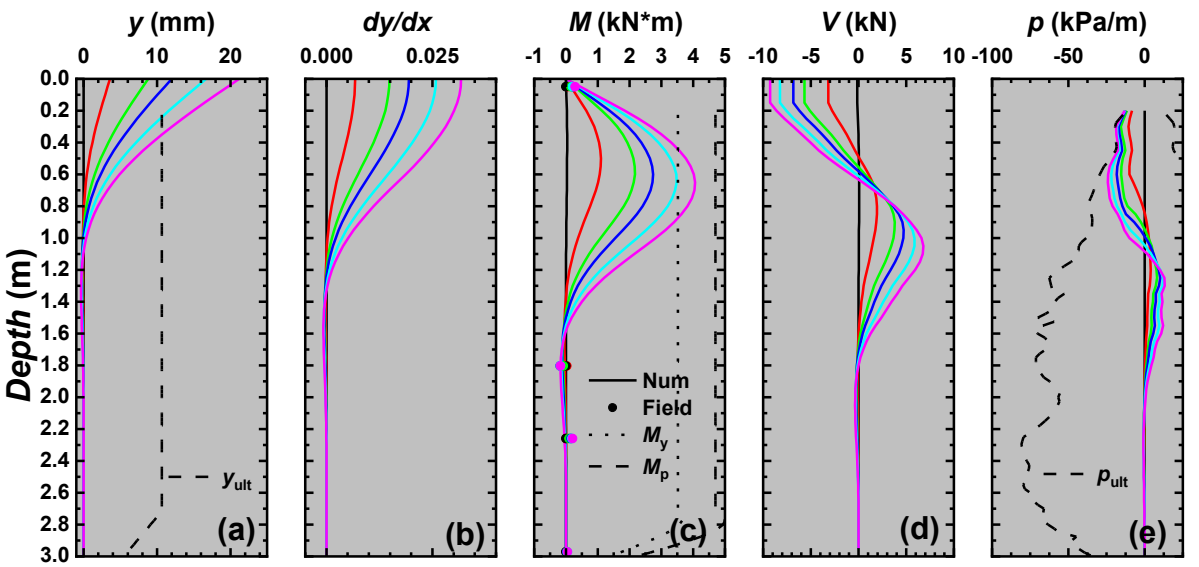

Figure 6.14. The distributions of the (a) lateral displacement, (b) pile shaft cross-sectional plane rotation, (c) bending moment, (d) shear force and (e) lateral soil-shaft stress of pile P5 at South Campus. Note: The pile exhibited a long pile failure mode.

The predicted distribution of the M of the instrumented pile P1 at Sandpit has the qualitative representative shape of a long pile under the free-head condition, as shown in Figure 6.15c. The predicted M is zero at the pile head; it reaches the M_{max} that exceeds M_p at a pile depth of 1.1 m ($9D_s$) and a minimal M at a pile depth of 2.35 m ($21D_s$). It can be seen that the pile has yielded. The distance to M_{max} (f) is measured in the field to be used for numerical model verification. The distance f was measured to be 0.9 m ($8D_s$), and it appears that the numerical model predicts the distance f quite accurately, as shown in Figure 6.15c. Also, the distributions of y and dy/dx are highest near the pile head and are minimal near the pile base. However, from the distribution of p, it seems that almost all of the soil has failed except for the soil at a pile depth ranging from 1.4 m to 1.7 m, where y was near zero. Therefore, pile P1 at Sandpit can also be classified as a transitional pile with mixed behavior as both the pile and soil have failed.

The predicted pile shaft and soil response of pile P4 have the qualitative representative shape of a short pile under the free-head condition. As shown in Figure 6.16c, M reaches M_{max} at a pile depth of 0.8 m ($9D_s$) and reaches a minimal M at a pile depth of 1.5 m ($17D_s$). The predicted M_{max} is less than M_y, indicating that the pile did not fail. The distributions of y and dy/dx are the highest near the pile head but are significant near the pile base, which shows that the pile is rotating. Although the pile experiences some bending, it has not failed. Based on the distribution of p, it seems that almost all the soil springs have reached p_{ult} except for the soil at a pile depth ranging between 1.1 m and 1.2 m, where y is near zero. Therefore, pile P4 at Sandpit can be classified as a short pile because the pile rotates without yielding, and the soil fails throughout the pile depth.

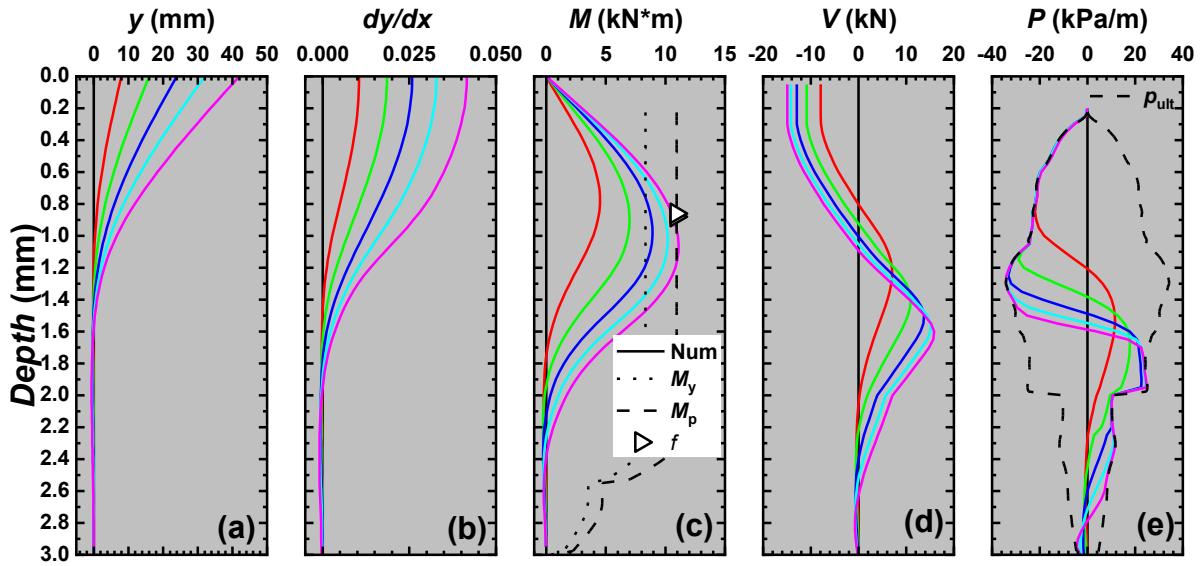

Figure 6.15. The distributions of the (a) lateral displacement, (b) pile shaft cross-sectional plane rotation, (c) bending moment, (d) shear force and (e) lateral soil-shaft stress of pile P1 at Sandpit. Note: The pile exhibited a transitional failure mode.

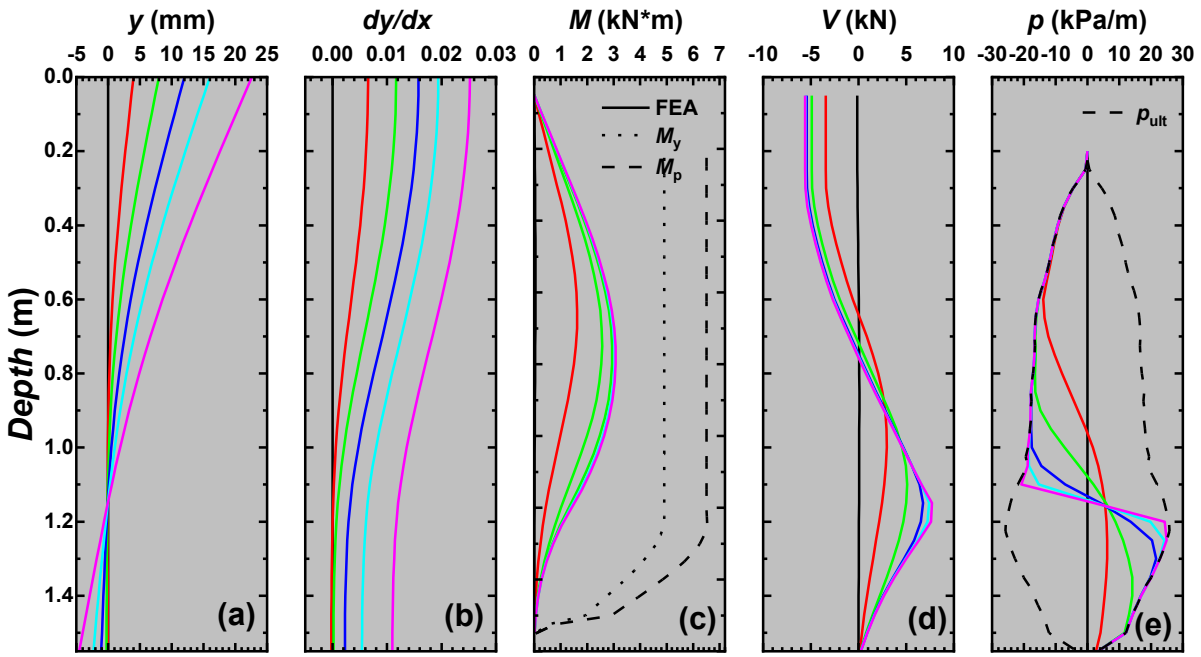

Figure 6.16. The distributions of the (a) lateral displacement, (b) pile shaft cross-sectional plane rotation, (c) bending moment, (d) shear force and (e) lateral soil-shaft stress of pile P4 at South Campus. Note: The pile exhibited a short pile failure mode.

Based on the pile shaft and soil responses of the selected pile, the following conclusions are drawn:

- The numerical models predict M_{max} and the location of M_{max} and the failure mode of the instrumented piles P1 and P3 at South Campus quite accurately. There is a significant divergence in the predicted and measured distribution of the M of pile P6 at Sherwood Park. This could perhaps be due to a thin layer of stiff clay fill.
- Pile P6 at Sherwood Park and P1, P3 and P5 at South Campus exhibit the characteristic of a long pile loaded under the free-head condition. The distribution of M is small near the pile head. It increases to a maximum value at a pile depth of $7D_s$. It decreases to a minimal value at a pile depth of $16D_s$ along the pile at Sherwood Park and at a pile depth ranging from $17D_s$ to $24D_s$ along the piles at South Campus, respectively. The piles at Sherwood Park and South Campus fail structurally as the M_{max} exceeds M_y. The predicted distribution of M is comparable to the measured distribution of M.
- The numerical models predict the distance f of pile P1 at Sandpit measured in the field. Pile P1 exhibits a mixed behaviour of long pile and short pile as both the pile and soil failed.
- Pile P4 exhibits the characteristic of a short pile because the pile rotates without yielding, and the soil failed throughout the pile depth.
- In general, the numerical models suitably simulate the pile shaft and soil response of the micro screw piles that are consistent with the lateral load field test results.

6.4.3. Mobilization of the Various Soil-pile Interactions

In this section, the lateral shaft, the vertical shaft, the thread bearing and the lateral thread reactions in the middle of each segment type, including smooth, threaded and tapered segments, of pile P6 at Sherwood Park, P1 at South Campus and P1 and P4 at Sandpit are be examined to show the

mobilization of various soil-pile interactions. These piles are selected as they have different lengths (1.5 m and 3 m) and are installed in different sites.

The mobilization of the lateral shaft, the vertical shaft, the thread bearing and the lateral thread reactions at the middle of each segment type of pile P6 at Sherwood Park are shown in Figure 6.17. At the middle of the smooth segment, a lateral thread stress of -14 kPa/mm, just below the ultimate stress of -16 kPa/mm, is developed, corresponding to a lateral displacement of 6 mm. Although the lateral displacements at the middle of the threaded (y = -0.5 mm) and the tapered (y = -0.1 mm) segments are small, the lateral thread stresses in the middle of the threaded (21 kPa/mm) and the tapered (8 kPa/mm) segments are significant. As the pile is mainly displaced laterally, the vertical displacement of the pile is minimal even though the pile is subjected to bending. Therefore, a negligible downward vertical shaft stress is developed in the middle of the smooth segment (-0.3 kPa) and a negligible upward vertical shaft stress is developed in the middle of the threaded (0.1 kPa) and the tapered (0.1 kPa) segments. Also, the thread bearing reactions at the middle of the threaded and the tapered segments are small because the cross-sectional plane rotations are minimal ($dy/dx = 0.01$). Minor lateral thread stresses of 8 kPa and 2 kPa are developed at the middle of the threaded and the tapered segments, corresponding to -0.5 mm and -0.1 mm, respectively. These stresses are equivalent to 0.65 kN and 0.04 kN over the entire threaded and tapered segments. Aside from the threaded and tapered segments experiencing small lateral displacements, the surface area of the thread is also small. Therefore, the lateral shaft reaction has the most significant contribution to the lateral response of this pile. A minor contribution comes from the lateral thread reactions and the contribution of the vertical shaft, and the thread bearing reactions are negligible.

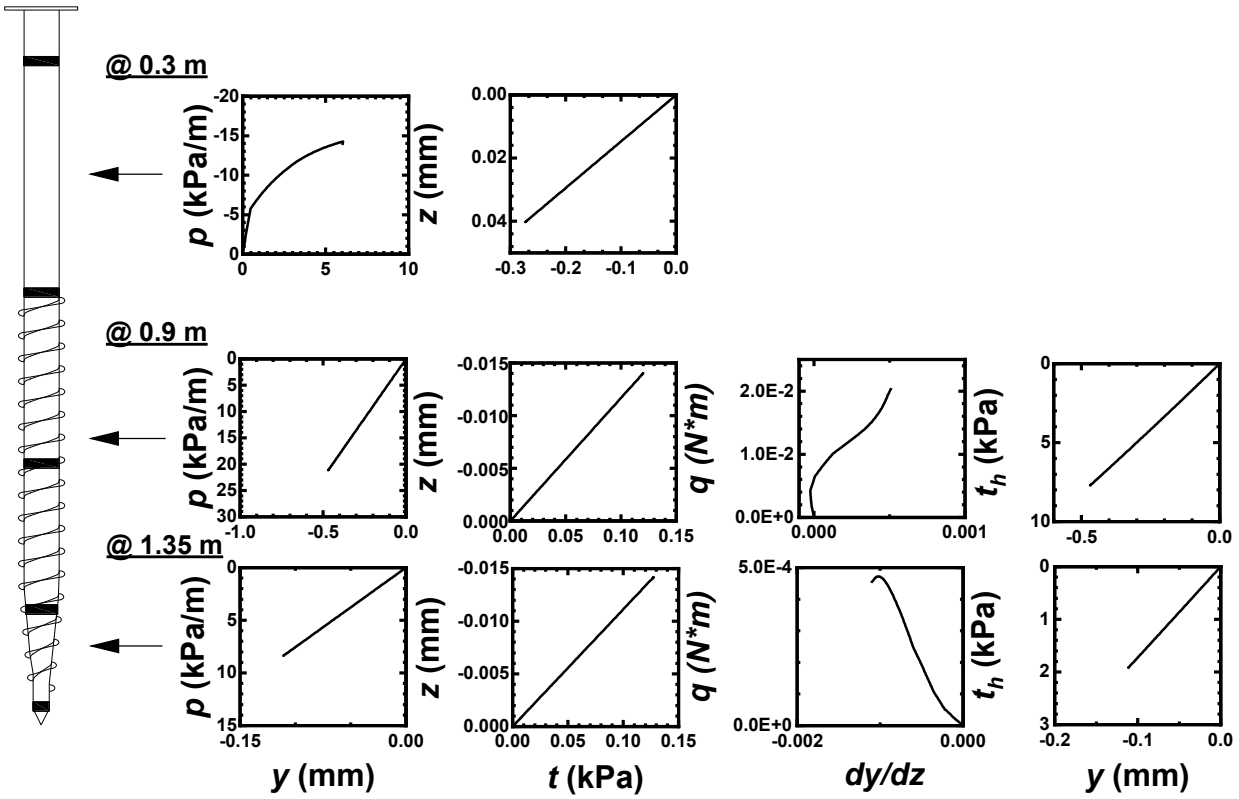

Figure 6.17. The lateral shaft reaction, the vertical the shaft reaction, the thread bearing reaction and the lateral thread reaction of pile P6 installed at Sherwood Park.

The lateral shaft, the vertical shaft, the thread bearing and the lateral thread reactions at the middle of each segment type of pile P1 at South Campus are shown in Figure 6.18. As pile P6 (Fig. 6.17) at Sherwood Park and pile P1 (Fig. 6.18) at South Campus both behave as long piles and the soils in which it they were embedded have similar strengths, the contribution of the individual reactions to the overall pile response is similar. Except that the tapered segment of pile P1 at South Campus is situated at a greater pile depth (2.65 m), the contribution of lateral shaft reactions (-0.9 kPa) at the middle of the tapered segment is minor as the lateral displacement is very small (0.02 mm).

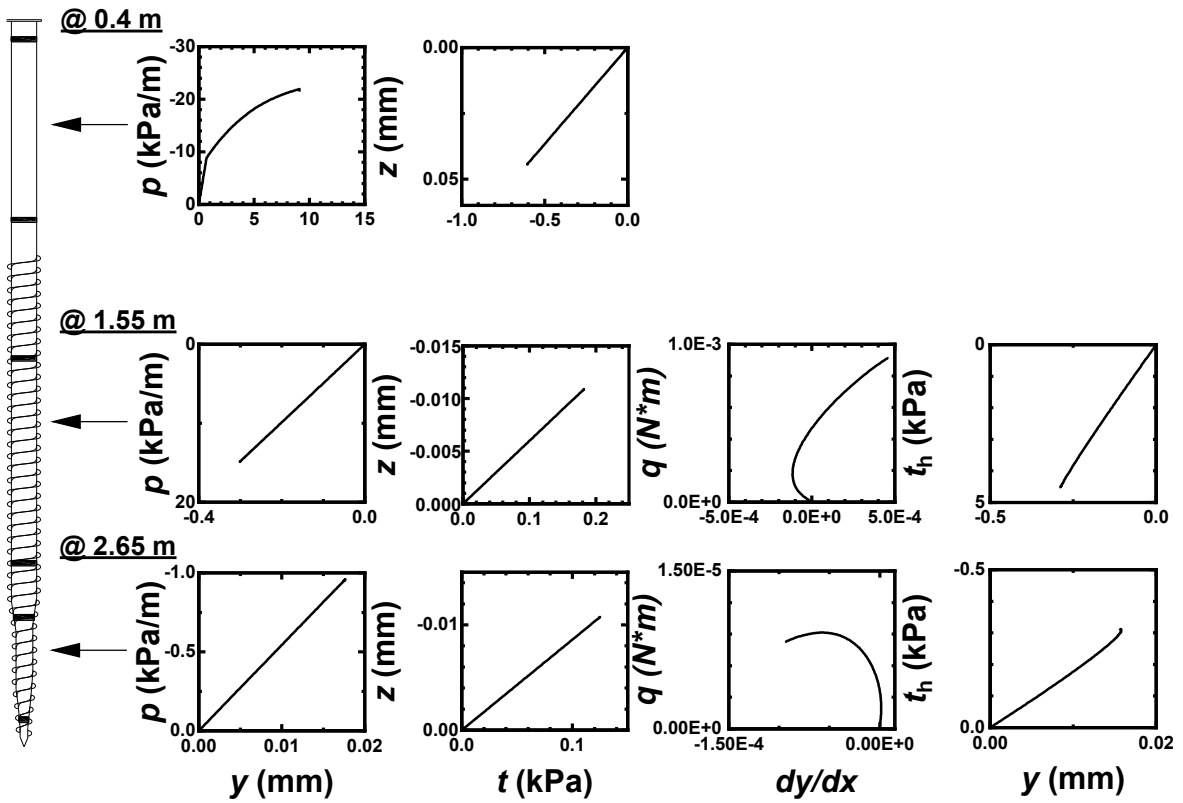

Figure 6.18. The lateral shaft reaction, the vertical shaft reaction, the thread bearing reaction and the lateral thread reaction of pile P1 installed at South Campus.

The lateral shaft, the vertical shaft, the thread bearing and the lateral thread reactions at the middle of each segment type of pile P1 at Sandpit are shown in Figure 6.19. A lateral shaft stress of -12 kPa/mm is developed at the middle of the smooth segment that is laterally displaced by 26 mm that had reached ultimate stress of 12 kPa/mm. All other components exhibit linear stress vs. displacement behavior, indicating that pile P1 exhibits the long pile failure mode, similar to the piles shown in Figures 6.17 and 6.18.

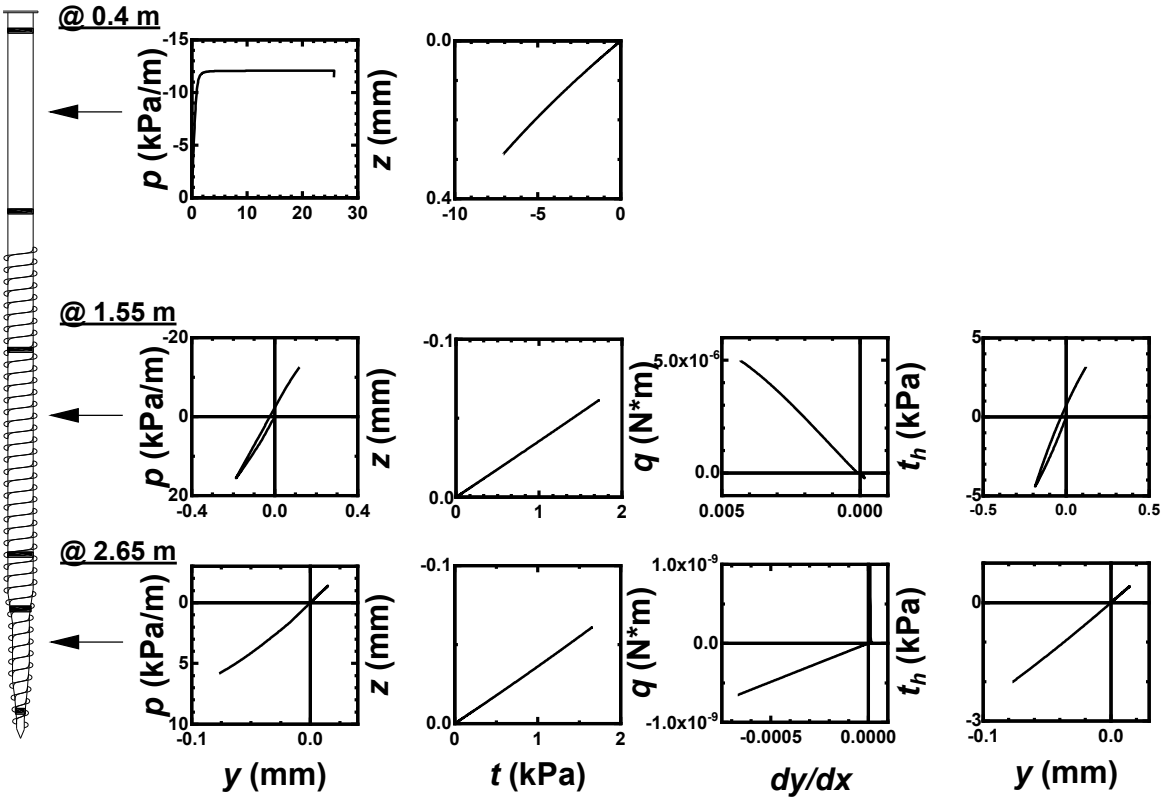

Figure 6.19. The lateral shaft reaction, the vertical shaft reaction, the thread bearing reaction and the lateral thread reaction of pile P1 installed at Sandpit.

The lateral shaft, the vertical shaft, the thread bearing and the lateral thread reactions at the middle of each segment type of pile P4 at Sandpit are shown in Figure. 6.19. The lateral shaft stress along the pile reaches the ultimate stress. As discussed in Section 6.4.2, pile P4 tested at Sandpit behaves as a short pile. Therefore, the soil is displaced sufficiently along the pile length except near the rotational axis. The lateral thread stresses in the middle of the threaded and tapered segments are -9 kPa and 16 kPa, corresponding to 3 mm and -3 m, respectively. A greater lateral thread reaction is mobilized along pile P4 compared to the other pile because the pile experiences greater lateral displacement near the pile base. Although the lateral thread stress over the threaded and tapered segments is equivalent to 0.9 kN and 0.3 kN, it is minor because of its short length.

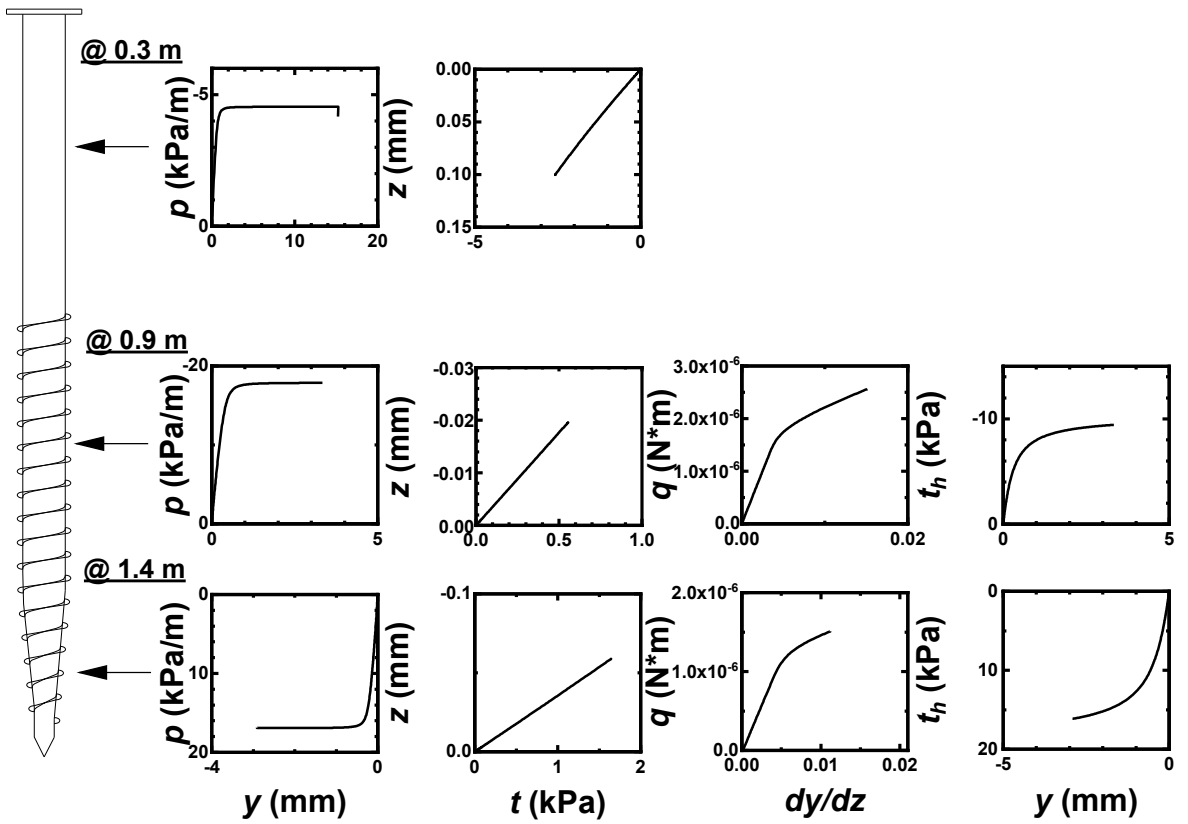

Figure 6.20. The lateral shaft reaction, the vertical shaft reaction, the thread bearing reaction and the lateral thread reaction of pile P4 installed at Sandpit.

Based on the predicted mobilization of various soil-pile interactions, the following conclusions may be drawn:

- Generally, large lateral shaft stress is developed along the piles. The largest lateral shaft stress is developed near the pile head, where the pile's lateral displacement is the largest. Significant lateral shaft stress is also developed near the base of the short pile.
- As the piles are mainly displaced laterally, the vertical shaft and the thread bearing reactions are negligible.
- Minor lateral thread stresses are developed at the threaded and the tapered segments. Greater lateral thread reactions are developed at the threaded and the tapered segments of the short pile

because the pile experiences greater lateral displacement near the pile base. Although the lateral thread stress is significant, it translates to minor force due to the small surface area of the thread.

- Therefore, the lateral response of the pile is mainly influenced by the lateral shaft reaction. The lateral response is slightly affected by the lateral thread reactions, and the contribution of the vertical shaft and the thread bearing reactions are negligible.

6.5. Sensitivity Analyses

A sensitivity analysis of pile P3 in clayey soil and sandy soil was carried out using the numerical model to examine the effect of the soil properties, the thread and the pile stickup on the lateral response. Initially, the lateral response of pile P3 in soil with benchmark soil properties, original thread and pile stickup was obtained. Then, the soil properties were varied to some commonly occurring ranges to examine which parameter had the greatest effect on the lateral response. Similarly, the effects of increasing the thread width and the addition of thread along the smooth segment were evaluated. Given that the test piles were embedded in the ground with different stickups, the effect of different stickups had to be verified. Then, the lateral response of the pile was obtained by changing the soil properties to certain commonly occurring values. The sensitivity, in terms of the percentage difference, of the ultimate lateral load capacity was defined as follows:

$$\eta = \left(\frac{P_{u-Y} - P_{u-Y0}}{P_{u-Y0}} \right) 100\% \tag{6-22}$$

where $P_{\text{u-Y0}}$ is the benchmark $P_{\text{u-Y}}$. The results of the sensitivity analysis including the P vs. Y curves and $P_{\text{u-Y}}$ of pile P3 in clayey soil are shown in Figure 6.21a and Table 6.3. Pile $P_{\text{u-Y}}$ is reduced by 40.2% when s_{u} is decreased to 50 kPa, and it is increased by 48.5% when s_{u} is increased to 100 kPa. The $P_{\text{u-Y}}$ does not change when γ' is decreased to 16 kN/m^3 or increased to 20 kN/m^3.

It can be seen that the lateral load capacity of the micro screw pile is significantly changed when s_u is decreased to 50 kPa or increased to 200 kPa.

The results of the sensitivity analyses, including the P vs. Y curves and the $P_{u\text{-}Y}$ of pile P3 in sandy soil, are shown in Figure 6.21b and Table 6.4. The $P_{u\text{-}Y}$ decreases by 34.8% when ϕ' is decreased to 30°, and it is increased by 55.9% when ϕ' is increased to 50°. The value of $P_{u\text{-}Y}$ changes minimally with the changes in γ', and it does not change with the change in D_r. It should be noted that γ' has more effect on pile $P_{u\text{-}Y}$ in sandy soils because of its role in increasing confining stress along the pile.

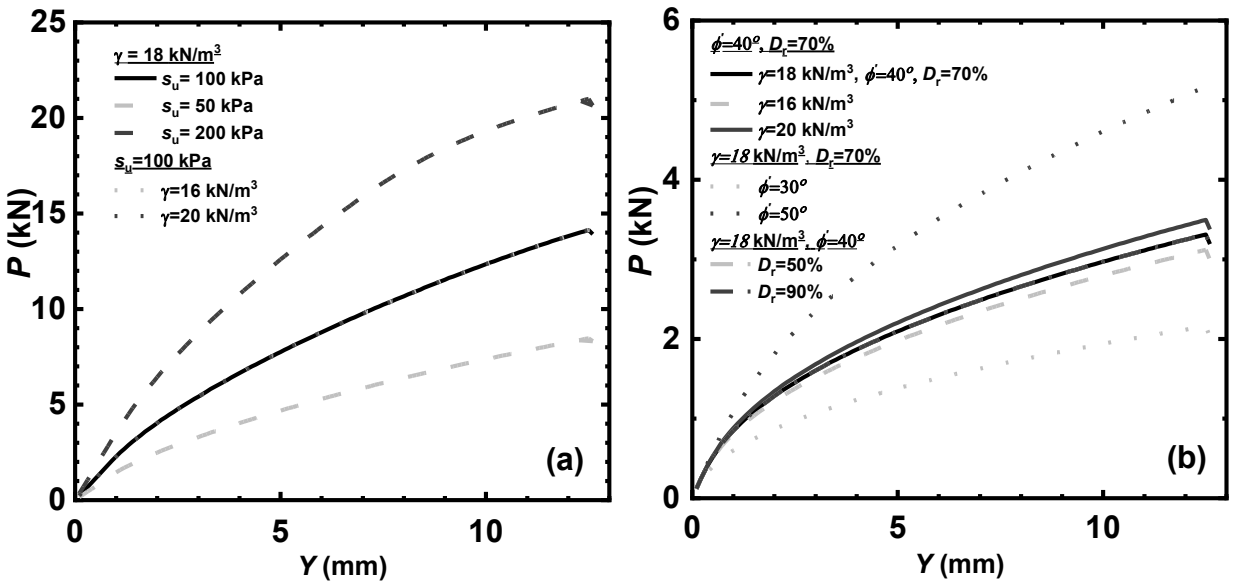

Figure 6.21. Results of the sensitivity analyses – Lateral load-displacement of pile P3 in (a) clay and (b) sand.

Table 6.3. Summary of the sensitivity analyses of pile P3 in clayey soil.

	γ' (kN/m^3)	s_u (kPa)	$P_{u\text{-}Y}$ (kN)	η (%)
Benchmark	18	100	13.9	N.A.
Change in s_u	18	50	8.3	-40.2
	18	200	20.7	+48.5
Change in γ'	16	100	13.9	-0.02
	20	100	13.9	+0.02

Table 6.4. Summary of the sensitivity analyses of pile P3 in sandy soil.

	γ' (kN/m^3)	D_r (kPa)	ϕ' (°)	$P_{u\text{-}Y}$ (kN)	η (%)
Benchmark	18	70	40	3.3	N.A.
Change in γ'	16	70	40	3.1	-5.9
	20	70	40	3.5	+5.3
Change in D_r	18	50	40	3.3	0
	18	90	40	3.3	0
Change in ϕ'	18	70	30	2.2	-34.8
	18	70	50	5.2	+55.9

The sensitivity of the lateral load capacity of pile P3 in a clayey soil and sandy soil to change in regard to the pile geometry and embedment was investigated. The results of the sensitivity analyses including P vs. Y curves and $P_{u\text{-}Y}$ are shown in Figure 6.22 and Table 6.5. The $P_{u\text{-}Y}$ of pile P3 in a clayey soil is significantly affected (+6.8%) by the addition of thread at the smooth segment, and it is not affected (0.05%) by increasing the width of the thread to 24 mm. Therefore, it is evident that the lateral response of the pile can be enhanced by adding thread at the smooth location where the lateral displacement and the cross-sectional plane rotation are highest. Moreover, the lateral response of the pile is not enhanced by increasing the thread width as the lateral displacement and cross-sectional plane rotation are very small at these pile depths.

However, the $P_{u\text{-}Y}$ of pile P3 in sandy soil is affected (+2.4% and +3.9%) by increasing the thread's width and the addition of thread at the smooth segment. Perhaps the lateral displacement of pile P3 in the sandy soil is large enough to affect the lateral thread reaction. Also, the lateral

response of the pile is significantly sensitive to pile stickup. Given that the diameter of this pile is small, even a small change in pile stickup can result in a significant change in the lateral response. Therefore, it is recommended that this pile be installed in the ground with a very small stickup.

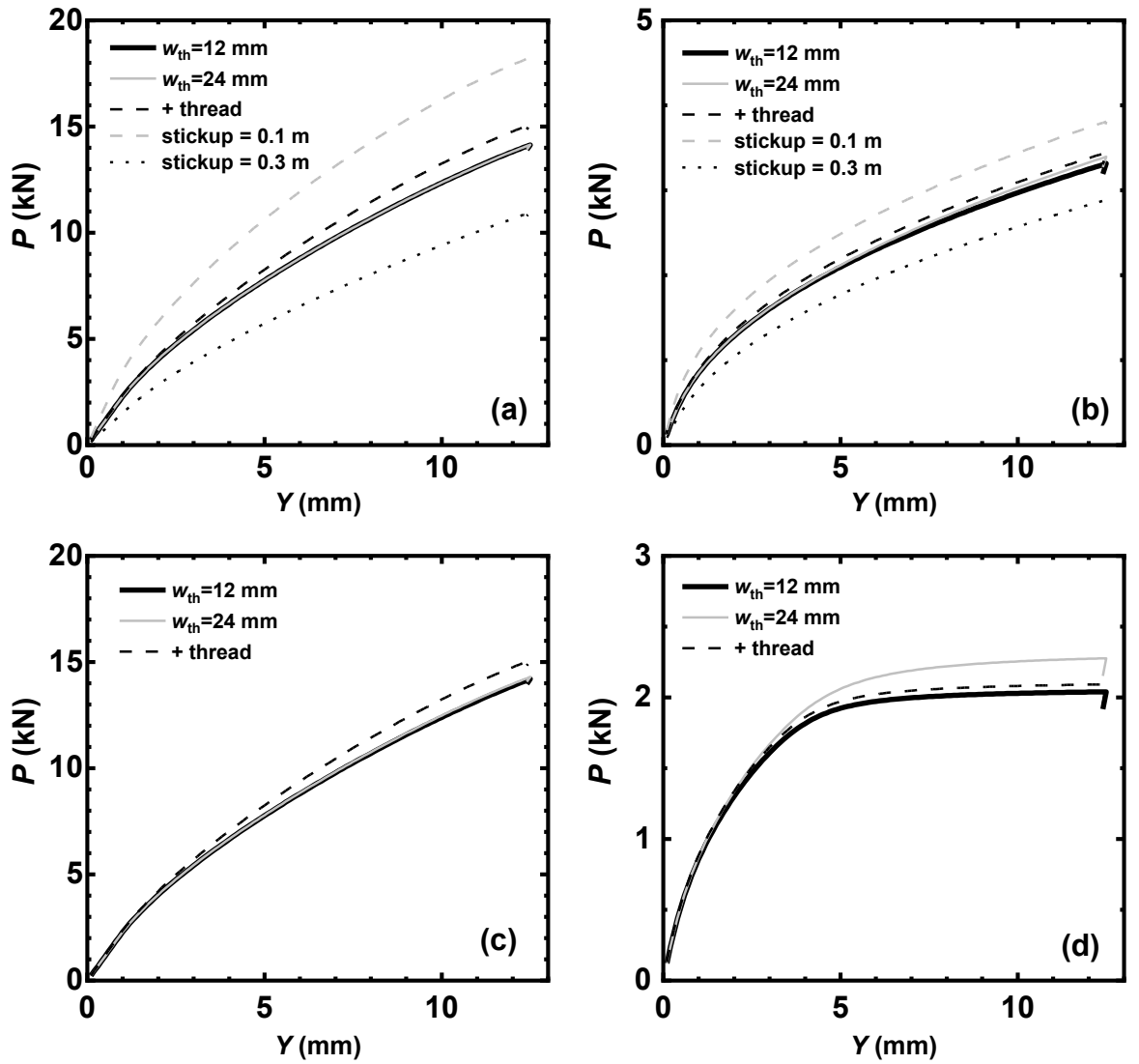

Figure 6.22. Results of the sensitivity analyses – Lateral load vs. displacement of piles (a) P3 in clayey soil and (b) P3 in sandy soil and (c) P4 in clayey soil and (d) P4 in sandy soil.

Table 6.5. Summary of the geometrical sensitivity analyses of pile P3.

	Pile P3 in a clayey soil		Pile P3 in a sandy soil	
	$P_{u\text{-}Y}$ (kN)	η (%)	$P_{u\text{-}Y}$ (kN)	η (%)
Benchmark	13.9	N.A.	3.3	N.A.
w_{th} = 24 mm	14.1	+0.05	3.4	+2.4
Addition of thread at the smooth segment	15.1	+6.80	3.4	+3.9
Pile stickup of 0.1 m	18.3	+29.1	3.8	+14.9
Pile stickup of 0.3 m	10.9	-22.6	2.9	-12.9

6.6. Conclusions and Limitations

The lateral responses of the piles tested at the three sites were obtained by numerical modelling in the OpenSEES program. The predicted and measured *P* vs. *Y* curves are compared. The distributions of lateral displacement (y) with lateral displacement corresponding to the ultimate lateral soil-shaft stress (y_{ult}), the cross-sectional plane rotation of the shaft (dy/dx), the bending moment (M) with the elastic bending moment (M_y) and plastic bending moment (M_p) and the shear force along the pile shaft (V) and lateral soil-shaft (p) with the ultimate lateral soil-shaft stress (p_{ult}) are obtained. The mobilization of the lateral shaft reaction, the vertical shaft reaction, the thread bearing reaction and the lateral thread reaction at the middle of each segment type along the pile are obtained. The lateral response sensitivity of the pile in a clayey and sandy soil to changes in soil properties and pile geometry is examined using the numerical model. Based on the numerical modelling, the following observations are drawn:

1. The numerical models provide a reasonable prediction of the measured response of the piles at the three sites. The measured *P* vs. *Y* curves of the piles at the early loading stages are smaller than the predicted *P* vs. *Y* curves, which can be due to the presence of soil cavities near the pile head observed after the pile installation. However, the *P* vs. *Y* curves of the piles are improved as the annular soil cavities were closed upon lateral loading.

2. Generally, the predicted and measured distributions of the bending moment are relatively comparable to each other. The distributions of the y, dy/dx, M, V and p of the piles at Sherwood Park and South Campus have the qualitative representative shape of a long pile with the free-head condition. Furthermore, the predicted M_{max} of piles P3 and P5 exceeds M_y, and the p only at specific small pile depths exceeds p_{ult}. Therefore, it is shown that the piles failed as long piles (or flexible piles) as plastic hinges were formed at some distance below the ground surface without the failure of a significant portion of the soil.
3. The predicted distribution the pile shaft of pile P1 at Sandpit has the qualitative representative shape of a long pile with the free-head condition. However, almost all of the soil reached the p_{ult} except near the rotational axis. The pile can be classified as a transitional pile with mixed behaviour as both the pile and soil failed. The distribution of pile P4 has the qualitative representative shape of a short pile with the free-head condition. Almost all the soil reached the p_{ult}, which further validates the short pile failure mode.
4. An examination of the soil-pile reactions shows that the lateral shaft reaction contributes the most to the lateral pile response of all the piles. The contribution of the lateral thread reaction is minor, and the contributions of the vertical shaft reaction and the thread bearing reaction are negligible. One pile at Sandpit behaves as a short pile in that the lateral soil-shaft reaction near the pile base also yielded.
5. The lateral load capacity of a pile in clayey soil is significantly affected by a change in s_u. The lateral load capacity of a pile in sandy soil is significantly affected by a change in ϕ'. In contrast, it is minimally affected by γ' and not very much by D_r. The lateral load capacity of a pile in clayey soil is significantly enhanced by the addition of thread along the smooth segment because the lateral displacement and cross-sectional plane rotation is the greatest at a shallow

pile depth. The lateral load capacity is not improved even when the thread width is doubled along the lower portion of the pile.

6. The lateral load capacity is affected by the addition of thread along the smooth segment and doubling the width of the existing thread in sandy soil. The lateral response of a pile is substantially affected by stickup because the pile diameter is relatively small and slender.

The lateral shaft resistance of pile in cohesive soils was represented by *p-y* springs as defined by Matlock (1970). Matlock (1970) defined *p-y* spring for a soft, submerged clay deposit. Field tests were conducted on fully instrumented, flexible, driven pipe piles (D = 320 mm) at Lake Austine and Sabine under static and cyclic loading. The lateral shaft resistance of pile in cohesionless soils was represented by *p-y* spring as defined by API (1993). This method was originally presented by Parker et al. (1970) from the research of small-diameter pipe piles and it was modified by O'Neill and Murchison (1983). The *p-y* curves was correlated from measured soil properties and response of instrumented, driven pipe pile (D = 50.8 mm). It should be noted that the *p-y* springs, also *t-z* springs and *q-z* springs, used in this research were initially developed for specific piles and specific soils. The micro screw piles are installed at the three sites using the torque method. However, these *p-y* springs, which were used in the current research, provide a relatively accurate prediction of pile response.

7. Conclusions and Limitations

This research characterizes the axial and lateral performance of micro screw piles based on field tests at three sites and numerical models.

7.1. Axial Performance of Micro Screw Piles in Sand

An axial load field test program was undertaken to develop the axial response of micro screw piles in sand. In total, 41 tests, including 21 compression tests and 18 tension tests, were performed. Eight piles were instrumented to obtain the axial load transfer. Relevant design parameters for the micro screw pile were obtained for the CPT-based method, effective stress method and empirical torque factor method by correlating the distributions of unit shaft resistance and appropriate soil parameters. The theoretical torque model was adopted for piles in sand. Based on the field test program, the following conclusions were drawn:

- Mostly the compressive but also the tensile Q_u of the piles is significantly affected by the tapered segment, especially for tapers in loose sand. The pile does not experience plunging failure during compression testing. Substantial displacement is required to achieve the ultimate state. The soil-pile interfaces of the smooth segment and the threaded segments in dense sand exhibit dilative behavior. The interface of the threaded segment in loose sand shows contractive behavior.
- The cylindrical shearing mode governs the failure of the threaded segments. The values of q_{sU} along the uniform (smooth and threaded) segments are not visibly affected by the loading direction. The values of q_{sU} along the tapered segments are estimated using CSM using the equivalent cylinder area. The average q_{sU} along the tapered segments is 7.1 times that of the value at the threaded segment.

- A correlation between the distribution of q_s and cone tip resistance q_c was developed for the CPT-based prediction method for pile capacities. The measured q_s and q_c along the smooth segment is comparable to Curve 2 reported by Bustamante and Gianeselli (1983). The median value of α along the threaded segment is less than that of the smooth segment, and the median value of α along the tapered segment is substantially less than that of the uniform segment.
- The median value of K_s along the uniform segment in compact sand is near the passive-state pressure coefficient. The median value of K_s along the uniform segments in loose sand is near $2K_0$, as suggested by CGS (2006) for driven piles. The average value of β along the tapered segment is greater than the uniform segment because of the soil-pile failure mechanism along the tapered segment.
- Based on the theoretical torque model, the estimated profiles of T, T_{max} and T_{end} are comparable to the measured profiles of T, T_{max} and T_{end}. The empirical torque factor K_T is greater for the piles in the compression tests than the tension tests. The proposed K_T values are similar to the values estimated using the empirical equation provided by Perko (2009).

7.2. Axial Cyclic Performance of Micro Screw Piles in Sand

A field test was performed to investigate the axial cyclic behavior of micro screw piles at Sandpit. The axial cyclic load was designed to simulate the vertical loads on the pile during an earthquake. Three piles were instrumented with SGs to measure the re-distribution of unit shaft resistance during the test. Both the overall pile and the individual pile segment response were examined. Key stability factors such as pile-head cumulative displacement, stiffness and equivalent damping ratio were obtained. In addition, the stiffness and equivalent damping ratio of the unit shaft resistance hysteresis of the individual pile segments were assessed. Based on the axial cyclic load field tests of the micro screw piles conducted at Sandpit, the following conclusions were made:

- The piles do not experience plunging failure or a reduction in axial capacity. The piles reach the serviceability limit state by accumulating a large displacement. The value of w_c increases with an increasing number of cycles in a nearly linear pattern. The final w_c varies between 5 mm and 35 mm. All the piles are considered unstable based on the normalized cyclic stability interaction diagram.
- The cyclic behavior of piles is affected by the load corresponding to the initial FS. A pile loaded to a lower FS experience a greater w_c and a lower K_l/K_u ratio, where the cyclic response includes more plastic deformation and is more unstable.
- The loading stiffness K_l of piles increases with an increasing number of cycles, and the K_l of the short piles increases much more than the long piles because of the effects of a greater taper length to total length proportion. The unloading stiffness K_u remains steady. The damping ratio ξ remains more or less unchanged with the number of cycles. The values of the ξ of piles P1 and P3 are smaller than other piles because these piles are loaded with a greater FS.
- The value of the q_s of the individual segment re-distributes: the q_s of the smooth and the threaded segments in compact sand remains unchanged, the q_s of the threaded segment in loose sand degrades because of the contractive behavior of loose sand and the q_s of the tapered segment in loose sand increases significantly.
- The values of the k_l of the tapered segment are the greatest, and the k_l of the smooth segment are the least. The tapered segment k_l exhibits the greatest increase, which means the taper contributes the most to the overall increase in the stiffness of the entire pile. The values of the ζ of the individual segment remain unchanged with an increasing number of cycles. The values of the ζ of the tapered segments are the greatest, and the values of the ζ of the smooth and threaded segments are the least.

7.3. Field Lateral Performance of Micro Screw Piles

A field test program was undertaken to investigate the lateral response of micro screw piles in cohesive and cohesionless soils. Six piles at Sherwood Park, 22 piles at South Campus and 18 piles at sandpit were tested. Selected piles were instrumented with SGs to measure the distribution of the bending moment. The locations of the maximum curvature of the test piles at Sandpit were documented. The pile failure mode was found using the distributions of the bending moment, the location of maximum curvature and Broms's (1964) and Meyerhof and Yilcin's (1984) criteria. Based on a limited number of small-scale and full-scale tests along with theoretical and numerical research, it was concluded that the effect of the helix on lateral response was negligible. Therefore, the lateral capacity of the pile was estimated by only considering the pile shaft and assuming long pile failure mode. Based on the field test program, the following conclusions were drawn:

- Generally, the pile P_{ult} increases with increasing diameter and not with increasing length because the effective length of these piles with the same diameter is the same. The value of the P_{ult} of pile P6 (L = 1.5 m and D_s = 76.1 mm) is slightly greater than pile P5 (L = 3 m and D_s = 76.1 mm) because the pile P6 thread is located at a shallower depth.
- The DBM of the instrumented pile P6 at Sherwood Park and P1, P3 and P5 at South Campus exhibits the representative shape of a long pile under the free-head condition, where the pile deformation is minimal near the pile base. In addition, the ratio of $\Delta M/\Delta Y$ decreases in the vicinity of $Y_{u\text{-}Y}$ and $Y_{u\text{-}DB}$, which suggests that the piles have failed structurally. The deformed shape of the piles at Sandpit also indicates that the piles have failed as long piles.
- The lateral response of pile P6 at Sherwood Park and P1 and P3 at South Campus is probably mainly affected by the soil at the shallow depths of $7D_s$, $10D$ and $10D_s$, respectively. Therefore, the threads are not efficient in improving the lateral response of the piles.

- Consistent with the observed failure mode, Broms's (1964a, b) and Meyerhof and Yilcin's criteria suggest that all the piles (P1–P6) behave as long piles at these sites. Broms's method provides a marginally smaller estimate of the measured ultimate lateral capacity of the piles at Sherwood Park and Sandpit. Perhaps the underestimation is due to neglecting the threads when estimating the lateral capacity of the piles. The capacities of the piles at South Campus are significantly overestimated by this method.
- The effect of the taper on the lateral response of the pile is negligible in the sense that the pile deformation is minimal along these depths. The DBM is the greatest along the uniform segment where the cross-sectional area is the greatest. Therefore, the placement of the tapered segment at the bottom of the pile is an efficient way to increase the pile and soil capacity.

7.4. Numerical Modelling of the Lateral Behaviour of Micro Screw Piles

Numerical models were developed on the OpenSEES platform to simulate the lateral response of the micro screw pile. A comprehensive method that modelled the different components of soil-pile reactions was developed. Aside from the typical soil-pile reactions, the thread-bearing reaction was modelled by a series of zero-length fiber sections with appropriate soil reactions. Furthermore, instead of typical elastic beam-column elements, the pile shaft was modelled as fiber sections, which better represents the pile response. The model was verified against the field test results obtained at the three sites. The contributions of the individual soil-pile reactions were assessed. Finally, a sensitivity analysis was conducted to evaluate the effect of soil properties and specific pile geometry. Based on this method, the following conclusions are drawn:

- The model provides a reasonable prediction of the measured response of the piles at the three sites. The lateral response of the pile at the early loading state is overestimated because of the

annular soil cavity development. The lateral response of the pile is improved as the annular soil cavity is closed.

- Generally, the distribution of the predicted and measured bending moment is reasonably comparable. The distribution of the y, dy/dx, M, V and p of the piles at Sherwood Park and South Campus has the qualitative representative shape of a long pile with the free-head condition. Furthermore, the predicted M_{max} of piles P3 and P5 exceeds M_y, and the p only at specific small depths exceeds p_{ult}.
- The distribution of pile P1 at Sandpit has the qualitative representative shape of a long pile with the free-head condition. However, almost all the soil has reached p_{ult}, except near the rotational axis. The distribution of pile P4 has the qualitative representative shape of a short pile where the pile deformation and movement are significant near the pile base and all of the soil had failed.
- The lateral capacity of the pile in clayey soil is significantly affected by the change in s_u. The lateral capacity of the pile in sandy soil is significantly affected by the change in ϕ', while it is minimally affected by γ' and not very much by D_r. The lateral capacity of the pile in a clayey soil is significantly enhanced by the addition of thread along the smooth segment because the lateral displacement and cross-sectional plane rotation is the greatest at shallow depths. The lateral capacity is not improved even when the thread width is doubled along the lower portion of the pile.
- The lateral capacity of the pile in sandy soil is affected by increasing the addition of thread along the smooth segment and doubling the width of the existing thread. The lateral response of the pile is substantially affected by stickup because the pile's diameter is relatively small and slender.

7.5. Limitations

For the axial cyclic load field test results, the following limitations should be noted if the results are to be used in practice:

- First, more tests at a variety of $a_{eq.pk}$ and FS are needed to establish the comprehensive cyclic behavior of piles subjected to a large spectrum of cyclic loads (e.g., earthquakes, wind and waves).
- Secondly, the loading scheme is pseudo-static instead of dynamic, and hence the effect of loading rates is neglected.

For the lateral load field test results, the following limitations should be noted:

- The pile was laterally loaded under the free-head condition by equipping the hydraulic jack with two hinges. However, some moments could be developed at the pile head.
- The smoothened lateral load-displacement curve was accurate to within a couple of kilonewtons because the load fluctuated due to the hydraulic fluid heating and cooling.
- There are some subjective errors associated with obtaining ultimate lateral capacity by using DeBeer (1968).
- The DBM was obtained at the discrete locations of selected piles. A better DBM could be obtained by adding extra SGs.
- The ultimate lateral capacity was estimated using the soil properties interpreted from CPT readings. The effect of the pile installation on soil disturbance was not considered.

References

Abd Elaziz, A.Y. and El Naggar, M.H. 2012. Axial behaviour of hollow core micropiles under monotonic and cyclic loadings. Geotechnical Testing Journal, 35(2): pp. 249–260.

Al Baghdadi, T. 2018. Screw piles as offshore foundations: Numerical and physical modelling. PhD thesis, Department of Civil Engineering, University of Dundee, Dundee, UK.

Al-Baghdadi, T., Davidson, C., Brown, M., Knappett, J., Brennan, A., Augarde, C.E., Coombs, W.M., Wang, L., Richards, D. and Blake, A. 2017. CPT based design procedure for installation torque prediction for screw piles installed in sand. In 8th Offshore Site Investigation and Geotechnics International Conference: "Smarter Solutions for Future Offshore Developments." Society for Underwater Technology, pp. 346–353.

Algie, T.B. 2011. Nonlinear rotational behaviour of shallow foundations on cohesive soil. PhD Thesis, Department of Civil and Environmental Engineering, the University of Auckland, Auckland, New Zealand.

American Petroleum Institute (API). 1993. Production Department (1993) recommended practice for planning, designing, and constructing fixed offshore platforms: Working stress design. American Petroleum Institute, Washington, D.C.

Ang, A.H.S. and Tang, W.H. 1984. Probability concepts in engineering planning and design, vol. 2: Decision, risk, and reliability. John Wiley & Sons, New York.

ASTM. 2007a. Standard test method for deep foundations under lateral load. ASTM D3966/D3966M (reapproved 2013). American Society for Testing and Materials, West Conshohocken, USA.

ASTM. 2007b. Standard test methods for deep foundations under static axial compressive loads. ASTM D1143-07. American Society for Testing and Materials, West Conshohocken, USA.

ASTM. 2007c. Standard test methods for deep foundations under static axial tensile loads. ASTM D3689-07. American Society for Testing and Materials, West Conshohocken, USA.

Bagheri, F. and El Naggar, M.H. 2013. Effects of the installation disturbance on the behavior of the multi-helix anchors in sands. 66th Canadian Geotechnical Conference, Montreal, Quebec, pp. 13.

Bagheri, F. and El Naggar, M.H. 2015. Effects of installation disturbance on behavior of multi-helix piles in structural clays, DFI Journal – The journal of the deep foundations institute, 9(2): pp. 80–91.

Banerjee, P.K. and Davies, T.G. 1978. The behaviour of axially and laterally loaded single piles embedded in nonhomogeneous soils. Geotechnique, 28(3): pp. 309–326.

Bayrock, L.A. 1958. Glacial geology of Galahad-Hardisty district, Alberta. Research Council of Alberta, Edmonton, Canada. Vol. 57, No. 3.

Beer, F.P., Johnston Jr, E.R., DeWolf, J.T., DeWolf, J.T. and Oler, J.W. 2006. Mechanics of materials. 4th edition. McGraw-Hill, New York.

Bhushan, K., Haley, S.C. and Fong, P.T. 1979. Lateral load tests on drilled piers in stiff clays. Journal of the Geotechnical Engineering Division, 105(8): pp. 969–985.

Boulanger, R.W., Kutter, B.L., Brandenberg, S.J., Singh, P. and Chang, D. 2003. Pile foundations in liquefied and laterally spreading ground during earthquakes: Centrifuge experiments & analyses. Report No. UCD/CGM-03/01, Center for Geotechnical Modeling, Department of Civil and Environmental Engineering, University of California, Davis, California.

Boulon, M. 1986. Physical and numerical simulation of lateral shaft friction along offshore piles in sand. In Proceedings of the 3rd Int. Conf. on Numerical Methods in Offshore Piling. pp. 127–147.

Bozozuk, M. 1978. Bridge foundation moves. Transportation Research Report 678. Transportation Research Board, Washington, D.C.

Broms, B.B. 1964a. Lateral resistance of piles in cohesionless soils. Journal of the Soil Mechanics and Foundations Division, 90(3): pp. 123–158.

Broms, B. B. 1964b. Lateral resistance of piles in cohesive soils. Journal of the Soil Mechanics and Foundations Division, 90(2): pp. 27–64.

Bustamante, M. and Gianeselli, L. 1983. Prevision de la capacite portante des pieux par la methode penetrometrique. Compte Rendu de Recherche FAER, Laboratoire Central des Ponts et Chanssees, 1.05.02.2.

Bustamante, M. and Gianeselli, L. 1982. Pile bearing capacity prediction by means of static penetrometer CPT. In Proceedings of the 2nd European Symposium on Penetration Testing. pp. 493–500.

California Department of Transportation (Caltrans). 2019. Seismic design criteria. Version 2. California Department of Transportation, Sacramento, California.

Canadian Geotechnical Society (CGS). 2006. Canadian foundation engineering manual. Bitech Publishers, Richmond, British Columbia, Canada.

Carreño, R., Lotfizadeh, K.H., Conte, J.P. and Restrepo, J.I. 2020. Material model parameters for the Giuffrè-Menegotto-Pinto uniaxial steel stress-strain model. Journal of Structural Engineering, 146(2): pp. 04019205.

Castello, R.R. 1980. Bearing capacity of driven piles in sand. PhD thesis, Department of Civil and Environmental Engineering, Texas A&M University, Texas, USA.

Chopra, A.K. 2007. Dynamics of structures. Pearson Education.

Coyle, H.M. and Reese, L.C. 1966. Load transfer for axially loaded pile in clay. Journal of the Soil Mechanics and Foundations Division, 92(2): pp. 1–26.

Cuthbertson-Black, R. 2001. The interaction between a flighted steel pipe pile and frozen sand. MSc thesis, Department of Civil and Geological Engineering, University of Manitoba, Winnipeg, Canada.

Davidson, C., Al-Baghdadi, T., Brown, M., Brennan, A., Knappett, J., Augarde, C., Coombs, W., Wang, L., Richards, D. and Blake, A. 2018. A modified CPT based installation torque prediction for large screw piles in sand. Cone Penetration Testing, Delft, Netherlands, pp. 255–261.

DeBeer, E.E. 1968. Proefondervindlijke bijkrage tot de studie van het grensdraag vermogen van zand onder funderingen op staal. Tijdshift der Openbar Verken van Belgie, No. 6, 1967 and Nos. 4, 5 and 6, 1968.

Dennis, N.D. and Olson, R.E. 1983. Axial capacity of steel pipe piles in sand. In Geotechnical Practice in Offshore Engineering, pp. 389–402. ASCE.

DIN. 2006a. Cold formed welded structural hollow sections of non-alloy and fine grain steels-Part 1: Technical delivery conditions. DIN EN 10219-1. German Institute for Standardization.

DIN. 2006b. Cold formed welded structural hollow sections of non-alloy and fine grain steels-Part 1: Tolerances, dimensions and sectional properties. DIN EN 10219-2. German Institute for Standardization.

Drbe, O.F.E.H. and El Naggar M.H. 2015. Axial monotonic and cyclic compression behaviour of hollow-bar micropiles. Canadian Geotechnical Journal, 52(4): pp. 426–441.

Edwards, D. 1993. Gravel bar blues. In Edmonton beneath our feet. Edited by J. Godfrey. Edmonton Geological Society, Edmonton. pp. 67–72

El Aziz. A.Y.A. 2012. Performance of hollow bar micropiles under axial and lateral loads in cohesive soils. Ph.D. Thesis, Department of Civil and Environmental Engineering, the University of Western Ontario, London, ON.

El Naggar M.H. and Abdelghany Y. June 2007. Helical screw piles (HSP) capacity for axial cyclic loadings in cohesive soils. In Proceedings of the 4th International Conference on Earthquake Geotechnical Engineering. Thessaloniki-Greece. pp. 25–28.

El Naggar M.H. and Wei, J.Q. 2000. Cyclic response of axially loaded tapered piles. Geotechnical Testing Journal, 23(1): pp. 100–115.

El Naggar, M.H. and Sakr, M. 2000. Evaluation of axial performance of tapered piles from centrifuge tests. Canadian Geotechnical Journal, 37(6): pp. 1295–1306.

El Naggar, M.H. and Sakr, M. 2002. Cyclic response of axially loaded tapered piles. International Journal of Physical Modelling in Geotechnics, 2(4): pp. 1–12

El Naggar, M.H., Shayanfar, M.A., Kimiaei, M. and Aghakouchak, A.A. 2005. Simplified BNWF model for nonlinear seismic response analysis of offshore piles with nonlinear input ground motion analysis. Canadian Geotechnical Journal, 42(2): pp. 565–380.

El Sharnouby M.M. and El Naggar M.H. 2012. Axial monotonic and cyclic performance of fibre-reinforced polymer (FRP)-steel fibre-reinforced helical pulldown micropiles (FRP-RHPM). Canadian Geotechnical Journal, 49(12): pp. 1378–1392.

El Sharnouby, M.M.M. 2012. Monotonic and cyclic behaviour of steel fibre-reinforced and FRP-steel fibre-reinforced helical pulldown micropiles. PhD thesis, Department of Civil and Environmental Engineering, The University of Western Ontario, London, Canada.

Elkasabgy, M and El Naggar, M.H. 2013. Dynamic response of vertically loaded helical and driven steel piles. Canadian Geotechnical Journal, 50(5): pp. 521–535.

Elkasabgy, M.A. and El Naggar, M.H. 2015. Lateral performance of large-capacity helical piles. In Proceeding of the International Foundations Congress and Equipment Expo 2015.

Elsawy, M.K., El Naggar, M.H., Cerato, A and Elgamal, A. 2019. Seismic performance of helical piles in dry sand from large-scale shaking table tests. Geotechnique, 69(12): pp. 1071–1085.

Elsherbiny, Z.H. and El Naggar, M.H. 2013. Axial compressive capacity of helical piles from field tests and numerical study. Canadian Geotechnical Journal, 50(12): pp. 1191–1203.

Fahmy, A. and El Naggar, M.H. 2015. Lateral performance of helical tapered piles in sand. In Proceedings of the Canadian Geotechnical Conference GeoQuebec, Quebec City, Quebec.

Fahmy, A. and El Naggar, M.H. 2017. Axial and lateral performance of spun-cast ductile iron helical tapered piles in clay. In Proceedings of the Institution of Civil Engineers-Geotechnical Engineering, 170(6): pp. 503–516.

Fellenius, B.H. 1989. Predicted and observed axial behavior of piles. In Proceedings of the Symposium on Driven Pile Bearing Capacity Prediction, American Society of Civil Engineers, New York. pp. 75–115.

Fellenius, B.H. 2002. Discussion of "side resistance in piles and drilled shafts" by Michael W. O'Neill. Journal of Geotechnical and Geoenvironmental Engineering, 128(5): pp. 446–448.

Fenton, M.M., Moran, S.R., Teller, J.T. and Clayton, L. 1983. Quaternary stratigraphy and history in the southern part of the Lake Agassiz Basin. In Glacial Lake Agassiz, 26: pp. 49–74.

Gavin, K., Doherty, P. and Spagnoli, G. 2013. Prediction of the installation torque resistance of large diameter helical piles in dense sand. In Proceedings of the 1st International Geotechnical Symposium of Helical Foundations. Amherst, MA.

Golub, G.H. and Welsch, J.H. 1969. Calculation of Gauss quadrature rules, Mathmatics of computation, 23(106): 221-230

Guo, P.X., Xiao, Y. and Kunnath, S.K. 2014. Performance of laterally loaded H-piles in sand. Soil Dynamics and Earthquake Engineering Journal, 67: pp. 316–325.

Guo, Z. 2017. Field behaviour of steel threaded micropiles under axial load in cohesive soils. MSc Thesis, Department of Civil and Environmental Engineering, University of Alberta, AB, Canada.

Guo, Z. and Deng, L. 2018. Field behaviour of screw micropiles subjected to axial loading in cohesive soils. Canadian Geotechnical Journal, 55(1): pp. 34–44.

Guo, Z., Khidri, M. and Deng, L. 2019. Field loading tests of screw micropiles under axial cyclic and monotonic loads. Acta Geotechnica, 14(6): pp. 1843–1856.

Hanna, T.H., Sivapalan, E. and Senturk, A. 1978. The behaviour of dead anchors subjected to repeated and alternating loads. Ground Engineering, 11(3).

Hirany, A. & Kulhawy, F.H. 1988. Conduct and interpretation of load tests on drilled shaft foundations: Volume 1, Detailed guidelines. Report No. EPRI-EL-5915-Vol. 1, Electric Power Research Institute, Palo Alto, California.

Houlsby, G. T. 1991. How the dilatancy of soils affects their behaviour. In Proceedings of the 10th European Conference on Soil Mechanics and Foundation Engineering, Florence.

Hoyt, R. M. and Clemence, S.P. 1989. Uplift capacity of helical anchors on soil. In Proceedings of the 12th International Conference on Soil Mechanics and Foundation Engineering, Rio de Janeiro, Brazil. Vol. 2. pp. 1019–1022.

International Code Council. 2012. Acceptance criteria for screw foundation systems (SFSs). AC443 Report, International Code Council Evaluation Service, Whittier, California.

International Code Council. 2013. Acceptance criteria for helical systems and devices. AC358 Report, International Code Council Evaluation Service, Whittier, California.

Jamiolkowski, M., Lo Presti, D. and Manassero, M. 2003. Evaluation of relative density and shear strength of sands from CPT and DMT. In Soil Behavior and Soft Ground Construction. pp. 201–238.

Jardine, R.J. and Standing, J.R. 2012. Field axial cyclic loading experiments on piles driven in sand. Soils and Foundations, 52(4): pp. 723–736.

Jeffrey, J.R., Brown, M.J., Knappett, J.A., Ball, J. and Caucis, K. 2016. CHD pile performance: Part I – physical modelling. In Proceedings of the Institution of Civil Engineers – Geotechnical Engineering, 169(5): pp. 436–454.

Khidri, M. and Deng, L. 2021. Field axial cyclic loading tests of screw micropiles in cohesionless soil. Soil Dynamics and Earthquake Engineering, 143: pp. 106601.

Khidri, M. and Deng, L. 2022. Field axial loading of screw micropile in sand. Canadian Geotechnical Journal, 59(3): pp. 458–472.

Knappet, J.A., Brown, M.J., Brennan, A.J. and Hamilton, L. 2014. Optimising the compressive behaviour of screw piles in sand for marine renewable energy applications. Conference on Piling and Deep Foundations, Stockholm, Sweden, 21st–23rd May 2014.

Kodikara, J.K. and Moore, I.D. 1993. Axial response of tapered piles in cohesive frictional ground. Journal of Geotechnical Engineering, 119(4): pp. 675–693.

Kramer, S.L. 1996. Geotechnical earthquake engineering. Pearson Education, Upper Saddle River, New Jersey.

Kulhawy, F.H. and Mayne, P.H. 1990. Manual on estimating soil properties for foundation design. Report EL-6800, Electric Power Research Institute, Palo Alto, California.

Kunnath, S.K., Erduran, E., Chai, Y.H. and Yashinsky, M. 2008. Effect of near-fault vertical ground motions on seismic response of highway overcrossings. Journal of Bridge Engineering, 13(3): pp. 282–290.

Kurian, N.P. and Shah, S.J. 2009. Studies on the behaviour of screw piles by finite element method. Canadian Geotechnical Journal, 46(6): pp. 627–638.

Ladanyi, B. and Guichaoua, A. 1985. Bearing capa city and settlement of shaped piles in permafrost. In Proceedings of the International Conference on Soil Mechanics and Foundation Engineering. Vol 11. pp. 1421–1427.

Laplace, P.S. 1810. Memoire su les integrals definies et leur application aux probabilities, et specialement a la reherchu du milieu qu'il faut choisir entre les resultats de observations. Memoires de l'Academic des Sci 279-347

Li, Z, Haigh, S.K. and Bolton, M.D. 2010. The behavior of a single pile under cyclic axial loads. Deep Foundations and Geotechnical In Situ Testing. pp. 143–148.

Li, W. 2016. Axial and lateral behavior of helical piles under static loads. MSc thesis, Department of Civil and Environmental Engineering, University of Alberta, Edmonton, Canada.

Liu, A.H., Stewart, J.P., Abrahamson, N.A. and Moriwaki, Y. 2001. Equivalent number of uniform stress cycles for soil liquefaction analysis. Journal of Geotechnical and Geoenvironmental Engineering, 127(2): pp. 1017–1026.

Lunne, T., Berre, T. and Strandvik, S. 1997. Sample disturbance effects in soft low plastic Norwegian clay. In Symposium on Recent Developments in Soil and Pavement MechanicsCAPES-Fundacao Coordenacao do Aperfeicoamento de Pessoal de Nivel Superior; CNPq-Conselho Nacional de Desenvolvimento Cientifico a Tecnologico; FAPERJ-Fundacao de Ampora a Pesquisa do Estado do Rio de Janeiro; FINEP-Financiadora de Estudos e Projetos.

Manandhar, S. and Yasufuku, N. 2013. Vertical bearing capacity of tapered piles in sands using cavity expansion theory. Soils and Foundations, 53(6): pp. 853–867.

Mansour, M.A. 2019. Performance of pressure grouted helical piles under monotonic axial and lateral loading. PhD thesis, Department of Civil and Environmental Engineering, The University of Western Ontario, London, Canada.

Matlock, H. 1970. Correlations for design of laterally loaded piles is soft clay. Offshore Technology in Civil Engineering's Hall of Fame Papers from the Early Years, pp. 77–94.

Mayne, P. 2005. Integrated ground behavior: In-situ and lab tests. In Deformation Characteristics of Geomaterials, 2: pp. 155–177.

Mayne, P. 2006. Undisturbed sand strength from seismic cone tests. The 2nd James K. Mitchell lecture. Geomech. Geoeng, 1(4): pp. 239–258.

Mayne, P.W., Peuchen, J. and Bouwmeester, D. 2010. Estimation of soil unit weight from piezocone readings in onshore soils. In Proceedings of the 2nd International Symposium on Cone Penetration Testing, Huntington Beach, California.

Mazzoni, S., McKenna, F., Scott, M.H., Fenves, G.L. 2006. OpenSees command language manual. Pacific Earthquake Engineering Research (PEER) Center, Berkeley, California

Meyerhof, G.G. 1976. Bearing capacity and settlement of pile foundations. Journal of the Geotechnical Engineering Division, ASCE, 102(3): pp. 195–228.

Meyerhof, G.G. and Ranjan, G. 1972. The bearing capacity of rigid piles under inclined loads in sand. I: Vertical piles. Canadian Geotechnical Journal, 9(4): pp. 430–446.

Meyerhof, G.G. and Sastry, V.V.R.N. 1985. Bearing capacity of rigid piles under eccentric and inclined loads. Canadian Geotechnical Journal, 22(3): pp. 267–276.

Meyerhof, G.G. and Yalcin, A.S. 1984. Pile capacity for eccentric inclined load in clay. Canadian Geotechnical Journal, 21(3): pp. 389–396.

Meyerhof, G.G. and Adams, J. 1968. The ultimate uplift capacity of foundations. Canadian Geotechnical Journal, 5(4): pp. 225–244.

Meyerhof, G.G., Mathur, S.K. and Valsangkar, A.J. 1981. Lateral resistance and deflection of rigid walls and piles in layered soils. Canadian Geotechnical Journal, 18(2): pp. 159–170.

Mitsch, M.P. and Clemence, S.P. 1985. The uplift capacity of helix achors in sand. In Proceedings of the Uplift Behavior of Anchor Foundation in Soil, ASCE. pp. 26–27.

Mooney, J. S., Adamczak, S. and Clemence, S.P. 1985. Uplift capacity of helical anchors in clay and silt. In Proceedings of the Uplift Behavior of Anchor Foundation in Soil, ASCE.

Mosher, R.L. 1984. Load-transfer criteria for numerical analysis of axially loaded piles in sand. Part 1: Load-transfer criteria, Final Report, Army Engineer Waterways Experiment Station, Vicksburg, Mississippi.

Mosher, R.L. and Dawkins, W.P. 2000. Theoretical manual for pile foundations. Report No. ERDC/ITL-TR-00-5, Engineering research and development center, Vicksburg, Mississippi.

Narasimha Rao, S., Prasad, Y.V.S.N. and Veeresh, C. 1993. Behaviour of embedded model screw anchors in soft clay. Geotechnique, 43(4): pp. 605–614.

Narasimha Rao, S., Prasad, Y.V.S.N. and Shetty, M.D. 1991. The behaviour of model screw piles in cohesive soils. Soils and Foundations, 31(2): pp. 35–50.

O'Neill, M. and Murchison, J. 1983. An evaluation of p-y relationships in sands. Report GTDF02-83, Department of Civil Engineering, University of Houston, Houston, Texas.

O'Neill, M.W. 2001. Side resistance in piles and drilled shafts. Journal of Geotechnical and Geoenvironmental Engineering, 127(1): pp. 3–16.

O'Neill, M.W. 2002. Closure to "Side resistance in piles and drilled shafts" by Michael W. O'Neill. Journal of Geotechnical and Geoenvironmental Engineering, 128(5): pp. 450–450.

O'Neill, M.W. and Reese, L.C. 1999. Drilled shafts: Construction procedures and design methods. Report No. FHWA-IF-99-025, U.S. Department of Transportation, Federal Highway Administration (FHWA), New Jersey, Washington, D.C.

Papadopoulou, K., Saoglou, H. and Papadopoulos, V. 2014. Finite element analyses and experimental investigation of helical micropiles. Geotechnical and Geological Engineering, 32(4): pp. 949–963.

Parker, F. Jr., and Reese, L.C. 1970. Experimental and analytical study of behavior of single piles in sand under lateral and axial loading. Research Report No. 117-2, Center for Highway Research, The university of Texas, Austin, Texas.

PEER. 2016. Open System for Earthquake Engineering Simulation (OpenSees). Pacific Earthquake Engineering Research Center. University of California, Berkeley, California.

Perko, H.A. 2009. Helical piles: A practical guide to design and installation. John Wiley & Sons, New Jersey.

Poulos, H.G. 1980. Ultimate lateral pile capacity in a two-layered soil. Geotechnical Engineering, 16(1): pp. 25–37.

Poulos, H.G. 1989. Cyclic axial loading analysis of piles in sand. Journal of Geotechnical Engineering, 115(6): pp. 836–852.

Poulos, H.G. and Davis, E.H. 1980. Pile foundation analysis and design. New York, NY.

Poulos, H.G. and Sim, K.B. 1990. Engineered piles to improve cyclic load capacity. Marine Georesources & Geotechnology, 9(2): pp. 131–140.

Prakash, S. and Sharma, H.D. 1990. Pile foundations in engineering practice. John Wiley & Sons, New Jersey.

Prasad, Y.V. and Rao, S.N. 1996. Lateral capacity of helical piles in clays. Journal of Geotechnical Engineering, 122(11): pp. 938–941.

Puri, V.K., Stephenson, R.W., Dziedzic, E. and Goen, L. 1984. Helical anchor piles under lateral loading. In Laterally loaded deep foundations: Analysis and performance. West Conshohocken, Pennsylvania.

Randolph, M.F. and Murphy, B.S. 1985. Shaft capacity of driven piles in clay. In Offshore Technology Conference. OnePetro.

Reese, L.C. and O'Neill, M.W. 1987. Drilled shafts: Construction procedures and design methods. Report No. FHWA-HI-88-042. FHWA-HI-88-042, U.S. Department of Transportation, Federal Highway Administration, Office of Implementation, McLean.

Reese, L.C. and Welch, R.C. 1975. Lateral loading of deep foundations in stiff clay. Journal of the Geotechnical Engineering Division, ASCE, 101(GT7): pp. 633–649.

Reese, L.C., Cox, W.R. and Koop, F.D. 1974. Analysis of laterally loaded piles in sand. In Proceedings of the Sixth Offshore Technology Conference, Houston, Texas.

Rimoy, S.P., Jardine, R.J. and Standing, J.R. 2013. Displacement response to axial cycling of piles driven in sand. In Proceedings of the Institution of Civil Engineers-Geotechnical Engineering, 166(2): pp. 131–146.

Robertson, P.K. 2004. Evaluating soil liquefaction and post-earthquake deformations using the CPT. Geotechnical & Geophysical Site Characterization, Vol. 1 (Proc. ISC-2, Porto), Millpress, Rotterdam, pp. 233–249.

Robertson, P.K. and Cabal, K.L. 2012. Guide to cone penetration testing for geotechnical engineering. Gregg Drilling and Testing Inc., Signal Hill, California.

Robinsky, E. and Morrison, C. 1964. Sand displacement and compaction around model friction piles. Canadian Geotechnical Journal, 1(2): pp. 81–93.

Robinsky, E., Sagar, W. and Morrison, C. 1964. Effect of shape and volume on the capacity of model piles in sand. Canadian Geotechnical Journal, 1(4): pp. 189–204.

Rollins, K., Olsen, R., Egbert, J., Olsen, K., Jensen, D. and Garrett, B. 2003. Response, analysis, and design of pile groups subjected to static & dynamic lateral loads. Report No. UT-03.03, Utah Department of Transportation, Salt Lake, Utah.

Rybnikov, A. 1990. Experimental investigations of bearing capacity of bored-cast-in-place tapered piles. Soil Mechanics and Foundation Engineering, 27(2): pp. 48–52.

Sakr, M. 2009. Performance of helical piles in oil sand. Canadian Geotechnical Journal, 46(9): pp. 1046–1061.

Sakr, M. El Naggar, M.H. and Nehdi, M. 2004. Lateral behaviour of composite tapered piles in dense sand. In Proceedings of the Institution of Civil Engineers-Geotechnical Engineering, 158(3): pp. 145–157.

Sakr, M. and El Naggar, M.H. 2003. Centrifuge modeling of tapered piles in sand. Geotechnical Testing Journal, 26(1): pp. 22–35.

Salgado, R. 2008. The engineering of foundations. McGraw-Hill, New York.

Sanzeni, A. and Danesi, E.G. 2019. Behaviour of screw micropiles subjected to axial tensile and compressive loading. International Journal of Geotechnical Engineering, pp. 1–12.

Sastry, V.V.R.N., Meyerhof, G.G. and Koumoto, T. 1986. Behaviour of rigid piles in layered soils under eccentric and inclined loads. Canadian Geotechnical Journal, 23(4): pp. 451–457.

Seed, H.B., Idriss, I.M., Makdisi, F. and Banerjee, J. 1975. Representation of irregular stress time histories of equivalent uniform stress series in liquefaction analysis. Report No. EERC pp. 75–29. Earthquake Engineering Research Center, University of California, Berkeley, California.

Spagnoli, G. 2017. A CPT-based model to predict the installation torque of helical piles in sand. Marine Georesources & Geotechnology, 35(4): pp. 578–585.

Stuedlein, A.W. and Gurtowski, T.M. 2012. Reliability of shaft resistance for augured cast-in-place piles in granular soils. In Full-scale testing and foundation design: Honoring Bengt H. Fellenius, pp.722–736.

Tomlinson, M.J. 1957. The adhesion of piles driven in clay soils. In Proceedings of the 4th International Conference on Soil Mechanics and Foundation Engineering, London, UK, 2: pp. 66–71.

Tsuha, C.D.H.C. and Aoki, N. 2010. Relationship between installation torque and uplift capacity of deep helical piles in sand. Canadian Geotechnical Journal, 47(6): pp. 635–647.

U.S. Army Corps of Engineers (USACE). 1991. Design of pile foundation. In U.S. Army corps of Engineers (USACE). 1991. Design of Pile Foundations, Engineer Manual EM 1110-2-2906, Washington, D.C.

Vijayvergiya, V.N. 1977. Load-movement characteristics of piles. In Proceeding of the Ports 77 4th Annual Symposium of the American Society of Civil Engineers, Waterway, Port, Coastal and Ocean Division, Long Beach, California, (2): pp. 269–284.

Wei, J. and El Naggar, M.H. 1998. Experimental study of axial behaviour of tapered piles. Canadian Geotechnical Journal, 35(4): pp. 641–654.

Zhang, D. 1999. Predicting capacity of helical screw piles in Alberta soils. MSc thesis, Department of Civil and Environmental Engineering, University of Alberta, Edmonton, Canada.

Appendix A: Additional Site Characterization Results and Torque Readings

Additional site investigation results at Sandpit include:

- photos of boreholes with SPT testing
- a schematic of soil stratigraphy Sandpit based on borehole drilling and distribution of SPT-N_{160}
- profile of water content
- Profile of water content
- Particle size distribution of sand
- Specific gravity of sand
- Maximum and minimum void ratio and maximum and minimum dry density of sand
- Constant-volume friction angle

Furthermore, measured continuous installation torque records of the piles at South Campus attached.

Figure A.1. Photos of borehole with SPT testing at Sandpit

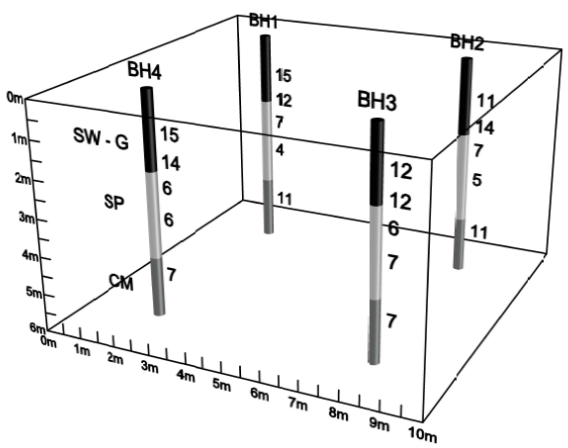

A.2. A schematic of soil stratigraphy at Sandpit based on borehole drilling and distribution of SPT-$N_{1,60}$ at Sandpit

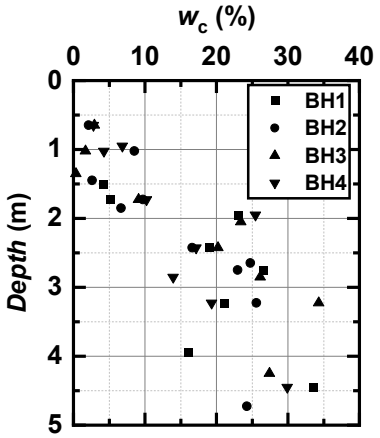

Figure A.3. Profile of water content at Sandpit

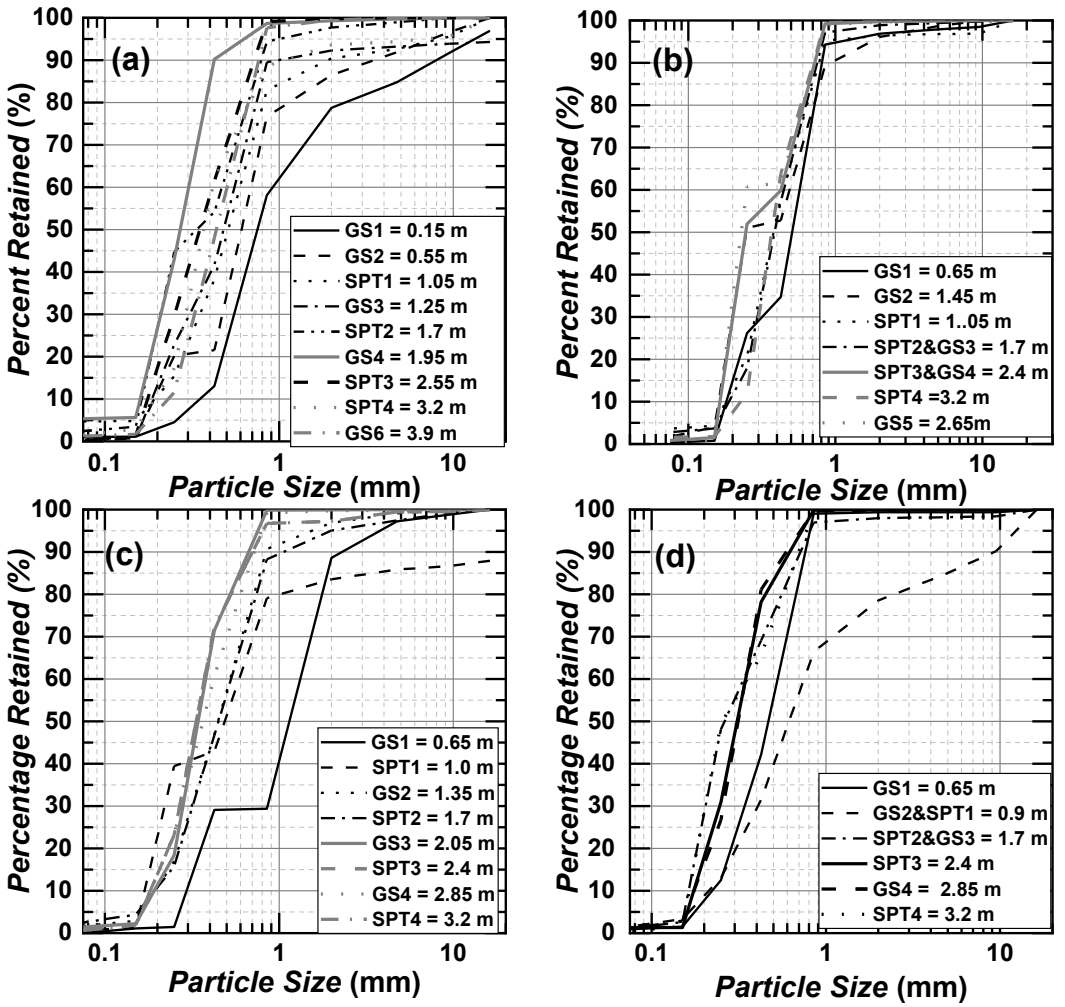

Figure A.4. Particle size distribution of sand at Sandpit at: (a) BH1, (b) BH2, (c) BH3, and (d) BH4.

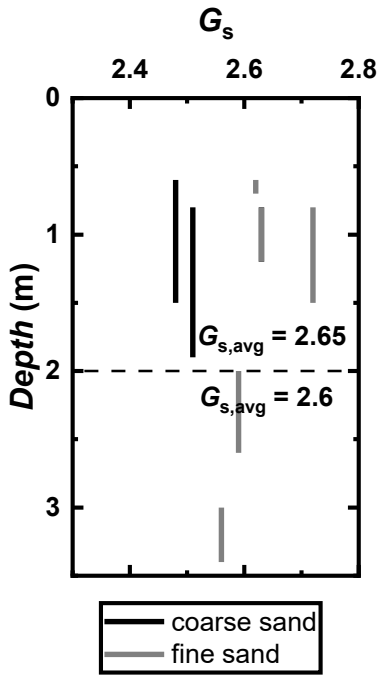

Figure A.5. Specific gravity of sand at Sandpit

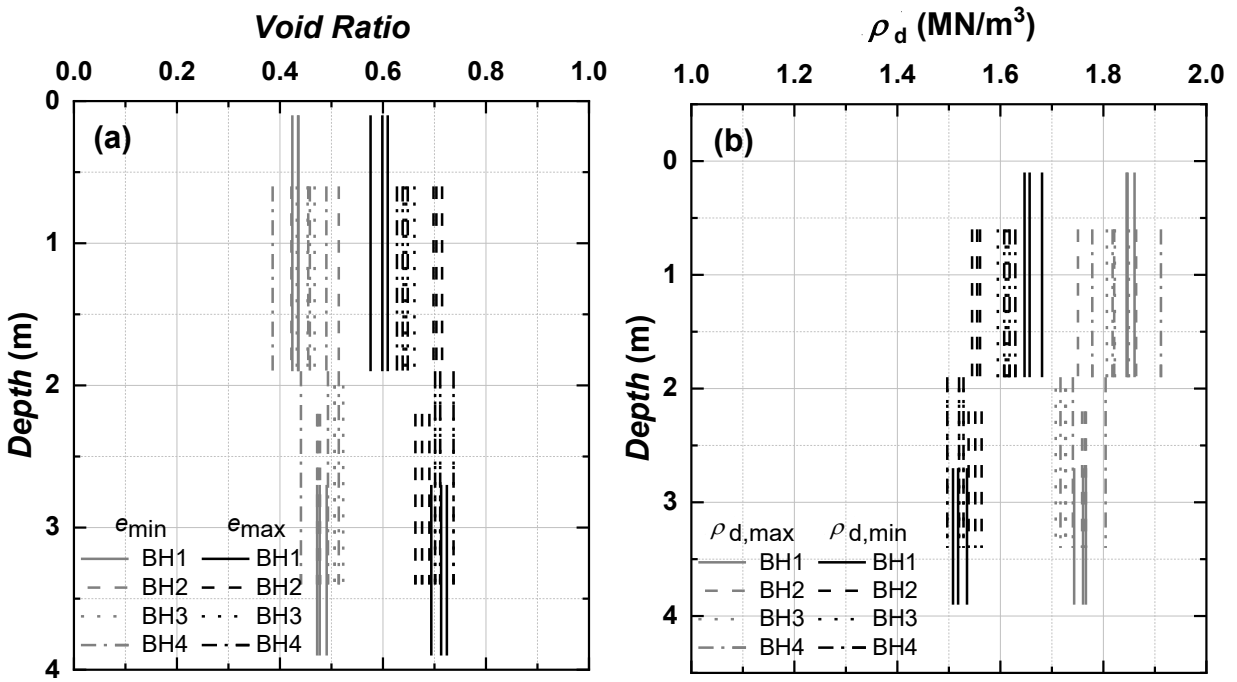

Figure A.6. (a) Minimum and maximum void ratio and (b) minimum and maximum dry density of sand at Sandpit

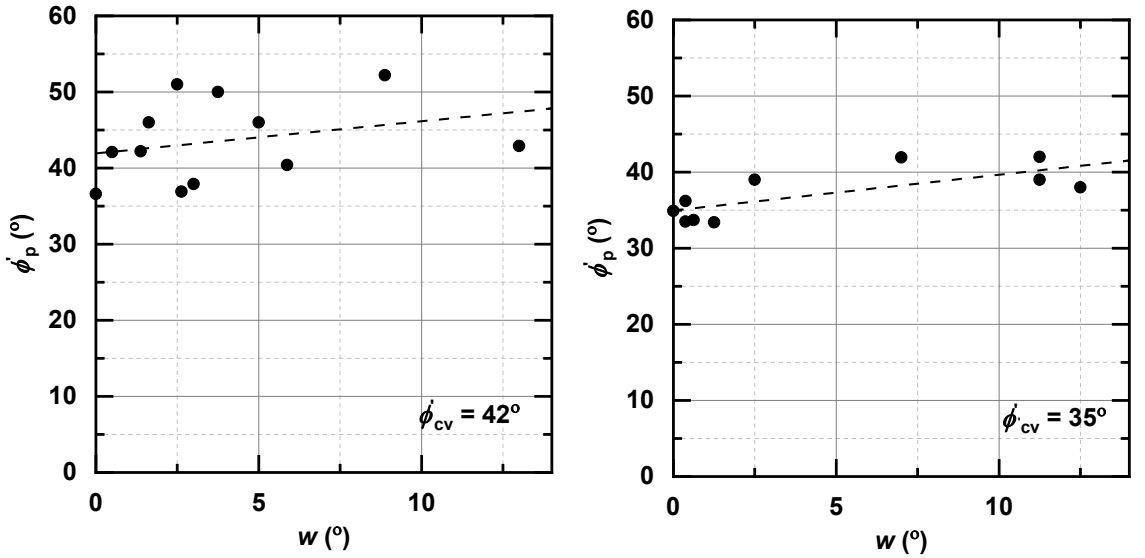

A.7. Constant-volume friction angle of sand at Sandpit

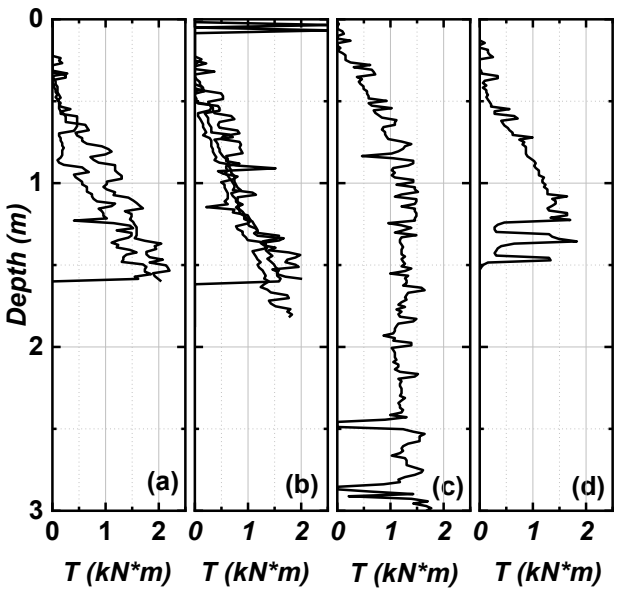

Figure A.8. Measured continuous torque readings of piles: (a) P2, (b) P4, (c) P5 and (d) P6 at South Campus

Table A.1. Particle size data of sand at Sandpit

	Depth	Gravel	Sand	Fines	D_{10}	D_{30}	D_{60}	C_u	C_c	Group Symbol
BH1										
GS1	0.1-0.2	21.2	77.7	1.1	1.0	0.6	0.4	2.6	1.0	SP-G
GS2	0.5-0.6	13.5	86.3	0.2	0.7	0.5	0.2	3.6	1.7	SW
SPT1	0.8-1.3	9.6	85.7	4.7	0.6	0.4	0.2	3.2	1.0	SW
GS3	1.2-1.3	7.7	91.9	0.4	0.6	0.3	0.2	3.1	0.9	SP
SPT2	1.5-1.9	2.3	95.3	2.4	0.5	0.2	0.2	2.9	0.6	SP
GS4	1.9-2.0	0.7	94.0	5.3	0.3	0.2	0.2	1.9	0.9	SP
SPT3&GS5	2.4-2.9	0.2	99.4	0.4	0.4	0.3	0.2	2.3	0.9	SP
SPT4	3-3.4	6.4	92.1	1.5	0.4	0.3	0.2	2.1	1.1	SW
GS6	3.9-4.0	0.5	98.2	1.3	0.5	0.3	0.2	2.3	0.9	SP
BH2										
GS1	0.6-0.7	3.1	96.5	0.4	0.6	0.3	0.2	3.2	1.0	SP
SPT1	0.8-1.3	3.5	92.8	3.6	0.4	0.3	0.2	2.4	1.0	SP
GS2	1.4-1.5	3.9	94.4	1.8	0.5	0.2	0.2	3.1	0.5	SP
SPT2&GS3	1.5-1.9	1.1	96.1	2.8	0.5	0.3	0.2	2.3	1.0	SP
SPT3 & GS4	2.2-2.6	0.3	98.9	0.8	0.4	0.2	0.2	2.6	0.6	SP
SPT4	3-3.4	0.1	98.3	1.6	0.4	0.3	0.2	1.8	1.0	SP
GS5	2.6-2.7	0.3	99.3	0.4	0.4	0.2	0.2	2.5	0.6	SP
BH3										
GS1	0.6-0.7	11.4	88.6	0	1.4	0.9	0.3	4.8	1.7	SW
SPT1	0.8-1.2	16.4	82.8	0.8	0.6	0.2	0.2	3.6	0.5	SP
GS2	1.3-1.4	3.1	95.2	1.7	0.6	0.3	0.2	2.8	1.0	SP
SPT2	1.5-1.9	4.9	92.8	2.5	0.6	0.3	0.2	2.8	1.0	SP
GS3	2.0-2.1	0.1	98.5	1.4	0.4	0.3	0.2	2.0	1.1	SW
GS4	2.8-2.9	0.2	98.7	1.1	0.4	0.3	0.2	2.2	1.0	SP
SPT4	3-3.4	2.8	96.5	0.7	0.4	0.3	0.2	2.0	1.1	SW
BH4										
GS1	0.6-0.7	0.6	98.5	0.9	0.6	0.4	0.2	2.5	1.0	SP
GS2 & SPT1	0.8-1.2	21.4	77.0	1.6	0.8	0.4	0.2	3.5	1.0	SP
SPT2 & GS3	1.5-1.9	2.0	96.8	1.1	0.3	0.2	0.2	2.1	0.8	SP
SPT3	2.2-2.6	0	98.7	1.3	0.4	0.2	0.2	2.0	1.0	SP
GS4	2.8-2.9	0.1	98.9	1.0	0.4	0.3	0.2	2.0	1.1	SW
SPT4	3-3.4	0.2	99.3	0.5	0.4	0.2	0.2	2.2	0.7	SP

Appendix B: Additional Results of Axial Load Field Tests

In regards to axial load field test results, additional tables, figures and backup calculations are shown which includes the following:

- The summary of coefficient α over 35 individual pile segment at different soil types.
- The summary of coefficient K_s and β over 35 individual pile segments at different soil types.
- The schematic of test setup for axial load field test
- The raw axial load vs. normalized axial displacement of 41 piles.
- The smoothened axial load vs. normalized axial displacement of 41 piles.
- The approximate method to obtain the value of Q_u of selected piles.
- Additional measured and estimated continuous torques with pile penetration depth
- The smoothening process of the raw axial load vs. normalized displacement of a pile.
- Backup calculations of the CPT-based method for micro screw piles.
- Backup calculations to determine the coefficient of K_s
- Backup calculations to determine the coefficient β
- Backup calculation for estimation of the ultimate capacities of the micropiles using the coefficient β.
- Backup calculations to get the K_t of each micro screw pile in compression and tension

Table B1. The summary of coefficient α over the individual pile segments at different soil types.

Shaft segment type in soil type	$q_{c.avg}$ (MPa)	Pile	Seg.	$q_{c,\,avg}$ (kPa)	q_{sU} (kPa)	α	$\alpha_{med.}$
Smooth segment in moderate compact sand with gravel	5–2	P5-C4	1	8909.9	141.4	63.0	101.6
		P5-C5	1	9184.9	94.3	97.4	
		P3-C4	1	7703.9	84.4	91.2	
		P3-C5	1	8909.9	84.2	105.8	
		P1-C3	1	7703.9	51.4	149.9	
		P5-T3	1	9894.5	39.0	254.0	
		P3-T3	1	9656.6	84.3	114.5	
		P1-T3	1	8346.6	106.4	78.4	
Smooth segment in compact to very compact sand with gravel	>12	P5-C4	2	18157.1	80.0	226.9	222.7
		P5-C5	2	17831.9	80.1	222.7	
		P5-T3	2	17392.1	88.4	196.7	
Threaded segment in compact to very compact sand with gravel	>12	P5-C4	3	9760.9	67.4	144.8	183.3
		P5-C4	4	7954.1	29.9	265.6	
		P5-C5	3	9504.8	45.0	211.2	
		P3-C4	3	12175.9	123.2	98.8	
		P3-C4	4	7937.7	12.4	639.1	
		P3-C5	3	11170.0	94.7	117.9	
		P3-C5	4	7787.2	11.3	689.4	
		P1-C3	3	10143.5	60.1	168.7	
		P5-T3	3	8620.5	43.5	197.9	
		P3-T3	3	10151.4	66.7	152.3	
		P3-T3	4	7524.9	22.6	332.4	
		P1-T3	3	9577.6	59.4	161.3	
Threaded segment in moderate compact sand with gravel	5-12	P3-C4	2	19720.7	44.7	440.9	397.4 (440.9)
		P3-C5	2	19829.3	98.0	202.4	
		P1-C3	2	~~18655.9~~	~~22.5~~	~~827.9~~	
		P3-T3	2	19490.7	55.1	353.8	
		P1-T3	2	18539.4	41.0	452.6	
Tapered segment in moderate compact sand with gravel under compressive loading	5-12	P5-C4	5	5954.1	~~40.3~~	~~147.9~~	36.2 (58.3)
		P3-C4	5	6003.5	103.0	58.3	
		P3-C5	5	5624.5	~~48.3~~	~~116.5~~	
		P1-C3	4	8030.7	222.0	36.2	
		P1-C3	5	5954.1	271.2	22.0	
Tapered segment in moderate compact sand with gravel under tensile loading	5-12	P5-T3	5	5366.9	147.6	36.4	41.9
		P1-T3	4	7852.2	118.6	66.2	
		P1-T3	5	5719.1	136.6	41.9	

Note: The values q_{sU} over pile P1-C3 segment 2, pile P5-C4 segment 5 and pile P3-C5 segment 5 have been not used to determine α_{min}.

Table B2. The summary of coefficient K_s and β over the individual pile segments at different soil types.

Segment type in soil type	Pile	Seg.	q_{sU} (kPa)	$\sigma'_{v1,avg}$ (kPa)	$\phi'_{p,avg}$ (kPa)	K_s	$K_{s,med.}$	$\sigma'_{v2,avg}$ (kPa)	β	$\beta_{med.}$
Upper smooth segment in compact sand with gravel	P5-C4	1	141.4	6.4	41.9	33.4	20.6	6.3	22.3	13.8
	P5-C5	1	94.3	6.6	42.1	21.4		6.6	14.4	
	P3-C4	1	84.4	5.5	41.0	24.0		5.4	15.6	
	P3-C5	1	84.2	6.4	41.9	19.9		6.3	13.3	
	P1-C3	1	51.4	5.5	41.0	14.6		5.4	9.5	
	P5-T3	1	39.0	7.3	42.6	7.9		7.3	5.4	
	P3-T3	1	84.3	7.1	42.4	17.7		7.0	12.0	
	P1-T3	1	106.4	5.9	41.5	27.4		5.9	18.1	
Lower smooth segment in compact sand with gravel	P5-C4	2	80.0	19.8	46.1	5.4	5.4	19.6	4.1	4.1
	P5-C5	2	80.1	20.4	45.9	5.3		20.2	4.0	
	P5-T3	2	88.4	21.5	45.6	5.6		21.4	4.1	
Upper threaded segment in compact sand with gravel	P5-C4	3	67.4	28.3	41.5	2.7	2.6	29.2	2.3	2.3
	P5-C5	3	45.0	28.5	41.3	1.8		29.5	1.5	
	P3-C4	2	44.7	16.1	47.1	2.6		16.0	2.8	
	P3-C4	3	123.2	26.0	43.0	5.1		26.3	4.7	
	P3-C5	2	98.0	17.5	46.9	5.2		17.3	5.7	
	P3-C5	3	94.7	27.0	42.4	3.8		27.5	3.4	
	P1-C3	2	22.5	17.7	46.6	1.2		17.5	1.3	
	P1-C3	3	60.1	28.4	41.8	2.4		29.1	2.1	
	P5-T3	3	43.5	29.9	40.7	1.7		31.1	1.4	
	P3-T3	2	55.1	19.3	46.5	2.7		19.1	2.9	
	P3-T3	3	66.7	28.2	41.8	2.6		28.9	2.3	
	P1-T3	2	41.0	18.6	46.4	2.1		18.4	2.2	
	P1-T3	3	59.4	29.0	41.5	2.3		29.9	2.0	
Lower threaded segment in loose sand	P5-C4	4	29.9	32.9	40.7	1.1	0.6	34.6	0.9	0.5
	P3-C4	4	12.4	32.5	40.6	0.4		34.1	0.4	
	P3-C5	4	11.3	33.1	40.6	0.4		34.8	0.3	
	P3-T3	4	22.6	33.8	40.4	0.8		35.6	0.6	
Tapered segment in loose sand under compressive load	P5-C4	5	~~40.3~~	~~36.2~~	~~39.5~~	~~1.3~~	7.7 (3.6)	~~37.6~~	~~1.1~~	6.3 (2.7)
	P3-C4	5	103.0	36.1	39.5	3.5		37.6	2.7	
	P3-C5	5	~~48.3~~	~~37.0~~	~~39.6~~	~~1.6~~		~~38.2~~	~~1.3~~	
	P1-C3	4	222.0	33.3	40.8	7.7		35.1	6.3	
	P1-C3	5	271.2	36.2	39.5	9.1		37.6	7.2	
Tapered segment in loose sand under tensile load	P3-T3	5	147.6	37.7	39.8	4.7	4.5	38.8	3.8	3.6
	P1-T3	4	118.6	33.7	40.7	4.1		35.5	3.3	
	P1-T3	5	136.6	36.7	39.6	4.5		38.0	3.6	

Note: The values q_{sU} over pile pile P5-C4 segment 5 and pile P3-C5 segment 5 have been not used to determine K_s and β.

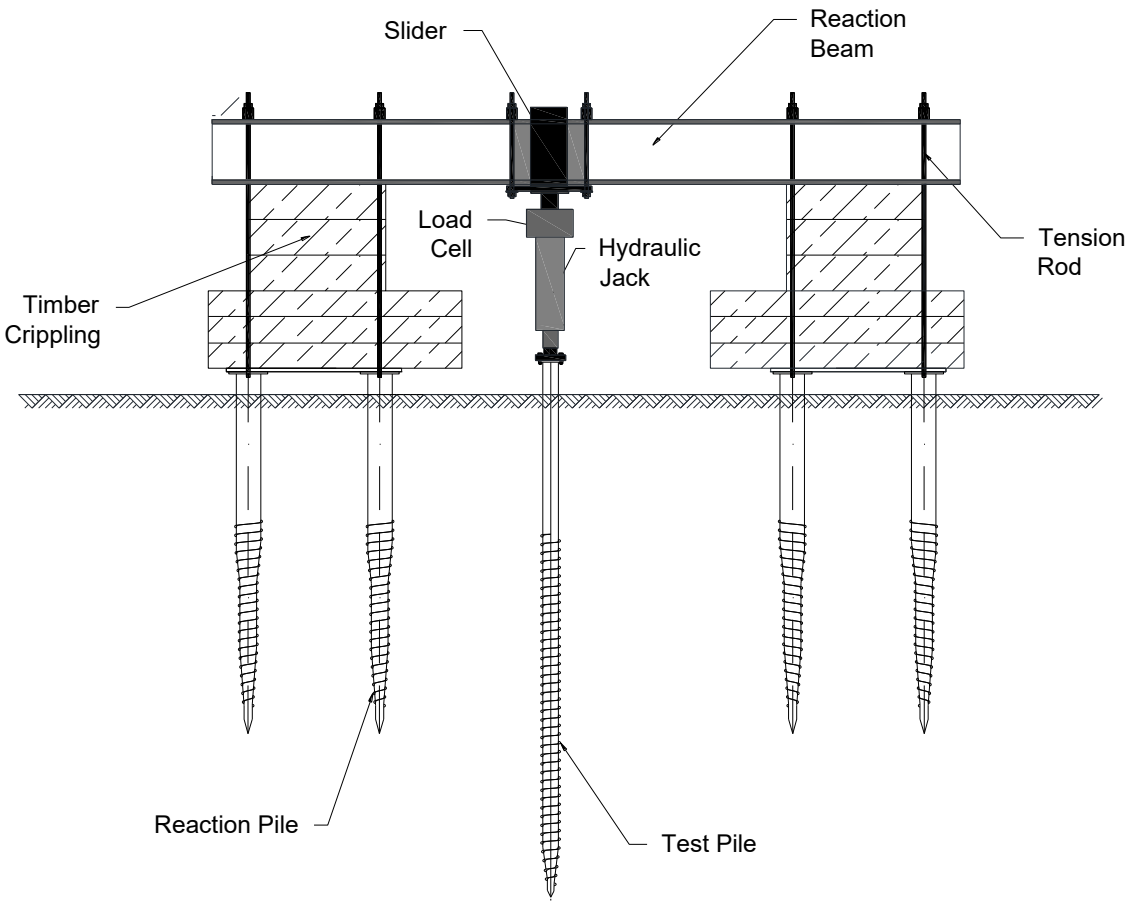

Figure B.1. Schematic of test setup for axial load field test

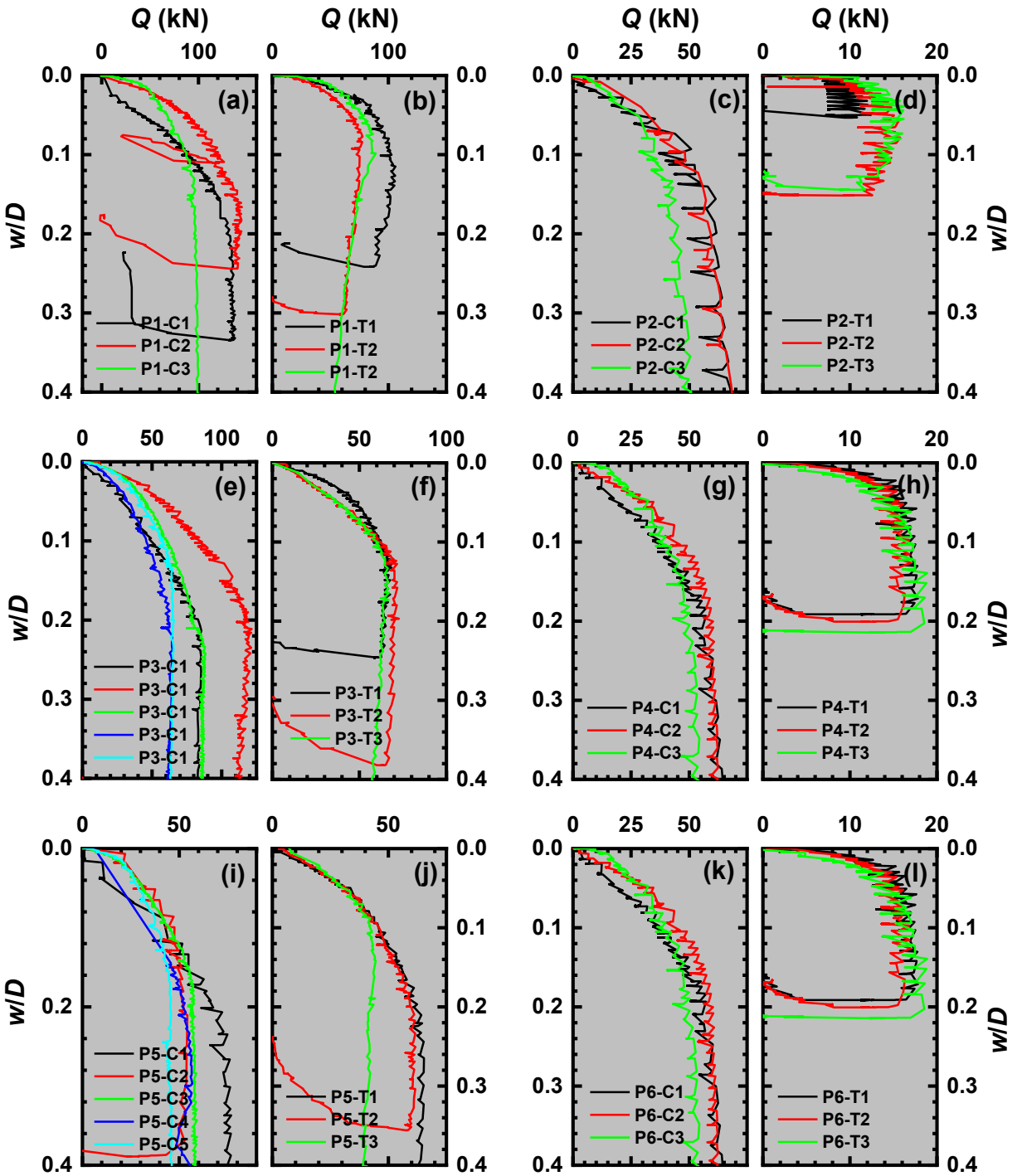

Figure B.2. Raw axial load (Q) vs. normalized axial displacement (w/D) of the pile: (a) P1 in comp., (b) P1 in tens., (c) P2 in comp., (d) P2 in tens., (e) P3 in comp., (f) P3 in tens., (g) P4 in comp., (h) P4 in tension, (i) P5 in comp., (j) P5 in tens., and (k) P6 in comp., (l) P6 in tens. at Sandpit.

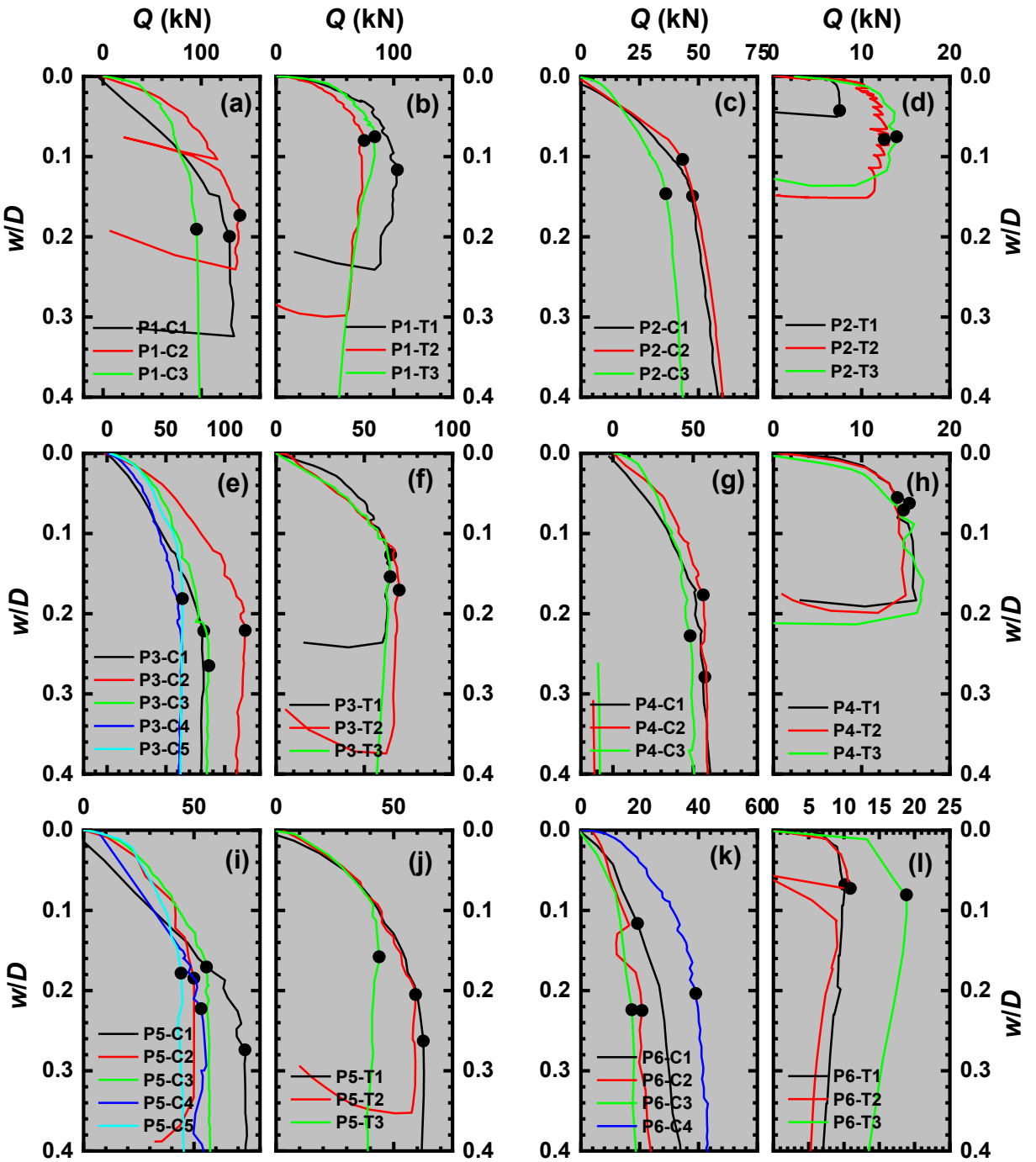

Figure B.3. Smoothened axial load (Q) vs. normalized axial displacement (w/D) of the pile: (a) P1 in comp., (b) P1 in tens., (c) P2 in comp., (d) P2 in tens., (e) P3 in comp., (f) P3 in tens., (g) P4 in comp., (h) P4 in tension, (i) P5 in comp., (j) P5 in tens., and (k) P6 in comp., (l) P6 in tens. at Sandpit.

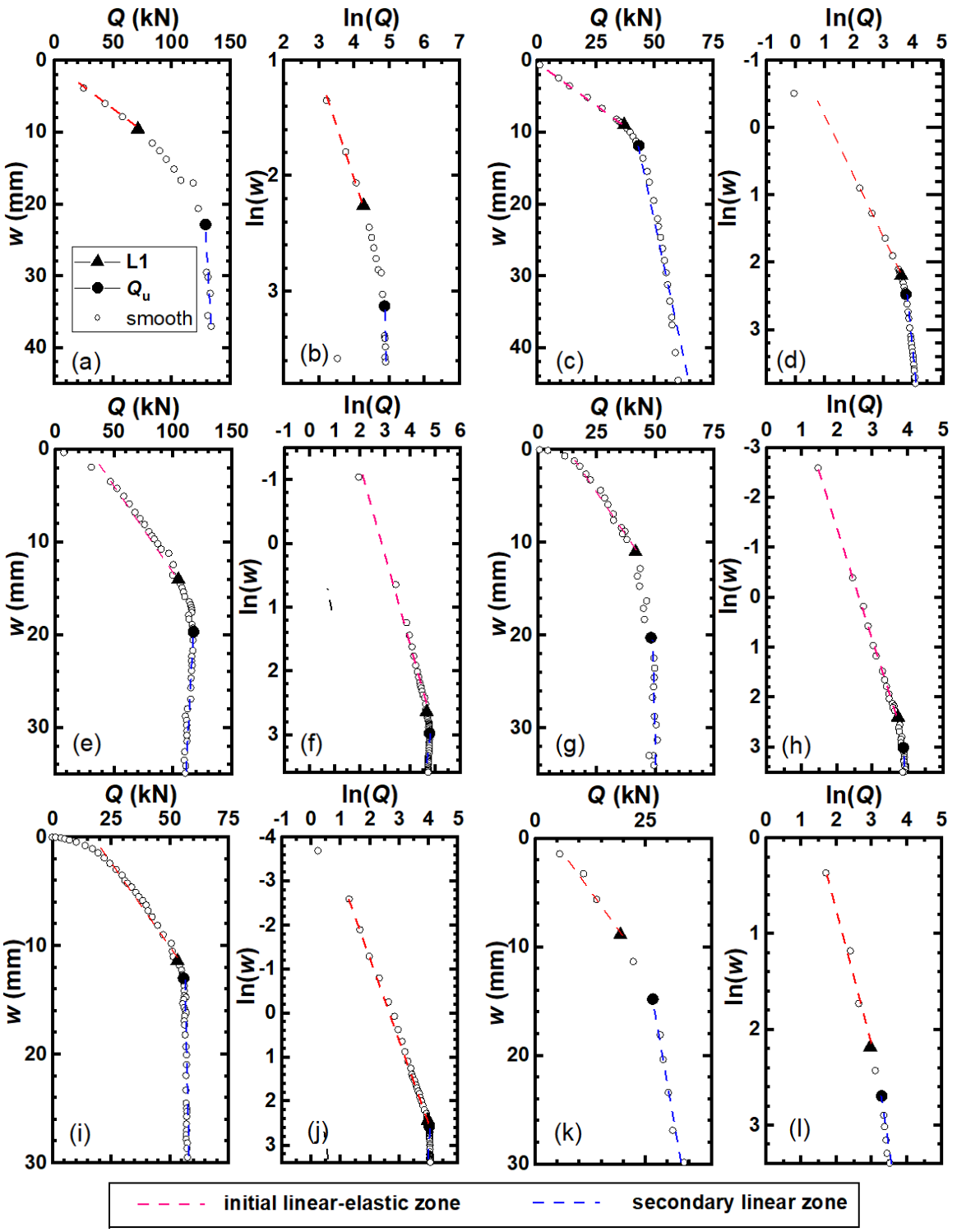

Figure B.4. Approximate method to obtain the value of Q_u of the pile: (a) and (b) P1 in comp., (c) and (d) P2 in comp., (e) and (f) P3 in comp., (g) and (h) P4 in tens., (i) and (j) P5 in comp., and (k) and (l) P6 in comp.

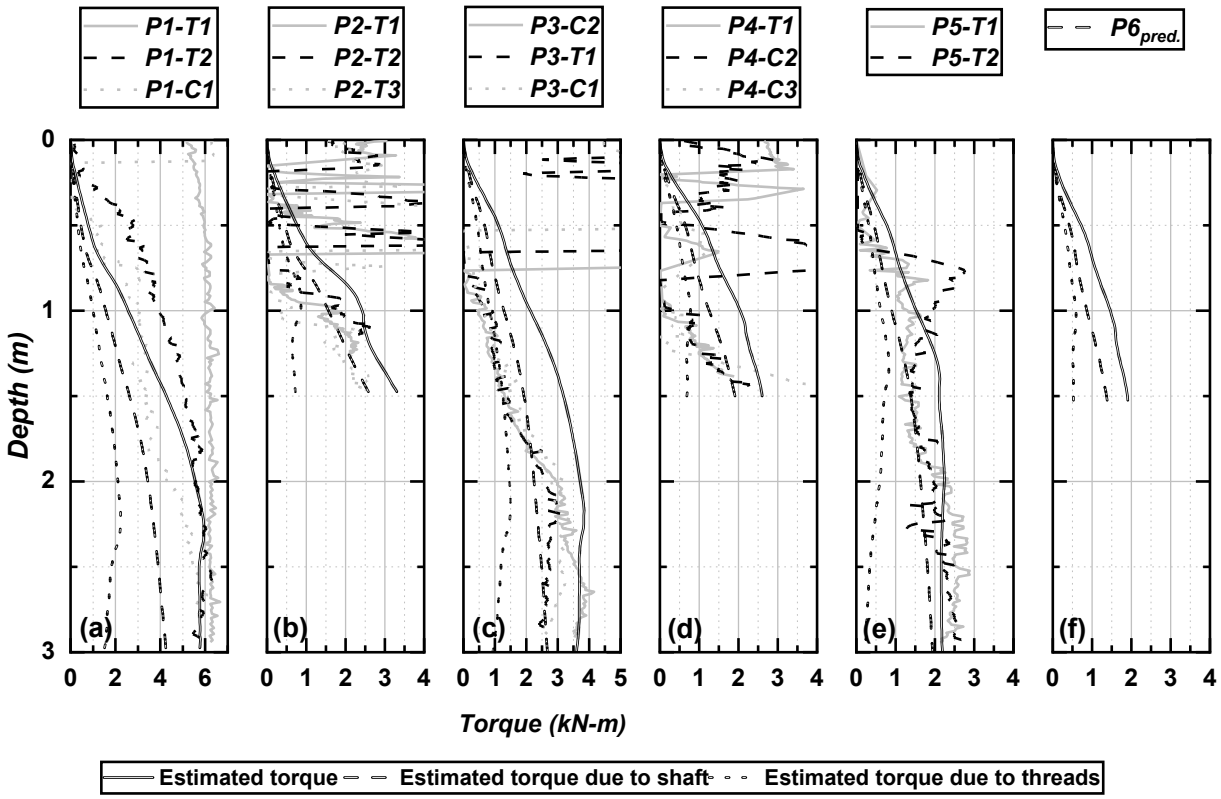

Figure B.5. Measured and estimated continuous torques with pile penetration depth for pile: (a) P1, (b) P2, (c) P3, (d) P4, (e) P5 and (f) P6 at Sandpit.

The Smoothening Process of the Raw Axial Load vs. Normalized Displacement of a Pile

Axial Compression Load Test

Project = "CCMC Load Tests" *InstallationDate* = "July 9, 2018" *TestDate* = "July 9, 2018"

PileNumber = "Pile 56" *PileModel* = "M114X3000" *ZeroReadings* := 6.24 *kN*

Data := READEXCEL ("..\..\Breuneheum\Field Testing – Piling\Daily Data\Pile 56 – July 9, 2018 – Instrumented – M114X3000 – Tension.xlsx", "P56!A3:Y5150")

$Time := Data^{\langle 2 \rangle}\ min$ $LP1 := Data^{\langle 4 \rangle}\ mm - Data_{0,4}\ mm$ $LP2 := Data^{\langle 5 \rangle}\ mm - Data_{0,5}\ mm$

$LoadCell := Data^{\langle 7 \rangle}\ kN$ $w_{raw} := \frac{(LP1 + LP2)}{2}$ $Q_{raw} := LoadCell - ZeroReadings$

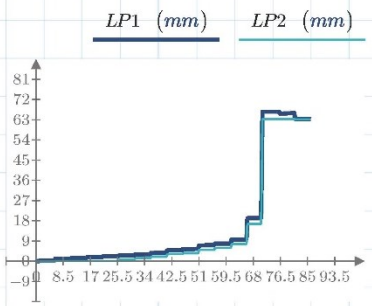

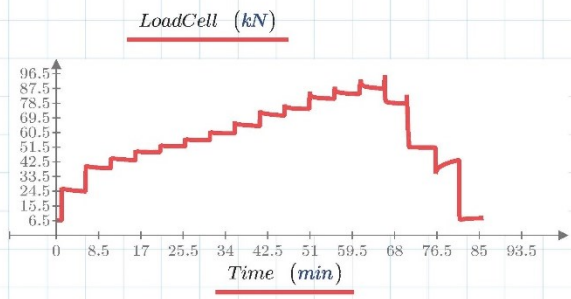

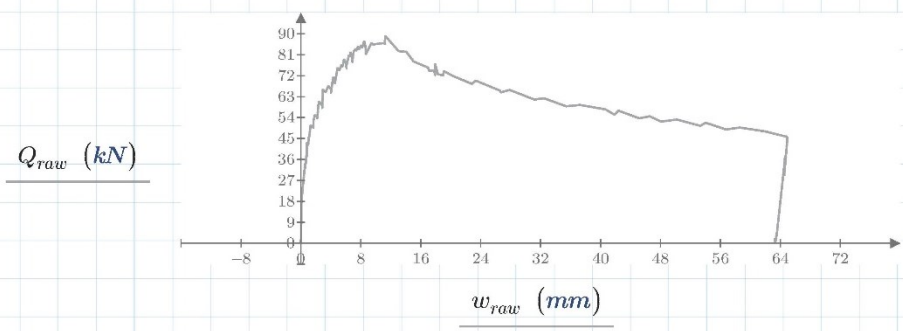

Step 1 of smoothing raw Q vs w

$Q_{smooth1}(Q, s) :=$

$j \leftarrow 0$
$i \leftarrow 0$
$n \leftarrow \text{rows}(Q)$
$localmax_i \leftarrow Q_j$
for $j \in 1, 2..n-10$
  if $\left(\text{abs}\left(Q_j - Q_{j-1}\right) > s\ kN\right)$
    $i \leftarrow i + 1$
    $localmax_i \leftarrow Q_{j-1}$
  $j \leftarrow j + 1$
$localmax$

$w_{smooth1}(Q, w, s) :=$

$j \leftarrow 0$
$i \leftarrow 0$
$n \leftarrow \text{rows}(Q)$
$localmax_i \leftarrow Q_j$
$dispmax_i \leftarrow w_j$
for $j \in 1, 2..n-10$
  if $\left(\text{abs}\left(Q_j - Q_{j-1}\right) > s\ kN\right)$
    $i \leftarrow i + 1$
    $localmax_i \leftarrow Q_{j-1}$
    $dispmax_i \leftarrow w_{j-1}$
  $j \leftarrow j + 1$
$dispmax$

Select the first value from two value whose load difference is s (kN). This steps gives the upper and lower bound of the curve.

$s := 0.05$ $\quad Q_{smooth1} := Q_{smooth1}(Q_{raw}, s)$ $\quad w_{smooth1} := w_{smooth1}(Q_{raw}, w_{raw}, s)$

$Q_{raw}\ (kN)$

$Q_{smooth1}\ (kN)$

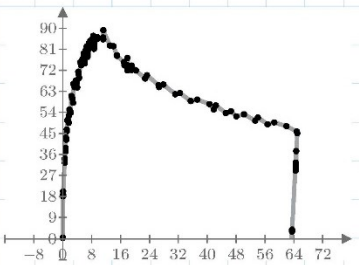

$w_{raw}\ (mm)$

$w_{smooth1}\ (mm)$

$Q_{raw}\ (kN)$

$Q_{smooth1}\ (kN)$

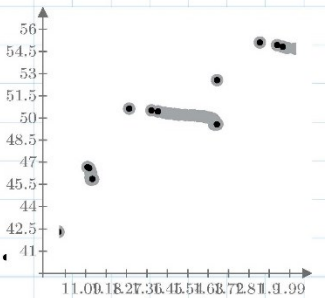

$w_{raw}\ (mm)$

$w_{smooth1}\ (mm)$

Step 2 of smoothing raw Q vs w

$Q_{LMin}(Q, r) :=$

$r \leftarrow r$
$n \leftarrow \text{floor}\left(\frac{\text{rows}(Q) - 1}{r}\right)$
$j \leftarrow 0$
$i \leftarrow 0$
for $i \in 0, 1..n-1$
  $LMin_i \leftarrow Q_j$
  for $j \in 1 + r \cdot i, 2 + r \cdot i..r + r \cdot i$
    if $Q_j < LMin_i$
      $LMin_i \leftarrow Q_j$
    $j \leftarrow j + 1$
  $i \leftarrow i + 1$
$LMin$

Find local min from a given number of data

$Q_{LMax}(Q, r) :=$

$r \leftarrow r$
$n \leftarrow \text{floor}\left(\frac{\text{rows}(Q) - 1}{r}\right)$
$j \leftarrow 0$
$i \leftarrow 0$
for $i \in 0, 1..n-1$
  $LMax_i \leftarrow Q_j$
  for $j \in 1 + r \cdot i, 2 + r \cdot i..r + r \cdot i$
    if $Q_j > LMax_i$
      $LMax_i \leftarrow Q_j$
    $j \leftarrow j + 1$
  $i \leftarrow i + 1$
$LMax$

Find local max from a given number of data

$n := 3$ $\quad Q_{smooth2min} := Q_{LMin}(Q_{smooth1}, n)$

$n := 3$ $\quad Q_{smooth2max} := Q_{LMax}(Q_{smooth1}, n)$

$w_{LMin}(Q, w, r) :=$

$r \leftarrow r$
$n \leftarrow \text{floor}\left(\frac{\text{rows}(Q) - 1}{r}\right)$
$j \leftarrow 0$
$i \leftarrow 0$
for $i \in 0, 1..n-1$
  $QLMin_i \leftarrow Q_j$
  $wLMin_i \leftarrow w_j$
  for $j \in 1 + r \cdot i, 2 + r \cdot i..r + r \cdot i$
    if $Q_j < QLMin_i$
      $LMin_i \leftarrow Q_j$
      $wLMin_i \leftarrow w_j$
    $j \leftarrow j + 1$
  $i \leftarrow i + 1$
$wLMin$

$w_{LMax}(Q, w, r) :=$

$r \leftarrow r$
$n \leftarrow \text{floor}\left(\frac{\text{rows}(Q) - 1}{r}\right)$
$j \leftarrow 0$
$i \leftarrow 0$
for $i \in 0, 1..n-1$
  $QLMax_i \leftarrow Q_j$
  $wLMax_i \leftarrow w_j$
  for $j \in 1 + r \cdot i, 2 + r \cdot i..r + r \cdot i$
    if $Q_j > QLMax_i$
      $QLMax_i \leftarrow Q_j$
      $wLMax_i \leftarrow w_j$
    $j \leftarrow j + 1$
  $i \leftarrow i + 1$
$wLMax$

$w_{smooth2min} := w_{LMin}(Q_{smooth1}, w_{smooth1}, n)$

$w_{smooth2max} := w_{LMax}(Q_{smooth1}, w_{smooth1}, n)$

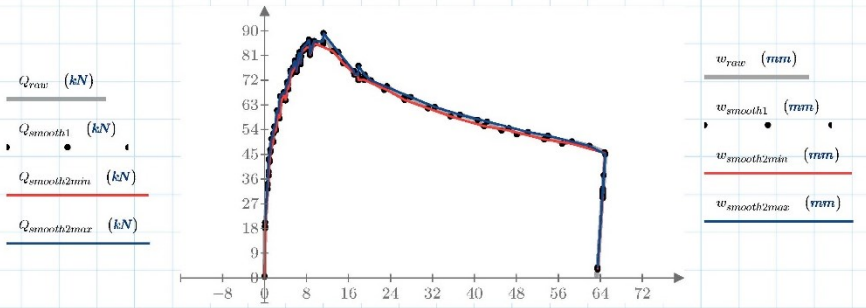

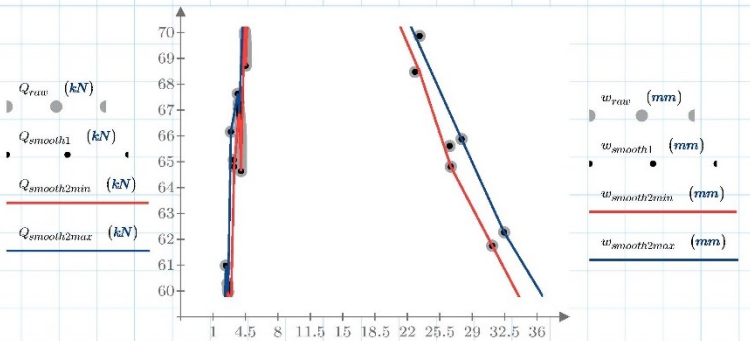

Step 3 of smoothing raw Q vs w

$r := 2$ $\quad Q_{smooth3} := \text{movavg}\left(Q_{smooth2min}, r\right)$ $\quad w_{smooth3} := \text{movavg}\left(w_{smooth2min}, r\right)$

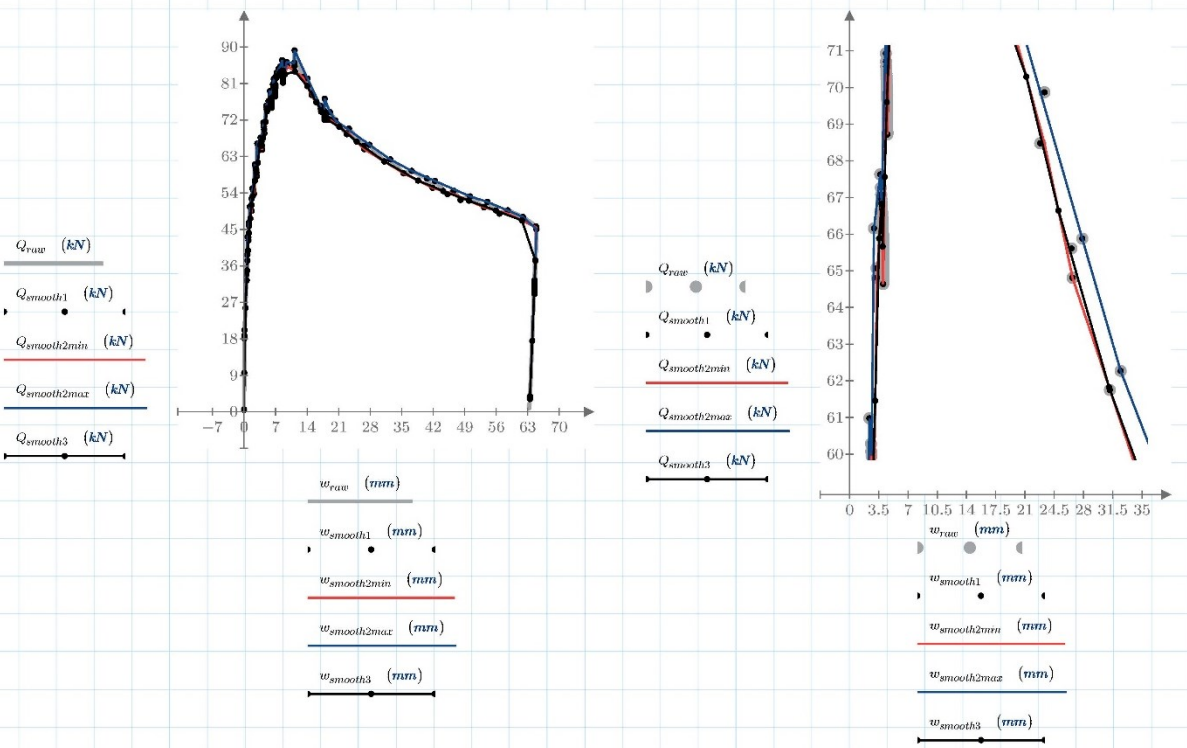

Backup Calculations of the CPT-Based Method for Micro Screw Piles

Unit Shaft Resistance

$$q_{s.P1.C3} := \begin{bmatrix} 51.39117 \\ 22.53505 \\ 60.11845 \\ 222.03653 \\ 271.21586 \end{bmatrix} \quad Depth_{P1.C3} := \begin{bmatrix} 0 \\ 0.5575 \\ 1.324 \\ 2.0135 \\ 2.3615 \\ 2.6805 \end{bmatrix} \quad q_{s.P3.C4} := \begin{bmatrix} 84.4319 \\ 44.72909 \\ 123.23406 \\ 12.42017 \\ 103.01332 \end{bmatrix} \quad Depth_{P3.C4} := \begin{bmatrix} 0 \\ 0.5645 \\ 1.158 \\ 1.7835 \\ 2.3575 \\ 2.6725 \end{bmatrix}$$

$$q_{s.P3.C5} := \begin{bmatrix} 84.21048 \\ 97.9576 \\ 94.72792 \\ 11.29595 \\ 48.2722 \end{bmatrix} \quad Depth_{P3.C5} := \begin{bmatrix} 0 \\ 0.6495 \\ 1.243 \\ 1.8685 \\ 2.4425 \\ 2.7575 \end{bmatrix} \quad q_{s.P5.C4} := \begin{bmatrix} 141.35705 \\ 80.00662 \\ 67.41593 \\ 29.94945 \\ 40.26207 \end{bmatrix} \quad Depth_{P5.C4} := \begin{bmatrix} 0 \\ 0.65432 \\ 1.46932 \\ 1.89332 \\ 2.35982 \\ 2.67582 \end{bmatrix}$$

$$q_{s.P5.C5} := \begin{bmatrix} 94.32384 \\ 80.08196 \\ 45.0122 \end{bmatrix} \quad Depth_{P5.C5} := \begin{bmatrix} 0 \\ 0.684 \\ 1.499 \\ 1.923 \end{bmatrix} \quad q_{s.P5.T3} := \begin{bmatrix} 38.9497 \\ 88.44154 \\ 43.54921 \end{bmatrix} \quad Depth_{P5.T3} := \begin{bmatrix} 0 \\ 0.764 \\ 1.579 \\ 2.003 \end{bmatrix}$$

$$q_{s.P3.T3} := \begin{bmatrix} 84.34213 \\ 55.0859 \\ 66.67408 \\ 22.63973 \\ 147.57244 \end{bmatrix} \quad Depth_{P3.T3} := \begin{bmatrix} 0 \\ 0.7406 \\ 1.3341 \\ 1.9596 \\ 2.5336 \\ 2.8486 \end{bmatrix} \quad q_{s.P1.T3} := \begin{bmatrix} 106.43756 \\ 40.9601 \\ 59.37229 \\ 118.59131 \\ 136.60732 \end{bmatrix} \quad Depth_{P1.T3} := \begin{bmatrix} 0 \\ 0.6125 \\ 1.379 \\ 2.0685 \\ 2.4165 \\ 2.7355 \end{bmatrix}$$

Cone Penetration Test Data

$$q_{c.CPT}^{(0)} := \text{READEXCEL}\left(\text{“..\..\..\Breuneheum\Site Investigation\CPT\(CPT)\CPT1qc.xlsx”, “Sheet1!A1:A121”}\right)$$

$$q_{c.CPT}^{(1)} := \text{READEXCEL}\left(\text{“..\..\..\Breuneheum\Site Investigation\CPT\(CPT)\CPT2qc.xlsx”, “Sheet1!A1:A121”}\right)$$

$$q_{c.CPT}^{(2)} := \text{READEXCEL}\left(\text{“..\..\..\Breuneheum\Site Investigation\CPT\(CPT)\CPT3qc.xlsx”, “Sheet1!A1:A121”}\right)$$

$$q_{c.CPT}^{(3)} := \text{READEXCEL}\left(\text{“..\..\..\Breuneheum\Site Investigation\CPT\(CPT)\CPT4qc.xlsx”, “Sheet1!A1:A121”}\right)$$

Average CPT qc reading over an individual pile segment

The above two function are used to calculate the average CPT-qc reading over an individual pile segment

$$Data_{ave}\left(Data_1, Data_2, Data_3\right) := \left\| \begin{array}{l} TOL \leftarrow 0.025 \\ \text{for } i \in 0,1..\text{rows}\left(Data_1\right) - 2 \\ \quad Interpolation_i \leftarrow \text{mean}\left(\text{lookup}\left(\begin{bmatrix} Data_{1_i} \\ Data_{1_{i+1}} \end{bmatrix}, Data_2, Data_3, \text{“range”}\right)\right) \\ \quad Interpolation_i \\ Interpolation \end{array} \right.$$

$$q_{c.CPT.avg} := \left\| \begin{array}{l} \text{for } i \in 0,1..51 \\ \quad q_{c.CPT.avg_i} \leftarrow q_{c.CPT_{i,2}} \\ \quad q_{c.CPT.avg_i} \\ \text{for } i \in 52,53..\text{rows}\left(q_{c.CPT}\right) - 1 \\ \quad q_{c.CPT.avg_i} \leftarrow \text{mean}\left(q_{c.CPT_{i,0}}, q_{c.CPT_{i,1}}, q_{c.CPT_{i,2}}, q_{c.CPT_{i,3}}\right) \\ \quad q_{c.CPT.avg_i} \\ q_{c.CPT.avg} \end{array} \right.$$

The tip resistance of CPT 1, CPT 2 and CPT 4 were effected by frost. The ground at CPT-3 was heat thread. Therefore, we are using CPT-3 tip resistance from the ground surface to a depth of 1.3 m. Afterward, we are taking the average of the four CPT readings.

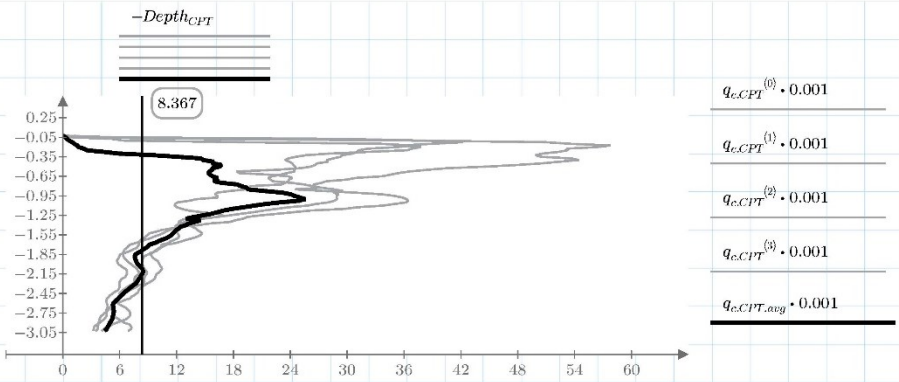

$q_{c.P1.C3.CPT} := Data_{ave}\left(Depth_{P1.C3}, Depth_{CPT}, q_{c.CPT.avg}\right)$
$q_{c.P3.C4.CPT} := Data_{ave}\left(Depth_{P3.C4}, Depth_{CPT}, q_{c.CPT.avg}\right)$
$q_{c.P3.C5.CPT} := Data_{ave}\left(Depth_{P3.C5}, Depth_{CPT}, q_{c.CPT.avg}\right)$
$q_{c.P5.C4.CPT} := Data_{ave}\left(Depth_{P5.C4}, Depth_{CPT}, q_{c.CPT.avg}\right)$
$q_{c.P5.C5.CPT} := Data_{ave}\left(Depth_{P5.C5}, Depth_{CPT}, q_{c.CPT.avg}\right)$
$q_{c.P1.T3.CPT} := Data_{ave}\left(Depth_{P1.T3}, Depth_{CPT}, q_{c.CPT.avg}\right)$
$q_{c.P3.T3.CPT} := Data_{ave}\left(Depth_{P3.T3}, Depth_{CPT}, q_{c.CPT.avg}\right)$
$q_{c.P5.T3.CPT} := Data_{ave}\left(Depth_{P5.T3}, Depth_{CPT}, q_{c.CPT.avg}\right)$

The average CPT qc over the individual pile segments of eight instrumented pile

Calculate the friction coefficient, alpha

$$\alpha\left(Data_1, Data_2\right) := \left\| \begin{array}{l} \text{for } i \in 0,1..\text{rows}\left(Data_1\right)-1 \\ \quad \left\| \begin{array}{l} \text{if } Data_{2_i} \neq 0 \\ \quad \left\| \alpha_i \leftarrow \dfrac{Data_{2_i}}{Data_{1_i}} \right. \\ \alpha_i \end{array} \right. \\ \alpha \end{array} \right.$$

$\alpha_{P1.C3} := \alpha\left(q_{s.P1.C3}, q_{c.P1.C3.CPT}\right)$
$\alpha_{P3.C4} := \alpha\left(q_{s.P3.C4}, q_{c.P3.C4.CPT}\right)$
$\alpha_{P3.C5} := \alpha\left(q_{s.P3.C5}, q_{c.P3.C5.CPT}\right)$
$\alpha_{P5.C4} := \alpha\left(q_{s.P5.C4}, q_{c.P5.C4.CPT}\right)$
$\alpha_{P5.C5} := \alpha\left(q_{s.P5.C5}, q_{c.P5.C5.CPT}\right)$
$\alpha_{P1.T3} := \alpha\left(q_{s.P1.T3}, q_{c.P1.T3.CPT}\right)$
$\alpha_{P3.T3} := \alpha\left(q_{s.P3.T3}, q_{c.P3.T3.CPT}\right)$
$\alpha_{P5.T3} := \alpha\left(q_{s.P5.T3}, q_{c.P5.T3.CPT}\right)$

Collect the friction coefficient, alpha over the smooth segment (qc = 5-12 MPa)

$$Data_{sm.1}\left(D_1, D_2, D_3, D_4, D_5, D_6, D_7, D_8\right) := \left\| \begin{array}{l} \text{for } j \in 0,1..\text{cols}\left(D_1\right)-1 \\ \quad \left\| D_{sm.1}^{\langle j \rangle} \leftarrow \left[D1_{0,j} \;\; D2_{0,j} \;\; D3_{0,j} \;\; D4_{0,j} \;\; D5_{0,j} \;\; D6_{0,j} \;\; D7_{0,j} \;\; D8_{0,j} \right]^{\mathrm{T}} \right. \\ D_{sm.1} \end{array} \right.$$

D means data

$\alpha_{sm.1} := Data_{sm.1}\left(\alpha_{P5.C4}, \alpha_{P5.C5}, \alpha_{P3.C4}, \alpha_{P3.C5}, \alpha_{P1.C3}, \alpha_{P5.T3}, \alpha_{P3.T3}, \alpha_{P1.T3}\right)$

$\alpha_{sm.1.median} := \text{median}\left(\alpha_{sm.1}\right) = 101.591$

Collect the friction coefficient, alpha over the smooth segment (qc > 12 MPa)

$$Data_{sm.2}\left(D_1, D_2, D_3, D_4, D_5, D_6, D_7, D_8\right) := \left\| \begin{array}{l} \text{for } j \in 0,1..\text{cols}\left(D_1\right)-1 \\ \quad \left\| D_{sm.2}^{\langle j \rangle} \leftarrow \left[D1_{1,j} \;\; D2_{1,j} \;\; D6_{1,j} \right]^{\mathrm{T}} \right. \\ D_{sm.2} \end{array} \right.$$

$\alpha_{sm.2} := Data_{sm.2}\left(\alpha_{P5.C4}, \alpha_{P5.C5}, \alpha_{P3.C4}, \alpha_{P3.C5}, \alpha_{P1.C3}, \alpha_{P5.T3}, \alpha_{P3.T3}, \alpha_{P1.T3}\right)$

$\alpha_{sm.2.median} := \text{median}\left(\alpha_{sm.2}\right) = 222.671$

Collect the friction coefficient, alpha over the threaded segment (qc = 5-12 MPa)

$$Data_{th.1}(D_1, D_2, D_3, D_4, D_5, D_6, D_7, D_8) := \left\| \begin{array}{l} \text{for } j \in 0,1..\text{cols}(D_1) - 1 \\ \quad Data_{th.1}^{\langle j \rangle} \leftarrow \left[D_{1_{2,j}} \;\; D_{1_{3,j}} \;\; D_{2_{2,j}} \;\; NaN \;\; D_{3_{2,j}} \;\; D_{3_{3,j}} \;\; \ldots \right]^{\mathrm{T}} \\ Data_{th.1} \end{array} \right.$$

$$\alpha_{th.1} := Data_{th.1}(\alpha_{P5.C4}, \alpha_{P5.C5}, \alpha_{P3.C4}, \alpha_{P3.C5}, \alpha_{P1.C3}, \alpha_{P5.T3}, \alpha_{P3.T3}, \alpha_{P1.T3}) \qquad \alpha_{th.1} := \text{filterNaN}(\alpha_{th.1})$$

$$\alpha_{th.1.median} := \text{median}(\alpha_{th.1}) = 183.336$$

Collect the friction coefficient, alpha over the threaded segment (qc > 12 MPa)

$$Data_{th.2}(D_1, D_2, D_3, D_4, D_5, D_6, D_7, D_8) := \left\| \begin{array}{l} \text{for } j \in 0,1..\text{cols}(D_1) - 1 \\ \quad Data_{th.2}^{\langle j \rangle} \leftarrow \left[D_{3_{1,j}} \;\; D_{4_{1,j}} \;\; D_{5_{1,j}} \;\; D_{7_{1,j}} \;\; D_{8_{1,j}} \right]^{\mathrm{T}} \\ Data_{th.2} \end{array} \right.$$

$$\alpha_{th.2} := Data_{th.2}(\alpha_{P5.C4}, \alpha_{P5.C5}, \alpha_{P3.C4}, \alpha_{P3.C5}, \alpha_{P1.C3}, \alpha_{P5.T3}, \alpha_{P3.T3}, \alpha_{P1.T3})$$

$$\alpha_{th.2.median} := \text{median}(\alpha_{th.2}) = 440.893$$

$$\alpha_{th.2.median} := \text{median}(\alpha_{th.2'}) = 397.359$$

Collect the friction coefficient, alpha over the tapered segment in compression (qc = 5 -12 MPa)

$$Data_{t.c}(D_1, D_2, D_3, D_4, D_5, D_6, D_7, D_8) := \left\| \begin{array}{l} \text{for } j \in 0,1..\text{cols}(D_1) - 1 \\ \quad D_{t.c}^{\langle j \rangle} \leftarrow \left[D_{1_{4,j}} \;\; NaN \;\; D_{3_{4,j}} \;\; D_{4_{4,j}} \;\; D_{5_{3,j}} \;\; D_{5_{4,j}} \right]^{\mathrm{T}} \\ D_{t.c} \end{array} \right.$$

$$\alpha_{t.c} := Data_{t.c}(\alpha_{P5.C4}, \alpha_{P5.C5}, \alpha_{P3.C4}, \alpha_{P3.C5}, \alpha_{P1.C3}, \alpha_{P5.T3}, \alpha_{P3.T3}, \alpha_{P1.T3}) \qquad \alpha_{t.c} := \text{filterNaN}(\alpha_{t.c})$$

$$\alpha_{t.c.median} := \text{median}(\alpha_{t.c}) = 58.279$$

$$\alpha_{t.c.median} := \text{median}(\alpha_{t.c'}) = 36.168$$

Collect the friction coefficient, alpha over the tapered segment in tension (qc = 5 -12 MPa)

$$Data_{t.t}(D_1, D_2, D_3, D_4, D_5, D_6, D_7, D_8) := \left\| \begin{array}{l} \text{for } j \in 0,1..\text{cols}(D_1) - 1 \\ \quad D_{t.t}^{\langle j \rangle} \leftarrow \left[NaN \;\; D_{7_{4,j}} \;\; D_{8_{3,j}} \;\; D_{8_{4,j}} \right]^{\mathrm{T}} \\ D_{t.t} \end{array} \right.$$

$$\alpha_{t.t} := Data_{t.t}(\alpha_{P5.C4}, \alpha_{P5.C5}, \alpha_{P3.C4}, \alpha_{P3.C5}, \alpha_{P1.C3}, \alpha_{P5.T3}, \alpha_{P3.T3}, \alpha_{P1.T3}) \qquad \alpha_{t.t} := \text{filterNaN}(\alpha_{t.t})$$

$$\alpha_{t.t.median} := \text{median}(\alpha_{t.t}) = 41.865$$

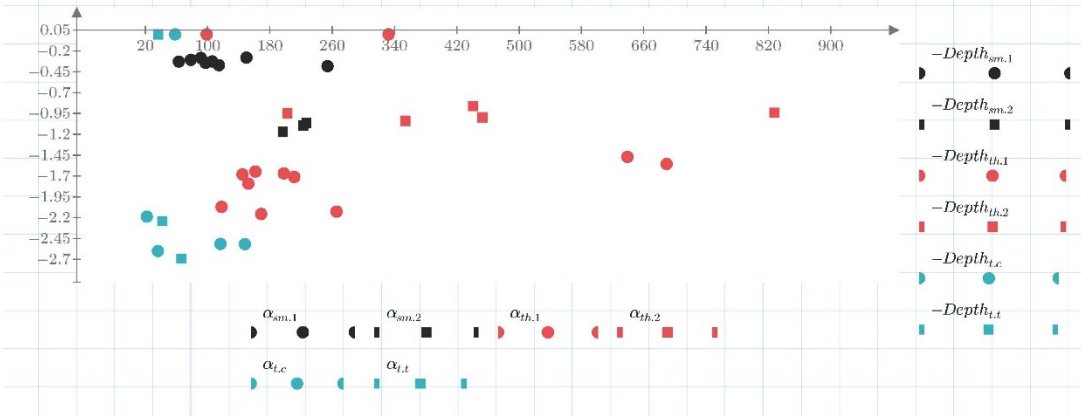

Backup Calculations to Determine the Coefficient of K_s

Unit Shaft Resistance

$$q_{s.P1.C3} := \begin{bmatrix} 51.39117 \\ 22.53505 \\ 60.11845 \\ 222.03653 \\ 271.21586 \end{bmatrix} \quad Depth_{P1.C3} := \begin{bmatrix} 0 \\ 0.5575 \\ 1.324 \\ 2.0135 \\ 2.3615 \\ 2.6805 \end{bmatrix} \quad q_{s.P3.C4} := \begin{bmatrix} 84.4319 \\ 44.72909 \\ 123.23406 \\ 12.42017 \\ 103.01332 \end{bmatrix} \quad Depth_{P3.C4} := \begin{bmatrix} 0 \\ 0.5645 \\ 1.158 \\ 1.7835 \\ 2.3575 \\ 2.6725 \end{bmatrix}$$

$$q_{s.P3.C5} := \begin{bmatrix} 84.21048 \\ 97.9576 \\ 94.72792 \\ 11.29595 \\ 48.2722 \end{bmatrix} \quad Depth_{P3.C5} := \begin{bmatrix} 0 \\ 0.6495 \\ 1.243 \\ 1.8685 \\ 2.4425 \\ 2.7575 \end{bmatrix} \quad q_{s.P5.C4} := \begin{bmatrix} 141.35705 \\ 80.00662 \\ 67.41593 \\ 29.94945 \\ 40.26207 \end{bmatrix} \quad Depth_{P5.C4} := \begin{bmatrix} 0 \\ 0.65432 \\ 1.46932 \\ 1.89332 \\ 2.35982 \\ 2.67582 \end{bmatrix}$$

$$q_{s.P5.C5} := \begin{bmatrix} 94.32384 \\ 80.08196 \\ 45.0122 \end{bmatrix} \quad Depth_{P5.C5} := \begin{bmatrix} 0 \\ 0.684 \\ 1.499 \\ 1.923 \end{bmatrix} \quad q_{s.P5.T3} := \begin{bmatrix} 38.9497 \\ 88.44154 \\ 43.54921 \end{bmatrix} \quad Depth_{P5.T3} := \begin{bmatrix} 0 \\ 0.764 \\ 1.579 \\ 2.003 \end{bmatrix}$$

$$q_{s.P3.T3} := \begin{bmatrix} 84.34213 \\ 55.0859 \\ 66.67408 \\ 22.63973 \\ 147.57244 \end{bmatrix} \quad Depth_{P3.T3} := \begin{bmatrix} 0 \\ 0.7406 \\ 1.3341 \\ 1.9596 \\ 2.5336 \\ 2.8486 \end{bmatrix} \quad q_{s.P1.T3} := \begin{bmatrix} 106.43756 \\ 40.9601 \\ 59.37229 \\ 118.59131 \\ 136.60732 \end{bmatrix} \quad Depth_{P1.T3} := \begin{bmatrix} 0 \\ 0.6125 \\ 1.379 \\ 2.0685 \\ 2.4165 \\ 2.7355 \end{bmatrix}$$

Cone Penetration Test Data

$\sigma_{v.e} := \text{READEXCEL}(\text{".\Average values of all CPT.xlsx"}, \text{"Sheet1!j3:j123"})$

$\phi_p := \text{READEXCEL}(\text{".\Average values of all CPT.xlsx"}, \text{"Sheet1!i3:i123"})$

The CPT 1, CPT 2 and CPT 4 were effected by frost. The ground at CPT-3 was heat thread. Therefore, we are using data from CPT-3.

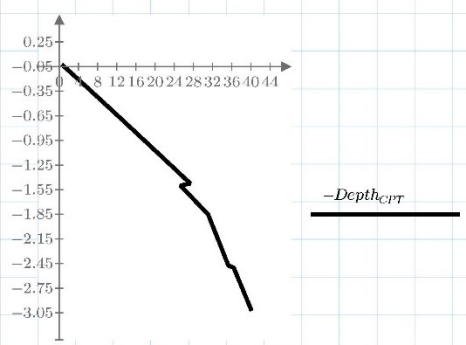

$\sigma_{v.e}$

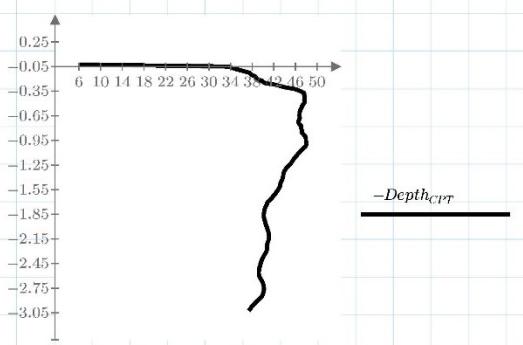

ϕ_p

Average effective stress and peak friction angle interpreted from CPT readings over an individual pile segment

$$Data_{ave}(Data_1, Data_2, Data_3) := \left\| \begin{array}{l} TOL \leftarrow 0.025 \\ \text{for } i \in 0, 1 .. \text{rows}(Data_1) - 2 \\ \quad \left\| \begin{array}{l} Interpolation_i \leftarrow \text{mean}\left(\text{lookup}\left(\begin{bmatrix} Data_{1_i} \\ Data_{1_{i+1}} \end{bmatrix}, Data_2, Data_3, \text{"range"}\right)\right) \\ \quad Interpolation_i \end{array} \right. \\ Interpolation \end{array} \right.$$

$$\sigma_{v.e.P5.C4.CPT} := Data_{ave}\left(Depth_{P5.C4}, Depth_{CPT}, \sigma_{v.e}\right) \qquad \phi_{p.P5.C4.CPT} := Data_{ave}\left(Depth_{P5.C4}, Depth_{CPT}, \phi_p\right) \cdot \frac{\pi}{180}$$

$$\sigma_{v.e.P5.C5.CPT} := Data_{ave}\left(Depth_{P5.C5}, Depth_{CPT}, \sigma_{v.e}\right) \qquad \phi_{p.P5.C5.CPT} := Data_{ave}\left(Depth_{P5.C5}, Depth_{CPT}, \phi_p\right) \cdot \frac{\pi}{180}$$

$$\sigma_{v.e.P3.C4.CPT} := Data_{ave}\left(Depth_{P3.C4}, Depth_{CPT}, \sigma_{v.e}\right) \qquad \phi_{p.P3.C4.CPT} := Data_{ave}\left(Depth_{P3.C4}, Depth_{CPT}, \phi_p\right) \cdot \frac{\pi}{180}$$

$$\sigma_{v.e.P3.C5.CPT} := Data_{ave}\left(Depth_{P3.C5}, Depth_{CPT}, \sigma_{v.e}\right) \qquad \phi_{p.P3.C5.CPT} := Data_{ave}\left(Depth_{P3.C5}, Depth_{CPT}, \phi_p\right) \cdot \frac{\pi}{180}$$

$$\sigma_{v.e.P1.C3.CPT} := Data_{ave}\left(Depth_{P1.C3}, Depth_{CPT}, \sigma_{v.e}\right) \qquad \phi_{p.P1.C3.CPT} := Data_{ave}\left(Depth_{P1.C3}, Depth_{CPT}, \phi_p\right) \cdot \frac{\pi}{180}$$

$$\sigma_{v.e.P5.T3.CPT} := Data_{ave}\left(Depth_{P5.T3}, Depth_{CPT}, \sigma_{v.e}\right) \qquad \phi_{p.P5.T3.CPT} := Data_{ave}\left(Depth_{P5.T3}, Depth_{CPT}, \phi_p\right) \cdot \frac{\pi}{180}$$

$$\sigma_{v.e.P3.T3.CPT} := Data_{ave}\left(Depth_{P3.T3}, Depth_{CPT}, \sigma_{v.e}\right) \qquad \phi_{p.P3.T3.CPT} := Data_{ave}\left(Depth_{P3.T3}, Depth_{CPT}, \phi_p\right) \cdot \frac{\pi}{180}$$

$$\sigma_{v.e.P1.T3.CPT} := Data_{ave}\left(Depth_{P1.T3}, Depth_{CPT}, \sigma_{v.e}\right) \qquad \phi_{p.P1.T3.CPT} := Data_{ave}\left(Depth_{P1.T3}, Depth_{CPT}, \phi_p\right) \cdot \frac{\pi}{180}$$

Collect the coefficient of lateral earth pressure, Ks over the upper smooth segment $\delta := 0.8$

$$K_{P5}\left(q_s, \sigma_{v.e.}, \phi\right) := \left\| \begin{array}{l} \text{for } i \in 0,1..1 \\ \quad K_i \leftarrow \dfrac{q_{s_i}}{\sigma_{v.e._i} \cdot \tan\left((\delta) \cdot \phi_i\right)} \\ \text{for } i \in 2,3..\text{rows}\left(q_s\right) - 1 \\ \quad K_i \leftarrow \dfrac{q_{s_i}}{\sigma_{v.e._i} \cdot \tan\left(\phi_i\right)} \\ K \end{array} \right\| \qquad K_{P3P1}\left(q_s, \sigma_{v.e.}, \phi\right) := \left\| \begin{array}{l} \text{for } i \in 0 \\ \quad K_i \leftarrow \dfrac{q_{s_i}}{\sigma_{v.e._i} \cdot \tan\left((\delta) \cdot \phi_i\right)} \\ \text{for } i \in 1,2..\text{rows}\left(q_s\right) - 1 \\ \quad K_i \leftarrow \dfrac{q_{s_i}}{\sigma_{v.e._i} \cdot \tan\left(\phi_i\right)} \\ K \end{array} \right\|$$

$$K_{P5.C4.p} := K_{P5}\left(q_{s.P5.C4}, \sigma_{v.e.P5.C4.CPT}, \phi_{p.P5.C4.CPT}\right) \qquad K_{P5.C5.p} := K_{P5}\left(q_{s.P5.C5}, \sigma_{v.e.P5.C5.CPT}, \phi_{p.P5.C5.CPT}\right)$$

$$K_{P3.C4.p} := K_{P3P1}\left(q_{s.P3.C4}, \sigma_{v.e.P3.C4.CPT}, \phi_{p.P3.C4.CPT}\right) \qquad K_{P3.C5.p} := K_{P3P1}\left(q_{s.P3.C5}, \sigma_{v.e.P3.C5.CPT}, \phi_{p.P3.C5.CPT}\right)$$

$$K_{P1.C3.p} := K_{P3P1}\left(q_{s.P1.C3}, \sigma_{v.e.P1.C3.CPT}, \phi_{p.P1.C3.CPT}\right) \qquad K_{P5.T3.p} := K_{P5}\left(q_{s.P5.T3}, \sigma_{v.e.P5.T3.CPT}, \phi_{p.P5.T3.CPT}\right)$$

$$K_{P3.T3.p} := K_{P3P1}\left(q_{s.P3.T3}, \sigma_{v.e.P3.T3.CPT}, \phi_{p.P3.T3.CPT}\right) \qquad K_{P1.T3.p} := K_{P3P1}\left(q_{s.P1.T3}, \sigma_{v.e.P1.T3.CPT}, \phi_{p.P1.T3.CPT}\right)$$

$$K_P := \tan\left(\left(45 + \frac{\phi_p}{2}\right) \cdot \frac{\pi}{180}\right)^2 \qquad K_a := 2 \cdot \left(1 - \sin\left(\phi_p \cdot \left(\frac{\pi}{180}\right)\right)\right)$$

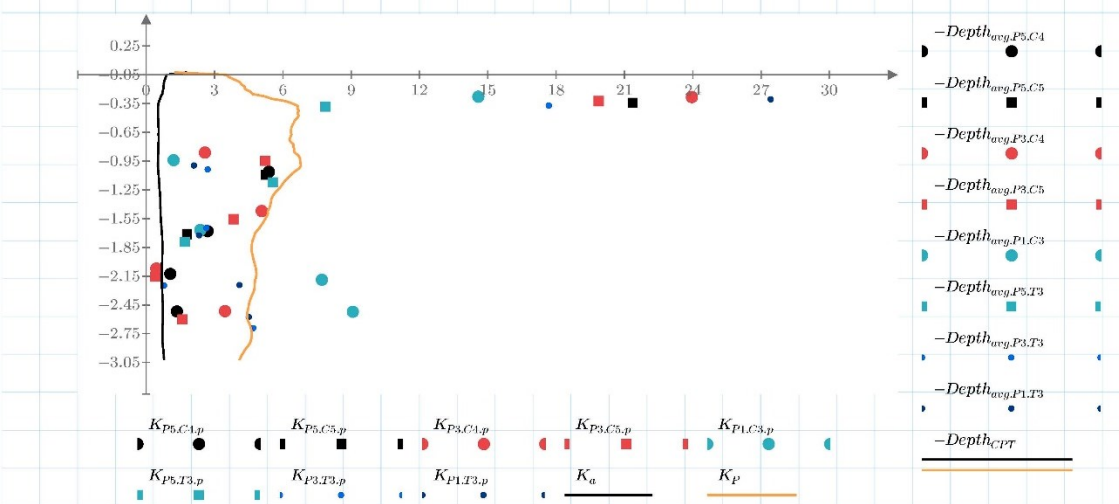

Collect the coefficient of lateral earth pressure, Ks over the upper smooth segment

$$Data_{sm.1}(D_1, D_2, D_3, D_4, D_5, D_6, D_7, D_8) := \left| \begin{array}{l} \text{for } j \in 0,1..\text{cols}(D_1) - 1 \\ \quad D_{sm.1}^{\langle j \rangle} \leftarrow \left[D1_{0,j} \;\; D2_{0,j} \;\; D3_{0,j} \;\; D4_{0,j} \;\; D5_{0,j} \;\; D6_{0,j} \;\; D7_{0,j} \;\; D8_{0,j} \right]^{T} \\ D_{sm.1} \end{array} \right.$$

$$K_{sm.1} := Data_{sm.1}(K_{P5.C4.p}, K_{P5.C5.p}, K_{P3.C4.p}, K_{P3.C5.p}, K_{P1.C3.p}, K_{P5.T3.p}, K_{P3.T3.p}, K_{P1.T3.p})$$

$K_{sm.1.median} := \text{median}(K_{sm.1}) = 20.614$ $K_{sm.1.mean} := \text{mean}(K_{sm.1}) = 20.763$

Collect the coefficient of lateral earth pressure, Ks over the lower smooth segment

$$Data_{sm.2}(D_1, D_2, D_3, D_4, D_5, D_6, D_7, D_8) := \left| \begin{array}{l} \text{for } j \in 0,1..\text{cols}(D_1) - 1 \\ \quad D_{sm.2}^{\langle j \rangle} \leftarrow \left[D1_{1,j} \;\; D2_{1,j} \;\; D6_{1,j} \right]^{T} \\ D_{sm.2} \end{array} \right.$$

$$K_{sm.2} := Data_{sm.2}(K_{P5.C4.p}, K_{P5.C5.p}, K_{P3.C4.p}, K_{P3.C5.p}, K_{P1.C3.p}, K_{P5.T3.p}, K_{P3.T3.p}, K_{P1.T3.p}) = \begin{bmatrix} 5.387 \\ 5.261 \\ 5.561 \end{bmatrix}$$

$K_{sm.2.median} := \text{median}(K_{sm.2}) = 5.387$ $K_{sm.2.mean} := \text{mean}(K_{sm.2}) = 5.403$

Collect the coefficient of lateral earth pressure, Ks over the upper threaded segment

$$Data_{th.1}(D_1, D_2, D_3, D_4, D_5, D_6, D_7, D_8) := \left| \begin{array}{l} \text{for } j \in 0,1..\text{cols}(D_1) - 1 \\ \quad D_{th.1}^{\langle j \rangle} \leftarrow \left[D1_{2,j} \;\; D2_{2,j} \;\; NaN \;\; D3_{1,j} \;\; D3_{2,j} \;\; D4_{1,j} \;\; D4_{2,j} \;\; \ldots \right]^{T} \\ D_{th.1} \end{array} \right.$$

$K_{th.1} := Data_{th.1}(K_{P5.C4.p}, K_{P5.C5.p}, K_{P3.C4.p}, K_{P3.C5.p}, K_{P1.C3.p}, K_{P5.T3.p}, K_{P3.T3.p}, K_{P1.T3.p})$ $K_{th.1} := \text{filterNaN}(K_{th.1})$

$K_{th.1.median} := \text{median}(K_{th.1}) = 2.577$ $K_{th.1.mean} := \text{median}(K_{th.1}) = 2.577$

Collect the coefficient of lateral earth pressure, Ks over the lower threaded segment

$$Data_{th.2}(D_1, D_2, D_3, D_4, D_5, D_6, D_7, D_8) := \left| \begin{array}{l} \text{for } j \in 0,1..\text{cols}(D_1) - 1 \\ \quad D_{th.2}^{\langle j \rangle} \leftarrow \left[D1_{3,j} \;\; D3_{3,j} \;\; D4_{3,j} \;\; D7_{3,j} \right]^{T} \\ D_{th.2} \end{array} \right.$$

$$K_{th.2} := Data_{th.2}(K_{P5.C4.p}, K_{P5.C5.p}, K_{P3.C4.p}, K_{P3.C5.p}, K_{P1.C3.p}, K_{P5.T3.p}, K_{P3.T3.p}, K_{P1.T3.p})$$

$K_{th.2.median} := \text{median}(K_{th.2}) = 0.615$ $K_{th.2.mean} := \text{mean}(K_{th.2}) = 0.672$

Collect the coefficient of lateral earth pressure, Ks over the tapered segment in compression

$$Data_{t.c}(D_1, D_2, D_3, D_4, D_5, D_6, D_7, D_8) := \left| \begin{array}{l} \text{for } j \in 0,1..\text{cols}(D_1) - 1 \\ \quad Data_{t.c}^{\langle j \rangle} \leftarrow \left[D1_{4,j} \;\; NaN \;\; D3_{4,j} \;\; D4_{4,j} \;\; D5_{3,j} \;\; D5_{4,j} \right]^{T} \\ Data_{t.c} \end{array} \right.$$

$K_{t.c.p} := Data_{t.c}(K_{P5.C4.p}, K_{P5.C5.p}, K_{P3.C4.p}, K_{P3.C5.p}, K_{P1.C3.p}, K_{P5.T3.p}, K_{P3.T3.p}, K_{P1.T3.p})$ $K_{t.c.p} := \text{filterNaN}(K_{t.c.p})$

$K_{t.c.median} := \text{median}(K_{t.c.p'}) = 7.714$ $K_{t.c.median} := \text{mean}(K_{t.c.p'}) = 6.749$

$K_{t.c.median} := \text{median}(K_{t.c.p}) = 3.461$ $K_{t.c.median} := \text{mean}(K_{t.c.p}) = 4.635$

Collect the coefficient of lateral earth pressure, Ks over the tapered segment in tension

$$Data_{t.t}\left(D_1, D_2, D_3, D_4, D_5, D_6, D_7, D_8\right) := \left\| \begin{array}{l} \text{for } j \in 0,1..\text{cols}\left(D_1\right)-1 \\ \quad \left\| D_{t.t}^{\langle j \rangle} \leftarrow \begin{bmatrix} NaN & D7_{4,j} & D8_{3,j} & D8_{4,j} \end{bmatrix}^{\mathrm{T}} \right. \\ D_{t.t} \end{array} \right.$$

$$K_{t.t.p} := Data_{t.t}\left(K_{P5.C4.p}, K_{P5.C5.p}, K_{P3.C4.p}, K_{P3.C5.p}, K_{P1.C3.p}, K_{P5.T3.p}, K_{P3.T3.p}, K_{P1.T3.p}\right) \qquad K_{t.t.p} := \text{filterNaN}\left(K_{t.t.p}\right)$$

$$K_{t.t.median} := \text{median}\left(K_{t.t.p}\right) = 4.504 \qquad K_{t.t.median} := \text{mean}\left(K_{t.t.p}\right) = 4.433$$

Backup Calculations to Determine the Coefficient β

Unit Shaft Resistance

$$q_{s.P1.C3} := \begin{bmatrix} 51.39117 \\ 22.53505 \\ 60.11845 \\ 222.03653 \\ 271.21586 \end{bmatrix} \quad Depth_{P1.C3} := \begin{bmatrix} 0 \\ 0.5575 \\ 1.324 \\ 2.0135 \\ 2.3615 \\ 2.6805 \end{bmatrix} \quad q_{s.P3.C4} := \begin{bmatrix} 84.4319 \\ 44.72909 \\ 123.23406 \\ 12.42017 \\ 103.01332 \end{bmatrix} \quad Depth_{P3.C4} := \begin{bmatrix} 0 \\ 0.5645 \\ 1.158 \\ 1.7835 \\ 2.3575 \\ 2.6725 \end{bmatrix}$$

$$q_{s.P3.C5} := \begin{bmatrix} 84.21048 \\ 97.9576 \\ 94.72792 \\ 11.29595 \\ 48.2722 \end{bmatrix} \quad Depth_{P3.C5} := \begin{bmatrix} 0 \\ 0.6495 \\ 1.243 \\ 1.8685 \\ 2.4425 \\ 2.7575 \end{bmatrix} \quad q_{s.P5.C4} := \begin{bmatrix} 141.35705 \\ 80.00662 \\ 67.41593 \\ 29.94945 \\ 40.26207 \end{bmatrix} \quad Depth_{P5.C4} := \begin{bmatrix} 0 \\ 0.65432 \\ 1.46932 \\ 1.89332 \\ 2.35982 \\ 2.67582 \end{bmatrix}$$

$$q_{s.P5.C5} := \begin{bmatrix} 94.32384 \\ 80.08196 \\ 45.0122 \end{bmatrix} \quad Depth_{P5.C5} := \begin{bmatrix} 0 \\ 0.684 \\ 1.499 \\ 1.923 \end{bmatrix} \quad q_{s.P5.T3} := \begin{bmatrix} 38.9497 \\ 88.44154 \\ 43.54921 \end{bmatrix} \quad Depth_{P5.T3} := \begin{bmatrix} 0 \\ 0.764 \\ 1.579 \\ 2.003 \end{bmatrix}$$

$$q_{s.P3.T3} := \begin{bmatrix} 84.34213 \\ 55.0859 \\ 66.67408 \\ 22.63973 \\ 147.57244 \end{bmatrix} \quad Depth_{P3.T3} := \begin{bmatrix} 0 \\ 0.7406 \\ 1.3341 \\ 1.9596 \\ 2.5336 \\ 2.8486 \end{bmatrix} \quad q_{s.P1.T3} := \begin{bmatrix} 106.43756 \\ 40.9601 \\ 59.37229 \\ 118.59131 \\ 136.60732 \end{bmatrix} \quad Depth_{P1.T3} := \begin{bmatrix} 0 \\ 0.6125 \\ 1.379 \\ 2.0685 \\ 2.4165 \\ 2.7355 \end{bmatrix}$$

Cone Penetration Test Data

$\sigma_{v.e} := \text{READEXCEL}(\text{".\Average values of all CPT.xlsx"}, \text{"Sheet1!p3:P123"})$

We used the average value of effecive vertical stress as the unit weight interpreted from CPT readings was not effected by frost.

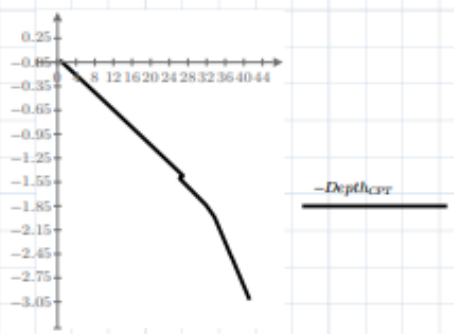

$-Depth_{CPT}$

$\sigma_{v.e}$

Average effective vertical stress interpreted from CPT readings over an individual pile segment

$$Data_{ave}(Data_1, Data_2, Data_3) := \left| \begin{array}{l} TOL \leftarrow 0.025 \\ \text{for } i \in 0, 1 .. \text{rows}(Data_1) - 2 \\ \quad Interpolation_i \leftarrow \text{mean}\left(\text{lookup}\left(\begin{bmatrix} Data_{1_i} \\ Data_{1_{i+1}} \end{bmatrix}, Data_2, Data_3, \text{"range"}\right)\right) \\ \quad Interpolation_i \\ Interpolation \end{array} \right.$$

$$\sigma_{v.e.P5.C4.CPT} := Data_{ave}\left(Depth_{P5.C4}, Depth_{CPT}, \sigma_{v.e}\right) \qquad \sigma_{v.e.P1.C3.CPT} := Data_{ave}\left(Depth_{P1.C3}, Depth_{CPT}, \sigma_{v.e}\right)$$
$$\sigma_{v.e.P5.C5.CPT} := Data_{ave}\left(Depth_{P5.C5}, Depth_{CPT}, \sigma_{v.e}\right) \qquad \sigma_{v.e.P5.T3.CPT} := Data_{ave}\left(Depth_{P5.T3}, Depth_{CPT}, \sigma_{v.e}\right)$$
$$\sigma_{v.e.P3.C4.CPT} := Data_{ave}\left(Depth_{P3.C4}, Depth_{CPT}, \sigma_{v.e}\right) \qquad \sigma_{v.e.P3.T3.CPT} := Data_{ave}\left(Depth_{P3.T3}, Depth_{CPT}, \sigma_{v.e}\right)$$
$$\sigma_{v.e.P3.C5.CPT} := Data_{ave}\left(Depth_{P3.C5}, Depth_{CPT}, \sigma_{v.e}\right) \qquad \sigma_{v.e.P1.T3.CPT} := Data_{ave}\left(Depth_{P1.T3}, Depth_{CPT}, \sigma_{v.e}\right)$$

Calculate the combined shaft resistance factor, beta

$$\beta\left(Data_1, Data_2\right) := \left| \begin{array}{l} \text{for } i \in 0,1..\text{rows}\left(Data_1\right)-1 \\ \quad \text{if } Data_{2_i} \neq 0 \\ \quad\quad \alpha_i \leftarrow \dfrac{Data_{2_i}}{Data_{1_i}} \\ \quad \alpha_i \\ \alpha \end{array} \right.$$

$$\beta_{P5.C4} := \beta\left(\sigma_{v.e.P5.C4.CPT}, q_{s.P5.C4}\right)$$
$$\beta_{P5.C5} := \beta\left(\sigma_{v.e.P5.C5.CPT}, q_{s.P5.C5}\right)$$
$$\beta_{P3.C4} := \beta\left(\sigma_{v.e.P3.C4.CPT}, q_{s.P3.C4}\right)$$
$$\beta_{P3.C5} := \beta\left(\sigma_{v.e.P3.C5.CPT}, q_{s.P3.C5}\right)$$
$$\beta_{P1.C3} := \beta\left(\sigma_{v.e.P1.C3.CPT}, q_{s.P1.C3}\right)$$
$$\beta_{P5.T3} := \beta\left(\sigma_{v.e.P5.T3.CPT}, q_{s.P5.T3}\right)$$
$$\beta_{P3.T3} := \beta\left(\sigma_{v.e.P3.T3.CPT}, q_{s.P3.T3}\right)$$
$$\beta_{P1.T3} := \beta\left(\sigma_{v.e.P1.T3.CPT}, q_{s.P1.T3}\right)$$

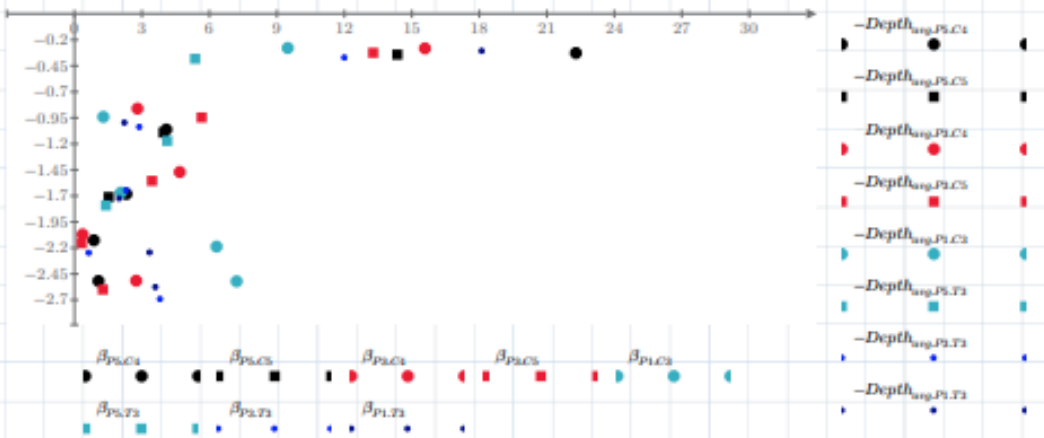

Collect the combined shaft resistance factor over the upper smooth segment

$$Data_{sm.1}\left(D_1, D_2, D_3, D_4, D_5, D_6, D_7, D_8\right) := \left| \begin{array}{l} \text{for } j \in 0,1..\text{cols}\left(D_1\right)-1 \\ \quad D_{sm.1}{}^{\langle j \rangle} \leftarrow \left[D_{1_{0,j}} \;\; D_{2_{0,j}} \;\; D_{3_{0,j}} \;\; D_{4_{0,j}} \;\; D_{5_{0,j}} \;\; D_{6_{0,j}} \;\; D_{7_{0,j}} \;\; D_{8_{0,j}} \right]^T \\ D_{sm.1} \end{array} \right.$$

$$\beta_{sm.1} := Data_{sm.1}\left(\beta_{P5.C4}, \beta_{P5.C5}, \beta_{P3.C4}, \beta_{P3.C5}, \beta_{P1.C3}, \beta_{P5.T3}, \beta_{P3.T3}, \beta_{P1.T3}\right)$$

$\beta_{sm.1.median} := \text{median}\left(\beta_{sm.1}\right) = 13.818$ $\qquad$ $\beta_{sm.1.mean} := \text{mean}\left(\beta_{sm.1}\right) = 13.807$

Collect the combined shaft resistance factor over the lower smooth segment

$$Data_{sm.2}\left(D_1, D_2, D_3, D_4, D_5, D_6, D_7, D_8\right) := \left| \begin{array}{l} \text{for } j \in 0,1..\text{cols}\left(D_1\right)-1 \\ \quad D_{sm.2}{}^{\langle j \rangle} \leftarrow \left[D_{1_{1,j}} \;\; D_{2_{1,j}} \;\; D_{6_{1,j}} \right]^T \\ D_{sm.2} \end{array} \right.$$

$$\beta_{sm.2} := Data_{sm.2}\left(\beta_{P5.C4}, \beta_{P5.C5}, \beta_{P3.C4}, \beta_{P3.C5}, \beta_{P1.C3}, \beta_{P5.T3}, \beta_{P3.T3}, \beta_{P1.T3}\right)$$

$\beta_{sm.2.median} := \text{median}\left(\beta_{sm.2}\right) = 4.087$ $\qquad$ $\beta_{sm.2.mean} := \text{mean}\left(\beta_{sm.2}\right) = 4.057$

Collect the combined shaft resistance factor over the upper threaded segment

$$Data_{th.1}(D_1, D_2, D_3, D_4, D_5, D_6, D_7, D_8) := \left| \begin{array}{l} \text{for } j \in 0,1..\text{cols}(D_1) - 1 \\ \quad D_{th.1}^{\langle j \rangle} \leftarrow \left[D_{1_{2,j}} \;\; D_{2_{2,j}} \;\; \textit{NaN} \;\; D_{3_{1,j}} \;\; D_{3_{2,j}} \;\; D_{4_{1,j}} \;\; D_{4_{2,j}} \;\; \ldots \right]^T \\ D_{th.1} \end{array} \right.$$

$\beta_{th.1} := Data_{th.1}(\beta_{P5.C4}, \beta_{P5.C5}, \beta_{P3.C4}, \beta_{P3.C5}, \beta_{P1.C3}, \beta_{P5.T3}, \beta_{P3.T3}, \beta_{P1.T3})$ $\quad \beta_{th.1} := \text{filterNaN}(\beta_{th.1})$

$\beta_{th.1.median} := \text{median}(\beta_{th.1}) = 2.305$ $\quad \beta_{th.1.mean} := \text{median}(\beta_{th.1}) = 2.305$

Collect the combined shaft resistance factor over the lower threaded segment

$$Data_{th.2}(D_1, D_2, D_3, D_4, D_5, D_6, D_7, D_8) := \left| \begin{array}{l} \text{for } j \in 0,1..\text{cols}(D_1) - 1 \\ \quad D_{th.2}^{\langle j \rangle} \leftarrow \left[D_{1_{3,j}} \;\; D_{3_{3,j}} \;\; D_{4_{3,j}} \;\; D_{7_{3,j}} \right]^T \\ D_{th.2} \end{array} \right.$$

$$\beta_{th.2} := Data_{th.2}(\beta_{P5.C4}, \beta_{P5.C5}, \beta_{P3.C4}, \beta_{P3.C5}, \beta_{P1.C3}, \beta_{P5.T3}, \beta_{P3.T3}, \beta_{P1.T3}) = \begin{bmatrix} 0.865 \\ 0.364 \\ 0.325 \end{bmatrix}$$

$\beta_{th.2.median} := \text{median}(\beta_{th.2}) = 0.5$ $\quad \beta_{th.2.mean} := \text{mean}(\beta_{th.2}) = 0.547$

Collect the combined shaft resistance factor over the tapered segment in compression

$$Data_{t.c}(D_1, D_2, D_3, D_4, D_5, D_6, D_7, D_8) := \left| \begin{array}{l} \text{for } j \in 0,1..\text{cols}(D_1) - 1 \\ \quad Data_{t.c}^{\langle j \rangle} \leftarrow \left[D_{1_{4,j}} \;\; \textit{NaN} \;\; D_{3_{4,j}} \;\; D_{4_{4,j}} \;\; D_{5_{3,j}} \;\; D_{5_{4,j}} \right]^T \\ Data_{t.c} \end{array} \right.$$

$\beta_{t.c.p} := Data_{t.c}(\beta_{P5.C4}, \beta_{P5.C5}, \beta_{P3.C4}, \beta_{P3.C5}, \beta_{P1.C3}, \beta_{P5.T3}, \beta_{P3.T3}, \beta_{P1.T3})$ $\quad \beta_{t.c.p} := \text{filterNaN}(\beta_{t.c.p})$

$\beta_{t.c.median} := \text{median}(\beta_{t.c.p}) = 6.318$ $\quad \beta_{t.c.median} := \text{mean}(\beta_{t.c.p}) = 5.424$

$\beta_{t.c.median} := \text{median}(\beta_{t.c.p}) = 2.745$ $\quad \beta_{t.c.median} := \text{mean}(\beta_{t.c.p}) = 3.721$

Collect the the combined shaft resistance factor over the tapered segment in tension

$$Data_{t.t}(D_1, D_2, D_3, D_4, D_5, D_6, D_7, D_8) := \left| \begin{array}{l} \text{for } j \in 0,1..\text{cols}(D_1) - 1 \\ \quad D_{t.t}^{\langle j \rangle} \leftarrow \left[\textit{NaN} \;\; D_{7_{4,j}} \;\; D_{8_{3,j}} \;\; D_{8_{4,j}} \right]^T \\ D_{t.t} \end{array} \right.$$

$\beta_{t.t.p} := Data_{t.t}(\beta_{P5.C4}, \beta_{P5.C5}, \beta_{P3.C4}, \beta_{P3.C5}, \beta_{P1.C3}, \beta_{P5.T3}, \beta_{P3.T3}, \beta_{P1.T3})$ $\quad \beta_{t.t.p} := \text{filterNaN}(\beta_{t.t.p})$

$\beta_{t.t.median} := \text{median}(\beta_{t.t.p}) = 3.596$ $\quad \beta_{t.t.median} := \text{mean}(\beta_{t.t.p}) = 3.579$

Backup Calculations to Determine the Coefficient β

$$Q_{u.P1.C} = \beta_{sm.1}\sigma_{v2,avg.1}A_{s.1} + \beta_{th.1}\sigma_{v2,avg.2}A_{s.2} + \beta_{t.c.2}\sigma_{v2,avg.3}A_{s.3} + \beta_{th.2}\sigma_{v2,avg.4}A_{s.4} + \beta_{t.c.2}\sigma_{v2,avg.5}A_{s.5}$$
$$Q_{u.P1.T} = \beta_{sm.1}\sigma_{v2,avg.1}A_{s.1} + \beta_{th.1}\sigma_{v2,avg.2}A_{s.2} + \beta_{t.t.2}\sigma_{v2,avg.3}A_{s.3} + \beta_{th.2}\sigma_{v2,avg.4}A_{s.4} + \beta_{t.t.2}\sigma_{v2,avg.5}A_{s.5}$$

$$Q_{u.P3.C} = \beta_{sm.1}\sigma_{v2,avg.1}A_{s.1} + \beta_{th.1}\sigma_{v2,avg.2}A_{s.2} + \beta_{th.2}\sigma_{v2,avg.3}A_{s.3} + \beta_{t.c.2}\sigma_{v2,avg.4}A_{s.4}$$
$$Q_{u.P3.T} = \beta_{sm.1}\sigma_{v2,avg.1}A_{s.1} + \beta_{th.1}\sigma_{v2,avg.2}A_{s.2} + \beta_{th.2}\sigma_{v2,avg.3}A_{s.3} + \beta_{t.c.2}\sigma_{v2,avg.4}A_{s.4}$$

$$Q_{u.P5.C} = \beta_{sm.1}\sigma_{v2,avg.1}A_{s.1} + \beta_{sm.1'}\sigma_{v2,avg.2}A_{s.2} + \beta_{th.1}\sigma_{v2,avg.3}A_{s.3} + \beta_{th.2}\sigma_{v2,avg.4}A_{s.4} + \beta_{t.c.2}\sigma_{v2,avg.5}A_{s.5}$$
$$Q_{u.P5.T} = \beta_{sm.1}\sigma_{v2,avg.1}A_{s.1} + \beta_{sm.1'}\sigma_{v2,avg.2}A_{s.2} + \beta_{th.1}\sigma_{v2,avg.3}A_{s.3} + \beta_{th.2}\sigma_{v2,avg.4}A_{s.4} + \beta_{t.t.2}\sigma_{v2,avg.5}A_{s.5}$$

$$Q_{u.P2.C} = \beta_{sm.1}\sigma_{v2,avg.1}A_{s.1} + \beta_{th.1}\sigma_{v2,avg.2}A_{s.2} + \beta_{t.c.1}\sigma_{v2,avg.3}A_{s.3} + \beta_{th.1}\sigma_{v2,avg.4}A_{s.4} + \beta_{t.c.1}\sigma_{v2,avg.5}A_{s.5}$$
$$Q_{u.P2.T} = \beta_{sm.1}\sigma_{v2,avg.1}A_{s.1} + \beta_{th.1}\sigma_{v2,avg.2}A_{s.2} + \beta_{t.t.1}\sigma_{v2,avg.3}A_{s.3} + \beta_{th.1}\sigma_{v2,avg.4}A_{s.4} + \beta_{t.t.1}\sigma_{v2,avg.5}A_{s.5}$$

$$Q_{u.P4.C} = \beta_{sm.1}\sigma_{v2,avg.1}A_{s.1} + \beta_{th.1}\sigma_{v2,avg.2}A_{s.2} + \beta_{t.c.1}\sigma_{v2,avg.3}A_{s.3}$$
$$Q_{u.P4.T} = \beta_{sm.1}\sigma_{v2,avg.1}A_{s.1} + \beta_{th.1}\sigma_{v2,avg.2}A_{s.2} + \beta_{t.c.1}\sigma_{v2,avg.3}A_{s.3}$$

$$Q_{u.P6.C} = \beta_{sm.1}\sigma_{v2,avg.1}A_{s.1} + \beta_{th.1}\sigma_{v2,avg.2}A_{s.2} + \beta_{t.c.1}\sigma_{v2,avg.3}A_{s.3}$$
$$Q_{u.P6.T} = \beta_{sm.1}\sigma_{v2,avg.1}A_{s.1} + \beta_{th.1}\sigma_{v2,avg.2}A_{s.2} + \beta_{t.t.1}\sigma_{v2,avg.3}A_{s.3}$$

Pile diminsions

$Depth_{P1} := [0 \;\; 0.815 \;\; 2.316 \;\; 2.529 \;\; 2.655 \;\; 2.981 \;\; 3.033]^T$ $r_{P1} := [0.057 \;\; 0.069 \;\; 0.069 \;\; 0.069 \;\; 0.05 \;\; 0.05 \;\; 0.033 \;\; 0.002]^T$

$Depth_{P2} := [0 \;\; 0.626 \;\; 0.831 \;\; 1.031 \;\; 1.143 \;\; 1.481 \;\; 1.538]^T$ $r_{P2} := [0.057 \;\; 0.069 \;\; 0.069 \;\; 0.05 \;\; 0.05 \;\; 0.031 \;\; 5 \cdot 10^{-4}]^T$

$Depth_{P3} := [0 \;\; 0.904 \;\; 2.735 \;\; 3.015 \;\; 3.078]^T$ $r_{P3} := [0.044 \;\; 0.056 \;\; 0.056 \;\; 0.056 \;\; 0.035 \;\; 0.001]^T$

$Depth_{P4} := [0 \;\; 0.596 \;\; 1.218 \;\; 1.501 \;\; 1.566]^T$ $r_{P4} := [0.044 \;\; 0.056 \;\; 0.056 \;\; 0.035 \;\; 0.001]^T$

$Depth_{P5} := [0 \;\; 1.792 \;\; 2.714 \;\; 3.036 \;\; 3.077]^T$ $r_{P5} := [0.038 \;\; 0.038 \;\; 0.05 \;\; 0.05 \;\; 0.05 \;\; 0.029 \;\; 0.002]^T$

$Depth_{P6} := [0 \;\; 0.594 \;\; 1.195 \;\; 1.521 \;\; 1.565]^T$ $r_{P6} := [0.038 \;\; 0.05 \;\; 0.05 \;\; 0.028 \;\; 0.003]^T$

$\beta_{sm.1} := 13.818$ $\beta_{sm.2} := 4.087$ $\beta_{th.1} := 2.305$ $\beta_{th.2} := 0.5$ $\beta_{t.c} := 6.318$ $\beta_{t.t} := 3.596$

$Stickup := \text{READEXCEL}(\text{".\pile displacement at ultimate.xlsx"}, \text{"Sheet1!D2:G42"})$

$\sigma_{v.e} := \text{READEXCEL}(\text{"..\after second review\Soil Properties method\Average values of all CPT.xlsx"}, \text{"Sheet1!P3:P182"})$

Qult of P1

$$
\begin{aligned}
Q_{ult}(z, R, \beta) := \;& Index_{SG.P1} \leftarrow \text{round}\left(\frac{z}{0.025}\right) \\
& \text{for } j \in 0,1..6 \\
& \quad \text{for } i \in Index_{SG.P1_j}, Index_{SG.P1_j}+1..Index_{SG.P1_{j+1}} \\
& \quad\quad \sigma_{avg_j} \leftarrow \sum_{i=Index_{SG.P1_j}}^{Index_{SG.P1_{j+1}}} \frac{\left(\sigma_{v.e_i}\right)}{Index_{SG.P1_{j+1}} - Index_{SG.P1_j}} \\
& \sigma_{avg} \\
& \text{for } i \in 0,1..2 \\
& \quad Q_i \leftarrow \beta_i \cdot \sigma_{avg_i} \cdot \left(z_{i+1} - z_i\right) \cdot 2 \cdot \pi \cdot R_i \\
& \text{for } i \in 3 \\
& \quad Q_i \leftarrow \beta_i \cdot \sigma_{avg_i} \cdot 2\,\pi \cdot \left(z_{i+1} - z_i\right) \cdot \left(\frac{\left(R_i^{\,2} + R_{i+1}^{\,2} + R_i \cdot R_{i+1}\right)}{3}\right)^{0.5} \\
& \text{for } i \in 4 \\
& \quad Q_i \leftarrow \beta_i \cdot \sigma_{avg_i} \cdot \left(z_{i+1} - z_i\right) \cdot 2 \cdot \pi \cdot R_i \\
& \text{for } i \in 5 \\
& \quad Q_i \leftarrow \beta_i \cdot \sigma_{avg_i} \cdot 2 \cdot \pi \cdot \left(z_{i+1} - z_i\right) \cdot \left(\frac{\left(R_i^{\,2} + R_{i+1}^{\,2} + R_i \cdot R_{i+1}\right)}{3}\right)^{0.5} \\
& \text{for } i \in 6 \\
& \quad Q_i \leftarrow \beta_i \cdot \sigma_{avg_i} \cdot 2 \cdot \pi \cdot \left(z_{i+1} - z_i\right) \cdot \left(\frac{\left(\left(R_i - 0.024\right)^2 + \left(R_{i+1}\right)^2 + \left(R_i - 0.024\right) \cdot \left(R_{i+1}\right)\right)}{3}\right)^{0.5} \\
& \left[Q_0 \;\; Q_1 \;\; Q_2 \;\; Q_3 \;\; Q_4 \;\; Q_5 \;\; Q_6 \;\; Q_0 + Q_1 + Q_2 + Q_3 + Q_4 + Q_5 + Q_6\right]
\end{aligned}
$$

$\beta_{P1.C} := [\beta_{sm.1} \;\; \beta_{th.1} \;\; \beta_{th.2} \;\; \beta_{t.c} \;\; \beta_{th.2} \;\; \beta_{t.c} \;\; \beta_{t.c}]^T$ $\beta_{P1.T} := [\beta_{sm.1} \;\; \beta_{th.1} \;\; \beta_{th.2} \;\; \beta_{t.t} \;\; \beta_{th.2} \;\; \beta_{t.t} \;\; \beta_{t.t}]^T$

$Depth_{TP3} := Depth_{P1}\left(\text{norm}\left(st.up._{P3}^{\langle 0 \rangle}\right)\right)$

$Q_{TP3} := Q_{ult}\left(Depth_{TP3}, r_{P1}, \beta_{P1.C}\right) = [32.468 \;\; 30.978 \;\; 2.481 \;\; 20.754 \;\; 0.909 \;\; 23.234 \;\; 0.748 \;\; 111.573]$ $Q_{TP3} := \text{norm}\left(Q_{TP3}^{\langle 7 \rangle}\right) = 111.573$

$Depth_{TP4} := Depth_{P1}\left(\text{norm}\left(st.up._{P4}^{\langle 0 \rangle}\right)\right)$

$Q_{TP4} := Q_{ult}\left(Depth_{TP4}, r_{P1}, \beta_{P1.C}\right) = [32.371 \quad 31.04 \quad 2.461 \quad 20.96 \quad 0.882 \quad 23.234 \quad 0.748 \quad 111.696]$ $Q_{TP4} := \text{norm}\left(Q_{TP4}^{\langle 7 \rangle}\right) = 111.696$

$Depth_{TP43} := Depth_{P1}\left(\text{norm}\left(st.up._{P43}^{\langle 0 \rangle}\right)\right)$

$Q_{TP43} := Q_{ult}\left(Depth_{TP43}, r_{P1}, \beta_{P1.C}\right) = [32.361 \quad 31.046 \quad 2.459 \quad 20.96 \quad 0.882 \quad 23.234 \quad 0.748 \quad 111.69]$ $Q_{TP43} := \text{norm}\left(Q_{TP43}^{\langle 7 \rangle}\right) = 111.69$

$Depth_{TP1} := Depth_{P1}\left(\text{norm}\left(st.up._{P1}^{\langle 0 \rangle}\right)\right)$

$Q_{TP1} := Q_{ult}\left(Depth_{TP1}, r_{P1}, \beta_{P1.T}\right) = [17.57 \quad 33.827 \quad 0.788 \quad 11.287 \quad 0.869 \quad 12.684 \quad 0.409 \quad 77.433]$ $Q_{TP1} := \text{norm}\left(Q_{TP1}^{\langle 7 \rangle}\right) = 77.433$

$Depth_{TP2} := Depth_{P1}\left(\text{norm}\left(st.up._{P2}^{\langle 0 \rangle}\right)\right)$

$Q_{TP2} := Q_{ult}\left(Depth_{TP2}, r_{P1}, \beta_{P1.T}\right) = [20.31 \quad 33.407 \quad 1.104 \quad 11.516 \quad 0.873 \quad 12.71 \quad 0.413 \quad 80.334]$ $Q_{TP2} := \text{norm}\left(Q_{TP2}^{\langle 7 \rangle}\right) = 80.334$

$Depth_{TP56} := Depth_{P1}\left(\text{norm}\left(st.up._{P56}^{\langle 0 \rangle}\right)\right)$

$Q_{TP56} := Q_{ult}\left(Depth_{TP56}, r_{P1}, \beta_{P1.T}\right) = [16.04 \quad 34.209 \quad 0.553 \quad 11.229 \quad 0.865 \quad 12.623 \quad 0.407 \quad 75.927]$ $Q_{TP56} := \text{norm}\left(Q_{TP56}^{\langle 7 \rangle}\right) = 75.927$

Oult of P3

$$Q_{ult}(z, R, \beta) := \left\| \begin{array}{l} Index_{SG.P1} \leftarrow \text{round}\left(\frac{z}{0.025}\right) \\ \left\| \begin{array}{l} \text{for } j \in 0,1..4 \\ \quad \left\| \begin{array}{l} \text{for } i \in Index_{SG.P1_j}, Index_{SG.P1_j}+1..Index_{SG.P1_{j+1}} \\ \quad \left\| \sigma_{avg_j} \leftarrow \sum_{i=Index_{SG.P1_j}}^{Index_{SG.P1_{j+1}}} \frac{\left(\sigma_{v.e_i}\right)}{Index_{SG.P1_{j+1}} - Index_{SG.P1_j}} \right\| \end{array} \right\| \\ \sigma_{avg} \end{array} \right\| \\ \text{for } i \in 0,1..2 \\ \quad \left\| Q_i \leftarrow \beta_i \cdot \sigma_{avg_i} \cdot \left(z_{i+1} - z_i\right) \cdot 2 \cdot \pi \cdot R_i \right\| \\ \text{for } i \in 3 \\ \quad \left\| Q_i \leftarrow \beta_i \cdot \sigma_{avg_i} \cdot 2 \cdot \pi \cdot \left(z_{i+1} - z_i\right) \cdot \left(\frac{\left(\left(R_i\right)^2 + \left(R_{i+1}\right)^2 + \left(R_i\right) \cdot \left(R_{i+1}\right)\right)}{3}\right)^{0.5} \right\| \\ \text{for } i \in 4 \\ \quad \left\| Q_i \leftarrow \beta_i \cdot \sigma_{avg_i} \cdot 2 \cdot \pi \cdot \left(z_{i+1} - z_i\right) \cdot \left(\frac{\left(\left(R_i - 0.024\right)^2 + \left(R_{i+1}\right)^2 + \left(R_i - 0.024\right) \cdot \left(R_{i+1}\right)\right)}{3}\right)^{0.5} \right\| \\ \left[Q_0 \quad Q_1 \quad Q_2 \quad Q_3 \quad Q_4 \quad Q_0+Q_1+Q_2+Q_3+Q_4\right] \end{array} \right\|$$

$\beta_{P3.C} := \left[\beta_{sm.1} \quad \beta_{th.1} \quad \beta_{th.2} \quad \beta_{t.c} \quad \beta_{t.c}\right]^T$ $\beta_{P3.T} := \left[\beta_{sm.1} \quad \beta_{th.1} \quad \beta_{th.2} \quad \beta_{t.t} \quad \beta_{t.t}\right]^T$

$Depth_{TP11} := Depth_{P3}\left(\text{norm}\left(st.up._{P11}^{\langle 0 \rangle}\right)\right)$

$Q_{TP11} := Q_{ult}\left(Depth_{TP11}, r_{P3}, \beta_{P3.C}\right) = [31.427 \quad 23.79 \quad 4.891 \quad 22.299 \quad 1.039 \quad 83.446]$ $Q_{TP11} := \text{norm}\left(Q_{TP11}^{\langle 5 \rangle}\right) = 83.446$

$Depth_{TP13} := Depth_{P3}\left(\text{norm}\left(st.up._{P13}^{\langle 0 \rangle}\right)\right)$

$Q_{TP13} := Q_{ult}\left(Depth_{TP13}, r_{P3}, \beta_{P3.C}\right) = [29.944 \quad 24.031 \quad 4.754 \quad 22.405 \quad 1.035 \quad 82.169]$ $Q_{TP13} := \text{norm}\left(Q_{TP13}^{\langle 5 \rangle}\right) = 82.169$

$Depth_{TP36} := Depth_{P3}\left(\text{norm}\left(st.up._{P36}^{\langle 0 \rangle}\right)\right)$

$Q_{TP36} := Q_{ult}\left(Depth_{TP36}, r_{P3}, \beta_{P3.C}\right) = [28.33 \quad 24.372 \quad 4.578 \quad 22.305 \quad 1.03 \quad 80.615]$ $Q_{TP36} := \text{norm}\left(Q_{TP36}^{\langle 5 \rangle}\right) = 80.615$

$Depth_{TP40} := Depth_{P3}\left(\text{norm}\left(st.up._{P40}^{\langle 0\rangle}\right)\right)$

$Q_{TP40} := Q_{ult}\left(Depth_{TP40}, r_{P3}, \beta_{P3.C}\right) = \begin{bmatrix} 31.316 & 23.859 & 4.869 & 22.405 & 0.922 & 83.371 \end{bmatrix}$ $Q_{TP40} := \text{norm}\left(Q_{TP40}^{\langle 5\rangle}\right) = 83.371$

$Depth_{TP42} := Depth_{P3}\left(\text{norm}\left(st.up._{P42}^{\langle 0\rangle}\right)\right)$

$Q_{TP42} := Q_{ult}\left(Depth_{TP42}, r_{P3}, \beta_{P3.C}\right) = \begin{bmatrix} 26.72 & 24.73 & 4.389 & 22.001 & 1.026 & 78.866 \end{bmatrix}$ $Q_{TP42} := \text{norm}\left(Q_{TP42}^{\langle 5\rangle}\right) = 78.866$

$Depth_{TP12} := Depth_{P3}\left(\text{norm}\left(st.up._{P12}^{\langle 0\rangle}\right)\right)$

$Q_{TP12} := Q_{ult}\left(Depth_{TP12}, r_{P3}, \beta_{P3.T}\right) = \begin{bmatrix} 14.626 & 27.268 & 2.861 & 12.009 & 0.561 & 57.324 \end{bmatrix}$ $Q_{TP12} := \text{norm}\left(Q_{TP12}^{\langle 5\rangle}\right) = 57.324$

$Depth_{TP14} := Depth_{P3}\left(\text{norm}\left(st.up._{P14}^{\langle 0\rangle}\right)\right)$

$Q_{TP14} := Q_{ult}\left(Depth_{TP14}, r_{P3}, \beta_{P3.T}\right) = \begin{bmatrix} 13.532 & 27.479 & 2.703 & 11.951 & 0.558 & 56.223 \end{bmatrix}$ $Q_{TP14} := \text{norm}\left(Q_{TP14}^{\langle 5\rangle}\right) = 56.223$

$Depth_{TP54} := Depth_{P3}\left(\text{norm}\left(st.up._{P54}^{\langle 0\rangle}\right)\right)$

$Q_{TP54} := Q_{ult}\left(Depth_{TP54}, r_{P3}, \beta_{P3.T}\right) = \begin{bmatrix} 15.804 & 27.014 & 3.03 & 12.067 & 0.563 & 58.479 \end{bmatrix}$ $Q_{TP54} := \text{norm}\left(Q_{TP54}^{\langle 5\rangle}\right) = 58.479$

Qult of P5

$$
\begin{aligned}
&Q_{ult}(z, R, \beta) := \\
&\quad Index_{SG.P1} \leftarrow \text{round}\left(\frac{z}{0.025}\right) \\
&\quad \text{for } j \in 0,1..5 \\
&\quad\quad \text{for } i \in Index_{SG.P1_j}, Index_{SG.P1_j}+1..Index_{SG.P1_{j+1}} \\
&\quad\quad\quad \sigma_{avg_j} \leftarrow \sum_{i=Index_{SG.P1_j}}^{Index_{SG.P1_{j+1}}} \frac{\left(\sigma_{v.e_i}\right)}{Index_{SG.P1_{j+1}} - Index_{SG.P1_j}} \\
&\quad \sigma_{avg} \\
&\quad \text{for } i \in 0,1..3 \\
&\quad\quad Q_i \leftarrow \beta_i \cdot \sigma_{avg_i} \cdot \left(z_{i+1} - z_i\right) \cdot 2 \cdot \pi \cdot R_i \\
&\quad \text{for } i \in 4 \\
&\quad\quad Q_i \leftarrow \beta_i \cdot \sigma_{avg_i} \cdot 2 \cdot \pi \cdot \left(z_{i-1} - z_i\right) \cdot \left(\frac{\left(R_i^{\,2} + R_{i+1}^{\,2} + R_i \cdot R_{i+1}\right)}{3}\right)^{0.5} \\
&\quad \text{for } i \in 5 \\
&\quad\quad Q_i \leftarrow \beta_i \cdot \sigma_{avg_i} \cdot 2 \cdot \pi \cdot \left(z_{i-1} - z_i\right) \cdot \left(\frac{\left(\left(R_i - 0.024\right)^2 + \left(R_{i+1}\right)^2 + \left(R_i - 0.024\right) \cdot \left(R_{i+1}\right)\right)}{3}\right)^{0.5} \\
&\quad \begin{bmatrix} Q_0 & Q_1 & Q_2 & Q_3 & Q_4 & Q_5 & Q_0 + Q_1 + Q_2 + Q_3 + Q_4 + Q_5 \end{bmatrix}
\end{aligned}
$$

$\beta_{P5.C} := \begin{bmatrix} \beta_{sm.1} & \beta_{sm.2} & \beta_{th.1} & \beta_{th.2} & \beta_{t.c} & \beta_{t.c} \end{bmatrix}^{\top}$ $\beta_{P5.T} := \begin{bmatrix} \beta_{sm.1} & \beta_{sm.2} & \beta_{th.1} & \beta_{th.2} & \beta_{t.t} & \beta_{t.t} \end{bmatrix}^{\top}$

$Depth_{TP24} := Depth_{P5}\left(\text{norm}\left(st.up._{P24}^{\langle 0\rangle}\right)\right)$

$Q_{TP24} := Q_{ult}\left(Depth_{TP24}, r_{P5}, \beta_{P5.C}\right) = \begin{bmatrix} 16.817 & 24.38 & 5.968 & 4.132 & 22.144 & 0.487 & 73.928 \end{bmatrix}$ $Q_{TP24} := \text{norm}\left(Q_{TP24}^{\langle 6\rangle}\right) = 73.928$

$Depth_{TP25} := Depth_{P5}\left(\text{norm}\left(st.up._{P25}^{\langle 0\rangle}\right)\right)$

$Q_{TP25} := Q_{ult}\left(Depth_{TP25}, r_{P5}, \beta_{P5.C}\right) = \begin{bmatrix} 16.817 & 23.485 & 6.678 & 3.943 & 22.126 & 0.363 & 73.413 \end{bmatrix}$ $Q_{TP25} := \text{norm}\left(Q_{TP25}^{\langle 6\rangle}\right) = 73.413$

$Depth_{TP37} := Depth_{P5}\left(\text{norm}\left(st.up._{P37}^{\langle 0\rangle}\right)\right)$

$$Q_{TP37} := Q_{ult}\left(Depth_{TP37}, r_{P5}, \beta_{P5.C}\right) = \begin{bmatrix} 16.817 & 23.771 & 6.35 & 4.018 & 22.045 & 0.365 & 73.365 \end{bmatrix} \quad Q_{TP37} := \text{norm}\left(Q_{TP37}^{\langle 6 \rangle}\right) = 73.365$$

$$Depth_{TP39} := Depth_{P5}\left(\text{norm}\left(st.up._{P39}^{\langle 0 \rangle}\right)\right)$$

$$Q_{TP39} := Q_{ult}\left(Depth_{TP39}, r_{P5}, \beta_{P5.C}\right) = \begin{bmatrix} 16.817 & 21.579 & 7.942 & 3.571 & 21.748 & 0.36 & 72.018 \end{bmatrix} \quad Q_{TP39} := \text{norm}\left(Q_{TP39}^{\langle 6 \rangle}\right) = 72.018$$

$$Depth_{TP41} := Depth_{P5}\left(\text{norm}\left(st.up._{P41}^{\langle 0 \rangle}\right)\right)$$

$$Q_{TP41} := Q_{ult}\left(Depth_{TP41}, r_{P5}, \beta_{P5.C}\right) = \begin{bmatrix} 16.817 & 21.491 & 8.043 & 3.548 & 21.748 & 0.36 & 72.006 \end{bmatrix} \quad Q_{TP41} := \text{norm}\left(Q_{TP41}^{\langle 6 \rangle}\right) = 72.006$$

$$Depth_{TP21} := Depth_{P5}\left(\text{norm}\left(st.up._{P21}^{\langle 0 \rangle}\right)\right)$$

$$Q_{TP21} := Q_{ult}\left(Depth_{TP21}, r_{P5}, \beta_{P5.T}\right) = \begin{bmatrix} 16.817 & 15.359 & 12.556 & 2.213 & 11.865 & 0.262 & 59.072 \end{bmatrix} \quad Q_{TP21} := \text{norm}\left(Q_{TP21}^{\langle 6 \rangle}\right) = 59.072$$

$$Depth_{TP22} := Depth_{P5}\left(\text{norm}\left(st.up._{P22}^{\langle 0 \rangle}\right)\right)$$

$$Q_{TP22} := Q_{ult}\left(Depth_{TP22}, r_{P5}, \beta_{P5.T}\right) = \begin{bmatrix} 16.817 & 16.585 & 11.661 & 2.486 & 11.981 & 0.264 & 59.793 \end{bmatrix} \quad Q_{TP22} := \text{norm}\left(Q_{TP22}^{\langle 6 \rangle}\right) = 59.793$$

$$Depth_{TP55} := Depth_{P5}\left(\text{norm}\left(st.up._{P55}^{\langle 0 \rangle}\right)\right)$$

$$Q_{TP55} := Q_{ult}\left(Depth_{TP55}, r_{P5}, \beta_{P5.T}\right) = \begin{bmatrix} 16.817 & 23.551 & 6.603 & 3.96 & 12.547 & 0.276 & 63.755 \end{bmatrix} \quad Q_{TP55} := \text{norm}\left(Q_{TP55}^{\langle 6 \rangle}\right) = 63.755$$

Qult of P2

$$Q_{ult}(z, R, \beta) := \left\| \begin{array}{l} Index_{SG.P1} \leftarrow \text{round}\left(\frac{z}{0.025}\right) \\ \left\| \begin{array}{l} \text{for } j \in 0, 1..5 \\ \quad \left\| \begin{array}{l} \text{for } i \in Index_{SG.P1_j}, Index_{SG.P1_j}+1..Index_{SG.P1_{j+1}} \\ \quad \left\| \sigma_{avg_j} \leftarrow \sum_{i=Index_{SG.P1_j}}^{Index_{SG.P1_{j+1}}} \frac{\left(\sigma_{v.e_i}\right)}{Index_{SG.P1_{j+1}} - Index_{SG.P1_j}} \right. \end{array} \right. \\ \sigma_{avg} \end{array} \right. \\ \text{for } i \in 0, 1..1 \\ \quad \left\| Q_i \leftarrow \beta_i \cdot \sigma_{avg_i} \cdot \left(z_{i+1} - z_i\right) \cdot 2 \cdot \pi \cdot R_i \right. \\ \text{for } i \in 2 \\ \quad \left\| Q_i \leftarrow \beta_i \cdot \sigma_{avg_i} \cdot 2 \cdot \pi \cdot \left(z_{i+1} - z_i\right) \cdot \left(\frac{\left(R_i^{\,2} + R_{i+1}^{\,2} + R_i \cdot R_{i+1}\right)}{3}\right)^{0.5} \right. \\ \text{for } i \in 3 \\ \quad \left\| Q_i \leftarrow \beta_i \cdot \sigma_{avg_i} \cdot \left(z_{i+1} - z_i\right) \cdot 2 \cdot \pi \cdot R_i \right. \\ \text{for } i \in 4 \\ \quad \left\| Q_i \leftarrow \beta_i \cdot \sigma_{avg_i} \cdot 2 \cdot \pi \cdot \left(z_{i+1} - z_i\right) \cdot \left(\frac{\left(R_i^{\,2} + R_{i+1}^{\,2} + R_i \cdot R_{i+1}\right)}{3}\right)^{0.5} \right. \\ \text{for } i \in 5 \\ \quad \left\| Q_i \leftarrow \beta_i \cdot \sigma_{avg_i} \cdot 2 \cdot \pi \cdot \left(z_{i+1} - z_i\right) \cdot \left(\frac{\left(\left(R_i - 0.024\right)^2 + \left(R_{i+1}\right)^2 + \left(R_i - 0.024\right) \cdot \left(R_{i+1}\right)\right)}{3}\right)^{0.5} \right. \\ \left[Q_0 \;\; Q_1 \;\; Q_2 \;\; Q_3 \;\; Q_4 \;\; Q_5 \;\; Q_0 + Q_1 + Q_2 + Q_3 + Q_4 + Q_5 \right] \end{array} \right.$$

$$RF_c := 0.9835 = 0.984 \quad RF_t := 0.3308 \qquad RF_c \cdot \beta_{t.c} = 6.214 \qquad \beta_{t.t} \cdot RF_t = 1.19$$

$\beta_{P2.C} := \left[\beta_{sm.1}\ \ \beta_{th.1}\ \ \beta_{t.c}\cdot RF_c\ \ \beta_{th.2}\ \ \beta_{t.c}\cdot RF_c\ \ \beta_{t.c}\cdot RF_c\right]$ $\beta_{P2.T} := \left[\beta_{sm.1}\ \ \beta_{th.1}\ \ \beta_{t.t}\cdot RF_t\ \ \beta_{th.2}\ \ \beta_{t.t}\cdot RF_t\ \ \beta_{t.t}\cdot RF_t\right]$

$Depth_{TP6} := Depth_{P2}\left(\text{norm}\left(st.up._{P6}^{\langle 0\rangle}\right)\right)$

$Q_{TP6} := Q_{ult}\left(Depth_{TP6}, r_{P2}, \beta_{P2.C}\right) = [15.978\ \ 2.893\ \ 8.499\ \ 0.404\ \ 13.471\ \ 0.372\ \ 41.617]$ $Q_{TP6} := \text{norm}\left(Q_{TP6}^{\langle 6\rangle}\right) = 41.617$

$Depth_{TP7} := Depth_{P2}\left(\text{norm}\left(st.up._{P7}^{\langle 0\rangle}\right)\right)$

$Q_{TP7} := Q_{ult}\left(Depth_{TP7}, r_{P2}, \beta_{P2.C}\right) = [10.972\ \ 2.472\ \ 7.545\ \ 0.376\ \ 12.23\ \ 0.347\ \ 33.943]$ $Q_{TP7} := \text{norm}\left(Q_{TP7}^{\langle 6\rangle}\right) = 33.943$

$Depth_{TP9} := Depth_{P2}\left(\text{norm}\left(st.up._{P9}^{\langle 0\rangle}\right)\right)$

$Q_{TP9} := Q_{ult}\left(Depth_{TP9}, r_{P2}, \beta_{P2.C}\right) = [19.005\ \ 3.103\ \ 8.975\ \ 0.423\ \ 13.994\ \ 0.332\ \ 45.831]$ $Q_{TP9} := \text{norm}\left(Q_{TP9}^{\langle 6\rangle}\right) = 45.831$

$Depth_{TP5} := Depth_{P2}\left(\text{norm}\left(st.up._{P5}^{\langle 0\rangle}\right)\right)$

$Q_{TP5} := Q_{ult}\left(Depth_{TP5}, r_{P2}, \beta_{P2.T}\right) = [5.304\ \ 1.838\ \ 1.17\ \ 0.308\ \ 2.077\ \ 0.059\ \ 10.756]$ $Q_{TP5} := \text{norm}\left(Q_{TP5}^{\langle 6\rangle}\right) = 10.756$

$Depth_{TP8} := Depth_{P2}\left(\text{norm}\left(st.up._{P8}^{\langle 0\rangle}\right)\right)$

$Q_{TP8} := Q_{ult}\left(Depth_{TP8}, r_{P2}, \beta_{P2.T}\right) = [1.623\ \ 1.199\ \ 0.894\ \ 0.251\ \ 1.775\ \ 0.052\ \ 5.793]$ $Q_{TP8} := \text{norm}\left(Q_{TP8}^{\langle 6\rangle}\right) = 5.793$

$Depth_{TP10} := Depth_{P2}\left(\text{norm}\left(st.up._{P10}^{\langle 0\rangle}\right)\right)$

$Q_{TP10} := Q_{ult}\left(Depth_{TP10}, r_{P2}, \beta_{P2.T}\right) = [11.231\ \ 2.472\ \ 1.444\ \ 0.366\ \ 2.379\ \ 0.06\ \ 17.952]$ $Q_{TP10} := \text{norm}\left(Q_{TP10}^{\langle 6\rangle}\right) = 17.952$

Qult of P4

$$
\begin{aligned}
&Q_{ult}(z, R, \beta) := \Big\| \\
&\quad Index_{SG.P1} \leftarrow \text{round}\left(\frac{z}{0.025}\right) \\
&\quad \Big\| \text{for } j \in 0,1..3 \\
&\quad\quad \Big\| \text{for } i \in Index_{SG.P1_j}, Index_{SG.P1_j}+1..Index_{SG.P1_{j+1}} \\
&\quad\quad\quad \Big\| \sigma_{avg_j} \leftarrow \sum_{i=Index_{SG.P1_j}}^{Index_{SG.P1_{j+1}}} \frac{\left(\sigma_{v.c_i}\right)}{Index_{SG.P1_{j+1}} - Index_{SG.P1_j}} \\
&\quad\quad \sigma_{avg} \\
&\quad \text{for } i \in 0,1..1 \\
&\quad\quad Q_i \leftarrow \beta_i \cdot \sigma_{avg_i} \cdot \left(z_{i+1} - z_i\right) \cdot 2 \cdot \pi \cdot R_i \\
&\quad \text{for } i \in 2 \\
&\quad\quad Q_i \leftarrow \beta_i \cdot \sigma_{avg_i} \cdot 2 \cdot \pi \cdot \left(z_{i+1} - z_i\right) \cdot \left(\frac{\left(R_i^{\,2} + R_{i+1}^{\,2} + R_i \cdot R_{i+1}\right)}{3}\right)^{0.5} \\
&\quad \text{for } i \in 3 \\
&\quad\quad Q_i \leftarrow \beta_i \cdot \sigma_{avg_i} \cdot 2 \cdot \pi \cdot \left(z_{i+1} - z_i\right) \cdot \left(\frac{\left(\left(R_i - 0.024\right)^2 + \left(R_{i+1}\right)^2 + \left(R_i - 0.024\right) \cdot \left(R_{i+1}\right)\right)}{3}\right)^{0.5} \\
&\quad \left[Q_0\ \ Q_1\ \ Q_2\ \ Q_3\ \ Q_0 + Q_1 + Q_2 + Q_3\right]
\end{aligned}
$$

$\beta_{P4.C} := \left[\beta_{sm.1}\ \ \beta_{th.1}\ \ \beta_{t.c}\cdot RF_c\ \ \beta_{t.c}\cdot RF_c\right]^{\mathrm{T}}$ $\beta_{P4.T} := \left[\beta_{sm.1}\ \ \beta_{th.1}\ \ \beta_{t.t}\cdot RF_t\ \ \beta_{t.t}\cdot RF_t\right]^{\mathrm{T}}$

$Depth_{TP18} := Depth_{P4}\left(\text{norm}\left(st.up._{P18}^{\langle 0\rangle}\right)\right)$

$Q_{TP18} := Q_{ult}\left(Depth_{TP18}, r_{P4}, \beta_{P4.C}\right) = [11.341\ \ 8.372\ \ 13.331\ \ 0.599\ \ 33.643]$ $Q_{TP18} := \text{norm}\left(Q_{TP18}^{\langle 4\rangle}\right) = 33.643$

$$Depth_{TP19} := Depth_{P4}\left(\text{norm}\left(st.up._{P19}{}^{\langle 0\rangle}\right)\right)$$

$$Q_{TP19} := Q_{ult}\left(Depth_{TP19}, r_{P4}, \beta_{P4.C}\right) = \begin{bmatrix} 12.612 & 8.61 & 13.552 & 0.673 & 35.448 \end{bmatrix} \qquad Q_{TP19} := \text{norm}\left(Q_{TP19}{}^{\langle 4\rangle}\right) = 35.448$$

$$Depth_{TP20} := Depth_{P4}\left(\text{norm}\left(st.up._{P20}{}^{\langle 0\rangle}\right)\right)$$

$$Q_{TP20} := Q_{ult}\left(Depth_{TP20}, r_{P4}, \beta_{P4.C}\right) = \begin{bmatrix} 11.135 & 8.267 & 13.115 & 0.673 & 33.19 \end{bmatrix} \qquad Q_{TP20} := \text{norm}\left(Q_{TP20}{}^{\langle 4\rangle}\right) = 33.19$$

$$Depth_{TP15} := Depth_{P4}\left(\text{norm}\left(st.up._{P15}{}^{\langle 0\rangle}\right)\right)$$

$$Q_{TP15} := Q_{ult}\left(Depth_{TP15}, r_{P4}, \beta_{P4.T}\right) = \begin{bmatrix} 5.449 & 6.701 & 2.218 & 0.104 & 14.472 \end{bmatrix} \qquad Q_{TP15} := \text{norm}\left(Q_{TP15}{}^{\langle 4\rangle}\right) = 14.472$$

$$Depth_{TP16} := Depth_{P4}\left(\text{norm}\left(st.up._{P16}{}^{\langle 0\rangle}\right)\right)$$

$$Q_{TP16} := Q_{ult}\left(Depth_{TP16}, r_{P4}, \beta_{P4.T}\right) = \begin{bmatrix} 5.545 & 6.701 & 2.218 & 0.104 & 14.568 \end{bmatrix} \qquad Q_{TP16} := \text{norm}\left(Q_{TP16}{}^{\langle 4\rangle}\right) = 14.568$$

$$Depth_{TP17} := Depth_{P4}\left(\text{norm}\left(st.up._{P17}{}^{\langle 0\rangle}\right)\right)$$

$$Q_{TP17} := Q_{ult}\left(Depth_{TP17}, r_{P4}, \beta_{P4.T}\right) = \begin{bmatrix} 5.559 & 6.701 & 2.226 & 0.118 & 14.604 \end{bmatrix} \qquad Q_{TP17} := \text{norm}\left(Q_{TP17}{}^{\langle 4\rangle}\right) = 14.604$$

Qult of P6

$$\begin{aligned}
Q_{ult}(z, R, \beta) := \Bigg\| & Index_{SG.P1} \leftarrow \text{round}\left(\frac{z}{0.025}\right) \\
& \text{for } j \in 0,1..3 \\
& \quad \text{for } i \in Index_{SG.P1_j}, Index_{SG.P1_j}+1..Index_{SG.P1_{j+1}} \\
& \quad\quad \sigma_{avg_j} \leftarrow \sum_{i=Index_{SG.P1_j}}^{Index_{SG.P1_{j+1}}} \frac{\left(\sigma_{v.e_i}\right)}{Index_{SG.P1_{j+1}} - Index_{SG.P1_j}} \\
& \quad \sigma_{avg} \\
& \text{for } i \in 0,1..1 \\
& \quad Q_i \leftarrow \beta_i \cdot \sigma_{avg_i} \cdot \left(z_{i+1} - z_i\right) \cdot 2 \cdot \pi \cdot R_i \\
& \text{for } i \in 2 \\
& \quad Q_i \leftarrow \beta_i \cdot \sigma_{avg_i} \cdot 2 \cdot \pi \cdot \left(z_{i+1} - z_i\right) \cdot \left(\frac{\left(R_i{}^2 + R_{i+1}{}^2 + R_i \cdot R_{i+1}\right)}{3}\right)^{0.5} \\
& \text{for } i \in 3 \\
& \quad Q_i \leftarrow \beta_i \cdot \sigma_{avg_i} \cdot 2 \cdot \pi \cdot \left(z_{i+1} - z_i\right) \cdot \left(\frac{\left(\left(R_i - 0.024\right)^2 + \left(R_{i+1}\right)^2 + \left(R_i - 0.024\right) \cdot \left(R_{i+1}\right)\right)}{3}\right)^{0.5} \\
& \begin{bmatrix} Q_0 & Q_1 & Q_2 & Q_3 & Q_0 + Q_1 + Q_2 + Q_3 \end{bmatrix}
\end{aligned}$$

$$\beta_{P6.C} := \begin{bmatrix} \beta_{sm.1} & \beta_{th.1} & \beta_{t.c} \cdot RF_c & \beta_{t.c} \cdot RF_c \end{bmatrix}^{\mathrm{T}} \qquad \beta_{P6.T} := \begin{bmatrix} \beta_{sm.1} & \beta_{th.1} & \beta_{t.t} \cdot RF_t & \beta_{t.t} \cdot RF_t \end{bmatrix}^{\mathrm{T}}$$

$$Depth_{TP26} := Depth_{P6}\left(\text{norm}\left(st.up._{P26}{}^{\langle 0\rangle}\right)\right)$$

$$Q_{TP26} := Q_{ult}\left(Depth_{TP26}, r_{P6}, \beta_{P6.C}\right) = \begin{bmatrix} 10.755 & 7.338 & 13.241 & 0.24 & 31.574 \end{bmatrix} \qquad Q_{TP26} := \text{norm}\left(Q_{TP26}{}^{\langle 4\rangle}\right) = 31.574$$

$$Depth_{TP30} := Depth_{P6}\left(\text{norm}\left(st.up._{P30}{}^{\langle 0\rangle}\right)\right)$$

$$Q_{TP30} := Q_{ult}\left(Depth_{TP30}, r_{P6}, \beta_{P6.C}\right) = \begin{bmatrix} 8.898 & 6.926 & 12.806 & 0.24 & 28.87 \end{bmatrix} \qquad Q_{TP30} := \text{norm}\left(Q_{TP30}{}^{\langle 4\rangle}\right) = 28.87$$

$Depth_{TP31} := Depth_{P6}\left(\text{norm}\left(st.up._{P31}^{\langle 0\rangle}\right)\right)$

$Q_{TP31} := Q_{ult}\left(Depth_{TP31}, r_{P6}, \beta_{P6.C}\right) = [10.01 \quad 7.132 \quad 13.049 \quad 0.24 \quad 30.432]$ $\quad Q_{TP31} := \text{norm}\left(Q_{TP31}^{\langle 4\rangle}\right) = 30.432$

$Depth_{TP33} := Depth_{P6}\left(\text{norm}\left(st.up._{P33}^{\langle 0\rangle}\right)\right)$

$Q_{TP33} := Q_{ult}\left(Depth_{TP33}, r_{P6}, \beta_{P6.C}\right) = [11.718 \quad 7.543 \quad 13.433 \quad 0.244 \quad 32.938]$ $\quad Q_{TP33} := \text{norm}\left(Q_{TP33}^{\langle 4\rangle}\right) = 32.938$

$Depth_{TP27} := Depth_{P6}\left(\text{norm}\left(st.up._{P27}^{\langle 0\rangle}\right)\right)$

$Q_{TP27} := Q_{ult}\left(Depth_{TP27}, r_{P6}, \beta_{P6.T}\right) = [4.592 \quad 5.688 \quad 2.171 \quad 0.042 \quad 12.493]$ $\quad Q_{TP27} := \text{norm}\left(Q_{TP27}^{\langle 4\rangle}\right) = 12.493$

$Depth_{TP32} := Depth_{P6}\left(\text{norm}\left(st.up._{P32}^{\langle 0\rangle}\right)\right)$

$Q_{TP32} := Q_{ult}\left(Depth_{TP32}, r_{P6}, \beta_{P6.T}\right) = [3.428 \quad 5.273 \quad 2.078 \quad 0.054 \quad 10.833]$ $\quad Q_{TP32} := \text{norm}\left(Q_{TP32}^{\langle 4\rangle}\right) = 10.833$

$Depth_{TP57} := Depth_{P6}\left(\text{norm}\left(st.up._{P57}^{\langle 0\rangle}\right)\right)$

$Q_{TP57} := Q_{ult}\left(Depth_{TP57}, r_{P6}, \beta_{P6.T}\right) = [4.191 \quad 5.481 \quad 2.124 \quad 0.041 \quad 11.837]$ $\quad Q_{TP57} := \text{norm}\left(Q_{TP57}^{\langle 4\rangle}\right) = 11.837$

Coefficient of correlation of measured and estimated Qu

$$Q_{est} := \begin{bmatrix} Q_{TP3} \\ Q_{TP4} \\ Q_{TP43} \\ Q_{TP1} \\ \vdots \end{bmatrix} = \begin{bmatrix} 111.573 \\ 111.696 \\ 111.69 \\ 77.433 \\ \vdots \end{bmatrix} \qquad Q_{meas} := \begin{bmatrix} 128.78 \\ 139.48 \\ \vdots \end{bmatrix}$$

$mean_{Qu.est} := \text{mean}\left(Q_{est}\right) = 52.617$ $\qquad mean_{Qu.meas} := \text{mean}\left(Q_{meas}\right) = 53.477$

$$StandardDeviaton(data, mean) := \left| \begin{array}{l} data \leftarrow data \\ S.D. \leftarrow \left(\sum_{i=0}^{\text{rows}(data)-1} \frac{\left(data_i - mean\right)^2}{\text{rows}(data) - 1} \right)^{0.5} \end{array} \right|$$

$\sigma_{Qu.est} := StandardDeviaton\left(Q_{est}, mean_{Qu.est}\right) = 30.385$ $\qquad \sigma_{Qu.meas} := StandardDeviaton\left(Q_{meas}, mean_{Qu.meas}\right) = 33.418$

$$Covariance(data1, data2) := \left| \begin{array}{l} data1 \leftarrow data1 \\ data2 \leftarrow data2 \\ \frac{\left(\sum_{i=0}^{\text{rows}(data1)-1} \left(data1_i\right)\left(data2_i\right) \right)}{\text{rows}(data1)} - \frac{\left(\sum_{i=0}^{\text{rows}(data1)-1} data1_i \right)}{\text{rows}(data1)} \cdot \frac{\left(\sum_{i=0}^{\text{rows}(data2)-1} data2_i \right)}{\text{rows}(data2)} \end{array} \right|$$

$COV_{Tend.tension.Qu.tension} := Covariance\left(Q_{est}, Q_{meas}\right) = 891.701$

Correlation Coefficient (normalized covariance)

$\rho_{Temd.tension.Qu.tension} := \left(\frac{COV_{Tend.tension.Qu.tension}}{\sigma_{Qu.est} \cdot \sigma_{Qu.meas}}\right)^{0.5} = 0.937$ $\qquad R2 := \left(\text{corr}\left(Q_{meas}, Q_{est}\right)\right)^{0.5} = 0.949$

Using average percentage difference to find beta over the tapered segment in loose sand

$$Q_{u.est.Short.com} := \begin{bmatrix} Q_{TP6} \\ Q_{TP7} \\ \vdots \end{bmatrix} = \begin{bmatrix} 41.617 \\ 33.943 \\ \vdots \end{bmatrix} \qquad Q_{u.mea.Short.com} := \begin{bmatrix} 47.546 \\ \vdots \end{bmatrix}$$

$$PercentDifference_{comp} := \frac{Q_{u.est.Short.com}}{Q_{u.mea.Short.com}} \cdot 100 = \begin{bmatrix} 87.531 \\ \vdots \end{bmatrix} \qquad \text{mean}\left(PercentDifference_{comp}\right) = 100.001$$

$$Q_{u.est.Short.ten} := \begin{bmatrix} Q_{TP5} \\ \vdots \end{bmatrix} = \begin{bmatrix} 10.756 \\ \vdots \end{bmatrix} \qquad Q_{u.mea.Short.ten} := \begin{bmatrix} 7.5 \\ 12.59 \\ \vdots \end{bmatrix}$$

$$PercentDifference_{ten} := \frac{Q_{u.est.Short.ten}}{Q_{u.mea.Short.ten}} \cdot 100 = \begin{bmatrix} 143.416 \\ 46.014 \\ \vdots \end{bmatrix} \qquad \text{mean}\left(PercentDifference_{ten}\right) = 99.999$$

Backup Calculations to Get the K_t of each Micro Screw Pile in Compression And Tension

Empirical torque factor for piles

$$Reg.Const.Var\left(\mu_{data1},\mu_{data2}\right):=\left\|\begin{array}{l}\mu_{data1}\leftarrow\mu_{data1}\\ \mu_{data2}\leftarrow\mu_{data2}\\ \beta\leftarrow\left(\frac{\mu_{data2}}{\mu_{data1}}\right)\\ \beta\end{array}\right.$$

P1 - Tensile

$T_{end.tens.P1}:=\begin{bmatrix}6.603 & 5.549 & 5.115\end{bmatrix}^{T}$ $Q_{u.tens.P1}:=\begin{bmatrix}103.09 & 74.94 & 84.16\end{bmatrix}^{T}$

Size, Mean and Standard of Deviation

$n_{P1}:=\text{rows}\left(Q_{u.tens.P1}\right)=3$ $\mu_{Tend.tens.P1}:=\text{mean}\left(T_{end.tens.P1}\right)=5.756$ $\mu_{Qu.tens.P1}:=\text{mean}\left(Q_{u.tens.P1}\right)=87.397$

Linear Regression

$\beta_{Tend.tens.Qu.tens.P1}:=Reg.Const.Var\left(\mu_{Tend.tens.P1},\mu_{Qu.tens.P1}\right)=15.184$ $R2:=66.8\%$

P2 - Tensile

$T_{end.tens.P2}:=\begin{bmatrix}2.139 & 2.418 & 2.449\end{bmatrix}^{T}$ $Q_{u.tens.P2}:=\begin{bmatrix}7.5 & 12.59 & 13.96\end{bmatrix}^{T}$

Size, Mean and Standard of Deviation

$n_{P2}:=\text{rows}\left(Q_{u.tens.P2}\right)=3$ $\mu_{Tend.tens.P2}:=\text{mean}\left(T_{end.tens.P2}\right)=2.335$ $\mu_{Qu.tens.P2}:=\text{mean}\left(Q_{u.tens.P2}\right)=11.35$

Linear Regression

$\beta_{Tend.comp.Qu.comp.P2}:=Reg.Const.Var\left(\mu_{Tend.tens.P2},\mu_{Qu.tens.P2}\right)=4.86$ $R2:=42.7\%$

P3 - Tensile

$T_{end.tens.P3}:=\begin{bmatrix}2.325 & 2.914\end{bmatrix}^{T}$ $Q_{u.tens.P3}:=\begin{bmatrix}65.06 & 69.86\end{bmatrix}^{T}$

Size, Mean and Standard of Deviation

$n_{P3}:=\text{rows}\left(Q_{u.tens.P3}\right)=2$ $\mu_{Tend.tens.P3}:=\text{mean}\left(T_{end.tens.P3}\right)=2.62$ $\mu_{Qu.tens.P3}:=\text{mean}\left(Q_{u.tens.P3}\right)=67.46$

Linear Regression

$\beta_{Tend.tens.Qu.tens.P3}:=Reg.Const.Var\left(\mu_{Tend.tens.P3},\mu_{Qu.tens.P3}\right)=25.753$

P4 - Tensile

$T_{end.tens.P4}:=\begin{bmatrix}1.891 & 1.457 & 1.457\end{bmatrix}^{T}$ $Q_{u.tens.P4}:=\begin{bmatrix}15.41 & 14.05 & 14.75\end{bmatrix}^{T}$

Size, Mean and Standard of Deviation

$n_{P4}:=\text{rows}\left(Q_{u.tens.P4}\right)=3$ $\mu_{Tend.tensP4}:=\text{mean}\left(T_{end.tens.P4}\right)=1.602$ $\mu_{Qu.tens.P4}:=\text{mean}\left(Q_{u.tens.P4}\right)=14.737$

Linear Regression

$\beta_{Tend.tens.Qu.tens.P4}:=Reg.Const.Var\left(\mu_{Tend.tensP4},\mu_{Qu.tens.P4}\right)=9.201$

P5 - Tensile

$T_{end.tens.P5}:=\begin{bmatrix}2.17 & 2.542\end{bmatrix}^{T}$ $Q_{u.tens.P5}:=\begin{bmatrix}62.575 & 59.28\end{bmatrix}^{T}$

Size, Mean and Standard of Deviation

$n_{P5}:=\text{rows}\left(Q_{u.tens.P5}\right)=2$ $\mu_{Tend.tensP5}:=\text{mean}\left(T_{end.tens.P5}\right)=2.356$ $\mu_{Qu.tens.P5}:=\text{mean}\left(Q_{u.tens.P5}\right)=60.928$

Linear Regression

$\beta_{Tend.tens.Qu.tens.P5} := Reg.Const.Var\left(\mu_{Tend.tensP5}, \mu_{Qu.tens.P5}\right) = 25.861$

P1 - Comp

$T_{end.comp.P1} := \begin{bmatrix} 5.613 & 6.231 & 4.092 \end{bmatrix}^{T}$ $Q_{u.comp.P1} := \begin{bmatrix} 128.78 & 139.48 & 95.34 \end{bmatrix}^{T}$

Size, Mean and Standard of Deviation

$n_{P1} := \text{rows}\left(Q_{u.comp.P1}\right) = 3$ $\mu_{Tend.comp.P1} := \text{mean}\left(T_{end.comp.P1}\right) = 5.312$ $\mu_{Qu.comp.P1} := \text{mean}\left(Q_{u.comp.P1}\right) = 121.2$

Linear Regression

$\beta_{Tend.comp.Qu.comp.P1} := Reg.Const.Var\left(\mu_{Tend.comp.P1}, \mu_{Qu.comp.P1}\right) = 22.816$ $R2 := 98.9\%$

P2 - Comp

$T_{end.comp.P2} := \begin{bmatrix} 2.573 & 2.604 & 2.573 \end{bmatrix}^{T}$ $Q_{u.comp.P2} := \begin{bmatrix} 47.546 & 43.25 & 36.148 \end{bmatrix}^{T}$

Size, Mean and Standard of Deviation

$n_{P2} := \text{rows}\left(Q_{u.comp.P2}\right) = 3$ $\mu_{Tend.comp.P2} := \text{mean}\left(T_{end.comp.P2}\right) = 2.583$ $\mu_{Qu.comp.P2} := \text{mean}\left(Q_{u.comp.P2}\right) = 42.315$

Linear Regression

$\beta_{Tend.comp.Qu.comp.P2} := Reg.Const.Var\left(\mu_{Tend.comp.P2}, \mu_{Qu.comp.P2}\right) = 16.38$

P3 - Comp

$T_{end.comp.P3} := \begin{bmatrix} 2.48 & 3.534 \end{bmatrix}^{T}$ $Q_{u.comp.P3} := \begin{bmatrix} 82.24 & 117.5 \end{bmatrix}^{T}$

Size, Mean and Standard of Deviation

$n_{P3} := \text{rows}\left(Q_{u.comp.P3}\right) = 2$ $\mu_{Tend.comp.P3} := \text{mean}\left(T_{end.comp.P3}\right) = 3.007$ $\mu_{Qu.comp.P3} := \text{mean}\left(Q_{u.comp.P3}\right) = 99.87$

Linear Regression

$\beta_{Tend.comp.Qu.comp.P3} := Reg.Const.Var\left(\mu_{Tend.comp.P3}, \mu_{Qu.comp.P3}\right) = 33.213$ $R2 := 100\%$

P4 - Comp

$T_{end.comp.P4} := \begin{bmatrix} 1.736 & 2.046 & 1.922 \end{bmatrix}^{T}$ $Q_{u.comp.P4} := \begin{bmatrix} 57.28 & 56.34 & 48.125 \end{bmatrix}^{T}$

Size, Mean and Standard of Deviation

$n_{P4} := \text{rows}\left(Q_{u.comp.P4}\right) = 3$ $\mu_{Tend.comp.P4} := \text{mean}\left(T_{end.comp.P4}\right) = 1.901$ $\mu_{Qu.comp.P4} := \text{mean}\left(Q_{u.comp.P4}\right) = 53.915$

Linear Regression

$\beta_{Tend.comp.Qu.comp.P4} := Reg.Const.Var\left(\mu_{Tend.comp.P4}, \mu_{Qu.comp.P4}\right) = 28.356$

Pile information

$d_{P1} := 114.3\ mm$ $d_{P2} := 76.1\ mm$ $d_{P3} := 88.9\ mm$ $d_{P4} := 88.9\ mm$ $d_{P5} := 76.1\ mm$ $d_{P6} := 76.1\ mm$

$d_{eff.P1} := d_{P1}$ $d_{eff.P2} := d_{P2}$ $d_{eff.P3} := d_{P3}$ $d_{eff.P4} := d_{P4}$ $d_{eff.P5} := d_{P5}$ $d_{eff.P6} := d_{P6}$

Perko (2008)- Compression and Tension

$$K_t = \frac{\lambda_k}{d_{eff}^{0.92}}$$

λ_k = is a fittting factor equal to 1433 mm^0.92/m

d_{eff} = effective diameter

$\lambda_k := 1433$

$$K_{t.P1.c} := \frac{\lambda_k}{(114.3)^{0.92}} = 18.317 \qquad K_{t.P1.t} := 0.72 \cdot K_{t.P1.c} = 13.188$$

$$K_{t.P2.c} := \frac{\lambda_k}{(114.3)^{0.92}} = 18.317 \qquad K_{t.P2.t} := 0.27 \cdot K_{t.P2.c} = 4.945$$

$$K_{t.P3.c} := \frac{\lambda_k}{(88.9)^{0.92}} = 23.081 \qquad K_{t.P3.t} := 0.68 \cdot K_{t.P3.c} = 15.695$$

$$K_{t.P4.c} := \frac{\lambda_k}{(88.9)^{0.92}} = 23.081 \qquad K_{t.P4.t} := 0.27 \cdot K_{t.P4.c} = 6.232$$

$$K_{t.P5.c} := \frac{\lambda_k}{(76.1)^{0.92}} = 26.63 \qquad K_{t.P5.t} := 100 \cdot K_{t.P5.c} = 2.663 \cdot 10^3$$

$$K_{t.P6.c} := \frac{\lambda_k}{(76.1)^{0.92}} = 26.63$$

Appendix C: Additional Information of Lateral Load Field Test

In regards to lateral load field tests, the following information is included in this appendix:

- Site layout of the test pile, cone penetration tests and standard penetration tests at Sherwood Park and South Campus.
- The smoothening process of the raw lateral load vs displacement.
- An example of obtaining $P_{u\text{-}DB}$ based on DeBeer (1968).

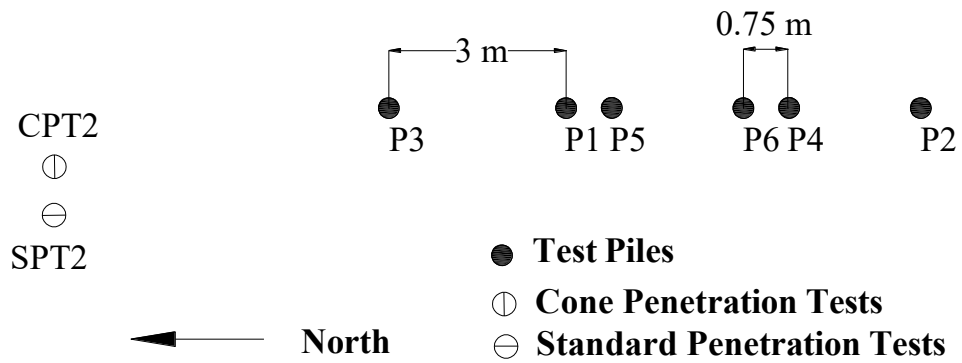

Figure C.1. Site layout of the lateral load field tested piles, cone penetration tests and standard penetration tests at Sherwood Park.

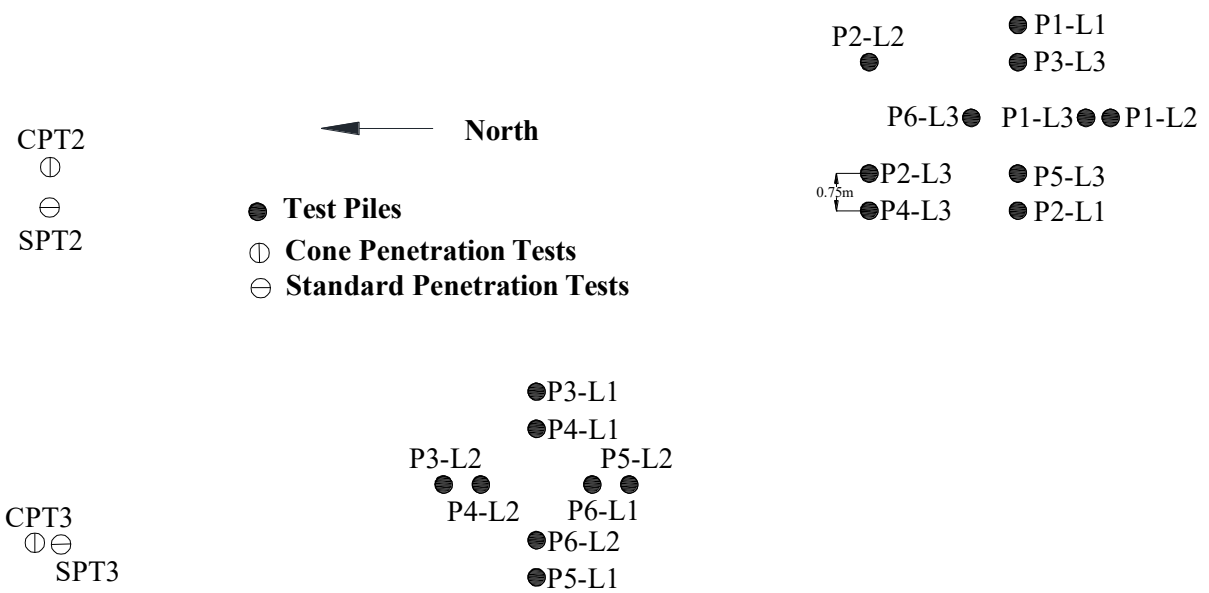

Figure C.2. Site layout of the lateral load field tested piles, cone penetration tests and standard penetration tests at South Campus.

The Smoothening Process of the Raw Lateral Load vs Displacement

Lateral Load Field Test

Project: CCMC Field Test **Pile Model: M114X3000** **Installation Date: August 30, 2018**

$Data := \text{READEXCEL}(\text{"..\..\Breuneheum\Lateral loading\Daily Log\63–August 29, 2018.xlsx"}, \text{"Sheet2!A3:L5608"})$

$Time := Data^{\langle 3 \rangle}\ min$

$LoadCell := Data^{\langle 7 \rangle}\ kN$

$P := LoadCell_{0,0} - LoadCell$

$LP1 := Data_{0,4}\ mm - Data^{\langle 4 \rangle}\ mm$

$LP2 := Data_{0,5}\ mm - Data^{\langle 5 \rangle}\ mm$

$LP3 := Data_{0,6}\ mm - Data^{\langle 6 \rangle}\ mm$

$Y := LP2$

Note 1: LP1 and LP2 were used to measure lateral displacement of the test pile. LP1 was not functioning properly. Therefore, LP1 was used as a measure of lateral displacement of the pile.

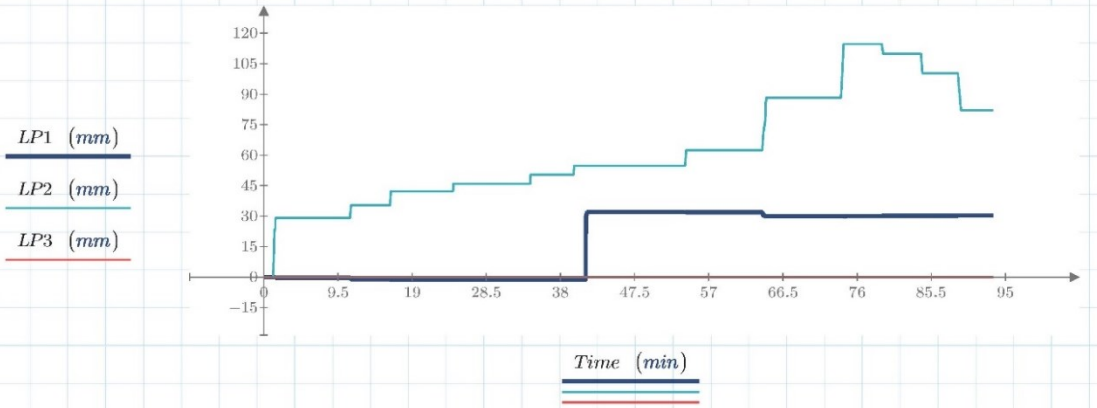

Note 2: LP3 was used to measure the lateral displacement of the reaction piles. The change of the lateral displacement in LP3 was zero.

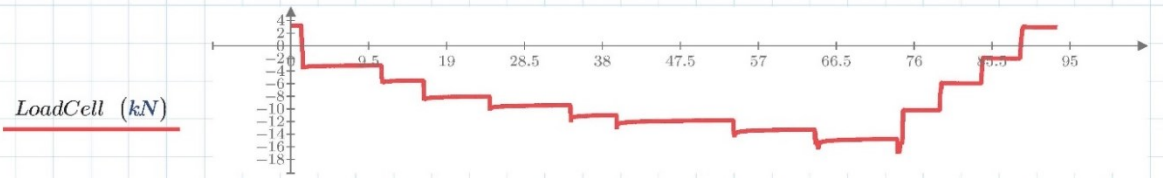

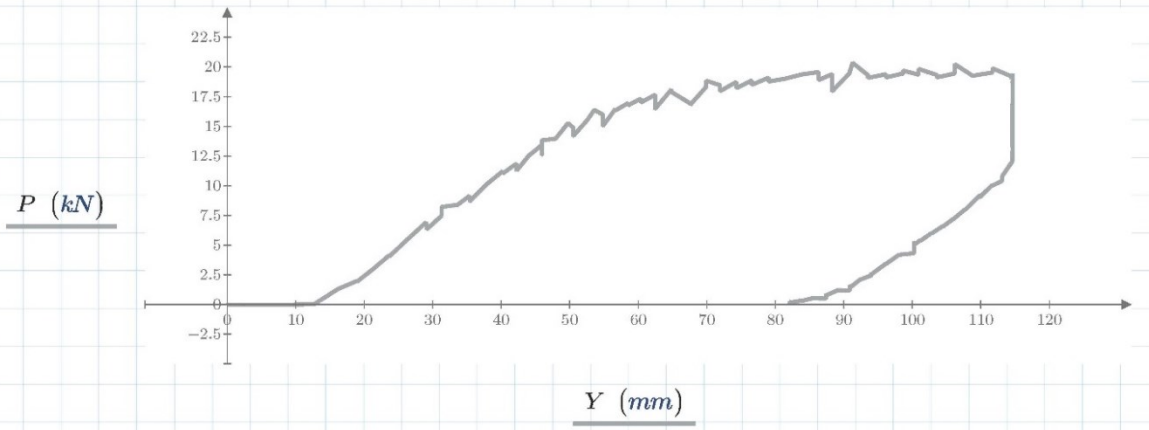

Note 3: The P vs Y curve was corrected because there was a small space in the hinge.

$$l := \begin{bmatrix} 0 \\ \vdots \end{bmatrix} = \begin{bmatrix} 0 \\ \vdots \end{bmatrix}$$

$$P_{smooth} := \left\| \begin{array}{l} \text{for } i \in 0,1..\text{rows}(l)-1 \\ \quad P_{smooth_i} \leftarrow P_{\text{norm}\left(\overset{i}{l}\right)} \\ \quad P_{smooth_i} \\ P_{smooth} \end{array} \right\|$$

$$Y_{smooth} := \left\| \begin{array}{l} \text{for } i \in 0,1..\text{rows}(l)-1 \\ \quad Y_{smooth_i} \leftarrow Y_{\text{norm}\left(\overset{i}{l}\right)} \\ \quad Y_{smooth_i} \\ Y_{smooth} \end{array} \right\|$$

$$t := 1 \qquad m := \frac{\left(P_{smooth_{t+1}} - P_{smooth_t}\right)}{\left(Y_{smooth_{t+1}} - Y_{smooth_t}\right)} = 0.384 \ \frac{kN}{mm}$$

$$b := P_{smooth_t} - m \cdot Y_{smooth_t} = -4.854 \ kN$$

$$x := \frac{(0-b)}{m} = 12.627 \ mm$$

$$P_{smooth.c} := \left\| \begin{array}{l} \text{for } i \in 0,1..t \\ \quad P_{smooth.c_i} \leftarrow 0 \ kN \\ \quad P_{smooth.c_i} \\ \text{for } i \in t+1,t+2..\text{rows}\left(P_{smooth}\right)-1 \\ \quad P_{smooth.c_i} \leftarrow P_{smooth_i} \\ \quad P_{smooth.c_i} \\ P_{smooth.c} \end{array} \right\|$$

$$Y_{smooth.c} := \left\| \begin{array}{l} \text{for } i \in 0,1..t \\ \quad Y_{smooth.c_i} \leftarrow 0 \ mm \\ \quad Y_{smooth.c_i} \\ Y_{smooth.c} \\ \text{for } i \in t+1,t+2..\text{rows}\left(Y_{smooth}\right)-1 \\ \quad Y_{smooth.c_i} \leftarrow Y_{smooth_i} - x \\ \quad Y_{smooth.c_i} \\ Y_{smooth.c} \end{array} \right\|$$

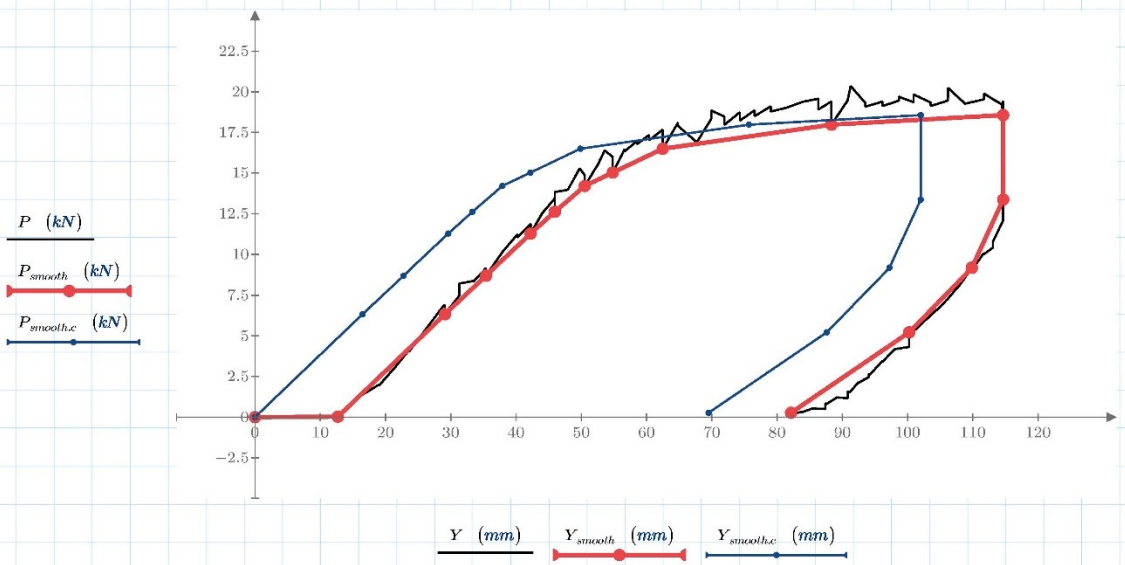

An Example of Obtaining $P_{u\text{-}DB}$ Based on DeBeer (1968)

$P_{uDB} := 15.025$ $Y_{uDB} := 42.193$

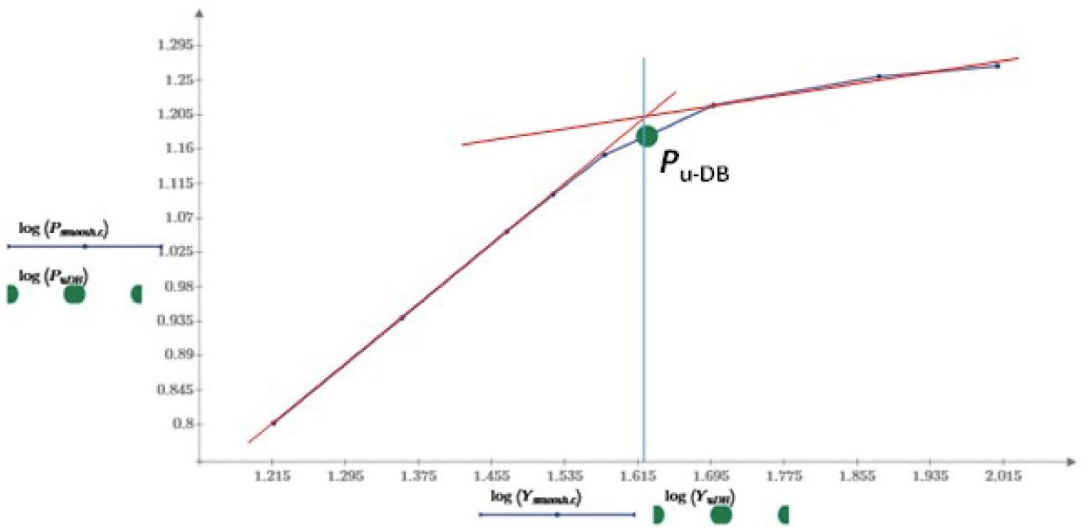

Note 4: The second ultimate lateral load (Pu-DB) was defined based on the DeBeer (1968) criterion. When plotting the P vs. Y curve in a double-logarithmic diagram, two approximate line will appear. One before and one after the ultimate lateral load. The intersection of these two lines was defined as the second ultimate lateral load (Pu-DB).

Appendix D: Additional Results of Lateral Cyclic Load Field Tests

The lateral load-displacement curve of the pile P4 tested at Sherwood Park is shown in Figure D.1. The overlap of the hysteresis over the 9 stages formed an envelope. This envelope had a similar pattern as the load- displacement curve of the monotonic lateral load field test that comprised an initial elastic zone with high stiffness, midway nonlinear transitional zone with decreasing stiffness and secondary linear zone with low stiffness. The hysteresis could be separated into two types: elastic hysteresis and plastic hysteresis. The elastic hysteresis was located near the first zone, and they are generally relatively linear and the area enclosed by the hysteresis was small. The plastic hysteresis was located near the third zone and they are generally non-linear and the area enclosed by the hysteresis was large. The time histories of the lateral load and displacement time are shown in Figure D.2. As shown in the Figure D.2, the load stays constant even with increasing displacement amplitude.

The stiffness of the pile (K) at each cycle was calculated using Equation D-1:

$$K = \frac{Q_{\max_i} - Q_{\min_i}}{w_{\max_i} - w_{\min_i}} \tag{D-1}$$

where $Q_{\max,i}$ and $Q_{\min,i}$ are the maximum and minimum load at each cycle and $w_{\max,i}$ and $w_{\min,i}$ are the maximum and minimum displacement at each cycle. The values of K at each cycle are shown in Figure D.2.b. As shown in the Figure D.2.b, the values of K decreased with the number of cycle and displacement amplitude. The value of K decreased steeply with the number of cycles during the first four stages. The value of K decreased modestly with the increased number of cycles during the 5^{th} to 9^{th} cycles. Therefore, two lines of best fit were drawn based on the regressed equation. Perhaps, the intersection of these two lines at the displacement of 16.6 mm could be an estimation of $Y_{ult.DeBeer}$.

The pile equivalent damping ratio (ξ) at each cycle was calculated using Equation D-2:

$$\xi = \frac{1}{4\pi}\frac{E_D}{E_s} \tag{D-2}$$

where E_D is the dissipated energy and E_s is the maximum strain energy in each cycle. The value of ξ each cycle is shown in Figure D.2.c. As shown in the Figure D.2.c, the values of ξ fluctuated around a constant value of 0.08 during the first five cycles. This was a mark of elastic response where the amount of energy dissipated was constantly small. The value of ξ increased dramatically with the number of cycles during 6th to 9th cycle. The increase of ξ shows that there was failure or plasticization of either the pile or the soil surrounding the pile because the amount of energy dissipated was increasing. In Figure D.2.c, two lines of best fit were drawn based on the regressed equation. The intersection of these two lines at the displacement of 33.2 mm was an estimation of $Y_{ult.DeBeer}$. As can be seen, there was a significant difference between the values of $Y_{ult.DeBeer}$ that was based on the stiffness and ξ values, which shows that this method was very inconsistent.

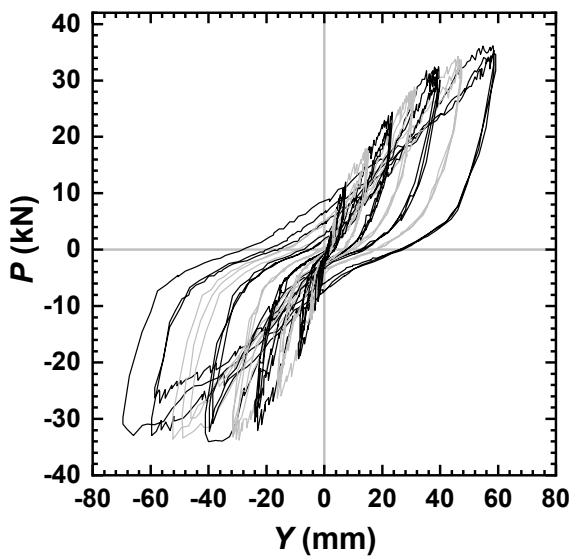

Figure D.1. Cyclic lateral load versus displacement of the pile P4 at Sherwood Park

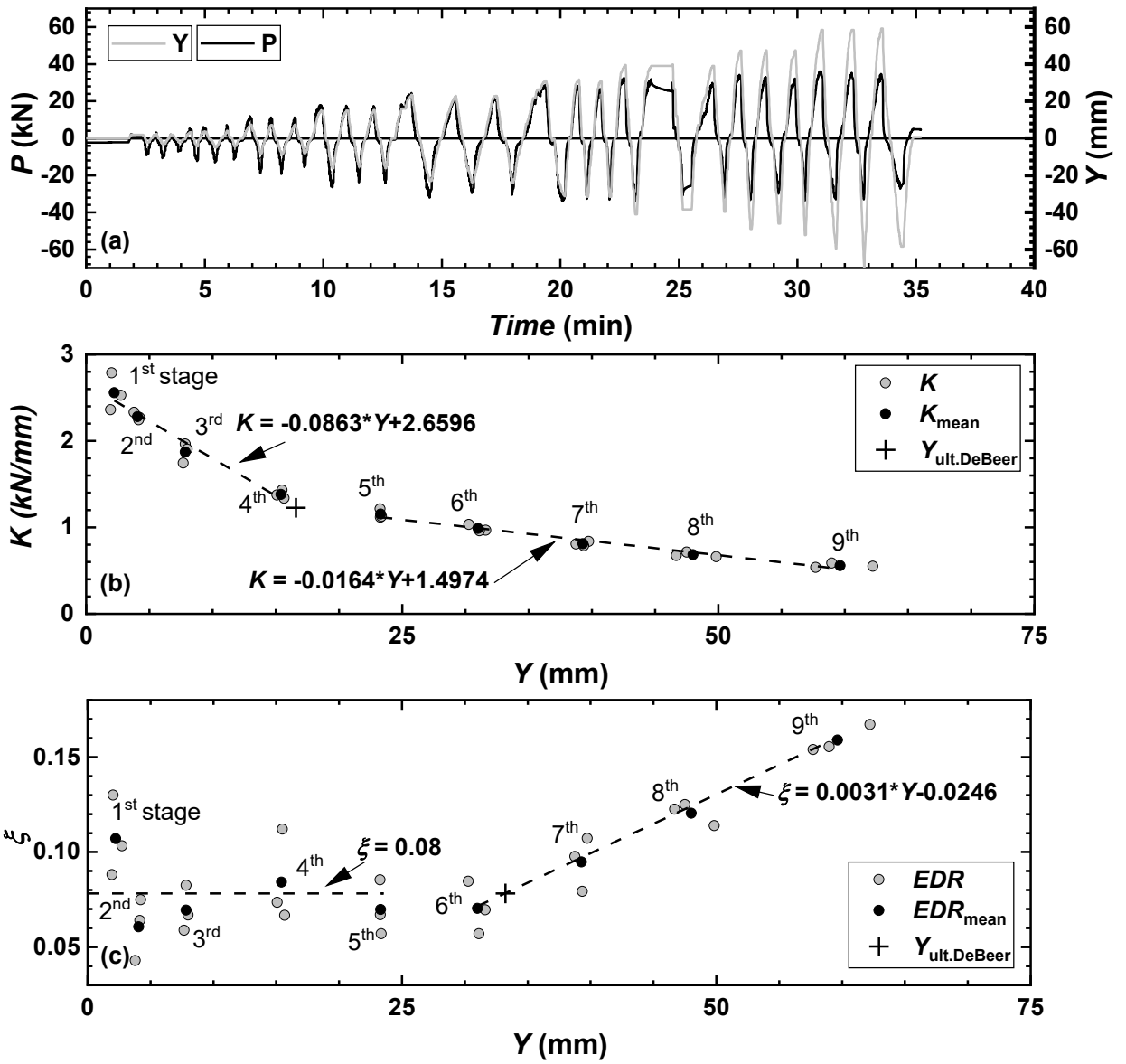

Figure D.2. Results of cyclic lateral load field test of the pile P4 at Sherwood Park: (a) lateral load and displacement time history, (b) stiffness of the pile and (c) equivalent damping ratio

Appendix E: OpenSEES Codes for Simulation of Micro Screw Pile Subjected to Lateral Loading

Classical Hermitian Polynomials (Laplace 1810)

hermitian polynomials can defined as following:

$(-1)^n e^{x^2} \frac{d^n}{dx^n} e^{-x^2}$ $\quad x := -1, -0.95 .. 1 = \begin{bmatrix} -1 \\ \vdots \end{bmatrix}$ (Laplace 1810)

The first elevent hermitian polynomials are defined as following:

$H_0 := 1$

$H_1 := 2\,x$

$H_2 := 4\,x^2 - 2$

$H_3 := 8\,x^3 - 12\,x$

$H_4 := 16\,x^4 - 48\,x^2 + 12$

$H_5 := 32\,x^5 - 160\,x^3 + 120\,x$

$H_6 := 64\,x^6 - 480\,x^4 + 720\,x^2 - 120$

$H_7 := 128\,x^7 - 1344\,x^5 + 3360\,x^3 - 1680\,x$

$H_8 := 256\,x^8 - 3584\,x^6 + 13440\,x^4 - 13440\,x^2 + 1680$

$H_9 := 512\,x^9 - 9216\,x^7 + 48384\,x^5 - 80640\,x^3 + 30240\,x$

$H_{10} := 1024\,x^{10} - 23040\,x^8 + 161280\,x^6 - 403200\,x^4 + 302400\,x^2 - 30240$

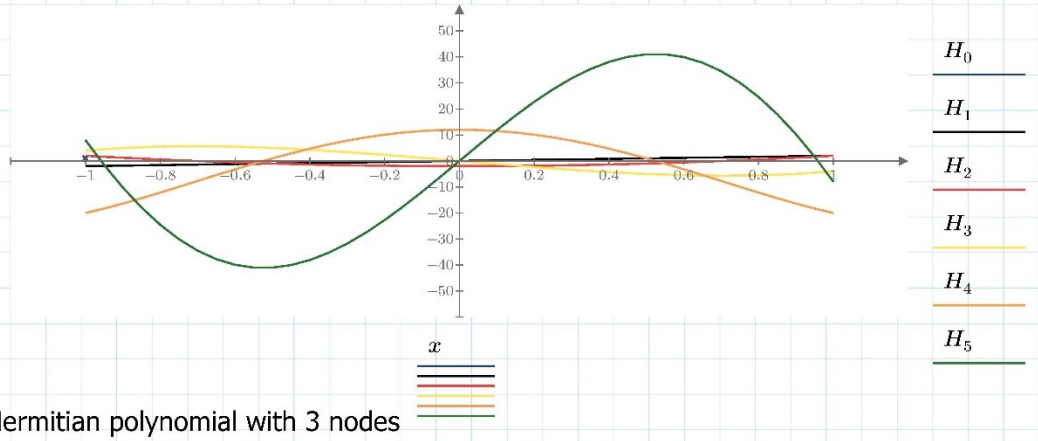

Hermitian polynomial with 3 nodes

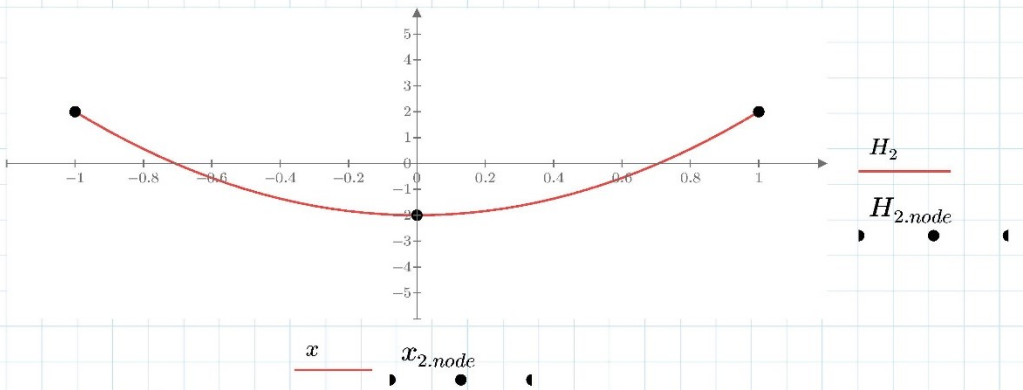

Gauss-Legendre quadrature (Golub and Welsch 1969)

Gauss-Legendre quadrature is a method to approximate the definite integral of a function by using quadrature weights and the root of the nth polynomial as shown in following:

$$\int_{-1}^{1} f(x)\,dx = \sum_{i=1}^{n} w_i \cdot f(x_i)$$

where n is the number of sample used, wi is the quadrature weights and xi is the root of the nth polynomial.
(Golub and Welsch 1969)

Main Program

This OpenSEES program simulates the lateral response of the micro screw pile by representing the lateral shaft reaction, the vertical shaft reaction, the thread bearing reaction and the lateral thread reaction as *p*-*y*, *t*-*z*, *q*-*z* and t_h-*y* spring. The soil reaction parameters are calculated in other OpenSEES program.

```
wipe
#=================================================================
# pile stickup length
set L1 0.2

# pile embedment length
set L2 2.8

# smooth pile length
set L3 0.815

# number of pile element
set Element 60

# total number of pile nodes
set PileNode [expr 1 + $Element]

# pile element length
set ElemSize [expr ($L1+$L2)/$Element]

# total number of spring nodes
set SpringNode [expr round([expr 1 + $L2 /$ElemSize])]

# model builder:
model basic -ndm 2 -ndf 3

#=================================================================
# create pile nodes
set count 0
for {set i 1} {$i <= $PileNode} {incr i} {
   set zCoord [expr $ElemSize*($i - 1)]
   if {$zCoord <= [expr $L1 + $L2]} {
      node $i 0.0 $zCoord
      set count [expr $count + 1]
   }
}

#=================================================================
#create spring nodes over embedded length of pile
set count 0
for {set i [expr $PileNode + 1]} {$i <= [expr $PileNode + $SpringNode]} {incr i} {
```

```
   set zCoord [expr $ElemSize*($i - $PileNode - 1) + $L1]
   if {$zCoord <= [expr $L1 + $L2 + 0.001]} {
      node $i 0.0 $zCoord
         node [expr $i + $SpringNode] 0.0 $zCoord
         set count [expr $count + 1]
                  }
}

#=========================================================================
# Boundary Condition at pile toe:
fix [expr round($PileNode)] 0 0 0;
fix [expr round([expr $PileNode + $SpringNode])] 0 0 0;

#=========================================================================
# fix spring nodes
set count 0
for {set i [expr $PileNode + $SpringNode + 1]} {$i <= [expr $PileNode + 2 * $SpringNode]}
{incr i} {
         fix $i 1 1 1
   set count [expr $count + 1]
}

#=========================================================================
# create spring nodes
for {set i [expr $PileNode + 1]} {$i <= [expr $PileNode + $SpringNode]} {incr i} {
   equalDOF $i [expr $i - $SpringNode] 1 2 3
   set count [expr $count + 1]
}

#=========================================================================
# transformation:
geomTransf Corotational 1

# time
timeSeries Linear 1
pattern Plain 1 1 {
load 1 30000. 0. 0.0
}

#=========================================================================
# create depth for pile length
set count 1
for {set i 1} {$i <= $PileNode} {incr i} {
         set z1($i) [expr $ElemSize*($i - 1)]

         # procedure to get inner diameter at each index
         source GetID.tcl;
```

```
	set ID1($i) [GetID $z1($i)];

	# procedure to get outer diameter at each index
	source GetOD.tcl;
	set OD1($i) [GetOD $z1($i)];

	set count [expr $count+1]
}

#=========================================================================
set count 1

# set soil reaction parameters
for {set i 1} {$i <= $SpringNode} {incr i} {
	#embebdment depth
	set z2($i) [expr $ElemSize*($i - 1)]

	# procedure to get su at each index
	source Getsu.tcl;
	set su($i) [Getsu $z2($i)];

	# procedure to get UW at each index
	source GetUW.tcl;
	set UW($i) [GetUW $z2($i)];

	# procedure to get 50 percent strain at each index
	source Gete50.tcl;
	set e50($i) [Gete50 $su($i)];

	# procedure to get coefficient J of clay at each index
	source GetJ.tcl;
	set J($i) [GetJ $su($i)];

	# procedure to get outer diameter at each index
	source GetID.tcl;
	set ID2($i) [GetID [expr $z2($i) + $L1]];

	# procedure to get outer diameter at each index
	source GetOD.tcl;
	set OD2($i) [GetOD [expr $z2($i) + $L1]];

	# procedure to get Pult at each index
	source CalcPult.tcl;
	set Pult($i) [CalcPult $UW($i) $z2($i) [expr $OD2($i) + 0.0] $su($i) $ElemSize 0.5];

	# procedure to get Tult at each index
	source CalcTult.tcl;
```

```
        set Tult($i) [CalcTult $su($i) $ElemSize $OD2($i)];

        # procedure to get Qult at each index
        source CalcQult.tcl;
        set Qult($i) [CalcQult $su($i) $OD2($i) $ID2($i)]

        # procedure to get Tult at each index
        source CalcTulth1.tcl;
        set Tulth1($i) [CalcTulth1 $z2($i) $ID2($i) $OD2($i) $ElemSize];

   set count [expr $count + 1]
}

#=========================================================================
# create pile material and element
set E 2.10e11;#psi 210GPa
set Fy 248.0e6; #248MPa
set b 0.1; #hardening ratio
set R0 15.0; #recommended value
set cR1 0.925; #recommended value
set cR2 0.15; #recommended value

uniaxialMaterial Steel02 5000 $Fy $E $b $R0 $cR1 $cR2

set count 0
for {set i 1} {$i <= $Element} {incr i} {
section Fiber $i {
   set subcircum 36
   set subradius 9
   patch circ 5000 $subcircum $subradius 0.0 0.0 [expr $ID1($i)/2] [expr $OD1($i)/2] 0.0 360.0
}
element dispBeamColumn $i $i [expr $i+1] 3 $i 1
}

#=========================================================================
# create Pyspring material
set count 1
for {set i 1} {$i <= $SpringNode} {incr i} {
     uniaxialMaterial PySimple1 $i 1 $Pult($i) [expr 1*2.5*$e50($i)*$OD2($i)] 0.1
     set count [expr $count + 1]
}

# create Pyspring element
set count 0
for {set i 1} {$i <= [expr $SpringNode]} {incr i} {
     element zeroLength [expr $i + $Element] [expr $i + $PileNode] [expr $i + $SpringNode +
     $PileNode] -mat $i -dir 1
```

```
    set count [expr $count + 1]
}

#=========================================================================
# built tzspring material
set count 1
for {set i 1} {$i <= $SpringNode} {incr i} {
    uniaxialMaterial TzSimple1 [expr $i + $SpringNode] 1 $Tult($i) 0.0016
    set count [expr $count + 1]
}

# create tzspring element
set count 0
# create spring elements
for {set i 1} {$i <= [expr $SpringNode]} {incr i} {
    element zeroLength [expr $i + $SpringNode + $Element] [expr $i + $PileNode] [expr $i +
    $SpringNode + $PileNode] -mat [expr $i + $SpringNode] -dir 2
    set count [expr $count + 1]
}

#=========================================================================
set skipnode [expr round([expr ($L3 - $L1)/0.05])];

# spring material properties
set count 1;
for {set i 1} {$i <= [expr $SpringNode - $skipnode]} {incr i} {
    uniaxialMaterial QzSimple1 [expr $i +  2 * $SpringNode]  1 $Qult([expr $i + $skipnode])
    [expr 0.008 * ($OD2([expr $i + $skipnode]) + 0.024)]
    set count [expr $count + 1]
}

#=========================================================================
# create zeroLengthSection using QzSimple1 material
set count 1;
for {set i 1} {$i <= [expr $SpringNode - $skipnode]} {incr i} {
section Fiber [expr $i + 200] {
    set subcircum 36
    set subradius 9
    patch circ [expr $i +  2 * $SpringNode] 36 9 0.0 0.0 [expr $OD2([expr $i + $skipnode])/2]
    [expr $OD2([expr $i + $skipnode])/2 + 0.012] 0.0 360.0
}
element zeroLengthSection [expr $i + 2 * $SpringNode + $Element] [expr $i + $PileNode] [expr
$i + $SpringNode + $PileNode] [expr $i + 200] -orient 0 1 0 1 0 0
}

#=========================================================================
# spring material properties
```

```
set count 1;
for {set i 1} {$i <= [expr $SpringNode - $skipnode]} {incr i} {
    uniaxialMaterial TzSimple1 [expr $i +  3 * $SpringNode - $skipnode]  1 $Tulth1([expr $i +
    $skipnode - 1]) 0.0016
    set count [expr $count + 1]
}

#=====================================================================
# create tzspring element
set count 0
# create spring elements
for {set i 1} {$i <= [expr $SpringNode - $skipnode]} {incr i} {
    element zeroLength [expr $i + 3 * $SpringNode + $Element - $skipnode] [expr $i + $PileNode
    + $skipnode] [expr $i + $SpringNode + $PileNode + $skipnode] -mat [expr $i + 3 *
    $SpringNode - $skipnode] -dir 1
    set count [expr $count + 1]
}

#=====================================================================
#Recorder:
recorder Node -file Nodedisp.out -time -nodeRange 1 61 -dof 1 disp
recorder Node -file Nodeforce.out -time -nodeRange 1 61 -dof 1 reaction
recorder Element -file pileForce.out  -time  -eleRange 1 60 globalForce

recorder Node -file pyNodedisp1.out  -time -node 1 -dof 1 disp
recorder Element -file pyelementForce1.out  -time  -ele 1 force
recorder Node -file tzNodedisp1.out  -time -node 1 -dof 1 disp
recorder Element -file tzelementForce1.out  -time  -ele 1 force


#Analysis
integrator DisplacementControl 1 1 0.0001
numberer RCM
system SparseGeneral
constraints Transformation
test NormDispIncr 1 100  0
algorithm Newton
analysis Static
analyze 171

integrator DisplacementControl 1 1 -0.0001
analyze 1

wipe
```

external program - Get inner diameter of pile P1

```
# This procedure is built to output inner diameter of the pile for a given depth.
proc GetID {z} {

# create inner diameter for segment 1 of pile (Diameter straight = 114.3 mm)
     if {(0<=$z) && ($z<=2.316)} {
     set ID 0.1071}
# create inner diameter for segment 2 of pile (Diameter Tapered)
     if {(2.317<=$z) && ($z<=2.5287)} {
     set ID [expr 0.1071+(0.1071-0.0648)*($z-2.317)/(2.317-2.5287)];}
# create inner diameter for segment 3 of pile (Diameter straight = 76.1 mm)
     if {(2.5288<=$z) && ($z<=2.6547)} {
     set ID 0.0689}
# create inner diameter for segment 4 of pile (Diameter Tapered)
     if {(2.6548<=$z) && ($z<=2.9806)} {
     set ID [expr 0.0689+(0.0689-0.025401)*($z-2.6548)/(2.6548-2.9806)];}
# create inner diameter for segment 5 of pile (Diameter Tapered)
     if {(2.9807<=$z) && ($z<=3.0326)} {
     set ID [expr 0.025401+(0.025401-0)*($z-2.9807)/(2.9807-3.0326)];}
return $ID;}
```

external program - Get outer diameter of pile P1

```
# This procedure is built to output outer diameter of the pile for a given depth.
proc GetOD {z} {

# create outer diameter for segment 1 of pile (Diameter straight = 114.3 mm)
     if {(0<=$z) && ($z<=2.316)} {
     set OD 0.1143}
# create outer diameter for segment 2 of pile (Diameter Tapered)
     if {(2.317<=$z) && ($z<=2.5287)} {
    set OD [expr 0.1143+(0.1143-0.07610)*($z-2.317)/(2.317-2.5287)];}
# create outer diameter for segment 3 of pile (Diameter straight = 76.1 mm)
     if {(2.5288<=$z) && ($z<=2.6547)} {
     set OD 0.07610}
# create outer diameter for segment 4 of pile (Diameter Tapered)
     if {(2.6548<=$z) && ($z<=2.9806)} {
     set OD [expr 0.07610+(0.07610-0.0411)*($z-2.6548)/(2.6548-2.9806)];}
# create outer diameter for segment 5 of pile (Diameter Tapered)
     if {(2.9807<=$z) && ($z<=3.0326)} {
     set OD [expr 0.0411+(0.0411-0.003)*($z-2.9807)/(2.9807-3.0326)];}

return $OD;}
```

external program - Get undrained shear strength

```
# This procedure is built to output Su for a given depth.
```

```
proc Getsu {z} {

# get and read the depth and su file
catch {open CPT7Depth.txt r} CPT7Depth ;
catch {open CPT7Su.txt r} CPT7Su  ;

# create Depth array and Su array
set Depth [split [read $CPT7Depth]];
set Su [split [read $CPT7Su]];

set LN [llength $Depth];

# create D and S array with index from 0 to 148
for {set i 0} {$i <= [expr $LN - 2]} {incr i} {
    set D($i) [lindex $Depth $i]
    set S($i) [lindex $Su $i]}

# use linear interpolation to get su at any depth
for {set i 0} {$i <= [expr $LN - 3]} {incr i} {
    if {($D($i)<=$z) && ($z<=$D([expr $i+1]))} {
    set su [expr 1000*($S($i)+($S([expr $i+1])-$S($i))*($z-$D($i))/($D([expr $i+1])-
    $D($i)))];}}

set i 0;
# create su for initial depths
if {(0<=$z) && ($z<=$D($i))} {
    set su [expr $S($i)*1000];}

return $su;}
```

external program - Get unit weight

```
proc GetUW {z} {

# get and read the depth and UW file
catch {open CPT7Depth.txt r} CPT7Depth ;
catch {open CPT7UW.txt r} CPT7UW  ;

# create Depth array and UW array
set Depth [split [read $CPT7Depth]];
set UW [split [read $CPT7UW]];

set LN [llength $Depth];

# create D and UWW array with index from 0 to 148
for {set i 0} {$i <= [expr $LN - 2]} {incr i} {
    set D($i) [lindex $Depth $i]
    set UWW($i) [lindex $UW $i]}
```

```
# use linear interpolation to get UWW at any depth
for {set i 0} {$i <= [expr $LN - 3]} {incr i} {
     if {($D($i)<=$z) && ($z<=$D([expr $i+1]))} {
     set UW [expr 1000*($UWW($i)+($UWW([expr $i+1])-$UWW($i))*($z-$D($i))/($D([expr
     $i+1])-$D($i)))];}}

set i 0;
# create UW for initial depths
if {(0<=$z) && ($z<=$D($i))} {
  set UW $UWW($i);}

return $UW;}
```

external program - Get J

```
# This program outputs coefficient J of clay

proc GetJ {su} {

if {$su <= 12500} {
     set J 0.28;}
if {(12510 <= $su) && ($su <= 25000)}  {
     set J 0.5;}
if {(25010 <= $su) && ($su <= 50000)}  {
     set J 0.83;}
if {(50010 <= $su) && ($su <= 100000)}  {
     set J 1.5;}
if {(100010 <= $su) && ($su <= 200000)}  {
     set J 2.84;}
if {(200010 <= $su) && ($su <= 400000)}  {
     set J 5.51;}
if {(400010 <= $su)}  {
     set J 10.85;}

return $J}
```

external program - Get ε_{50}

```
# This program calculates e50 of clay using Matlock (1970) equation.

proc Gete50 {su} {

if {$su <= 24000} {
set e50 0.02;}
if {(24010 <= $su) && ($su <= 48000)}  {
set e50 0.01;}
if {(48010 <= $su) && ($su <= 96000)}  {
set e50 0.007;}
```

```
if {(96010 <= $su) && ($su <= 192000)}  {
set e50 0.007;}
if {(192010 <= $su) && ($su <= 384000)}  {
set e50 0.007;}

return $e50}
```

external program - Get P_{ult} of clay

```
# This program calculates Pult of clay using Matlock (1970) equation.

proc CalcPult {UW z D su ElemSize J} {

# create Nc
set Nc [expr 3 + ($UW*$z)/$su+($J*$z)/$D]

# an upper limit Nc of 9
if {$Nc > 9} {
set Nc 9 ;}

# create pu
set Pult [expr $Nc*$su*$D*$ElemSize];

return $Pult}
```

external program - Get T_{ult} of clay

```
# This program calculates Tult of clay using Tomlinson (1957) equation.

proc CalcTult {su ElemSize D} {

# atmospheric pressure in kPa
set Pa 101325;
set pi 3.14159265359;

# calculate adhesion coefficient
set adhesioncoefficient [expr 0.21 + 0.26*$Pa/$su]

# an upper limit of 1 for adhesion coefficient
if {$adhesioncoefficient > 1} {
set adhesioncoefficient 1 ;}

# calculate Tult
set Tult [expr $adhesioncoefficient*$su*$pi*$D*$ElemSize];

return $Tult}
```

external program - Get Q_{ult} of clay

```
# This program calculates Qult of clay.
```

```
proc CalcQult {su OD ID} {

# define bearing capacity coefficient
set pi 3.14159265359
set Nc 9;

# calculate Qult
set Qult [expr $Nc*$su*$pi* (pow(($OD + 0.024),2) - pow($OD,2)) * 0.003086];

return $Qult}
```

external program - Get T_{ult} of clay in horizontal direction

```
# This program calculates Tult of clay using Tomlinson (1957) equation.

proc CalcTulth1 {z di do ElemSize} {

# get the friction angle at the required depth
source Getsu.tcl;
set su [Getsu $z];

# atmospheric pressure in kPa
set Pa 101325;
set pi 3.14159265359;


# calculate adhesion coefficient
set adhesioncoefficient [expr 0.21 + 0.26*$Pa/$su]

# an upper limit of 1 for adhesion coefficient
if {$adhesioncoefficient > 1} {
set adhesioncoefficient 1 ;}

# obtain the area of the upside and downside of the thread
set Area [expr (pow((pow(0.05,2) + pow($pi * $do,2)),0.5) + pow(pow(0.05,2)+pow($pi *
($do+0.024),2),0.5))/2 * 0.012 * 2]
puts "Area"
puts $Area

# calculate Tult
set Tulth1 [expr $su*$adhesioncoefficient*$Area];

return $Tulth1}
```

external program - Get friction angle of sand

```
# This procedure is built to output FA for a given depth.
```

```
proc GetFA {z} {

# get and read the depth and FA file
catch {open CPT3DepthSand.txt r} CPT3Depth ;
catch {open CPT3FASand.txt r} CPT3FA  ;

# create Depth array and FA array
set Depth [split [read $CPT3Depth]];
set FA [split [read $CPT3FA]];

set LN [llength $Depth];

# create D and FAA array with index
for {set i 0} {$i <= [expr $LN - 2]} {incr i} {
  set D($i) [lindex $Depth $i]
  set FAA($i) [lindex $FA $i]}

# use linear interpolation to get FA at any depth
for {set i 0} {$i <= [expr $LN - 3]} {incr i} {
    if {($D($i)<=$z) && ($z<=$D([expr $i+1]))} {
    set FA [expr ($FAA($i)+($FAA([expr $i+1])-$FAA($i))*($z-$D($i))/($D([expr $i+1])-
$D($i)))];}}

set i 0;
# create FA for initial depths
if {(0<=$z) && ($z<=$D($i))} {
    set FA [expr $FAA($i)];}

return $FA;}
```

external program - Get relative density of sand

```
# This procedure is built to output Dr for a given depth.

proc GetDr {z} {

# get and read the depth and Dr file
catch {open CPT3DepthSand.txt r} CPT3Depth ;
catch {open CPT3DrSand.txt r} CPT3Dr  ;

# create Depth array and Dr array
set Depth [split [read $CPT3Depth]];
set Dr [split [read $CPT3Dr]];

set LN [llength $Depth];

# create D and Drr array with index
for {set i 0} {$i <= [expr $LN - 2]} {incr i} {
```

```
    set D($i) [lindex $Depth $i]
    set Drr($i) [lindex $Dr $i]}

# use linear interpolation to get Dr at any depth
for {set i 0} {$i <= [expr $LN - 3]} {incr i} {
  if {($D($i)<=$z) && ($z<=$D([expr $i+1]))} {
  set Dr [expr ($Drr($i)+($Drr([expr $i+1])-$Drr($i))*($z-$D($i))/($D([expr $i+1])-$D($i)))];}}

set i 0;
# create Dr for initial depths
if {(0<=$z) && ($z<=$D($i))} {
    set Dr [expr $Drr($i)];}

return $Dr;}
```

external program- Get unit weight of sand

```
proc GetUW {z} {

# get and read the depth and UW file
catch {open CPT3DepthSand.txt r} CPT3Depth ;
catch {open CPT3UWSand.txt r} CPT3UW  ;

# create Depth array and UW array
set Depth [split [read $CPT3Depth]];
set UW [split [read $CPT3UW]];

set LN [llength $Depth];

# create D and UWW array with index from 0 to 148
for {set i 0} {$i <= [expr $LN - 2]} {incr i} {
    set D($i) [lindex $Depth $i]
    set UWW($i) [lindex $UW $i]}

# use linear interpolation to get UWW at any depth
for {set i 0} {$i <= [expr $LN - 3]} {incr i} {
  if {($D($i)<=$z) && ($z<=$D([expr $i+1]))} {
  set UW [expr 1000*($UWW($i)+($UWW([expr $i+1])-$UWW($i))*($z-$D($i))/($D([expr
$i+1])-$D($i)))];}}

set i 0;
# create UW for initial depths
if {(0<=$z) && ($z<=$D($i))} {
    set UW $UWW($i);}

return $UW;}
```

external program -Get vertical stress of the sand

```
# This procedure is built to output VS for a given depth.

proc GetVS {z} {

# get and read the depth and UW file
catch {open CPT3DepthSand.txt r} CPT3Depth ;
catch {open CPT3UWSand.txt r} CPT3UW  ;

# create Depth array and UW array
set Depth [split [read $CPT3Depth]];
set UW [split [read $CPT3UW]];

set LN [llength $Depth];

# create D and VSS array with index
for {set i 0} {$i <= [expr $LN - 1]} {incr i} {
  set D($i) [lindex $Depth $i]
  set UWW($i) [lindex $UW $i]}

# create D and VSS array with index

for {set i 0} {$i <= 0} {incr i} {
     set VSS($i) [expr 0.025*$UWW($i)]}
for {set i 1} {$i <= 72} {incr i} {
   set VSS($i) [expr 0.025* $UWW($i) + $VSS([expr $i - 1])]}

for {set i 73} {$i <= [expr $LN - 1]} {incr i} {
   set VSS($i) [expr 0.025* $UWW($i) + $VSS([expr $i - 1]) - 0.025*9.81]}

# use linear interpolation to get VS at any depth
for {set i 0} {$i <= [expr $LN - 1]} {incr i} {
     if {($D($i)<=$z) && ($z<=$D([expr $i+1]))} {
     set VS [expr ($VSS($i)+($VSS([expr $i+1])-$VSS($i))*($z-$D($i))/($D([expr $i+1])-
     $D($i)))];}}

set i 0;
# create VS  for initial depths
if {(0<=$z) && ($z<=$D($i))} {
     set VS  [expr $VSS($i)];}

set VS [expr $VS*1000]

return $VS;}
```

external program - Get k_f parameter

```
proc Getkf {z} {
```

```
# get FA at the required depth
source GetFA.tcl;
set FA [GetFA $z];

# assign kf for respective FA
if {(0<=$FA) && ($FA<=28)} {
     set kf [expr (11000000/28)*$FA]}
if {(28.001<=$FA) && ($FA<=31)} {
     set kf [expr ((19000000 - 11000000)/(31 - 28))*($FA - 28) + 11000000]}
if {(31.001<=$FA) && ($FA<=31.999)} {
     set kf 19000000}
if {(32<=$FA) && ($FA<=34)} {
     set kf [expr ((26000000 - 19000000)/(34 - 32))*($FA - 32) + 19000000]}
if {(34.001<=$FA) && ($FA<=34.999)} {
     set kf 26000000}
if {(35<=$FA) && ($FA<=38)} {
     set kf [expr ((34000000 - 26000000)/(38 - 35))*($FA - 35) + 26000000]}

if {38.001<=$FA} {
set kf 34000000}

return $kf;}
```

external program - Get *k* parameter

```
# This procedure is built to output Dr for a given depth.

proc Getk {z} {

# get Dr at the required depth
source GetDr.tcl;
set Dr [GetDr $z];

# assign k for respective Dr
if {$z <= 2} {
     set k [expr (0.0439 * pow($Dr,2) - 0.5036 * $Dr + 7.3929)*271447.137]
if {$k > 275} {
     set k [expr 275*271447.137]}}
if {$z > 2} {
     set k [expr (0.0206 * pow($Dr,2) - 0.0383 * $Dr + 4.4167)*271447.137]
if {$k > 150} {
     set k [expr 150*271447.137]}}

return $k;}
```

external program - Get y_{50} parameter

```
# This program calculates Y50 of sand using  using API (1993) method.

proc CalcY50 {z d} {

set pi 3.14159265359

# get the friction angle at the required depth
source GetFA.tcl;
set FA [GetFA $z];
set FA [expr $FA*$pi/180]

# get the UW at the required depth
source GetUW.tcl;
set UW [GetUW $z];

# procedure to obtain k for sand
source Getk.tcl;
set k [Getk $z];

# obtain the at rest earth pressure coefficient
set Ko [expr 1 - sin($FA)]

# obtain the active earth pressure coefficient
set Ka [expr pow(tan($pi/4 - $FA/2),2)]

set beta [expr $pi/4 + $FA/2]

set A [expr 3 - 0.8*$z/$d]

if {$A < 0.9} {
set A 0.9}
set C1 [expr ($Ko*tan($FA)*sin($FA))/(tan($beta - $FA)*cos($FA/2)) + (pow(tan($beta),2)*tan($FA/2))/tan($beta-$FA) + $Ko*tan($beta)*(tan($beta)*sin($beta)-tan($FA/2))]
set C2 [expr tan($beta)/tan($beta-$FA) - $Ka]
set C3 [expr $Ko*tan($FA)*pow(tan($beta),4) + $Ka*(tan($beta) - 1)]

# ultimate lateral capacity due to wedge failure
set Pst [expr ($C1*$z + $C2*$d)*$UW*$z]

# ultimate lateral capacity due to flow failure at depth
set Psd [expr $C3*$d*$UW*$z]

# choose the smallest of Pst and Psd for Pult
if {$Pst == $Psd} {
    set Pult $Psd}
```

```
if {$Pst > $Psd} {
    set Pult $Psd}
if {$Psd > $Pst} {
    set Pult $Pst}


# obtain the displacement at which 50% of Pult is mobilized.
if {$Pult == 0} {
    set halfY 0.1}

if {$Pult > 0} {
    set halfY [expr (0.5*log(0.5/$A + 1) - 0.5*log(1 - 0.5/($A)))*(($A*$Pult)/($k*$z))]}

return $halfY}
```

external program - Get z_{50} parameter for t_h-y Spring

```
# This program calculates Tult of clay using Mosher (1984) equation.

proc Calcz50th {z d ElemSize} {

set pi 3.14159265359

# get the friction angle at the required depth
source GetFA.tcl;
set FA [GetFA $z];
set FA [expr $FA*$pi/180]

# procedure to obtain vertical stress at required depth
source GetVS.tcl;
set VS [GetVS $z];

# procedure to get initial slope, kf
source Getkf.tcl;
set kf [Getkf $z];

# obtain the active earth pressure coefficient
set Ka [expr (1 + sin($FA))/ (1 - sin($FA))]

# obtain ultimate shaft capacity
set Tulth [expr $VS*tan(0.8*$FA)]

# obtain the displacement at which 50% of Tulth is mobilized.
set z50th [expr $Tulth/$kf]

if {$z50th == 0} {
set z50th 0.1}
```

```
# obtain Tulth considering the pile diameter and element size.
set Tulth [expr $Tulth*$pi*$d*$ElemSize];

return $z50th}
```

external program - Get z_{50} parameter for *t-z* spring

```
# This program calculates Tult of clay using Mosher (1984) equation.

proc Calcz50t {z d ElemSize} {

set pi 3.14159265359

# get the friction angle at the required depth
source GetFA.tcl;
set FA [GetFA $z];
set FA [expr $FA*$pi/180]

# procedure to obtain vertical stress at required depth
source GetVS.tcl;
set VS [GetVS  $z];

# procedure to get initial slope, kf
source Getkf.tcl;
set kf [Getkf $z];

# obtain the active earth pressure coefficient
set Ka [expr (1 + sin($FA))/ (1 - sin($FA))]

# obtain earth pressure coefficient using Castello (1980)
set K [expr pow(10,(log10($Ka) - 0.017*($z/$d)))]

# obtain horizontal stress
set HS [expr $VS*$K]

# obtain ultimate shaft capacity
set Tult [expr $HS*tan(0.8*$FA)]

# obtain the displacement at which 50% of Tult is mobilized.
set z50t [expr $Tult/$kf]

if {$z50t == 0} {
set z50t 0.1}

# obtain Tult considering the pile diameter and element size.
set Tult [expr $Tult*$pi*$d*$ElemSize];
```

```
return $z50t}
```

external program - Get P_{ult} in sand

```
# This program calculates Pult of sand using API (1993) method.

proc CalcPult {z d ElemSize} {

set pi 3.14159265359

# get the friction angle at the required depth
source GetFA.tcl;
set FA [GetFA $z];
set FA [expr $FA*$pi/180]

# get the UW at the required depth
source GetUW.tcl;
set UW [GetUW $z];

# procedure to obtain k for sand
source Getk.tcl;
set k [Getk $z];

# obtain the at rest earth pressure coefficient
set Ko [expr 1 - sin($FA)]

# obtain the active earth pressure coefficient
set Ka [expr pow(tan($pi/4 - $FA/2),2)]

set beta [expr $pi/4 + $FA/2]

set A [expr 3 - 0.8*$z/$d]
if {$A < 0.9} {
set A 0.9}

set C1 [expr ($Ko*tan($FA)*sin($FA))/(tan($beta - $FA)*cos($FA/2)) + (pow(tan($beta),2)*tan($FA/2))/tan($beta-$FA) + $Ko*tan($beta)*(tan($beta)*sin($beta)-tan($FA/2))]
set C2 [expr tan($beta)/tan($beta-$FA) - $Ka]
set C3 [expr $Ko*tan($FA)*pow(tan($beta),4) + $Ka*(tan($beta) - 1)]

# ultimate lateral capacity due to wedge failure
set Pst [expr ($C1*$z + $C2*$d)*$UW*$z]

# ultimate lateral capacity due to flow failure at depth
set Psd [expr $C3*$d*$UW*$z]

# choose the smallest of Pst and Psd for Pult
```

```
if {$Pst == $Psd} {
    set Pult $Psd}
if {$Pst > $Psd} {
    set Pult $Psd}
if {$Psd > $Pst} {
    set Pult $Pst}

# obtain the displacement at which 50% of Pult is mobilized.
if {$Pult == 0} {
    set halfY 0.1}
if {$Pult > 0} {
    set halfY [expr (0.5*log(0.5/$A + 1) - 0.5*log(1 - 0.5/($A)))*(($A*$Pult)/($k*$z))]}
if {$Pult == 0} {
    set Pult 0.642}

# obtain Pult considering the element size
set Pult [expr $Pult*$ElemSize];

return $Pult}
```

external program - Get T_{ult} in sand

```
# This program calculates Tult of sand using Mosher (1984) equation.

proc CalcTult {z d ElemSize} {

set pi 3.14159265359

# get the friction angle at the required depth
source GetFA.tcl;
set FA [GetFA $z];
set FA [expr $FA*$pi/180]

# procedure to obtain vertical stress at required depth
source GetVS.tcl;
set VS [GetVS  $z];

# procedure to get initial slope, kf
source Getkf.tcl;
set kf [Getkf $z];

# obtain the active earth pressure coefficient
set Ka [expr (1 + sin($FA))/ (1 - sin($FA))]

# obtain earth pressure coefficient using Castello (1980)
set K [expr pow(10,(log10($Ka) - 0.017*($z/$d)))]

# obtain horizontal stress
```

```
set HS [expr $VS*$K]

# obtain ultimate shaft capacity
set Tult [expr $HS*tan(0.8*$FA)]

# obtain the displacement at which 50% of Tult is mobilized.
set halfz [expr $Tult/$kf]

# obtain Tult considering the pile diameter and element size.
set Tult [expr $Tult*$pi*$d*$ElemSize];

return $Tult}
```

external program - Get Q_{ult} in sand

```
# This program calculates Qult of sand.

proc CalcQult {z OD ID} {

set e 2.718281884;
set pi 3.14159265359

# get the friction angle at the required depth
source GetFA.tcl;
set FA [GetFA $z];
set FA [expr $FA*$pi/180]

# procedure to obtain vertical stress at required depth
source GetVS.tcl;
set VS  [GetVS $z];

# define bearing capacity coefficient
set Nq [expr 0.1581*pow($e,0.1462*$FA)]

# obtain Qult
set Qult [expr $Nq*$VS*$pi* (pow($OD,2) - pow($ID,2)) * 0.003086];

return $Qult}
```

external program - Get t_{ult} for t_h-y spring in sand

```
# This program calculates Tulth of sand using Mosher (1984) equation.

proc CalcTulth {z di do ElemSize} {

set pi 3.14159265359

# get the friction angle at the required depth
source GetFA.tcl;
```

```
set FA [GetFA $z];
set FA [expr $FA * $pi/180]

# procedure to obtain vertical stress at required depth
source GetVS.tcl;
set VS [GetVS  $z];

# procedure to get initial slope, kf
source Getkf.tcl;
set kf [Getkf $z];

# obtain ultimate shaft capacity
set Tulth [expr $VS*tan(0.8*$FA)]

# obtain the displacement at which 50% of Tulth is mobilized.
set halfz [expr $Tulth/$kf]

# obtain the area of the upside and downside of the thread
set Area [expr (pow((pow(0.05,2) + pow($pi * $di,2)),0.5) + pow(pow(0.05,2)+pow($pi * $do,2),0.5))/2 * 0.012 * 2]

# obtain Tulth considering the threads area.
set Tulth [expr $Tulth*$Area];

return $Tulth}
```